Transport électronique dans les matériaux à changement de phase amorphe

Jennifer Luckas

Jennifer Luckas. Transport électronique dans les matériaux à changement de phase amorphe. Other [cond-mat.other]. Université Paris Sud - Paris XI; Rheinisch-westfälische technische Hochschule (Aix-la-Chapelle, Allemagne), 2012. English. NNT : 2012PA112157 . tel-00743474

HAL Id: tel-00743474
https://theses.hal.science/tel-00743474v1

Submitted on 19 Oct 2012

UNIVERSITE PARIS-SUD 11

ÉCOLE DOCTORALE : *Sciences et Technologies de l'Information des Télécommunications et des Systèmes*

Laboratoire de Génie électrique de Paris

DISCIPLINE *: PHYSIQUE*

THÈSE DE DOCTORAT

par

Jennifer Maria Luckas

Electronic transport in amorphous phase-change materials

Directeur de thèse :	Christophe LONGEAUD	Directeur de recherche (CNRS)
Co-directeur de thèse :	Matthias WUTTIG	Professeur (RWTH Aachen)

<u>Composition du jury</u> :

Rapporteurs :	Charles MAIN	PhD (University of Dundee)
	Christophe BICHARA	Directeur de recherche (CNRS)
Examinateurs :	Volker MEDEN	Professeur (RWTH Aachen)
	Jean-Paul KLEIDER	Directeur de recherche (CNRS)

Le monde est un livre dont chaque pas nous ouvre une page.

(Alphonse de Lamartine)

Synthèse

Transport électronique dans les matériaux amorphes à changement de phase

Le travail présenté dans cette thèse apporte un éclairage sur le transport électronique dans les matériaux amorphes à changement de phase. En particulier, le rôle des défauts localisés a été étudié systématiquement avec des méthodes bien connues dans la communauté photovoltaïque. Cette thèse présente la première étude expérimentale sur les défauts des matériaux à changement de phase désordonnés mettant en lumière le lien direct entre la densité des défauts et les phénomènes de transport électronique.

Introduction :

Les matériaux à changement de phase ont été largement utilisés pour le stockage d'information. Cette famille de matériaux offre la combinaison exceptionnelle d'une cinétique de cristallisation très rapide et d'un grand contraste de résistivité ou réflectivité entre leur état ordonné (cristallin) ou désordonné (amorphe) (voir figure 1). Ce phénomène de changement de phase est réversible et ouvre donc des perspectives d'applications comme des mémoires non volatiles [1,2].

Les transformations de phases sont réalisées en employant une source thermique comme un laser ou un champ électrique : pour provoquer la cristallisation une impulsion de puissance est appliquée qui chauffe le matériau au-dessus de sa température de cristallisation pendant une durée suffisante. De même façon, la transition vitreuse (cristallin -> amorphe) est réalisée en chauffant le matériau au-dessus de sa température de fusion suivi d'un refroidissement très rapide. Dans les matériaux à changement de phase la transition vitreuse a besoin d'une grande vitesse de refroidissement pour éviter la cristallisation. Par conséquent, les variations de phases sont effectuées très localement, dans des régions ayant une dimension de quelques nanomètres.
Ces deux variations très locales de conductivité et de réflectivité permettent d'inscrire une suite de 1 (e.g. forte conductivité) ou de 0 (e.g. faible conductivité) sur une couche mince et donc de stocker des informations. La lecture de ces suites de 1 et de 0 peut se faire par des moyens électriques en utilisant le changement de résistivité [1, 2]. Elle peut se faire également par des moyens optiques en utilisant le changement de réflectivité.

La technologie des matériaux à changement de phases permet des temps de transition aussi faibles que quelques nanosecondes [3, 4]. Par conséquent, cette technologie est très concurrentielle. Dans un proche avenir la technologie de matériaux à changement de phase peut détrôner les Mémoires flash. En outre, cette technologie non-volatile a le potentiel de remplacer les mémoires dynamiques à accès direct, qui appartiennent aux technologies volatiles. Une description détaillée sur les matériaux à changement de phase est présentée dans chapitre 2 de cette thèse

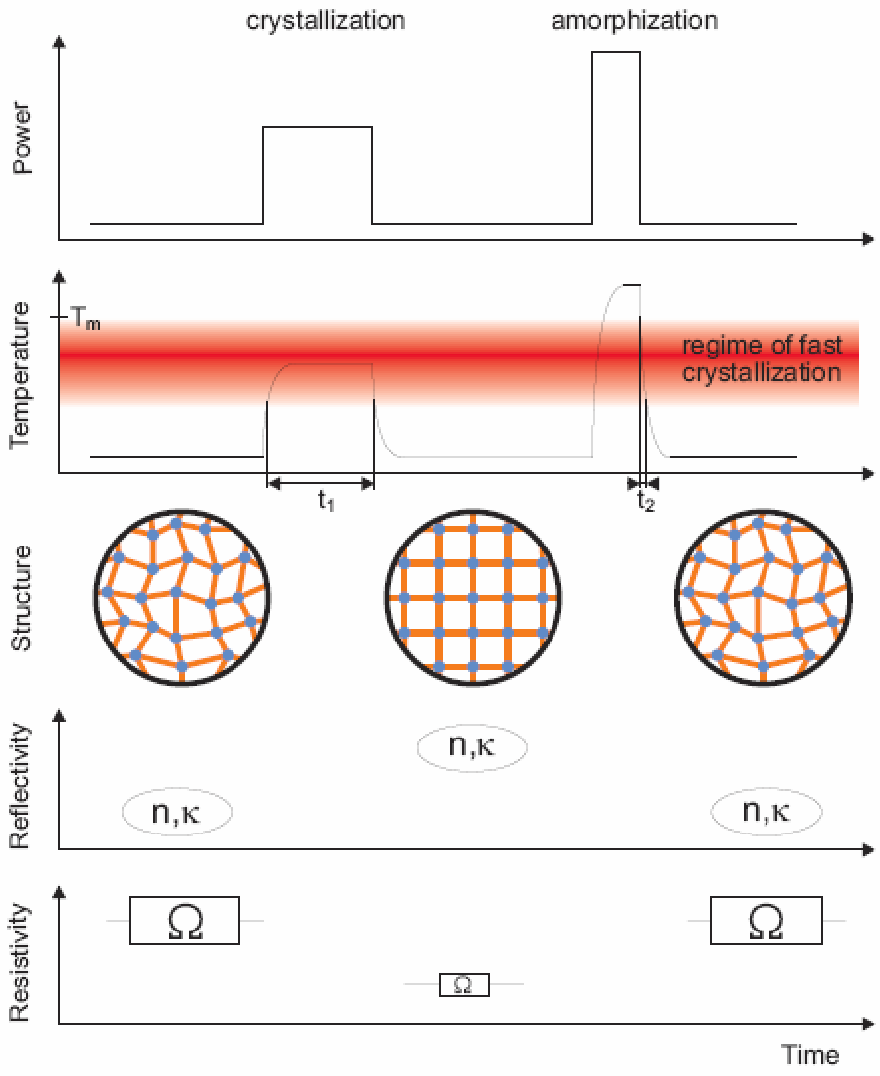

Figure 1: Les matériaux à changement de phase présentent une phase cristalline et une phase amorphe. Le changement de phase s'effectue sur une échelle de temps de quelques nanosecondes. En plus d'une cinétique de cristallisation très rapide, les phases amorphe et cristalline montrent un contraste exceptionnel de leurs propriétés physiques. L'état cristallin présente une grande réflectivité et faible résistivité. En revanche, la phase amorphe est caractérisée par une faible réflectivité et une forte résistivité. En pratique les transitions de phase sont induites par un laser ou un champ électrique chauffant le matériau pendant une durée appropriée soit au-dessus sa température de cristallisation ou de sa température de fusion. Le régime de la cristallisation rapide est matérialisé par l'ombrage rouge sur la figure. Figure d'après la référence [5].

Les matériaux à changement de phase se divisent en trois catégories (voir figure 2). Les matériaux de la première catégorie suivent la ligne pseudo-binaire entre GeTe et Sb_2Te_3, y compris $Ge_8Sb_2Te_{11}$, $Ge_2Sb_2Te_5$ et $Ge_1Sb_2Te_4$.

La deuxième catégorie des matériaux de changement de phase est constituée des alliages proches de la composition $Sb_{70}Te_{30}$. Le dopage par l'indium et l'argent améliore la stabilité thermique. Ainsi la température de cristallisation augmente de ~100°C ($Sb_{70}Te_{30}$) à ~170°C (AgInSbTe).

Les alliages avec de l'antimoine comme $Ge_{15}Sb_{85}$ ou GeSbMnSn constituent la troisième catégorie des matériaux à changement de phase. Cette troisième catégorie se distingue des autres car cette famille ne comprend pas de chalcogénures.

Les matériaux de la première et deuxième catégorie ont été largement utilisés dans le stockage optique des données dès l'année 1990 comme indiqué sur la figure 2.

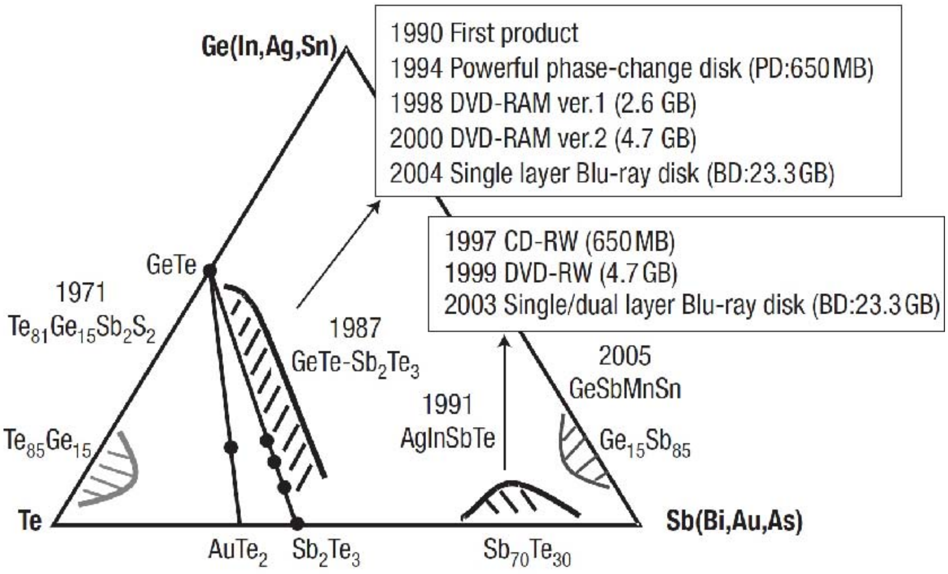
1990 First product
1994 Powerful phase-change disk (PD:650MB)
1998 DVD-RAM ver.1 (2.6 GB)
2000 DVD-RAM ver.2 (4.7 GB)
2004 Single layer Blu-ray disk (BD:23.3GB)

1997 CD-RW (650MB)
1999 DVD-RW (4.7GB)
2003 Single/dual layer Blu-ray disk (BD:23.3GB)

Figure 2: La plupart de matériaux à changement de phase connus sont contenus dans le diagramme ternaire des compositions Ge :Sb :Te. Les matériaux à changement de phase sont classés en trois catégories : La famille GeSbTe incluant les alliages suivant la ligne pseudo-binaire entre GeTe et Sb_2Te_3, la famille $Sb_{70}Te_{30}$ dopée et la famille composée d'alliages avec de l'antimoine. Les matériaux à changement de phase sont largement utilisés dans le stockage optique. Figure d'après la référence [1].

Les phénomènes de transport électroniques dans les matériaux à changement de phase amorphe

Les matériaux à changement de phase amorphes présentent des propriétés de transport électroniques extraordinaires. Le phénomène connu sous le nom de seuil de commutation dénote la chute en résistivité par application d'un champ électrique qui dépasse une valeur critique (threshold switching) [1, 3, 6]. Au dessus de ce champ électrique le matériau montre une conductivité très élevée en restant amorphe (amorphous ON state). Dans cet état excité la chaleur engendrée par effet Joule est suffisante pour provoquer la cristallisation (memory switching). Contrairement à la phase amorphe la phase cristalline présente une caractéristique tension courant linéaire (voir figure 3a).

Un autre phénomène important au regard d'applications industrielles est l'évolution de la résistance de l'état amorphe [7-10]. Au lieu du simple code binaire (0,1) les matériaux à changement de phase offrent la possibilité de réaliser un code à plusieurs niveaux comme (0, 1, 2, 3). La résistance d'une cellule mémoire est variable en ajustant le volume amorphe à l'intérieur de la cellule (voit figure 3b). Cependant la résistivité des matériaux à changement de phase amorphe n'est pas stable et il a été observé une croissance en fonction du temps ou en fonction de la température de recuit. L'évolution de la résistance de l'état amorphe limite la possibilité d'établir un stockage sur plusieurs niveaux, car ce phénomène peut entraîner la perte de données. Cette perte de donnée est illustrée par l'exemple de deux cellules mémoires en figure 3b. Originalement la cellule 1 et la cellule 2 ont été programmées dans deux états amorphes bien distincts. Toutefois, après 10^5 s il n'est plus possible de dissocier ces deux états ce qui a pour résultat d'avoir des données corrompues [11].

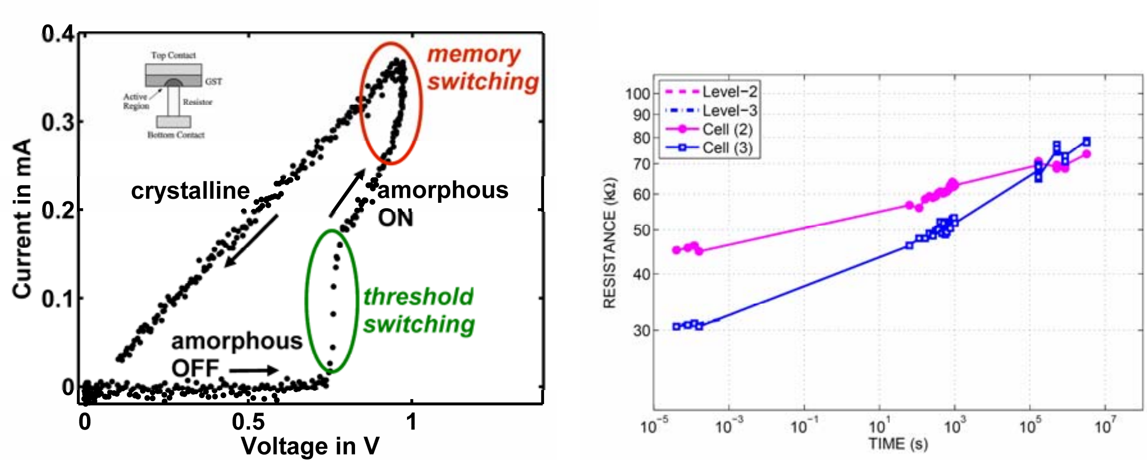

(a) **(b)**

Figure 3: Le seuil de Commutation (a) et l'évolution de la résistance de l'état amorphe (b) sont des phénomènes très importants. Cependant leur origine est encore mal connue. Cette thèse apporte un éclairage sur le rôle des défauts localisés dans ces deux phénomènes de transport électronique. Figure (a) d'après la référence [1] et figure (b) d'après la référence [11].

Plusieurs théories s'affrontent pour expliquer ces deux processus, toutes invoquant la présence de défauts limitant le transport de porteurs de charge [7-10]. Cependant, tandis que certains auteurs affirment que l'évolution de la résistivité est due à une diminution du nombre de défauts, d'autres prétendent au contraire qu'une augmentation des défauts en est responsable. Aucune expérience n'a pu donner d'évidences pour l'une ou l'autre hypothèse. Une description détaillée sur les différents modèles est présentée dans chapitre 3 de la thèse.

Méthodes appliquées dans cette thèse

Dans le cadre de cette thèse plusieurs méthodes expérimentales ont été combinées. La présente étude porte sur des couches minces amorphes déposées par pulvérisation cathodique. La structure amorphe a été vérifiée par la diffraction de rayons X. En revanche, la stœchiométrie des couches minces déposées a été mesurée par une microsonde de Castaing. Les propriétés optiques ont été étudiées en employant la techniques d’ellipsométrie et l’analyse infrarouge à transformée de Fourier. De plus, la photoconductivité et la conductivité d’obscurité ont été étudiées à différentes températures dans la plage 100 K - 500 K. Deux méthodes différentes ont été appliquées pour mettre en évidence les défauts localisés : soit la spectroscopie par déviation photothermique, soit la technique du photo courant modulé. Le stress mécanique a été mesuré par un système de mesure de courbure des films avec l’objectif d’étudier l’influence du stress sur la résistivité amorphe. Finalement, nous avons utilisé la spectrométrie d'absorption des rayons X (EXAFS) qui utilise principalement le rayonnement synchrotron pour l’étude de l'environnement atomique des films minces étudiés.
Une description plus détaillée des méthodes appliquées est donnée dans le chapitre 4 de cette thèse.

La pulvérisation cathodique

La pulvérisation cathodique est une méthode de dépôt de couche mince. Cette technique consiste en la condensation d’une vapeur issue d’une source solide, nommée cible, sur un substrat. Par conséquence, la pulvérisation cathodique permet facilement la synthèse de plusieurs matériaux en utilisant des cibles de différentes compositions.

La diffraction de rayons X

La diffraction de rayons X est une technique d'analyse fondée sur la diffraction des rayons X par la matière. Selon la relation Bragg-Brentano, les diffractogrammes des matériaux cristallins présente des maximums en intensité très pointus. En revanche, les structures amorphes sont caractérisées par des diffractogrammes montrant les maxima larges.

La microsonde de Castaing

La microsonde de Castaing est une méthode d'analyse stœchiométrique basée sur le bombardement de la surface d’une couche mince avec des électrons. Le spectre des rayons X émis sous cette sollicitation permet de déterminer la concentration des éléments compris dans la couche mince.

La technique d'ellipsométrie
L'ellipsométrie est une technique de caractérisation optique. Cette technique exploite le changement d'état de polarisation de la lumière après la réflexion de la lumière à la surface de l'échantillon étudié.

L'analyse infrarouge à transformée de Fourier
L'analyse infrarouge à transformée de Fourier est une technique de caractérisation optique fondé sur l'interféromètre de Michelson. Cette technique permet de mesurer la variation de la réflectivité en fonction de l'énergie des photons.

Photoconductivité et la conductivité d'obscurité
La photoconductivité et la conductivité d'obscurité à basse température (de 60 K à 300 K) ont été mesurées dans un cryostat en employant deux contacts. En revanche, la résistivité à haute température a été mesurée sous atmosphère neutre (argon) dans une géométrie à quatre points.

La spectroscopie par déviation photothermique
La spectroscopie par déviation photothermique est basée sur l'effet mirage. La surface de l'échantillon est illuminée par une source monochromatique et les recombinaisons chauffent le liquide qui l'entoure. La déviation d'un laser passant près à la surface donne des informations sur les défauts présents dans le matériau étudié.

La technique du photo courant modulé
Dans la technique du photo courant modulé l'échantillon est illuminée par une lumière monochromatique modulée en intensité. L'excitation bande à bande des porteurs engendre un photo courant modulé dont le déphasage avec l'excitation donne des informations concernant la densité de défauts.

Mesure du stress mécanique
La mesure de la courbure de la couche mince déposée sur un substrat offre la possibilité d'étudier l'évolution du stress mécanique lors d'un recuit de la couche mince.

La spectroscopie d'absorption des rayons X (EXAFS)
La spectroscopie d'absorption des rayons X (EXAFS) est une technique apportant des informations sur l'environnement atomique d'un élément donné. L'analyse de spectrométrie d'absorption des rayons X en utilisant principalement le rayonnement synchrotron offre la possibilité d'étudier l'ordre dans le matériau à l'échelle atomique.

Résultats de la thèse

Cette thèse comprend une combinaison de diverses méthodes expérimentales. La méthode du photo courant modulé s'est révélée être un outil de grande utilité pour étudier les défauts localisés dans les matériaux à changement de phase désordonnés alors que d'autres méthodes comme la spectroscopie par résonance électronique de spin ont échoué. Originalement la méthode du photo courant modulé a été développée pour l'étude des matériaux montrant une haute photoconductivité. Néanmoins, cette thèse a montré que cette méthode peut même être appliquée aux matériaux comme GeTe qui présentent une photoconductivité très faible à température ambiante.

L'amélioration des méthodes

L'étude sur des matériaux amorphes à changement de phase a permis l'amélioration de la méthode du photo courant modulé. Dans cette méthode l'échantillon est illuminé par une lumière monochromatique modulée périodiquement. Le flux modulé ($F=F_{dc}+F_{ac}\sin(\omega t)$) crée des porteurs libres par excitation à travers la bande d'énergies interdites. Grâce à l'interaction des porteurs libres avec des défauts localisés agissant comme pièges le photo courant et le flux d'excitation ne sont pas en phase, mais présentent un déphasage ϕ ($I_{ph}=I_{dc}+I_{ac}\sin(\omega t+\phi)$). En mesurant ce déphasage ϕ et l'amplitude du photo courant modulé I_{ac} , on obtient la densité des défauts N à l'énergie E_ω par la relation:

$$\frac{N(E_\omega)\cdot c}{\mu}=\frac{2}{\pi}Aq\mathrm{E}G_{ac}\cdot\frac{\sin(\phi)}{|I_{ac}|} \tag{1}$$

Le coefficient de capture c souligne l'interaction entre les défauts localisés et les porteurs libres : plus grande est la valeur de c, plus les porteurs libres sont piégés. Le paramètre μ dénote la mobilité des porteurs libres, E le champ électrique, q la charge électronique, A la section de conduction dans laquelle circule le courant et G_{ac} le taux de génération des porteurs libres. Ainsi, tous les paramètres du membre de droite de l'équation (1) sont connus expérimentalement. En revanche, les paramètres du membre de gauche, Nc/μ, correspondent à une densité d'états réduite. En effet, le transport électronique n'est pas dominé seulement par la densité des défauts N. Evidemment la mobilité des porteurs libres et leur interaction avec des pièges ont une influence sur le transport électronique. Ainsi, le transport électronique est vraiment contrôlé par la densité réduite Nc/μ au lieu de la densité N seule.

En pratique, le photo courant modulé est dominé par les pièges à l'énergie E_ω dont le taux d'émission e égale la fréquence d'excitation ω. De cette relation $e(E_\omega)=\omega$ on obtient pour les matériaux de type p comme GeTe ou $Ge_2Sb_2Te_5$ [12, 13, 14]:

$$\begin{aligned} &e_p(E_\omega)=\nu_p\exp(E-E_v/k_bT)\\ &\Leftrightarrow E_\omega=E-E_v=k_bT\ln(\nu_p/\omega) \end{aligned} \tag{2}$$

où le paramètre ν_p représente la fréquence de saut. La combinaison des équations (1) et (2) permet la spectroscopie de la densité réduite en variant la température T et la fréquence d'excitation ω. Selon l'équation (2), les états les plus proches du bord de la bande de valence E_v sont détectés par des mesures à hautes fréquences et les états les plus profonds par des mesures à basses fréquences à une température fixe. De la même façon, à fréquence d'excitation fixe, les défauts les plus proches de E_v sont détectés à basse température et les états les plus profonds sont détectables à plus hautes températures. Les mesures sont donc réalisées à différentes température et, pour chaque température, pour différentes fréquences d'excitation. Les pas de température et la gamme de fréquence d'excitation sont choisis pour qu'il y ait une plage commune d'énergies sondées entre deux températures consécutives La fréquence de saut ν est alors estimée par l'analyse des données en optimisant le chevauchement des courbes $Nc/\mu(E)$ obtenues à deux températures consécutives en variant la pulsation d'excitation ω.

On peut voir que l'équation (2) ne prend pas en compte une évolution du bord de la bande de valence avec la température. En effet, et en particulier dans les matériaux amorphes à changement de phase, la largeur de la bande d'énergies interdites change considérablement avec température, ce qui implique que le bord de la bande de valence évolue avec la température $E_v = E_v(T)$. Dans le cadre de cette thèse, il a été démontré que l'effet $E_v = E_v(T)$ peut être pris en compte simplement par des termes de correction. Généralement la bande d'énergies interdites diminue avec température [15]. Dans les matériaux à changement de phase on a observé par des méthodes optiques [16] que la largeur de la bande d'énergies interdites, E_g^{04}, varie de façon quadratique avec T

$$E_g^{04} = E_g(0) - \xi T^2 \tag{3}$$

Cette diminution de la largeur de la bande d'énergies interdites peut être expliquée par un rapprochement des bandes d'états étendus. Il a été montré que le rapprochement des deux bandes d'états étendus est essentiellement du au mouvement de la bande de valence, le bord de bande de conduction restant quasi fixe Nous avons envisagé deux scénarios différents pour prendre en compte cette évolution.

Correction Varshni :

Dans le premier scénario l'influence de la diminution de la bande d'énergies interdites est prise en compte en ajoutant systématiquement le terme $-\xi T^2$ à l'équation (2) :

$$E_\omega = E_v(T = 0\ K) + k_b T \ln(\nu_p/\omega) - \xi \cdot T^2 \tag{4}$$

Correction au prorata :

Dans le deuxième scénario, la correction de l'équation (2) prend en compte la position en énergie des états sondés. Par exemple, les états du milieu de la bande voient leur position corrigée par $-0.5 \cdot \xi T^2$ et les états proches de la bande de valence E_v voient leur position corrigée par $-\xi T^2$. Cette correction au pro rata de la position en énergie des pièges sondés donne:

$$\Delta E = k_b T \ln\left({}^{\nu_p}\!/_{\omega} \right) - \xi T^2 \left(1 - \frac{\Delta E}{E_g(T)} \right)$$

$$\Leftrightarrow E_\omega = E_v(T = 0K) + \frac{k_b T \ln\left({}^{\nu_p}\!/_{\omega} \right) - \xi T^2}{1 - {}^{\xi T^2}\!/_{E_{04}(T)}} \tag{5}$$

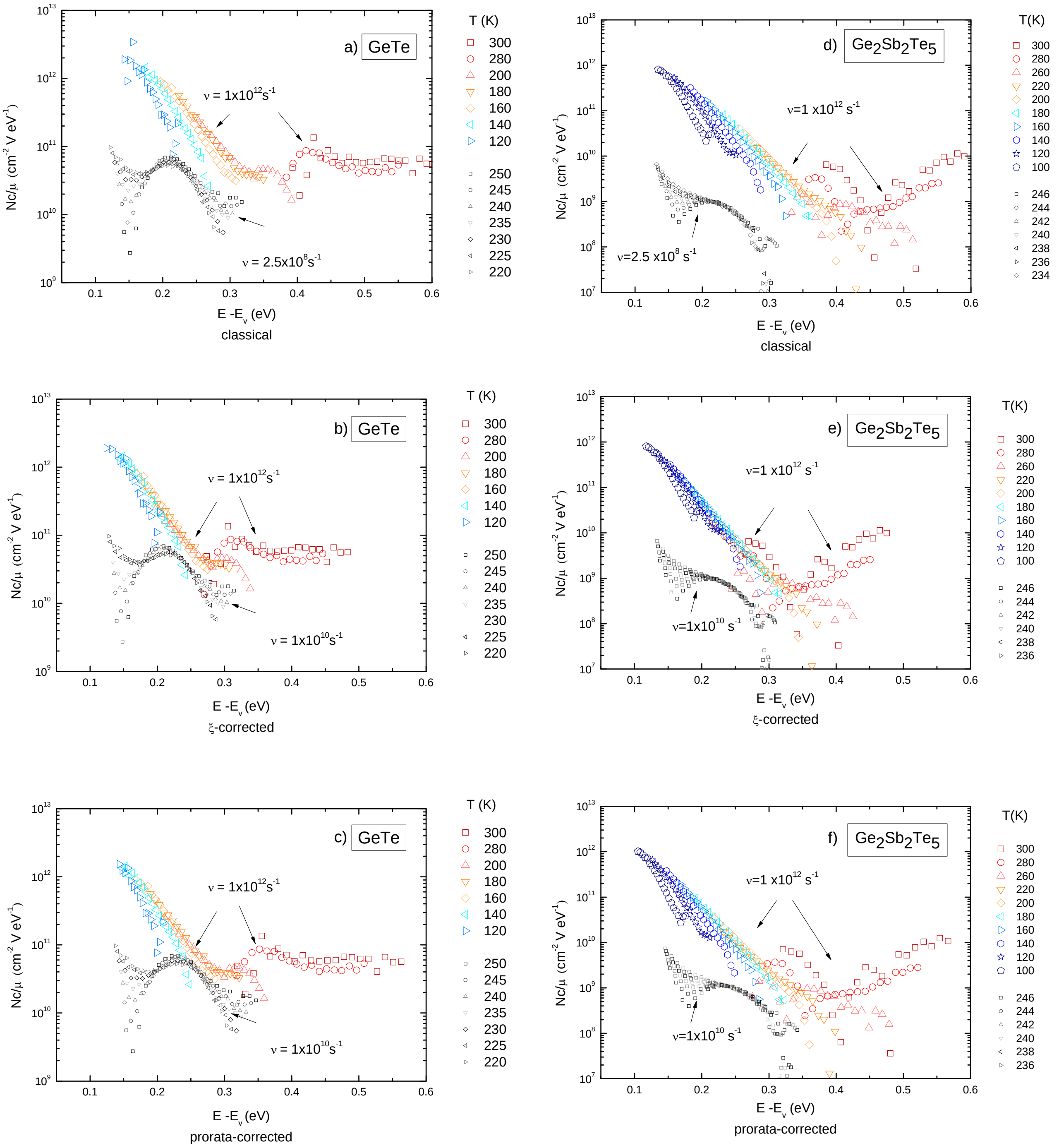

Figure 4 : Spectroscopie de la densité d'états obtenue par la méthode du photo courant modulé sur deux matériaux amorphes à changement de phase : a-GeTe et a-$Ge_2Sb_2Te_5$. Les données ont été traitées en appliquant soit l'équation (2) - le traitement classique (a,d)- soit l'équation (4) – la correction complète en ξ (b,e)-, soit l'équation (5) – la correction au pro rata (c,f)-. Les fréquences de saut ν obtenues en optimisant le chevauchement des courbes décrivant différents types de défauts (Queue de bande de valence mesurée de 120 K à 200 K, défaut à ~0.2 eV détecté de 220 K à 250 K et défauts profonds mesurés de 260 K à 300 K), sont également indiquées sur la figure. Figure d'après la référence [17].

La figure 4 montre l'effet des ces deux corrections proposées en prenant pour exemple a-GeTe et a-$Ge_2Sb_2Te_5$. Les spectres montrent trois différents types de défauts : la queue de bande de valence mesurée de 120 K à 200 K, un défaut à ~0.2 eV détecté de 220 K à 250 K et des défauts profonds mesurés de 260 K à 300 K.

Il a été montré [14] que la densité d'états du matériau sondé était donnée par l'enveloppe supérieure de l'ensemble des spectres de photo courant modulé obtenus à différentes températures et différentes fréquences. Le traitement classique des données selon l'équation (2) montre que les spectres obtenus à basse température et décrivant la queue de bande de valence s'écartent de l'enveloppe supérieure de façon importante, en particulier pour les mesures réalisées à basse fréquence (voir figures 4a et 4d). Ces écarts peuvent être attribués à l'influence du flux continu utilisé pour réaliser l'expérience. Le choix de la fréquence de saut ν se fait alors pour optimiser l'enveloppe supérieure et minimiser ces écarts. On constate cependant que ces écarts diminuent considérablement lorsque l'évolution avec la température de la bande d'énergies interdites est prise en compte (voir figures 4b, 4c, 4e 4f). Ces écarts ne sont donc pas uniquement dus à l'influence du flux continu.
Prendre en compte l'évolution de la largeur de la bande interdite permet également de raffiner les estimations des fréquences de saut. Ceci est particulièrement flagrant pour les défauts situés vers 0.2 eV au dessus de E_V. Le traitement des donnés classique donne une fréquence de saut de $\nu = 2.5\text{x}10^8$ s^{-1}, une valeur relativement faible. En pratique, on attend des fréquences de phonon typiques pour le matériau étudié de l'ordre de $\sim 10^{12}$ s^{-1} en général. Le traitement des données selon l'équation (4) ou l'équation (5) donne des fréquences de saut plus raisonnables, $\nu = 1\text{x}10^{10}$ s^{-1}.

En conséquence, les estimations de fréquences de saut trop petites ont probablement leur origine dans la non prise en compte de l'évolution de la bande interdite avec la température. Une description détaillée de l'amélioration de la méthode de photo courant modulé en prenant en compte cette évolution est donnée dans chapitre 5 de la thèse. L'influence de l'évolution de la largeur de la bande interdite sur des mesures réalisées sur du silicium amorphe hydrogéné est également présentée.

Influence de la densité des défauts localisés sur la commutation électrique des chalcogénures amorphes

La résistivité des chalcogénures amorphes chute lorsqu'on applique un champ électrique qui dépasse une valeur critique [1]. Le Tableau 1 donne ces valeurs critiques pour différents chalcogénures ainsi que la largeur de leur bande interdite à la température ambiante [2, 4] .

Tableau 1 : Champ électrique de seuil et largeur de bande interdite à la température ambiante pour différents chalcogénures amorphes.

matériau	bande interdite (eV)	Champ de seuil (V/µm)
$Ge_{15}Sb_{85}$	0.41	8
AgInSbTe	0.65	19
$Ge_{15}Te_{85}$	1.00	37
$Ge_2Sb_2Te_5$	0.80	56
GeTe	0.81	143

Evidemment, un matériau avec une petite bande interdite présente un faible champ d'électrique de seuil. Toutefois, les alliages $Ge_{15}Te_{85}$.,$Ge_2Sb_2Te_5$ et GeTe qui ont des largeurs de bande interdite voisines présentent de grandes différences dans leurs champs électriques critiques. Dans le cadre de cette thèse nous avons mesuré la densité d'états localisés avec l'objectif d'étudier l'influence des défauts sur le champ électrique de seuil.

La figure 5 montre les densités d'états obtenues pour a-GeTe, a-$Ge_2Sb_2Te_5$ et a-$Ge_{15}Te_{85}$ .en utilisant le traitement des données classique. Les matériaux à changement de phase, soit a-GeTe et a-$Ge_2Sb_2Te_5$ montrent trois différentes types des défauts : les états de la queue de bande de valence, un défaut à ~0.2 eV et des défauts profonds. En revanche, l'alliage a-$Ge_{15}Te_{85}$ – qui a une cinétique de cristallisation lente - présente seulement une queue de bande de valence.

La densité d'états réduite pour les états profonds situés vers le milieu de la bande d'énergie interdite est la plus grande pour a-GeTe ($Nc/\mu = 10^{11}\ cm^{-2}VeV^{-1}$) suivi de a-$Ge_2Sb_2Te_5$ ($Nc/\mu = 10^{10}\ cm^{-2}VeV^{-1}$). La densité la plus petite est obtenue pour a-$Ge_{15}Te_{85}$ stœchiométrique ($Nc/\mu = 10^{8}\ cm^{-2}VeV^{-1}$). Cette étude sur ces trois matériaux, ayant une largeur de bande d'énergie interdite comparable, montre bien que les matériaux caractérisés par un grand champ d'électrique de seuil présentent aussi une grande densité de défauts. Ce résultat implique que le phénomène de Seuil de Commutation est contrôlé par un mécanisme de génération - excitation à travers la bande d'énergie interdite par un fort champ électrique– et recombinaison des porteurs excités dans les défauts localisés. Cette étude est présentée de façon plus détaillée dans le chapitre 5 de cette thèse.

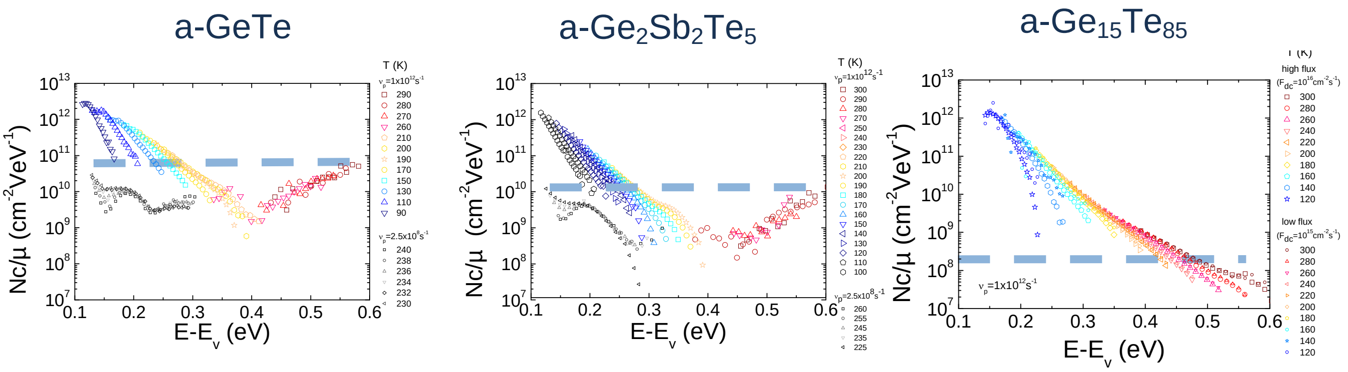

Figure 5 : Densité d’états *Nc/μ* mesuré sur a-GeTe, a-Ge$_2$Sb$_2$Te$_5$ et a-Ge$_{15}$Te$_{85}$. L’alliage GeTe montre un fort champ de seuil *E_t = 143 V/μm*, tandis que l’alliage a-Ge$_{15}$Te$_{85}$, plus riche en tellure, présente un champ critique *E_t= 37 V/μm*. Le champ électrique critique mesuré sur a-Ge$_2$Sb$_2$Te$_5$ se situe entre les deux *E_t = 56 V/μm*. Ces trois chalcogénures ne montrent pas de grandes différences de largeur de bande interdite pouvant expliquer les grandes différences dans leurs champs de seuil. Néanmoins, les matériaux qui présentent une grande densité d’états profonds montrent également un grand champ critique. Ce résultat implique que l’origine du phénomène de seuil de commutation se trouve dans un mécanisme de génération à travers la bande interdite et de recombinaison dans les défauts profonds.

Influence de la densité de défauts sur l’évolution de la résistivité amorphe

Il a été observé que la résistivité amorphe augmente avec le temps dans les matériaux à changement de phase suivant une loi de puissance [8]:

$$\rho(t)=\rho_0(t+t_0)^{\alpha} \qquad (6)$$

En général, le paramètre α dépend à la température de mesure. Dans une première étape dans cette partie de la thèse nous avons étudié l’évolution de la résistivité amorphe avec pour objectif de mettre en évidence le mécanisme à l’origine de cette évolution. L’alliage GeTe montre une grande évolution de sa résistivité amorphe, reflétée par une grande valeur α ~ 0.1. Ainsi, nous avons étudié l’influence du recuit et du vieillissement sur a-GeTe.

Étude sur a-GeTe

Dans le cadre de cette thèse on a observé que

- La résistivité augmente avec le recuit ainsi que l’énergie d’activation du courant d’obscurité.
- La conductivité d’obscurité montre une meilleure activation après recuit ou vieillissement à température d’ambiance.
- Un vieillissement de 3 mois à température ambiante a le même effet sur la conductivité d’obscurité qu’un recuit à 80 °C pendant une heure.
- La photoconductivité diminue après recuit.
- La bande d’énergie interdite s’ouvre par vieillissement ou recuit.
- Le stress mécanique diminue pendant le recuit.
- La phase amorphe semble plus ‘ordonnée’ après recuit.

- L’évolution des défauts ne montrent pas une caractéristique simple avec le vieillissement: bien que les états profonds disparaissent, le défaut à 0.2 eV augmente en densité. La queue de bande de valence demeure inchangée.

Ces résultats suggèrent que le phénomène d’évolution de la résistivité amorphe a son origine dans la relaxation de la structure désordonnée vers un état plus ordonné.

Étude sur les systèmes a-GeSnTe, a-GeSbTe et AgInSbTe

Dans une deuxième étape de la partie de cette thèse nous avons essayé d’identifier un matériau à changement de phase montrant une résistivité amorphe stable. Avec cet objectif nous avons étudié les systèmes GeSnTe qui sont encore mal connus.

En augmentant la concentration d’étain nous avons observé :

- Une réduction de la résistivité amorphe par deux ordres de grandeur.
- Une diminution de la température de cristallisation, de l’énergie d’activation du courant d’obscurité et la largeur de la bande interdite.
- Une réduction de la densité des défauts
- Un paramètre $\alpha(50°C)$, mesuré à 50 °C, décroissant de $\alpha = 0.129$ (a-GeTe) à $\alpha = 0.053$ (a-$Ge_2Sn_2Te_4$).

L’étude sur les systèmes GeSnTe a montré que les matériaux à changement de phase ayant une résistivité amorphe plus stable présentent une faible énergie d’activation du courant d’obscurité. Cette corrélation est vérifiée également pour les systèmes GeSbTe et AgInSbTe (voir Figure 6).

Le chapitre 6 donne une explication détaillée sur ces études sur le phénomène d’évolution de la résistivité amorphe. De plus, le lien entre l’évolution de la résistivité amorphe et le stress mécanique est discuté à l’exemple du GeTe et $Ge_2Sn_2Te_4$. Une description des méthodes utilisées est présentée dans chapitre 4 de cette thèse.

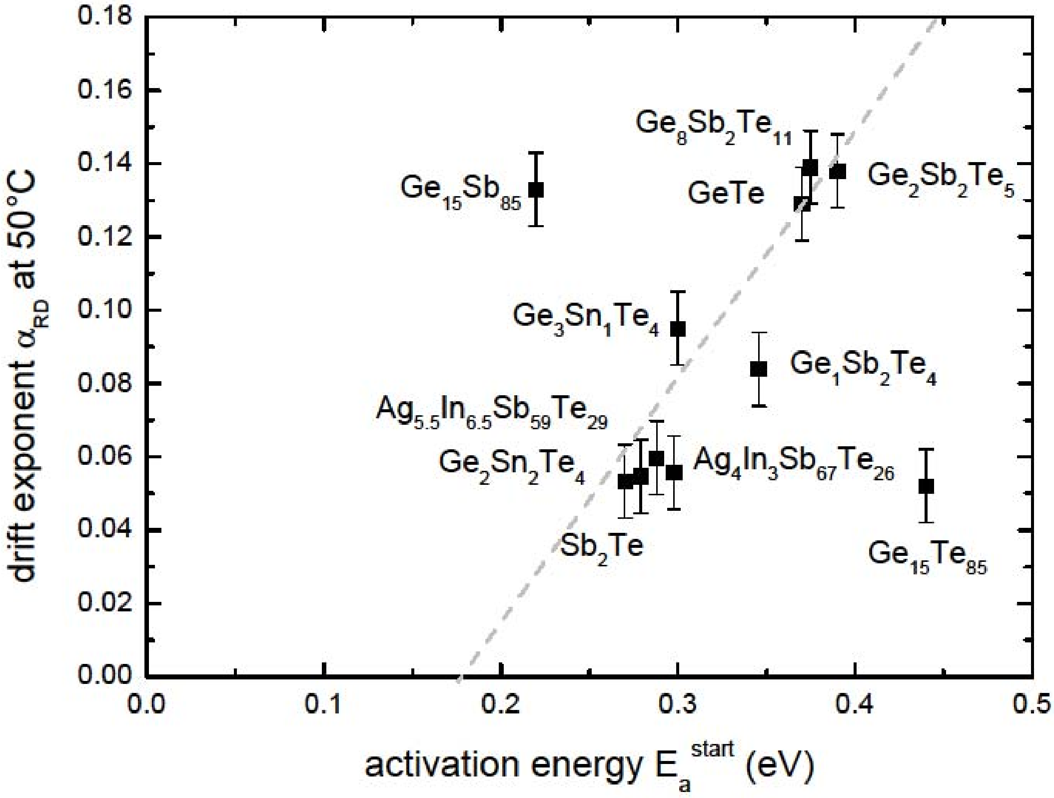

Figure 6 : Comparaison de l'évolution de la résistivité amorphe de différents matériaux à changement de phase pendant un recuit à 50 °C. La plupart des matériaux étudiés montrent une bonne corrélation entre le paramètre α*(50°C)* et l'énergie d'activation du courant d'obscurité E_a^{start} mesurée lors du chauffage. Cette étude montre bien que les matériaux à changement de phase présentant une résistivité plus stable présentent également une faible énergie d'activation E_a^{start}.

Listes des références

Cette liste donne les références citées dans ce résumé. Une liste des références plus détaillée se trouve dans l'annexe du manuscrit de cette thèse.

[1] M. Wuttig and N. Yamada, *Nat. Mat.* **6**, 824 (2007).
[2] S. Shportko, S. Kremers, M. Woda, D. Lencer, J. Robertson, M. Wuttig, *Nat. Mat.* **7**, 653 (2008)
[3] G. Bruns, P. Merkelbach, C. Schlockermann, M. Salinga, M. Wuttig, T.D. Happ, J.B. Philipp, M. Kund, *Appl. Phys. Lett.* **95**, 043108 (2009).
[4] D. Krebs, S. Raoux, C.T. Rettner, G.W. Burr, M. Salinga, M. Wuttig, *Appl.Phys. Lett.* **95**, 082101 (2009).
[5] M. Salinga, *Phase-change technology for non-volatile Electronic Memories*, RWTH Aachen, Diss., (2008).
[6] S.R. Ovshinsky, *Phys. Rev. Lett.* **21**, 1450 (1968).
[7] I.V. Karpov *et al.*, *J. Appl. Phys.* **102**, 124503 (2007).
[8] M. Boniardi, A. Redaelli, A. Pirovano, I. Tortorelli, F. Pellizzer, *J. Appl. Phys.* **105**, 084506 (2009)
[9] A. Pirovano, A. Lacaita, F. Pellizzer, S.A. Kostylev, A. Benvenuti, R.Bez, *International Electron Devices Meeting IEDM '07* **51**,714-719 (2004).
[10] D. Ielmini, S.Lavizzari, D.Sharma and A.L. Lacaita, *Appl. Phys Lett.* **92**, 193511 (2008).
[11] N. Papandreou, H. Pozidis, T. Mittelholzer, G. Close, M. Breitwisch, C. Lam, E-Eleftheriou, *3rd IEEE International Memory Workshop (IMW) IEEE,*(2011).
[12] H. Oheda, *J. Appl. Phys.* **52**, 6693 (1981).
[13] R. Brüggemann, C. Main, J. Berkin, S. Reynolds, *Philos. Mag. B* **62**, 29 (1990).
[14] C. Longeaud, J.P. Kleider, *Phys. Rev. B*, **45**, 11672 (1992).
[15] Y.P. Varshni, *Physica* **34**, 149 (1967).
[16] J. Stuke, *J. of non-cryst. solids* **4**, 1 (1970).
[17] J. Luckas , S. Kremers, D. Krebs, M. Salinga, M. Wuttig, C. Longeaud, *J. Appl. Phys.* **110**, 013719 (2011).

Abstract

Phase change materials combine a pronounced contrast in resistivity and reflectivity between their disordered amorphous and ordered crystalline state with very fast crystallization kinetics. Typical phase-change alloys are composed out of the elements germanium, antimony and tellurium. Due to the exceptional combination of properties phase-change materials find already broad application in non-volatile optical memories such as CD, DVD or Bluray Disc. Furthermore, this class of materials demonstrates remarkable electrical transport phenomena in their disordered state, which have shown to be crucial for their application in electronic storage devices. The threshold switching phenomenon denotes the sudden decrease in resistivity beyond a critical electrical threshold field. The threshold switching phenomenon facilitates the phase transitions at practical small voltages. Below this threshold the amorphous state resistivity is thermally activated and is observed to increase with time. This effect known as resistance drift seriously hampers the development of multi-level storage applications desired to increase the storage capacity of phase-change memory devices. Hence, understanding the physical origins of threshold switching and resistance drift phenomena is crucial to improve non-volatile phase-change memories. Even though both phenomena are often attributed to localized defect states in the band gap, the defect state density in amorphous phase-change materials has remained little studied.

Starting from a brief introduction of the physics of phase-change materials this thesis summarizes the most important models behind electrical switching and resistance drift with the aim to discuss the role of localized defect states. The centerpiece of this thesis is the investigation of defects state densities in different amorphous phase-change materials and electrical switching chalcogenides. On the basis of Modulated Photo Current (MPC) Experiments and Photothermal Deflection Spectroscopy, a sophisticated band model for the disordered phase of the binary phase-change alloy GeTe has been developed. By this direct experimental approach the band-model for a-GeTe is shown to consist of a shallow and deep defect band in addition to the band tail states.

Furthermore, this study on a-GeTe has shown that the data analysis within MPC experiments can be drastically improved. This thesis illustrates on the example of a-GeTe and a-$Ge_2Sb_2Te_5$, that the problem of unphysical low values for the attempt-to-escape frequency of the order $10^8 s^{-1}$ can be resolved by taking the temperature dependence of the band gap into account.

In this work the defect state density of three different electrical switching alloys a-GeTe, a-$Ge_2Sb_2Te_5$ and a-$Ge_{15}Te_{85}$ has been investigated. In a generation-recombination model the threshold field is expected to increase with increasing optical band gap and increasing mid gap-state density. However, a-GeTe, a-$Ge_2Sb_2Te_5$ and a-$Ge_{15}Te_{85}$ show a large variation in their corresponding electrical threshold fields, which can be not understood by their change in optical band gap value alone. This observation raises the question of the role of localized defect states. MPC experiments reveal that the measured density of mid gap states is observed to decrease with decreasing threshold field known from literature. This result favors a generation-recombination model behind electrical switching in amorphous chalcogenides as originally proposed by Adler.

To get a better understanding of resistance drift phenomena this study focuses on the evolution of resistivity on heating and ageing, activation energy of electronic conduction, optical band gap, defect state density, mechanical stress and nearest neighbor ordering in a-GeTe thin films. After heating the samples one hour at 140°C the activation energy for electric conduction increases by 30 meV, while the optical band gap increases by 60 meV. In addition to band gap opening MPC experiments on the same a-GeTe thin film at different sample ages have revealed complex trap kinetics. Ageing results in an increasing concentration of shallow defect states, whereas the detected density of deep mid gap states decreases. In contrast to both defect levels the conduction and valence band tail remained unaffected during resistance drift of a-GeTe thin films. These findings of the thesis clearly demonstrate the impact of band gap opening and defect annihilation on resistance drift in a-GeTe. Furthermore, drift phenomena observed in a-GeTe are compared to drift phenomena of covalent glasses known from literature. This comparison reveals wide differences between drift phenomena in chalcogenide and covalent glasses.

Furthermore this thesis discusses the stoichiometric dependence of resistance drift phenomena in a-GeSnTe phase-change alloys. A systematic decrease in the amorphous state resistivity, activation energy for electric conduction, optical band gap and defect density is observed with increasing tin content resulting in a low resistance drift for tin rich compositions such as a-$Ge_2Sn_2Te_4$. This study on GeSnTe systems demonstrates, that phase change alloys showing a more stable amorphous state resistivity are characterized by a low activation energy of electronic conduction. This finding found in GeSnTe alloys holds also true for GeSbTe and AgInSbTe systems. On the example of a-$Ge_2Sn_2Te_4$ and a-GeTe exhibiting a strong resistance drift, the evolution of the amorphous state resistivity is shown to be closely linked to the relaxation of internal mechanical stresses resulting in an improving structural ordering of the amorphous phase.

Contents

Contents . . . vii
List of Figures . . . xi
List of Tables . . . xiii

1 Introduction 1

2 Phase-Change Materials 5
- 2.1 Working Principle . . . 7
- 2.2 The Quest for Phase-Change Materials . . . 9
  - 2.2.1 Empiric Identification of Phase-Change Materials . . . 9
  - 2.2.2 Design Rules for Phase-Change Materials . . . 10
- 2.3 Physical Effects in Phase-Change Materials . . . 14
  - 2.3.1 The Optical Contrast - Effect of Resonant Bonding . . . 14
  - 2.3.2 The Threshold Switching Effect . . . 18
  - 2.3.3 The Resistance Drift Effect . . . 19
- 2.4 Aim and Structure of this work . . . 22

3 Electronic Transport in a-PCM: Short Review 23
- 3.1 Electronic Transport Models in Disordered Structures . . . 23
  - 3.1.1 Trap States . . . 23
  - 3.1.2 Defect State Models for a-PCM . . . 27
  - 3.1.3 Multiple-Trapping Transport Model . . . 30
  - 3.1.4 Hopping Transport Model . . . 30
- 3.2 Models describing the Threshold Switching Effect . . . 32
  - 3.2.1 Field Induced Nucleation Model . . . 32
  - 3.2.2 Small-Polaron Model . . . 33
  - 3.2.3 Carrier Injection Model . . . 36
  - 3.2.4 Poole-Frenkel Model . . . 38
- 3.3 Models describing the Resistance Drift effect . . . 43
  - 3.3.1 Structural relaxation described by a double-well potential . . . 43
  - 3.3.2 Valence Alternation Pair (VAP)-model . . . 45
  - 3.3.3 The Poole/Poole-Frenkel model . . . 47

4 Experimental methods 49
- 4.1 Thin Film Preparation by Sputter Deposition . . . 49
- 4.2 Electron Probe Micro-Analysis (EPMA) . . . 51

4.3 X-Ray techniques 53
  4.3.1 X-Ray Reflectometry (XRR) 53
  4.3.2 X-Ray Diffraction (XRD) 56
4.4 Optical methods 57
  4.4.1 Ellipsometry 57
  4.4.2 Fourier Transform-Infrared Spectroscopy 61
4.5 Electrical methods 64
  4.5.1 Heated four point Van-der-Pauw measurements 64
  4.5.2 Dark and photoconductivity in the low temperature limit 66
4.6 Methods to investigate DoS 68
  4.6.1 Modulated Photo Current Experiments (MPC) 68
  4.6.2 Photothermal Deflection Spectroscopy (PDS) 72
4.7 Measurement of internal stresses employing the Wafer Curvature method . . 74
4.8 Extended X-ray absorption fine structure (EXAFS) 76

5 Investigation of defect states in amorphous phase-change materials 81
5.1 Defect states in a-GeTe 81
  5.1.1 Dark- and Photoconductivity in a-GeTe 81
  5.1.2 Photothermal Deflection Spectroscopy on a-GeTe 90
  5.1.3 Modulated Photo Current Experiments performed on a-GeTe 92
  5.1.4 Influence of a temperature dependent band gap on the energy scale of Modulated Photo Current experiments 96
5.2 Study of photoconductivities and defect state densities in switchable chalcogenide glasses 107
  5.2.1 Photoconductivity 108
  5.2.2 Defect state densities 109
  5.2.3 Conclusion 111

6 Resistance drift phenomena 113
6.1 Drift phenomena in a-GeTe 113
  6.1.1 Dark and photoconductivity in aged and post-annealed a-GeTe thin films 114
  6.1.2 Defect state density in post-annealed and aged a-GeTe thin films . . 119
  6.1.3 Band gap in post-annealed a-GeTe thin films 123
  6.1.4 Stress relaxation in a-GeTe thin films 125
  6.1.5 Extended X-Ray Absorption Fine Structure measured in post-annealed a-GeTe thin films 126
6.2 Drift phenomena in covalent glasses 128
  6.2.1 Defect state density in a-Si/a-Si:H 128
  6.2.2 Stress relaxation and viscous flow in a-Si 131
  6.2.3 X-Ray Absorption Fine Structure in a-Si 133
  6.2.4 Dark and photoconductivity in a-Si/a-Si:H - The Staebler Wronski Effect 134

6.3 Stoichiometry dependence of resistance drift phenomena in a-PCM 136
  6.3.1 Resistivity change upon crystallization in GeSnTe phase-change alloys 136
  6.3.2 Optical band gaps in a-GeSnTe phase-change alloys 137
  6.3.3 Defect state densities in a-GeSnTe phase-change alloys 140
  6.3.4 Resistance drift measured in amorphous phase-change and chalcogenide alloys 142
6.4 Link between Stress relaxation and Resistance drift phenomena in a-PCM . 145

Bibliography **155**

List of Figures

1.1 Map of Sumer, Akkad, Babylonia and Assyria 1
1.2 First steps of data storage - Département des Antiquités Orientales, Musée du Louvre, Paris 3

2.1 Kurzweil's extension of Moore's law 6
2.2 Principle of Phase-Change Materials 8
2.3 Phase-change compounds visualized in the ternary Ge:Sb:Te-phase diagram . . . 10
2.4 Structure map giving design rules for phase-change materials 13
2.5 Optical contrast in phase-change materials and non phase-change materials . . . 14
2.6 Energy dependence of the dielectric functions within the harmonic oscillator model 15
2.7 Schematic view of the resonant bonding effect 18
2.8 The *threshold switching* phenomenon 20
2.9 Evolution of the cell resistance in amorphous and crystalline phase-change cells 21

3.1 Wave functions to describe extended and localized states 24
3.2 Driving forces in non-periodic systems 25
3.3 Localized trap states: Classification in imperfection and band tail states 26
3.4 Donor and acceptor like trap states 28
3.5 Defect state densities proposed in a-PCM 29
3.6 Band-Limited Transport model 31
3.7 Trap-Limited Transport model 31
3.8 Field Induced Nucleation 33
3.9 An illustration of polarons 35
3.10 Carrier Injection Model 37
3.11 Poole and Poole Frenkel model 39
3.12 Forward and Reverse thermal emission in the Poole/ Poole-Frenkel model 40
3.13 Threshold switching mechanism in the Poole/ Poole-Frenkel model 42
3.14 Structural relaxation model described by a double well potential 45
3.15 Valence Alternation Pair Model 46
3.16 Resistance drift described in the Poole/Poole-Frenkel model 48

4.1 Schematic set-up of a Sputtering system 50
4.2 Schematic set-up of a WDS electron probe micro-analyzer 52
4.3 Schematic view of a X-Ray $\theta/2\theta$ Scan 53
4.4 A typical XRR-Scan 55
4.5 X-Ray diffraction scan of a post annealed amorphous $Ge_2Sb_2Te_5$ thin film 56

4.6 Schematic principle of Ellipsometry measurements 60
4.7 Schematic principle of the FT-IR set-up used 61
4.8 FT-IR measurements in Reflectance mode 63
4.9 Geometry of the Van der Pauw method. 65
4.10 Schematic set up of the combined set-up used to perform Modulated Photo Current Experiments and measurements of the dark and photoconductivity 67
4.11 Illustration of a spectroscopic scan of the defect state concentration within the mobility band gap by Modulated Photo Current Experiments 71
4.12 Sensitivity of various techniques to measure optical absorption 72
4.13 Schematic set-up of a Photothermal Spectrometer 73
4.14 Schematic picture of a curvature Set-up 75
4.15 XANES and EXAFS regime of the X-ray absorption fine structure 76
4.16 EXAFS spectra of amorphous and crystalline GeTe measured at 10 K 79

5.1 Shockley-Read statistics for different generation conditions 87
5.2 Dark conductivity and conductivity measured under constant illumination . . . 89
5.3 PDS specta on a-GeTe 91
5.4 MPC spectra measured on a-GeTe samples deposited on different substrates each produced in a different sputtering run under same deposition conditions 95
5.5 Optical band gap of a-GeTe and a-$Ge_2Sb_2Te_5$ in dependence of temperature T . 97
5.6 Influence of a temperature dependent energy gap on the MPC energy scale in a-GeTe 104
5.7 Influence of a temperature dependent energy gap on the MPC energy scale in a-Si:H 106
5.8 Optical band gaps and Threshold fields measured for switchable chalcogenide glasses 107
5.9 Photoconductivity measured in amorphous deposited chalcogenides 110
5.10 MPC DoS measured in different switchable chalcogenides 112

6.1 Resistivity measured upon heating thin a-GeTe thin films one hour at different holding temperatures 114
6.2 Dark conductivity measured in postannealed and aged a-GeTe thin films 115
6.3 Photoconductivity measured in post-annealed a-GeTe thin films 118
6.4 PDS spectra measured in post-annealed a-GeTe thin films 119
6.5 Dark conductivity measured in the same a-GeTe thin film at different sample ages 120
6.6 MPC spectra measured in aged a-GeTe thin film 121
6.7 Optical band gaps studied in post-annealed a-GeTe thin films for several measurement and holding temperatures. 124
6.8 Mechanical stress measured in a 500 nm thick a-GeTe film by a curvature set-up 125
6.9 EXAFS spectra of post-annealed and amorphous deposited a-GeTe thin films measured at ambient temperature. 127
6.10 ESR spin density and optical band gaps measured at room tempeature on a-Si:H deposited via glow discharge at different substrate temperatures T_s. 129
6.11 Optical absorption edge of hydrogenated amorphous silicon a-Si:H measured by Photo Thermal Deflection Spectroscopy 130

6.12 Stress relaxation and proposed model for viscous flow in a-Si based on *flowing* dangling bond defects 132
6.13 EXAFS and XANES spectra measured in a-Si:H samples deposited by ion-beam sputtering at different substrate temperatures 133
6.14 The Staebler-Wronsi Effect 135
6.15 Resistivity change upon crystallization in GeSnTe phase-change alloys 137
6.16 Optical band gaps in a-GeSnTe alloys measured by FT-IR at different temperatures 139
6.17 Defect state density measured by MPC on different GeSnTe systems 141
6.18 Drift coefficient α_{RD} measured at 50°C for different a-GeSnTe phase-change alloys 142
6.20 Link between resistance drift and stress relaxation 147

List of Tables

2.1 Optical constants of phase-change and non phase-change materials 16

5.1 Varshni parameters of phase-change and non phase-change materials 98
5.2 Exponential growth factors g and temperatures T_{max} describing the temperature dependent photoconductivity in amorphous deposited GeTe, $Ge_{15}Te_{85}$ and $Ge_2Sb_2Te_5$ 108

6.1 Activation energies E_a describing the dark conductivity near room temperature and growth factors g as well as temperatutre T_{max} describing the photoconductivity in post-annealed and altered a-GeTe thin films. 117
6.2 Activation energies E_a compared to band gap opening induced by heating by heating for one hour at different holding temperatures 123
6.3 Activation energy E_a, optical band gap at T = 300 K $E_g(300)$, and T = 0 K $E_g(0)$ compared to ξ values measured for different a GeSnTe phase-change alloys. 138
6.4 Drift coefficient at 50°C and activation energy E_a at the beginning and at the end of the annealing time for different GeSnTe alloys. 143

Chapter 1

Introduction

The challenge of developing data storage and data sharing dates back until the early time of the Neolithic period from 8000 to 6000 BC - a time that was triggered by the Neolithic revolution, when the human man kind successfully cultivated crops and domesticated animals. This transition period from hunting and gathering to agriculture and settlement arose independently in several separate places worldwide.

However, most archaeological discoveries dating from this ancient time, were found in the Fertile Crescent in Mesopotamia: a landscape marked by the rivers Euphrates and Tigris, see Fig. 1.1. The region owes its historical relevance to regular rainfall and to the presence of nourish grass, wild goats and sheep making first farming possible, [Hr097].

Figure 1.1: Already in ancient times 8000 BC to 6000 BC, long before scripts have been invented the human man kind faced the challenge of data storage. Triggered by the Neolithic revolution followed a transition period from hunting and gathering to settlement and agriculture. Even though this fundamental change took place independently worldwide our image is mainly shaped by civilizations living in the Fertile Crescent, where regular rainfall and the presence of wild goats and sheep made farming possible [Hr097].

These earliest farmers of Mesopotamia lived in a traditional redistribution economy system and became concerned with keeping track of their produced goods [Sel05]. A data storage system was needed to pool community surpluses for religious festivals that constituted the lynch pin of the redistribution economy. To count community surpluses the Mesopotamian farmers invented counters made of clay in many different shapes including triangles, disks, cones, spheres, cylinders, tetrahedrons, biconoids or ovoids. Each shaped token is assigned a certain meaning. A small measure of grain is symbolized by a cone, a large measure of grain is symbolized by a sphere and the symbol of a disk stands for sheep or garment depending on its surface carving [SB02] .
Even though the invention was simple it is of largest importance. Citing Denise Schmandt-Besserat, who played a pioneering role in archeology by recognizing the importance of clay tokens, this accounting system "‘was the first visual code, the first abstract symbol system ever created for the sole purpose of communication"’. Certainly the practice of tokens was common throughout in the Near East, since about 8000 tokens could be found from Palestine, Anatolia, Syria, Mesopotamia and Iran [SB02, Rob07].
Around 3500 BC city administrators started to enclose tokens in ball shaped clay envelopes to keep accounters record orderly and tamper-proof. Archaeologists have unearthed some 80 of these clay balls with tokens intact [Rob07]. Picked up and shaken, they rattle. Under X-ray illumination they reveal a outline of tokens within, see Fig. 1.2. The purpose of such a filled envelope was most probable to guarantee the accuracy and authenticity of stored tokens symbolizing commodities and thus might have acted as a bill of lading. Tokens stored in a bag or tied together with a string could be easily tampered with. In contrast envelopes ensured a tamper-proof closure. In the event of a dispute concerning the traded goods, the clay ball could be broken and its content could be checked against the merchandise.
The outer surface of some envelopes bears impressions of tokens they contained. These impressions were made by stamping tokens onto the wet clay. Consequently the content could be checked without breaking the clay ball. After the creation of three dimensional abstract tokens to count surpluses these markings represent the first two dimensional abstraction of real objects. Many scholars led by Denise Schmandt-Besserat, support the theory that these impressions of tokens on the surface of sealing envelopes were a step forward of marking clay tablets with more complex signs, and the subsequent emergence of writing [SB09].

The introduction given to this thesis depicts the eagerness of the human man kind to pursue and distribute knowledge. The challenge of data storage dates back to prehistoric times and was already then strongly linked to economy. The first data storage technology, counters made of clay, was invented to keep track of traded goods. Impressions of these simple clay tokens on the wet surface of clay envelopes yielded finally to cuneiform and the invention of first scripts changed our world fundamentally. Like the invention of token sealed in envelopes, future data technologies will meet economic demands and have to satisfy the human thirst of knowledge; certainly future data storage technologies will change our life again.

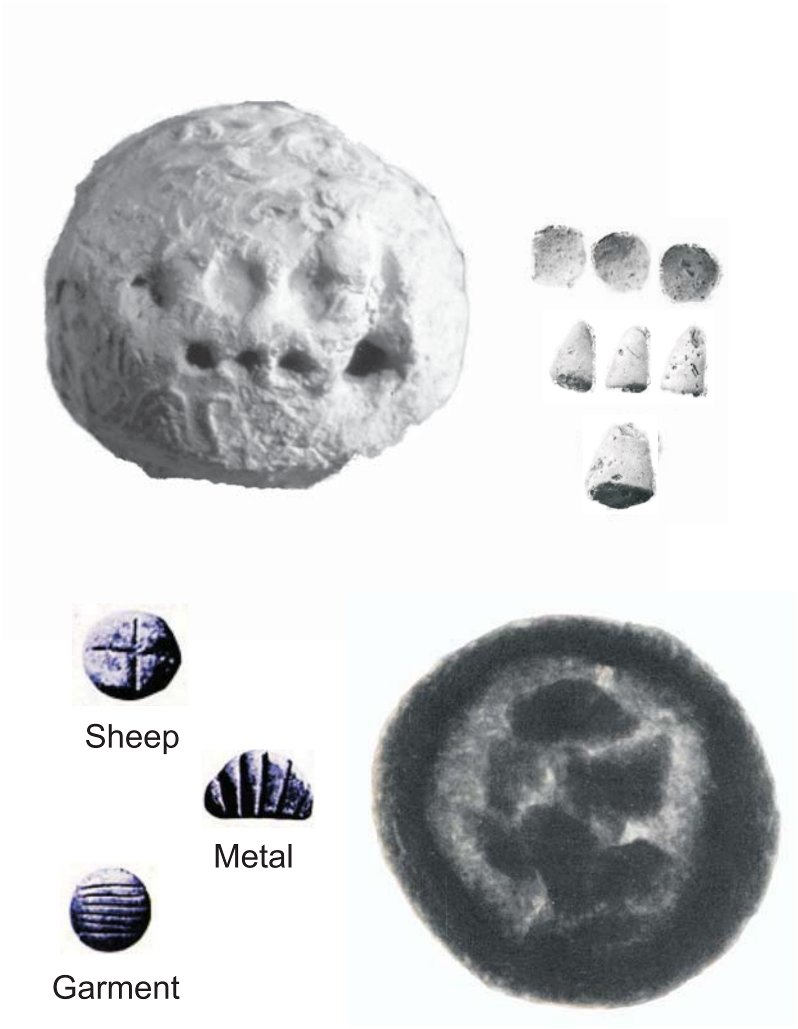

Figure 1.2: Clay tokens, later enclosed in a clay envelope shaped as a ball, are the first known invention of the human mankind to store and share information. In the Neolithic period (8000-6000 BC) tokens were used by the Mesopotamian farmers, who lived in a redistribution economy system, to count their surpluses they had to deliver to the community leaders. Each shaped token represented a certain good. A cone for example symbolizes a small measure of grain, a sphere a large measure of grain and a disk could mean sheep or garment depending on its surface carving. Around 3500 BC tokens were enclosed in clay envelopes. The outer surface of the envelope bears impressions of tokens enclosed within. The purpose of these enclosed tokens was most probably to guarantee the accuracy and authenticity of locally traded commodity. Many scholars are of the opinion that these two dimensional exterior marks of three dimensional objects represent the essential abstraction yielding to the emergence of writing [SB09]. Images published with permission from D. Schmandt-Besserat. Image source: [SBb, SBa]

Chapter 2

Phase-Change Materials

Different branches of industry collaborate to produce Microchips, the fundamental basis of our computer-dominated century. Important milestones on the way of developing smaller and smaller structures have to be achieved in various techniques to operate economically. The semiconductor industry uses the empiric Moore's law describing a long term trend in the history of computer hardware to guide their long term planning.
Shortly after the invention of integrated circuits Intel's co-founder Gordon E. Moore noted that the number of components in integrated circuits had doubled every year from 1958 to 1965. Based on this fact Moore predicted that this trend will continue "for at least ten years" [Moo65]. In 1975 he altered the formulation of his law over time to a doubling every two years. David House, an Intel colleague predicted integrated circuits would double in performance every 18 months [Moo05]. Consequently Moore's law exists in three different formulations giving a time span of doubling the density of components or transistors at minimum cost of either 12, 18 or 24 months.
Although Moore's law described initially a pure observation, the more widely it became accepted, the more it served as a goal for an entire industry. In consequence this forecast pushed both marketing and engineering departments of semiconductor manufacturers forward to ensure their competitiveness. In this respect, Moore's law can be viewed as a self-fulfilling prophecy. Even though Moore's law remains valid until today, the computer hardware technology based on transistors will certainly reach its physical limits [Lai08, KC06].

Futurists, such as Ray Kurzweil proclaim that the end of integrated circuits does not mean the end of Moore's law. According to Kurzweil Moore's law of integrated circuits "... *was not the first, but the fifth paradigm to provide accelerating price-performance. Computing devices have been consistently multiplying in power (per unit of time) from the mechanical calculating devices used in the 1890 U.S. Census, to Turing's relay-based "Robinson" machine that cracked the Nazi enigma code, to the CBS vacuum tube computer that predicted the election of Eisenhower, to the transistor-based machines used in the first space launches, to the integrated-circuit-based personal computer...*"[Kur01].

Kurzweil speculates that most probably some new type of technology will replace the integrated-circuit technology in future. Consequently Moore's Law will hold true long after reaching the end of the scalability of the transistor based technology in integrated circuits [Kur05].

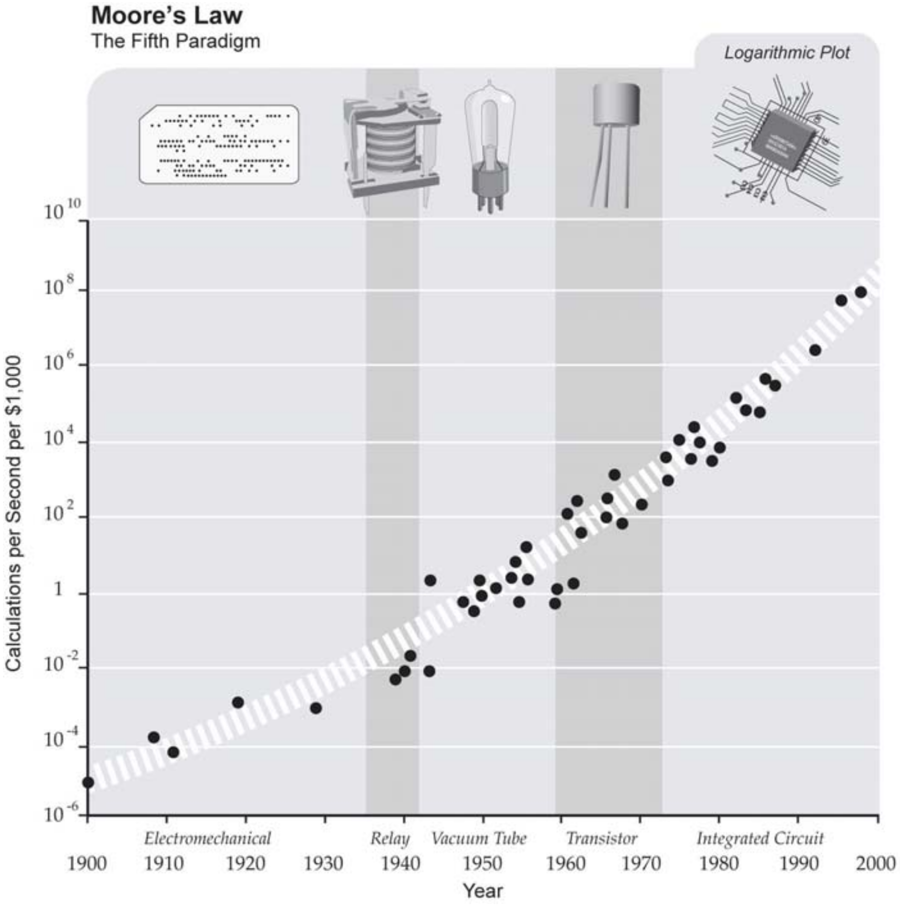

Figure 2.1: According to Moore's law the density of components or transistors in integrated circuits at minimum costs doubles within a certain time span, that varies in literature from 18 to 24 months. The Futurist Ray Kurzweil applied Moore's law to preceding data storage technologies: *"Moore's law of Integrated Circuits was not the first, but the fifth paradigm to forecast accelerating price-performance ratios. Computing devices have been consistently multiplying in power (per unit of time) from the mechanical calculating devices used in the 1890 U.S. Census, to relay-based "Robinson" machine that cracked the Lorenz cipher, to the CBS vacuum tube computer that predicted the election of Eisenhower, to the transistor-based machines used in the first space launches, to the integrated-circuit-based personal computer."*
Certainly the transistor based technology will reach their physical limit in a near future. A technology based on phase-change materials, that can be scaled to structural sizes of only a few nanometres offers the possibility to become their successors in respect to the maintenance of Moore's law. Image source: [Kur05]

Phase-change materials show a portfolio of extraordinary properties and offer the possibility to become this new type of future technology, especially in terms of scalability [Che06, RBB+08]. Starting with the working principle of Phase-Change media, this chapter describes briefly design rules for phase-change materials and the remarkable physics present in this exceptional class of materials.

2.1 Working Principle

The innovative technology of phase-change materials is conceptually easy. The whole success of this special class of materials is based on a remarkable combination of physical properties [WY07]. First of all the reflectivity or resistivity differs drastically between an amorphous and a crystalline phase enabling to store information in a binary code. In Fig. 3.9 the varying optical constants (refractive index n and absorption coefficient κ) and sizes of the resistors marked with Ω indicate the extremely different optical or electrical properties between a ordered crystalline and a disordered amorphous phase.

A small portion of a phase-change material can be switched reversibly between its ordered and disordered state. This phase transformation is very fast and can proceed on a nanosecond time scale [BMS+09]. Both crystallization and amorphization are thermally induced. Currently, either laser pulses or electrical pulses are employed to precisely control the necessary amount of heat. To operate the phase transformations the shape of the applied power pulse is very important [Bru07]. To crystallize an amorphous region a rather long power pulse is needed heating the material during a time sufficiently long above its crystallization temperature, so that all atoms rearrange in their crystal structure. The speed of crystallization, given by a short crystallization time t_1, is minimized in a certain temperature range, which is indicated in Fig. 3.9 by the intensity of the red shading. A crystalline region is re-amorphized using the melt quenching effect. Thereby a very short and high power pulse is employed to heat the sample above its melting temperature. Since only a spatially confined region is heated up, the induced heat is absorbed rapidly by the local environment. Consequently, the melt is cooled extremely fast within a very short time t_2. Once the temperature falls below a critical value, the glass transition temperature T_G, the atomic mobility is very small [Nem94]. Thus, crystallization is kinetically hampered even though energetically favourable. In this way the solid amorphous phase is obtained by "freezing" the liquid, also known as "‘melt-quenching"’ effect.

Information can be written in binary code by employing crystallization or amorphization pulses to spatially confined regions of switchable phase-change media. The read out of the stored information is possible using power pulses of sufficient low intensity leaving the physical properties of the active material unchanged [LSW11].

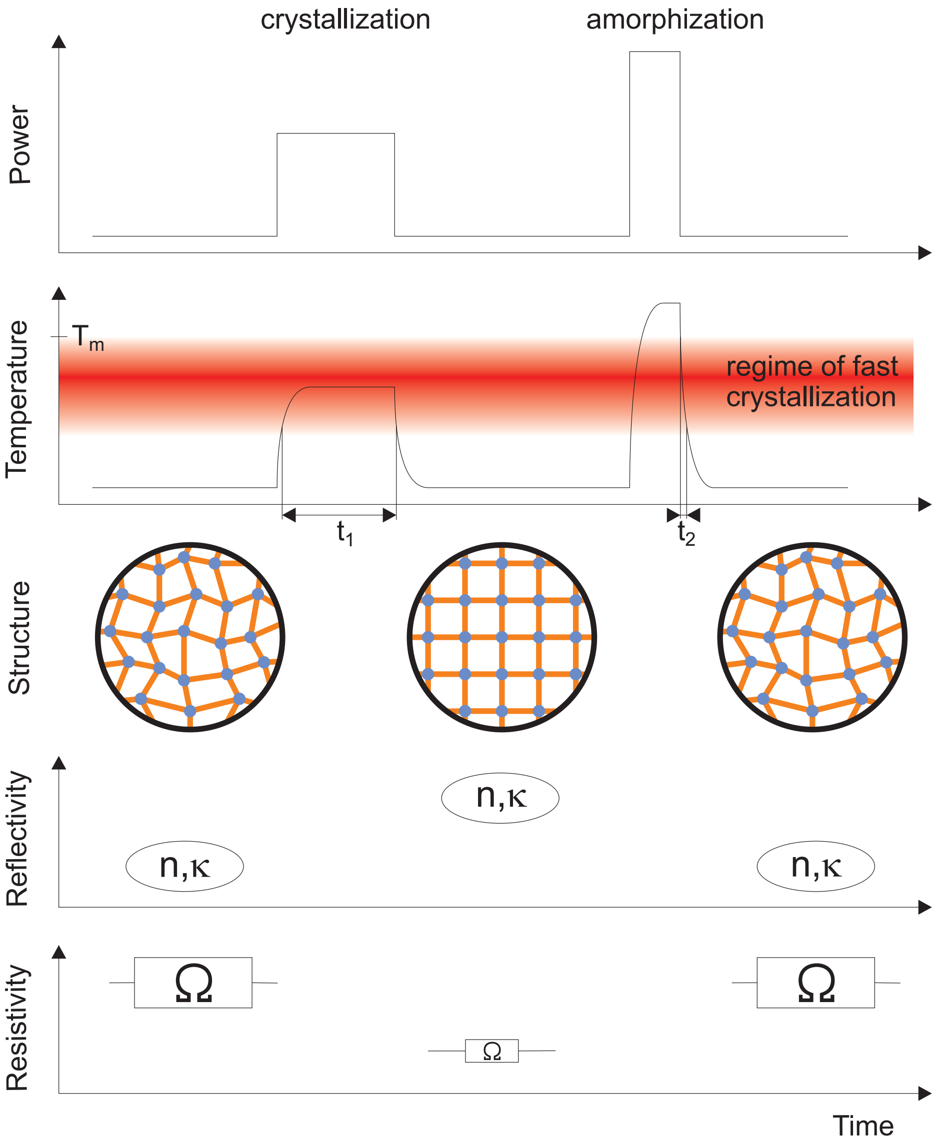

Figure 2.2: Phase-change materials exhibit a stable crystalline and metastable amorphous phase. The optical and electronic properties of both phases differ significantly, which is essential for the application in optical or electronic data storage. The phase transition is heat induced and occurs on a nanosecond time scale. To crystallize an amorphous bit a SET pulse is used, which heats the sample above its crystallization temperature. The system is then held at that temperature until all atoms have diffused to their lattice site. To amorphize a data bit, a rather short RESET pulse of high intensity is used, which melts the material. Since the liquid volume is small, it is cooled rapidly down so that the atoms have no time to find their lattice sites, i.e. the melt is 'frozen', to obtain the disordered amorphous phase. This effect is also known as melt-quenching.
Image source: [Sal08]

2.2 The Quest for Phase-Change Materials

Phase-change alloys combine exceptional properties: a drastic contrast in optical or electrical properties between an amorphous and a crystalline phase, very fast crystallization kinetics and a high scalability down to structural sizes of only a few nanometres. Identifying materials combining high contrast and very fast crystallization kinetics has been a challenging quest until design rules for phase-change materials could be developed.

2.2.1 Empiric Identification of Phase-Change Materials

First compositions that are identified to be phase-change materials are chalcogenide alloys. In 1968 S.R. Ovshinsky first observed reversible electrical switching between a highly resistive and a highly conductive state in $Ge_{10}Si_{12}Te_{48}As_{30}$ [Ovs68]. Only three years after this important discovery, rapid, reversible laser induced phase transformations were observed in the multinary alloy $Ge_{15}Sb_2Te_{81}S_2$ [FdMO71]. Both pioneering works triggered an application-oriented research into non-volatile data storage technologies based on chalcogenides. The main task for materials researchers to the present day has been to classify materials which are suitable for application. Researchers at IBM classified the binary alloy GeTe to be a phase-change material in 1986: GeTe combines a high contrast in reflectivity and resistivity with very fast crystallization kinetics enabling phase transitions on a nanosecond time scale [CRB86].

A first important family of phase-change materials was identified in 1988 by the research group of N.Yamada. Alloys lying on the pseudo-binary line connecting GeTe and Sb_2Te_3 in the ternary Ge:Sb:Te-phase diagram show the targeted combination of fast switching speeds and property contrast [YONA91, YOA+87]. To design rewritable optical discs three new technologies were needed in combination: the discovery of the GST family acting as encoding material, polycarbonate to hold the active layer and optical laser light sources delivering sufficiently small spot sizes. After a development time of 20 years the first product of rewritable optical disc based on phase-change materials entered the market in 1990. Since then this technology improved steadily in respect to data storage density, see Fig. (2.3).

Besides Sb_2Te_3 being an end point of the tie line, silver and indium doped $Sb_{70}Te_{30}$ compositions offer suitable properties [LPS+03]. Doping in the field of phase-change materials refers to doping concentrations in the percentage range, being much larger than in usual semiconductors such as silicon or germanium. Hence, doped phase-change materials located near $Sb_{70}Te_{30}$ in the Ge:Sb:Te-phase diagram constitute the second known family of phase-change materials. A prominent candidate of this family is the widely employed alloy AgInSbTe, also known as AIST [MAK+11].

A third family of phase-change materials attracted considerably interest in the last years, because this family does not contain any chalcogenide. Modification of antimony such as $Ge_{15}Sb_{85}$ show the extraordinary combination of fast crystallization speed and property contrast [SATM94, PSRK03]. In contrast to phase-change materials belonging to the first or second family, $Ge_{15}Sb_{85}$ is close to the eutectic composition [Che89]. Consequently, phase separation upon cycles of crystallization and vitrification is very likely in $Ge_{15}Sb_{85}$ [ZBE+10], whereas all materials mentioned before are single-phase materials.

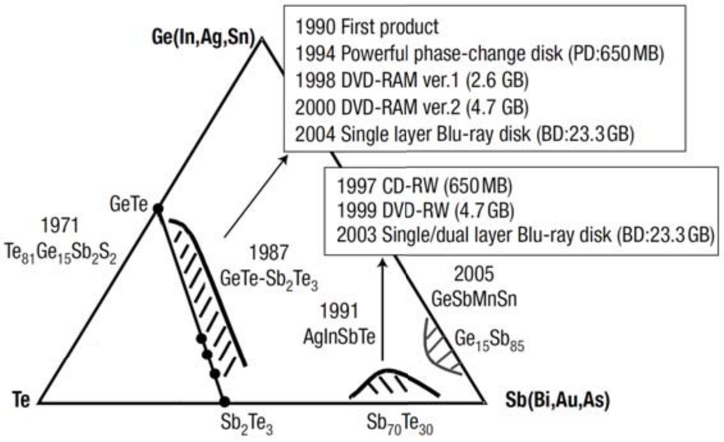

Figure 2.3: Most known phase-change materials can be found in the ternary Ge:Sb:Te diagram and are classified into three families. The first family of phase-change materials is described by the pseudo-binary tie line between GeTe and Sb_2Te_3 including GeTe, $Ge_2Sb_2Te_5$ or $Ge_1Sb_2Te_4$. Doped antimony tellurium compounds near the composition $Sb_{70}Te_{30}$ constitute the second family of phase-change materials. Modifications of antimony such as $Ge_{15}Sb_{85}$ form the third family and attract considerable interest because these compounds do not contain any chalcogenide. Next to each composition, indicated by the position within the GST-triangle, the respective application in optical data storage are stated. Image source: modified from [WY07].

2.2.2 Design Rules for Phase-Change Materials

The trial-and-error method identified many phase-change materials. Anyway the question, which has to be answered is why the identified compositions classified into three families work as phase-change materials and whether materials that are composed of other elements would work as well. Design rules predicting the combination of high contrast and fast crystallization kinetics from the stoichiometric composition facilitate application oriented material optimization. Recently it has been shown that design rules can be derived from the bonding configuration of neighbouring atoms in the crystalline state [LSG⁺08].

To identify design rule the authors concentrate on the crystalline structure of the first family of phase-change materials. These phase-change alloys lie on the pseudo-binary line between GeTe and Sb_2Te_3. So the first phase-change family includes $Ge_1Sb_4Te_7$, $Ge_1Sb_2Te_4$, $Ge_2Sb_2Te_5$, $Ge_3Sb_2Te_6$ and $Ge_8Sb_2Te_{11}$. All these alloys crystallize in a metastable rock-salt structure. Hereby the Te atoms occupy the anion lattice site and Ge, Sb and vacancies as well occupy the cation lattice site [MY02, YM00, NOT⁺00]. According to the 8-N rule describing covalent bonding we expect on average four bonds for germanium, three bonds for antimony and two bonds for tellurium. However, the coordination numbers derived from experiment of crystalline phase-change materials are significantly larger than expected from the 8-N rule valid for covalent bonding [RJ87, RXP07]. On the contrary, crystalline semiconductors such as Ge, Si and GaAs follow the 8-N rule. However, these materials show no drastic optical difference between a ordered and a disordered state [HR10]. Consequently, the strong optical contrast seems tocal be closely linked to the extraordinary crystalline state of phase-change materials.

A simple structure map allowing to predict the bonding mechanism and crystal structure for group V elements and binary IV-VI compounds was introduced by Littlewood [Lit80b, Lit80a]. In his work, which is an extension of the work carried out by St. John, Simons and Bloch [SB73, SJB74], he introduces two coordinates spanning up a diagram:

$$r'_\sigma = r_p^A - r_p^B \tag{2.1}$$

$$r_\pi^{-1} = \left[\left(r_p^A - r_s^A\right) + \left(r_p^B - r_s^B\right)\right]^{-1} \tag{2.2}$$

Hereby, r_s^X and r_p^X denote the valence radii of the $s-$ and $p-$ orbital of atom X, respectively. For different atoms the radii are published in reference [CP78].

Both coordinates defined in Eqs.(2.1)-(2.2) can be interpreted from a physical point of view. The coordinate r'_σ compares the size of atoms A and B. The more similar both atoms are the smaller is the charge transfer in a A-B bond. Consequently, r'_σ represents the ionic contribution of the bonding and gives a measure of ionicity. The covalency of a bond is measured by the coordinate r_π^{-1} in terms of hybridization. A hybrid state is a superposition of atomic s - and p -orbitals lowering the ground state energy. The first step to form a hybrid state is the excitation of one s -electron into a p -orbital, which costs energy. The tendency towards hybridization is large for low excitation energies, i.e. low energetic splitting between s - and p -levels. Thus the coordinate r_π serves as a measure of this splitting, since it measures the average difference between s - and p -radii. In order to have large values in the case of high tendency towards hybridization the reciprocal r_π^{-1} is employed. Even though this structure map proposed by Littlewood is based on the properties of free atoms, it works very well to gain insight into crystal structures in binary systems such as GeTe , GeSe or PbTe having on average five valence electrons per atom tantamount to three p - electrons [Lit80a].
However, phase-change materials are typically multinary alloys having an average number of p -electrons slightly larger than three. For instance $Ge_2Sb_2Te_5$ possesses on average $\frac{2\cdot2+2\cdot3+5\cdot4}{2+2+5} = 3.\overline{3}$ p -electrons per atom . Indeed, crystalline phase-change materials form large concentrations of vacancies resulting in a consistent number of three p - electrons per lattice site. To apply the framework of Littlewood to multinary compounds, the coordinates valid for AB systems given in Eqs.(2.1)-(2.2) have to be modified. Recently it has been shown that different cationic and anionic species can be averaged to treat a multinary compound as an effective AB-material [Len10]. A meaningful averaging procedure excludes extreme combinations such as carbon ($r_s = 0.38, r_p = 0.47$) with bismuth ($r_s = 0.72, r_p = 1.02$). Slight deviations from equal numbers of anions and cations are typically compensated by the formation of intrinsic vacancies [WLW+07].

So the generalized coordinates given by Eqs. 2.3-2.4 can be applied to A^{V}, $\mathrm{A}^{IV}\,\mathrm{B}^{VI}$, $\mathrm{A}_2^{IV}\mathrm{B}_2^{V}\mathrm{C}_5^{VI}$, $\mathrm{A}_1^{IV}\mathrm{B}_2^{V}\mathrm{C}_4^{VI}$ and $\mathrm{A}_1^{IV}\mathrm{B}_4^{V}\mathrm{C}_7^{VI}$ systems. The sum runs over all specific anions and cations of the alloy considered , weighted by their concentration n_i or n_j, respectively [LSG+08].

$$r'_\sigma = \underbrace{\left(\frac{\sum_i n_i \cdot r_{p,i}}{\sum_i n_i}\right)}_{Anions} - \underbrace{\left(\frac{\sum_j n_j \cdot r_{p,j}}{\sum_j n_j}\right)}_{Cations} \tag{2.3}$$

$$r_\pi^{-1} = \left[\underbrace{\left(\frac{\sum_i n_i \cdot (r_{p,i} - r_{s,i})}{\sum_i n_i}\right)}_{Anions} + \underbrace{\left(\frac{\sum_j n_j \cdot (r_{p,j} - r_{s,j})}{\sum_j n_j}\right)}_{Cations}\right]^{-1} \tag{2.4}$$

Fig. 2.4 shows a two-dimensional map illustrating the coordinates defined by Eqs. 2.3-2.4 of empirically identified phase-change alloys together with a large number of materials composed from group IV, V and VI elements. Occasionally the number of cations is very different from the number of anions, e.g. Sb_2Te_3 or Sb_2Te. Since these materials deviate considerably from the AB-scheme these materials should not be plotted in the same two-dimensional map as GeTe.

On this structure map tellurides, selenides, sulfides and oxides form well distinguishable bands. Phase-change materials, indicated by green circles are located in a small region on the map. Consequently, phase-change materials are characterized by a fixed ratio of ionicity and hybridization offering a simple design scheme to identify future phase-change materials.

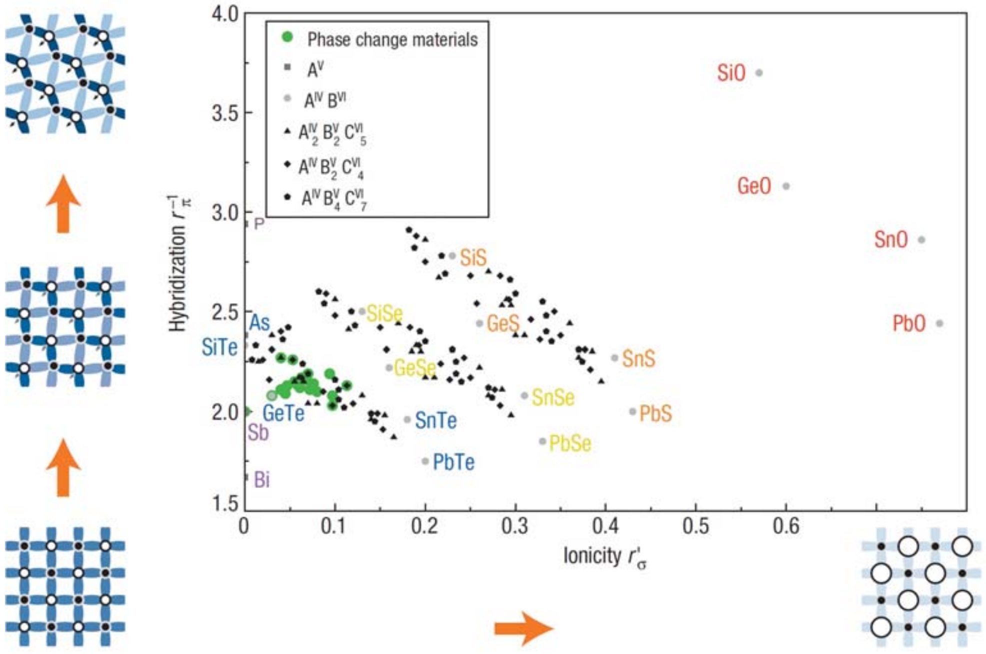

Figure 2.4: For materials having on average three p-electrons per atomic site and even number of anions and cations a two dimensional structure map can be constructed. This map is spanned by two coordinates; r'_σ a measure of ionicity and r_π^{-1} a measure of covalency of a bond. According to Eqs. 2.3-2.4 the coordinates for multinary compounds of group IV, V and VI elements are calculated employing the atomic radii of s - and p - orbitals known from [CP78].
Tellurides, selenides, sulfides and oxides form well distinguishable bands on the map. Phase change materials (green dots) are located in a small distinct region. Obviously phase change materials are characterized by a certain ratio of hybridization and ionicity. The proposed structure map reveals design rules for the classification of future phase change materials based on their stoichiometry, [Len10]. Image source: [LSG^{+}08]

2.3 Physical Effects in Phase-Change Materials

The application-oriented research on phase-change materials opened the possibility to design new non-volatile data storage technologies [WY07, PPM+11b].
Furthermore, the research on phase-change materials is driven by the desire to understand the scientific basis for their unique properties. Both, the crystalline and the amorphous state of phase-change materials show puzzling physical effects. A selection of the most prominent phenomena is presented in the following section.

2.3.1 The Optical Contrast - Effect of Resonant Bonding

In phase-change materials an extraordinary strong optical contrast between an amorphous and a crystalline state is observed. Fig. 2.5 compares optical spectra of the phase-change material GeTe to the non-phase change material SiO_2. The optical transmission measured in the amorphous and crystalline phase of SiO_2 does not differ within the visible range, i.e. from 380 nm to 780 nm. In contrast the phase-change material GeTe shows a significantly enhanced reflectivity in the crystalline state over the whole investigated wavelength range.

The optical properties of a solid can be completely described by the complex dielectric function $\varepsilon = \varepsilon_1 + i\varepsilon_2$. The complex dielectric function depends on the photon energy E of the incident electro-magnetic wave and describes its interaction with the solid. Hereby, the alternating electric field induces electric dipoles within the solid giving rise to polarization. Within the harmonic oscillator model the induced dipoles experience a restoring force proportional to their displacement. The real and imaginary part of the dielectric function for a dipole oscillor are shown schematically in Fig. 2.6. In a solid one distinguishes different kinds of possible

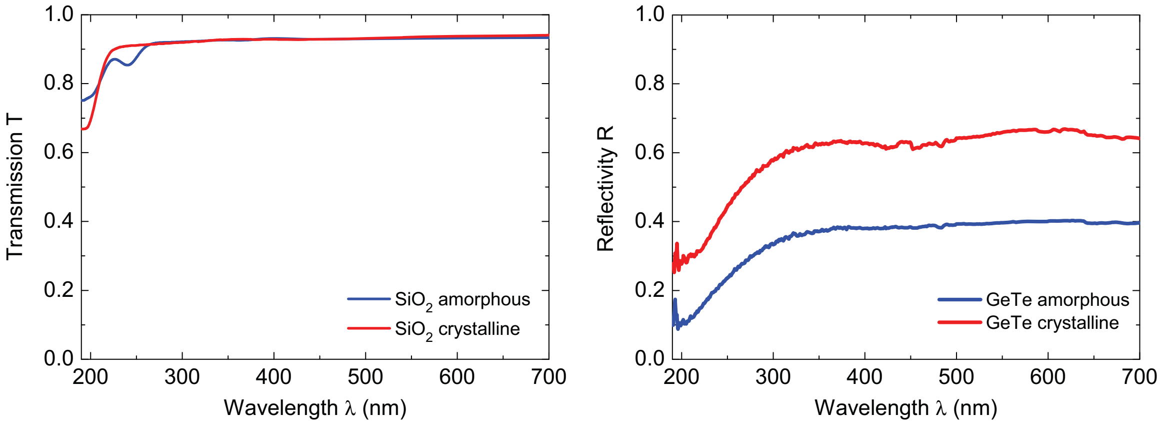

(a) SiO_2 **(b)** GeTe

Figure 2.5: In contrast to non phase-change materials phase-change materials such as GeTe show a pronounced contrast in optical properties between an amorphous and a crystalline phase in the visible range. Image source: [Mer11]

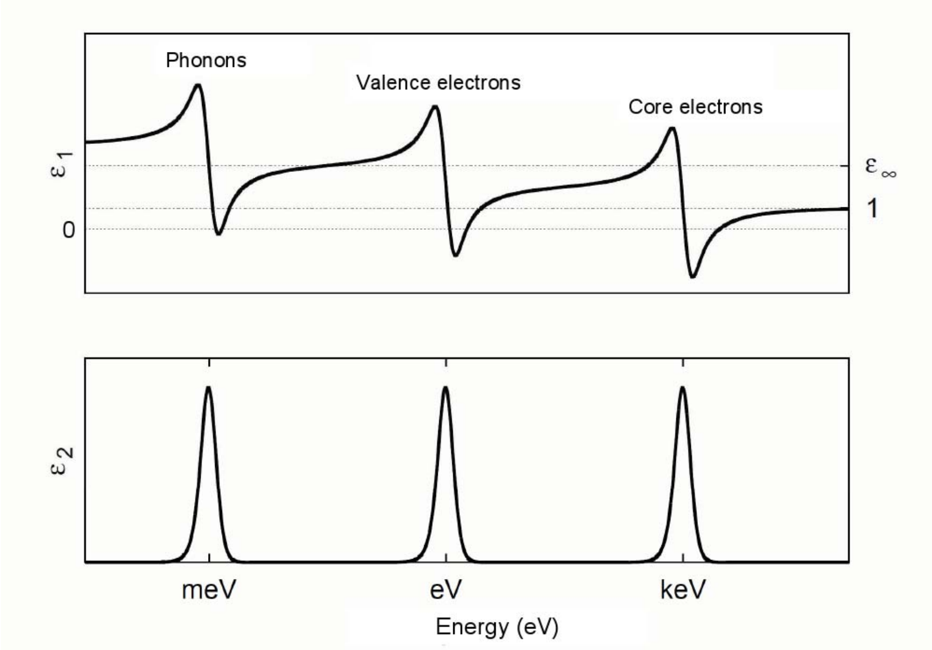

Figure 2.6: Polarization effects in a solid can be described within a harmonic oscillator model, where dielectric dipoles interacting with an alternating electric field are assumed to have a restoring force. Typical energy dependencies of the dielectric functions ε_1 and ε_2 within the harmonic oscillator model for different kinds of electronic contributions to the polarization are shown. The resonance energy for lattice vibration or phonon excitation lies within the meV range. Electronic polarizations of valence or core electrons have much higher resonance energies within the eV or keV, respectively. Image source: [Kre09]

contributions to the polarization, each characterized by a certain resonance energy. Vibrations of ionic sublattices are characterized by typical phonon resonance energies in the meV range. However, electronic polarization of valence or core electrons have much higher resonance energies in the eV or keV range, respectively.
Typical phonon energies in phase-change materials are reported to be lower than 30 meV, [SKW+08]. Consequently the optical dielectric constant ε_∞ illustrated in Fig. 2.6 can be defined as $\varepsilon_\infty = \varepsilon_1(E = 0.05\mathrm{eV})$. The values of ε_∞ in crystalline phase-change materials are typically two to three times larger than these measured for amorphous phase-change materials, see Tab.(2.1). However, non-phase change materials show no significant difference in the optical constant ε_∞ between their ordered and disordered state. Furthermore, the optical constants measured for amorphous phase-change materials of approximately 10 are quite similar to those obtained for non phase-change materials. This indicates that the origin of the pronounced optical contrast is linked to an extraordinary behavior of the crystalline state in phase-change materials.

Table 2.1: Optical dielectric constants ε_∞ and energy gaps E_g of phase-change materials (top) and non phase-change materials (bottom). In contrast to non phase-change materials phase-change materials show a strongly enhanced optical dielectric constant ε_∞ in their crystalline phase, whereas the ε_∞ values for phase-change and non-phase change materials are quite similar in the amorphous phase. This suggests that the pronounced optical contrast observed in phase-change materials originates from special properties of their crystalline state.

Material	ε_∞		E_g (eV)	
	Amorphous	Crystalline	Amorphous	Crystalline
GeTe	13.2 [1]	33.2 [1]	0.78 [1]	0.55 [1]
$Ge_2Sb_2Te_5$	16.0 [1]	33.3 [1]	0.77 [1]	0.48 [1]
$Ge_1Sb_2Te_4$	16.6 [1]	36.2 [1]	0.76 [1]	0.39 [1]
$Ge_2Sb_1Te_4$	14.5 [1]	29.8 [1]	0.80 [1]	0.61 [1]
AgInSbTe	19.6 [1]	52.8 [1]	0.63 [1]	0.18 [1]
Si	11.6 [2]	11.6 [2]		1.12 [3]
Ge	16.0 [2]	16.0 [2]		0.67 [4]
GaAs	12.0 [2]	12.0 [2]		1.43 [4]

[1] taken from Reference [SKW+08]

[2] taken from Reference [HR10]

[3] taken from Reference [SK07a]

[4] taken from Reference [IL02]

In solid state physics the dielectric function can be determined in the frame-work of quantum mechanics. In periodic crystals the electronic states are described by Bloch wave functions and the interband transitions are strongly linked to the the dipole matrix M element and the joint density of states $Z_{ij}(\omega)$, [IL02]:

$$\varepsilon_2(\omega) = \frac{\pi}{\varepsilon_0}\frac{e^2}{m^2\omega^2}\sum_{i,f}|M|^2 \cdot Z_{if}(\omega) \tag{2.5}$$

$$Z_{if}(\omega) = \frac{1}{(2\pi)^3}\int_{\hbar\omega=E_f-E_i}\frac{df_\omega}{|\nabla_k[E_f(k)-E_i(k)]|} \tag{2.6}$$

Consequently a significant change in optical properties can be explained either by a changing density of states or varying transition matrix elements. However, photoemission spectroscopy measurements and ab-initio molecular-dynamics calculations performed on crystalline and amorphous phase-change materials reveal quite similar density of states for both phases [KKI+07], [HE08]. Furthermore the decrease in band gap by about 50% observed for crystalline phase-change alloys is not sufficient to explain the strong incease in ε_∞ by a factor two to three. However, works recently carried out by Welnic et al. as well as Huang and Robertson [WPD+06, HR10] focus on the matrix transition elements defined by:

$$M = < i|\hat{p}|f > \tag{2.7}$$

where $\hat{p}$ is the dipole operator and i and f the initial and final states of the optical transition, respectively. Both studies show that the strong optical contrast originates from extremely high matrix transition elements observed for the crystalline state. These enhanced transition probabilities can be understood from the view point of resonant bonding [SKW+08].

We remember that many phase-change materials have on average three p -electrons and crystallize in a metastable rock-salt structure. Resonant bonding leads to ordering and alignment of these p -orbitals on adjacent molecular units. In this symmetric atomic arrangement, the valence electrons resonate between six bonds of the original cubic lattice. A schematic view of resonant bonding on the group V element Sb, being a phase change material as well, is presented in Fig. 2.7. For normal two-center bonds, the matrix element M is about one bond length. In consequence of resonance bonding the aligned chains yield to M values of typical two bond lengths giving rise to high transition matrix elements and coordination numbers higher than expected from the 8-N rule.

In the disordered amorphous phase the alignment of p -orbitals gets lost. Consequently the amorphous state is characterized by typical low dielectric constants $\varepsilon_\infty \approx 15$, which are quite comparable to those values observed for covalent bonded semiconductors such as Si, Ge or GaAs.

A highly symmetric atomic arrangement thus favors resonant bonding. Nevertheless, the structure map depicted in Fig. 2.4 shows that materials having a rather perfect cubic symmetry such as Bi, i.e. $r'_\sigma = r_\pi^{-1} \approx 0$, do not work as a phase-change material. The answer for this is given by the potential for atomic displacement: in undistorted and strongly distorted systems as well, the potential can be regarded as predominantly harmonic. In the case of rather weak distortions the potential resembles a very broad, flat box enabling large atomic movements on small thermal fluctuations, i.e. large Debye-Waller factors. The position of phase change materials on the map is strongly linked to a certain ratio of r'_σ to r_π^{-1}. This ratio indicates a balance between resonance bonding necessary to obtain strong optical contrast and large Debye-Waller factors possibly facilitating fast crystallization [LSG+08].

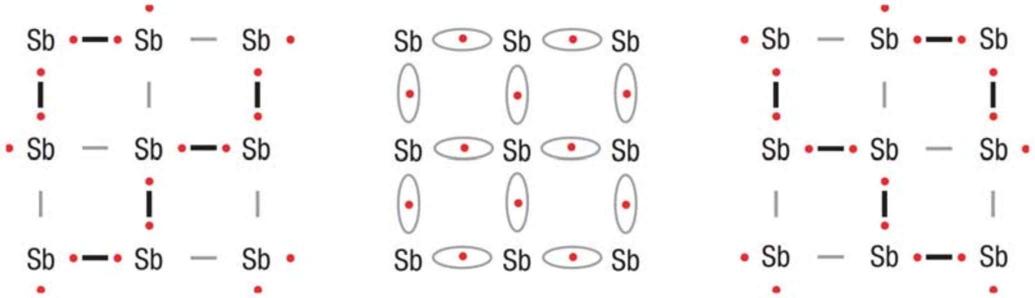

Figure 2.7: Schematic view of the resonant bonding effect exemplified on the group V element antimony in a undistorted cubic structure. The crystal structure of antimony can be represented by several contributing Lewis formulas, shown in the left and right-hand side. The actual structure is an intermediate between both canonical forms being illustrated in the middle. The high electron delocalization present in the resonance hybrid state results in an increasing electronic polarizability, i.e. high dielectric constants [SKW+08].
A synonym for the effect of resonant bonding or resonance is mesomerism.

2.3.2 The Threshold Switching Effect

Small confined volumes of a phase-change material can be electrically switched between an amorphous and a crystalline state. For electrical switching experiments different phase-change cell geometries have been developed in recent years [LKW05]. In Ovonic Unified Memory cells, abbrev. OUM, shown in the inset of Fig. 2.8, a thin phase-change film is contacted by a top and bottom contact [GLP02]. In OUM cells an additional resistor contacted to the bottom electrode acts as heating source. The active switchable region forms a mushroom cap near this heating resistor [RYC+06, PPL+07]. The heat induced phase transitions are controlled by short electrical pulses applied to the electrodes. The I-V characteristics measured on a phase change memory device during a crystallization pulse are shown in Fig. 2.8. Phase-change materials exhibit a pronounced contrast in resistivity between a highly conductive crystalline and a lowly conductive amorphous state. The I-V curves of the crystalline phase presented in Fig. 2.8 shows a linear increase with increasing voltage. In contrast, the amorphous state resistivity is remarkably non-linear. Below a certain voltage denoted as threshold voltage, the system is in the lowly conductive amorphous OFF-state. Here, the conductivity increases first linearly than exponentially and finally super-exponentially with increasing voltage applied to the cell [IZ07]. Exceeding the applied voltage above the critical threshold voltage leads to a sudden breakdown in resistivity by orders of magnitude. This is the *threshold switching* effect [Ovs68]. The highly conductive but still amorphous phase is known as the amorphous ON-state [PH71]. In the ON-state the conductivity increases linearly with increasing voltage. The high current densities present in the amorphous ON-state facilitate crystallization of an amorphous bit via Joule heating. This memory switch has to be well distinguished from the threshold switch, which is a phenomenon specific to the amorphous phase and does not involve a phase transition [WY07].

From a technical point of view, the threshold switching effect has important practical implications. Without this phenomenon taking place, large voltages would be needed to induce crystallization. The threshold switching effect enables to realize a voltage down-conversion and phase-change devices can be operated employing power pulses of a few Volts in amplitude. Indeed, the threshold voltage at which the threshold switching occurs depends on the amorphous volume of the cell, which has to be crystallized. The higher the volume the higher is the observed threshold voltage V_t. This implies that a critical electric threshold field $E_t \approx 10^6\text{V/m}$ rather than a threshold voltage yields to the sudden breakdown in resistivity [KRR+09].

Even though the threshold switching effect is crucial for the application of phase-change materials in electronic data storage devices, the underlying mechanisms remain an attractive puzzle to be solved in future research. The most prominent models describing this switching phenomenon will be explained in section 3.2.

2.3.3 The Resistance Drift Effect

Multi-level storage technologies aim to increase the storage density by differentiating more than two logical states per cell. In this way, the binary code could be replaced by a multinary code. In phase-change memory cells, the cell resistance can be systematically altered by varying the volume of the amorphous part of the cell. Consequently, electronic non-volatile data storage technologies based on phase change materials offer the possibility to design high density multi-level storage systems [PPS+10]. However, the amorphous state resistivity is observed to increase with time following a power law [BRP+09].

Fig. 2.9 shows the evolution of the cell resistance of a crystalline and a (partly) amorphous phase-change cell measured directly after the induced phase transition. Whereas the crystalline state resistivity is rather stable, the amorphous state resistivity increases significantly with time. The increase of the amorphous state resistivity over time is denoted as the resistance drift effect. This effect hampers the multi-level storage potential of phase-change materials in respect to information loss. Current research faces the challenge to overcome the resistance drift effect [PPM+11a]. Even though many theories are suggested, the underlying physics yielding to the resistance drift effect are still a point of controversial scientific discussion [KMK+07, PLP+04, IZ07, ISLL09]. A short overview of recently proposed mechanisms driving the resistance drift effect is presented in section 3.3 of this thesis.

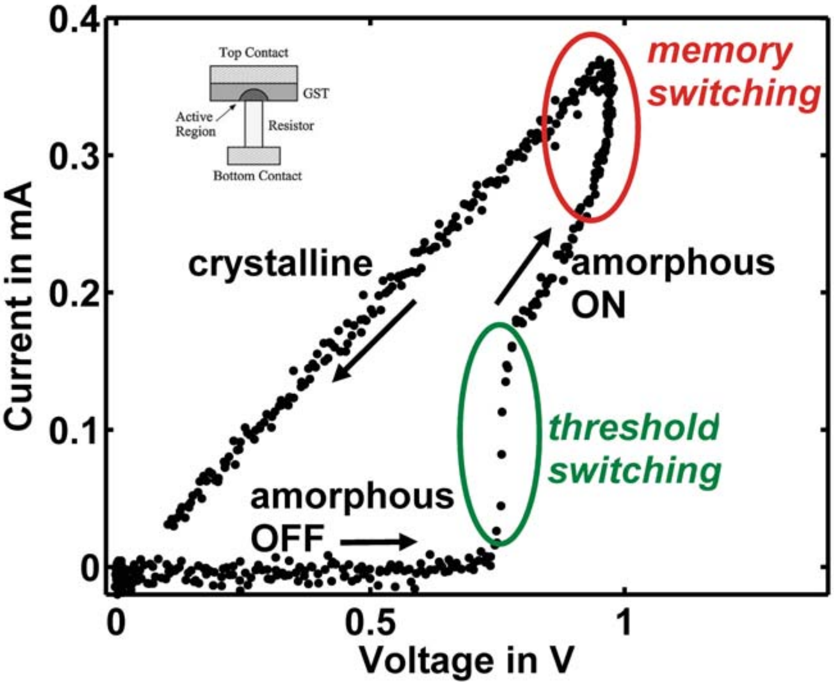

Figure 2.8: Typical current-voltage characteristics measured in a phase-change memory cell. An OUM cell is shown in the inset. At low voltages a significant difference exists between the conductivity in both phases that enables to read information at low electrical fields. Whereas the crystalline phase shows an ohmic behavior over the whole voltage range, the amorphous phase shows a remarkably non-linear behavior. At a critical electrical field, the conductivity increases suddenly by three orders of magnitude. Being in the highly conductive amorphous ON-state, the current density is high enough to induce the phase transition by Joule heating. Due to the sudden breakdown in resistivity, the memory switching is possible at technically applicable electrical fields. Thus, the *"threshold switching"* phenomenon is crucial for the application in the electronic data storage. However, the underlying physical mechanism is not yet completely understood. Image source: [WY07]; Inset taken from: [PLP$^+$04].

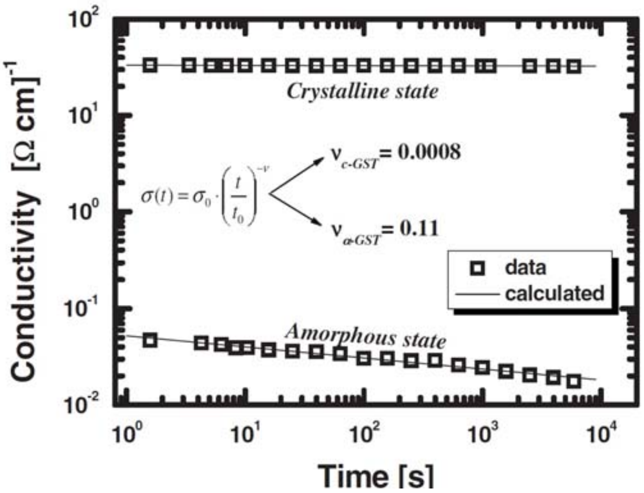

(a) Change in cell resistance over time

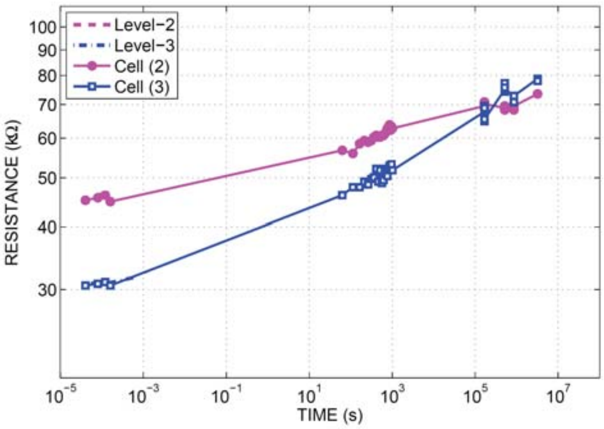

(b) Data corruption in amorphous phase-change cells

Figure 2.9: A phase-change memory cell can be reversibly switched between its highly conductive crystalline and lowly conductive amorphous state. The cell resistance in the amorphous state can be systematically varied by the volume of the amorphous part of the cell. This fact enables to program the cell to more than two logical states. To realize such a multi-level storage system, stable cell resistances are indispensable. The evolution of the cell resistance with time is measured directly after the induced phase transition. Whereas the crystalline state conductivity is rather stable, the amorphous state conductivity decreases significantly with time following a power law (a). The increasing amorphous state resistivity with time is known as the *"resistance drift"* effect and hampers the multi-level potential of phase-change materials, since it results in data corruption visualized in (b). Two phase-change cells are programmed to two different cell states. In both cells the cell resistance is observed to increase with time. However, due to different thermal histories, both cells show a different evolution in resitivity over time, i.e. a different drift exponent $\nu_{a\text{-}GST}$. Both cell states can no longer be distinguished after a time span of $10^5 s$. Image sources: [BRP⁺09, PPM⁺11a]

2.4 Aim and Structure of this work

The aim of this work is to gain a better insight into transport phenomena in amorphous phase-change materials. In literature different transport models describing the electronic transport properties in disordered structures have been reported. Based on a specific transport model, numerous theoretical models explaining the threshold switching and the resistance drift effect have been proposed for amorphous phase-change materials. The most prominent, even though controversial discussed theories are summarized in Chapter 3.

To improve the experimental basis of the proposed transport models, deposition, structural, optical, electrical and time resolved techniques are combined. Chapter 4 gives a short presentation of the sample preparation and different characterization techniques employed in the framework of this thesis.

Indeed, many transport models describing the electronic transport in amorphous phase-change alloys are based on localized defect states within the forbidden energy band gap. Due to the lack of long range order localized trap states are a characteristic feature of amorphous structures and play an important role for the electronic transport properties. This thesis provides a systematic and detailed study of defect state densities measured in various phase-change compounds. Chapter 5 concentrates on the defect state density measured in amorphous GeTe and other switchable chalcogenide alloys. The binary alloy GeTe is one of the first compounds identified as a phase-change material and thus offers a good set of references to the relevant literature. Furthermore, this material is of large industrial interest, because this alloy shows an exceptional combination of high crystallization temperature and fast crystallization speed. Furthermore, this chapter addresses the influence of defect states on threshold switching phenomena. A detailed study of resistance drift effects measured in a-GeTe compared to other phase-change and chalcogenide alloys is presented in Chapter 6. Moreover a possible link between resistance drift effect and relaxation of mechanical stresses within the amorphous deposited thin film is discussed at the end of this thesis.

Chapter 3

Electronic Transport in a-PCM: Short Review

This chapter gives a short review over the previous work carried out on transport properties in amorphous phase-change materials. In disordered structures localized trap states play an important role for the electronic transport properties. Their physical origin and their influence on the electronic transport are discussed in the first section of this chapter, followed by an overview of models describing the phenomena threshold switching and resistance drift.

3.1 Electronic Transport Models in Disordered Structures

Localized trap states are an intrinsic property of disordered materials. This section summarizes shortly the nature of defect states. Furthermore, defect state models proposed for amorphous phase-change materials and their influence on the electronic transport path are discussed.

3.1.1 Trap States

Extended states have non-localized wave functions. Consequently, carriers occupying an extended state contribute to the electronic conductivity. For example in a perfect crystal, the corresponding extended wave functions are plane waves with a lattice periodic modulated amplitude, known as Bloch functions, see Fig. 3.1a. Carriers occupying extended states are commonly denoted as free carriers. In contrast to extended states, a trap state exhibits an exponential decaying wave function, see Fig. 3.1b. Carriers occupying a trap state are localized in space and consequently do not contribute to the electronic transport as long as carrier transitions between localized states can be neglected.

Carrier localization: potential wins over kinetic Energy

The origin of carrier localization can be explained qualitatively in the frame work of quantum mechanics. In solid state physics, the lowest energetic state is favored. In consequence of the uncertainty relation, a large uncertainty in space, i.e. delocalized carriers, induces a low uncertainty in momentum,

$$\Delta x \cdot \Delta p \geq \hbar/2. \tag{3.1}$$

Thus, delocalization leads to a low average kinetic energy. In a perfect periodic potential, minimizing the kinetic energy is the only driving force resulting in extended Bloch functions. If the perfect periodicity is broken, for example by the presence of a positively charged imperfection, an additional driving force has to be considered. The potential energy of an electron will be significantly lower, if it stays near the positively charged imperfection and thus the corresponding electron state is localized. This example can be generalized to non-periodic potentials, i.e. localization is induced by minimizing the average potential energy.
Shortly summarized: Minimizing the kinetic energy is the driving force to create extended states, whereas minimizing the potential energy is the driving force to create localized states, illustrated in Fig. 3.2. The origin of carrier localization is thus given by the gain of potential over kinetic energy in that regime, [Zal83].

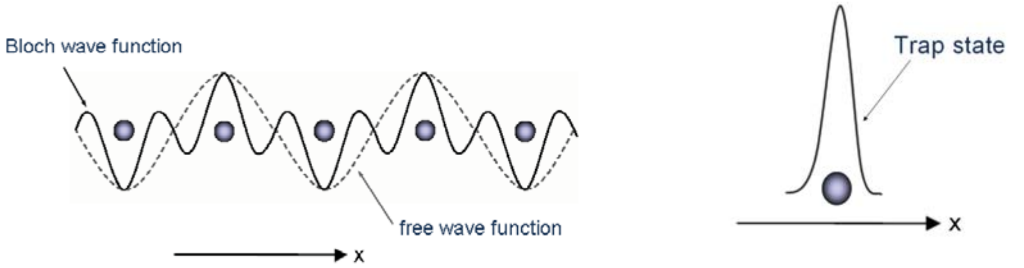

(a) perfect crystal: extended Bloch function **(b)** trap state: localized wave function

Figure 3.1: An extended state contributes to the electronic conduction, for example in a perfect crystal the probability to find a Bloch electron is the same for each unit cell. In opposite a *trap state* possesses exponentially decaying wave function and thus is localized in space. Consequently, trapped carriers do not contribute to the electronic conduction as long as carrier transitions between localized states can be neglected. See for further information [Zal83]

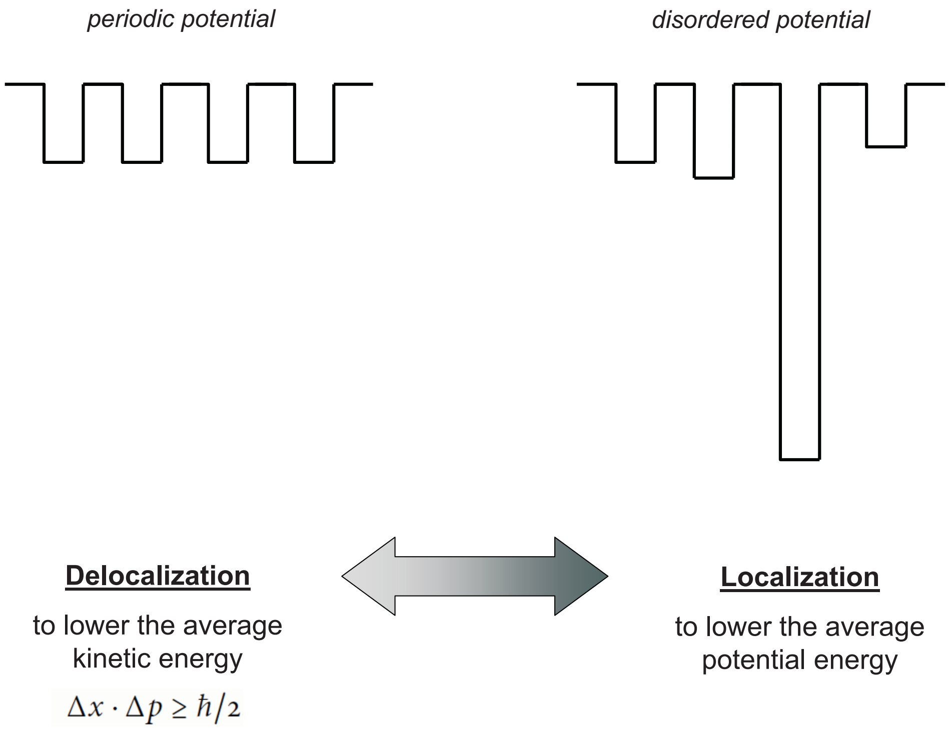

Figure 3.2: Driving forces in non-periodic systems. To lower the kinetic energy ‘Delocalization’ is favored, but ’Localization’ may lead to a lower potential energy.

Classification in defect band and band tail states

Trap states, which are described by a localized wave function, can be classified into defect band and band tail states depending on their physical origin. This classification is briefly explained in the following.

Defect band states result from over- or under coordinated atoms and thus can be also present in a crystal. It is well known, that the density of states describing a perfect three dimensional crystal follows a square root behavior. In crystalline systems the band gap is well defined and in the case of saturated bonds no energetic states exist within the band gap region $E_v < E < E_c$. However, over- or under coordinated atoms may create localized energetic states within the band gap, where the overlap in wavefunction results in a defect band for high defect concentrations, see Fig. 3.3a.

The lack of long range order in disordered systems gives rise to additional localized defect states which do not originate from over- or under coordinated atoms. In comparison with ordered crystalline materials the band gap in amorphous systems is not sharply defined: varying bond lengths and bond angles cause exponentially decaying band tail states reaching from the band edges into the gap, see Fig. 3.3b. A small value of the density of states $D(E)$ indicates that the corresponding configuration of bond lengths and bond angles is rarely realized, resulting in a small overlap of wave functions and thus in localization [IL02]. The mobility band gap is defined as the energetic region between the valence and conduction band edge and divides localized from delocalized states. In disordered systems the mobility band gap is in general not equal to the optical band gap in contrast to crystalline systems.

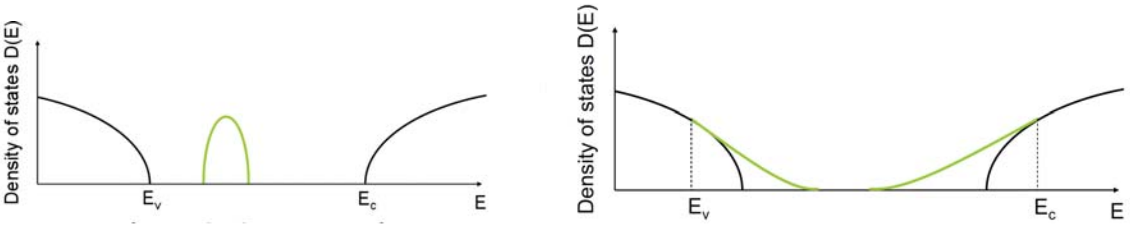

(a) Imperfection band **(b)** Band tails

Figure 3.3: Trap states are classified in imperfection bands (a) and band tail states (b), both presented in green colour. Imperfection bands are caused by structural defects, for example dopants or dangling bonds. In disordered structures, where bond lengths and bond angles vary, the band gap is not as sharply defined as in a ordered crystalline system: Exponentially decaying band tail states reach from the mobility band edges E_v and E_c into the gap. The typical density of states of a perfect crystal is shown in black for comparison.

Classification in acceptor and donor like trap states

Trap states capture free carriers from the bands. The charge state of the trap is changed due to such a capture process [Adl71]. Donor like tap states are defined to be neutral if occupied by an electron and positively charged if empty. Hence, empty donor states create a positive donor concentration N_D^+. Acceptor like states are neutral if empty and negatively charged if occupied by an electron. Consequently, occupied acceptor states give rise to a negative acceptor concentration N_A^-.

This classification of trap states as donor or acceptor like is an analog to the case of doped semiconductors [IL02]. Doping silicon of valency four with a group V element forms the so called donor level. At 0 K temperature the donor level is completely filled. With increasing temperature electrons at these donor states are excited into the conduction band and the Fermi level shifts with increasing temperature below the donor level, see Fig. 3.4. The emptied donor states build up a positively space charge. Likewise, doping silicon with a group III element, the missing electron creates an energy level near the valence band edge. This acceptor level is empty at 0 K temperature and is getting filled with increasing temperature due to thermal excitation. Consequently, the Fermi level shifts above the acceptor level with increasing temperature, see Fig. 3.4.

The position of the Fermi level is determined by charge neutrality, i.e. the positive charge given by the donor concentration N_D^+ and free hole concentration p must compensate the negative charge given by the acceptor concentration N_A^- and free electron concentration n, [IL02]:

$$N_D^+ + p = N_A^- + n \tag{3.2}$$

In disordered systems the band tail reaching from the valence band edge E_v into the band gap has donor character. The band tail coming from the conduction band E_c has acceptor character. In some materials trap states can capture more than one hole or electron from the bands [BDM+11]. These trap states are defined as amphoteric [Wal89]. In the presence of amphoteric trap states the charge neutrality relation given by Eq. 3.2 is given by a more complicated expression [YA75, BK87].

3.1.2 Defect State Models for a-PCM

Different band models have been proposed for chalcogenide glasses, where the most prominent ones are the Cohen-Fritzsche-Ovshinsky (CFO) and the Valence-Alternation-Pair model (VAP), both illustrated in Fig. 3.5. In both models the Fermi level E_F is pinned at mid gap [CFO69, KAF76a].

The CFO-model [CFO69] is based on the assumption that most atoms satisfy their valence requirements. The valence band edge E_v and the conduction band edge E_c sharply divide localized from delocalized states. Energetic states within the mobility gap $E_v < E < E_c$ are localized and energetic states beyond the band edges are delocalized, see Fig. 3.2. Consequently, the defect density within the band gap consists of the valence and conduction band tail, which

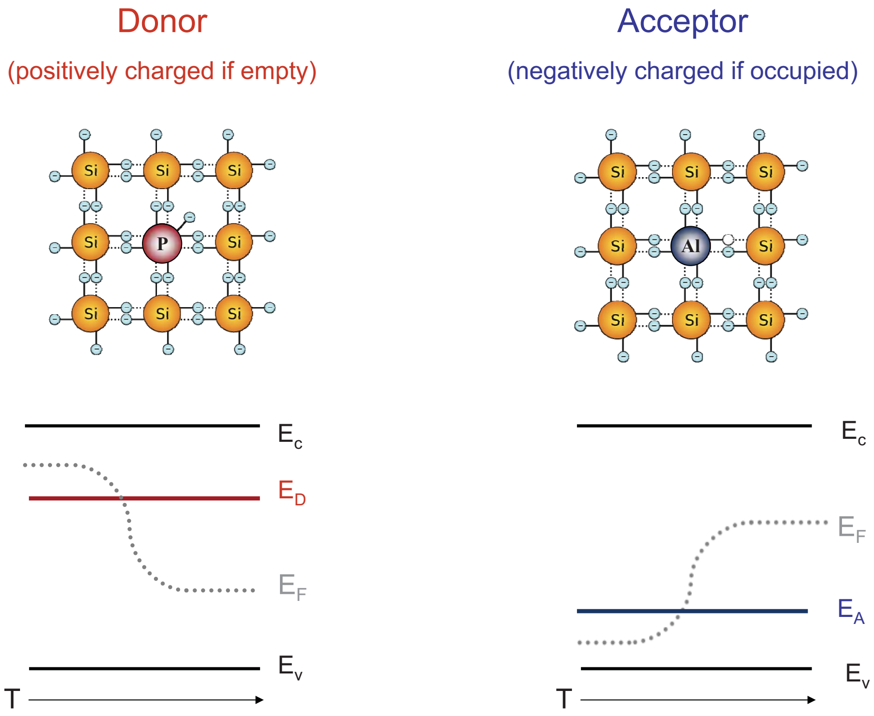

Figure 3.4: Donor and acceptor like trap states are defined in analogy to doped semiconductors. Donor / donor like states are neutral if occupied and singly positively charged if unoccupied by an electron. Likewise, acceptor or acceptor like states are singly negatively charged if occupied and neutral if empty [IL02].

are supposed to overlap in a certain range. Empty valence band tail states give rise to a random distribution of localized positive space charge. Likewise, conduction band tail states have acceptor character building up a randomly distributed negative space charge, if occupied by an electron. The Fermi level is fixed under the condition of charge neutrality near the center of the gap, where the total density of states is near its minimum.

In contrast to the CFO- model the VAP model proposes the presence of defects resulting from over- or undercoordination, respectively [KAF76a]. Due to covalent bonding, chalcogenides exhibit divalent bonding denoted as C_2^0 center , where C stands for chalcogen, the subscript gives the covalent coordination and the superscript the charge state. The expected existence of one dimensional Te-Te chains give rise to a high concentration of electrons, which do not ordinarily participate in covalent bonding, so called lone pairs. In the amorphous phase lone pairs have a wide spectrum of orientations resulting in diverse lone pair interactions, which induces a pronounced width of the valence band. Broken bonds along the Te-Te chain create valence-alternation pairs (VAPs): a three-fold overcoordinated, positively charged defect C_3^+

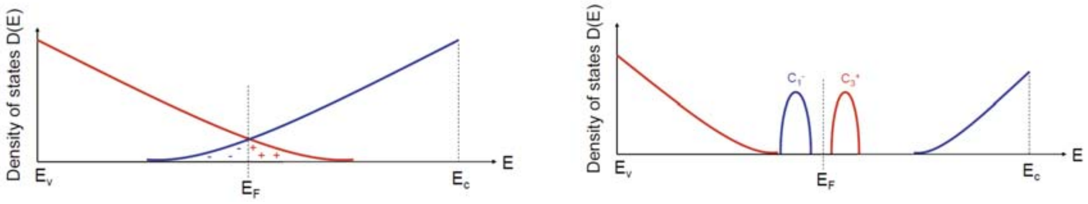

(a) CFO Model **(b)** VAP Model

Figure 3.5: The most prominent models proposed for a-PCM or chalcogenide glasses are the CFO and VAP model. In the CFO model overlapping valence and conduction band tails give rise to compensated local space charges. In the VAP model structural defects along the Te-Te chain result in simply charged defects known as C_3^+ and C_1^-, respectively.

and a negatively charged, one fold undercoordinated defect C_1^-. The donor like defects C_3^+ create a defect band energetically located above the Fermi energy E_F. The C_1^- defect creates a band of acceptor states located below the Fermi energy E_F. Valence-Alternation Pairs are expected to be at the origin of a large defect concentration in the range of 10^{17} to $10^{20}\mathrm{cm}^{-3}$ in chalcogenide glasses [BS80]. Obviously, the adddition or removal of an electron to a localized C_3^+ or C_1^- defect results in a change of local bonding. This lattice relaxation at the defect may lower the coulomb energy E_{coul} by an amount W giving the energy correlation energy E_{cor},

$$E_{\text{cor}} = \frac{e^2}{4\pi\varepsilon_0\varepsilon r} - W \tag{3.3}$$

Defects with negative correlation energy, such as Valence-Alternation Pairs, are referred to as negative U-centers. Negative U defects pin the Fermi energy, i.e. the position of the Fermi level changes only very little with varied defect occupancy. In contrast, if defects are characterized by a positive U, the Fermi level strongly depends on the trap occupancy and thus is expected to shift significantly with varied temperature or doping concentration [Str91a].

3.1.3 Multiple-Trapping Transport Model

The presence of localized trap states has a strong influence on the electronic properties in a disordered solid. For example, the position of the Fermi level is defined by the presence of states within the band gap. Furthermore, localized defect states have a strong influence on the main electronic transport path in disordered systems. To describe the electronic transport in amorphous systems, the mobility band gap is generally of paramount importance. Energetic states E lying within the mobility band gap, i.e. $E_v < E < E_c$ are localized. States lying beyond the valence band edge E_v or conduction band edge E_c are delocalized and form the valence band or conduction band, respectively. In the multiple-trapping transport model the electronic transport is dominated by free carriers. In n-type materials the transport is dominated by free electrons having an energy $E > E_c$. Vice versa, holes of energy $E < E_v$ control the electronic transport in p-type materials. By applying an electric field, free carriers drift through the specimen. Thereby free carriers interact with localized trap states. Empty trapping centers capture free carriers from the band. In Fig. 3.6, these multiple trapping processes are exemplified for a free electron being trapped from the conduction band. While occupying a trap state the electron is localized and thus does not contribute to the electronic conduction, until it is thermally released back to the conduction band. While drifting in direction of the applied electric field a free electron is captured and released several times. These multiple trapping and release processes hamper the electronic transport, since the electron does not contribute to the electronic conductivity while occupying a localized defect state.

In systems, where the electronic transport can be described within the multiple-trapping transport model, the conductivity decreases in general with increasing trap state density.

3.1.4 Hopping Transport Model

In disordered materials, a further transport mechanism is possible. Instead of being thermally released back to the band, a trapped carrier can tunnel from trap to trap. This transport channel is known as the hopping conduction path. Especially at low temperatures this transport channel is expected to be dominating, since the activation energy for hopping W is much lower than the activation energy for multiple trapping E_a.

In the case that the electronic transport is governed by hopping processes a higher number of trap states leads to an increasing conductivity, because (i) the overlap of wave functions between neighboring trap states is increased and (ii) the probability that two neighbour trap states having a similar energy increases too.

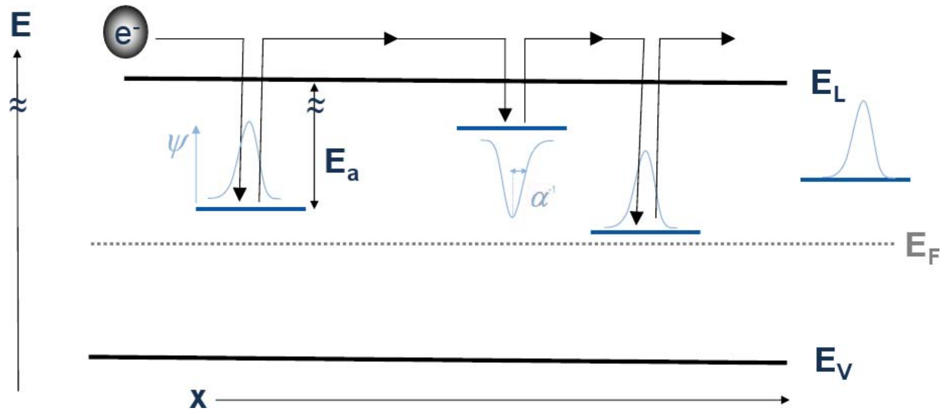

Figure 3.6: Multiple-Trapping Transport model - Band transport interrupted by multiple capture and release processes. If Multiple trapping is the main transport channel, the conductivity decreases generally with increasing number of trap states due to a higher number of capture processes.

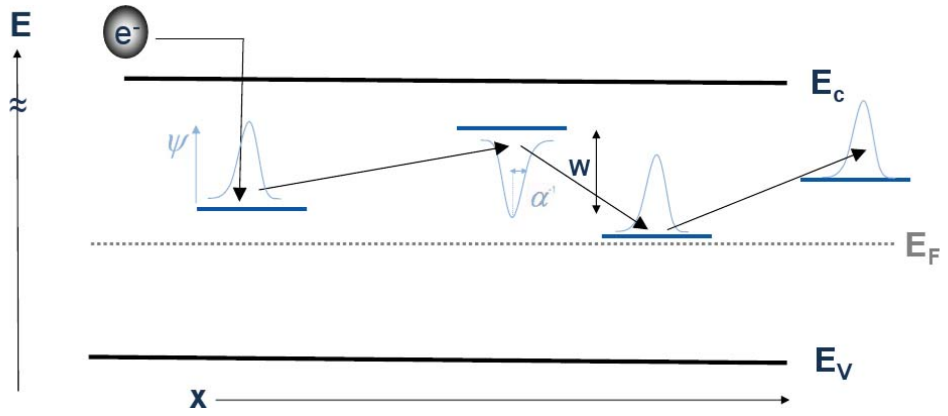

Figure 3.7: Hopping Transport model - Jumping from trap to trap. Especially at low temperatures hopping conduction is expected to be the main transport channel. If hopping is dominating the conductivity increases with increasing number of trap states, since more hopping sites are available.

3.2 Models describing the Threshold Switching Effect

This section is devoted to models explaining the threshold switching effect, which describes the sudden increase in conductivity above a critical electrical field of about $E_t \approx 10^6\,\mathrm{V/m}$. Many models have been discussed to explain this phenomenon illustrated in Fig. 2.8. Whereas some models relate the sudden increase in conductivity to trap kinetics, other models propose a increasing carrier mobility or field induced crystalline nucleus formation to be the physical origin of this puzzling effect.

3.2.1 Field Induced Nucleation Model

In this model, the system remains in the high resistive amorphous OFF state until a crystalline filament nucleates within a strong electric field forming a conductive path between both electrodes identified as the amorphous ON state of the phase-change memory cell, see Fig. 2.8 and Fig 3.8. A short discussion of this threshold switching model is given below.

The phase-change cell consisting of a thin phase change film sandwiched between two electrodes can be considered as a simple capacitor. Before switching the thin phase change film of thickness l is considered to be uniform and completely amorphous. In this capacitor model, a bias V results in an electric field $E_0 = V/l$. With increasing bias highly conductive crystalline particles start to appear. These crystalline particles have dipole moment $p \propto E_0$, which interact with the electric field. The dipole interaction reduces the system energy and thus facilitates nucleation. The actual switching phenomenon starts with the nucleation of a long crystalline cylinder of radius R and height h, where $(h >> R)$. The highly conductive cylinder concentrates the electric field resulting in a drastic electrical field enhancement near the cylinder end $E \approx (h/R)^2 E_0$. The strong electric field facilitates nucleation of further spherical particles triggering a process of cylinder growth via subsequent nucleation of spheres forming a conductive path within an amorphous environment, see Fig. 3.8. In the case of electrical field removal, conductive particles disappear if they have not reached a sufficient size. In particular, the growth of the crystalline filament is interrupted if the time given to grow within a strong electric field ($E_0 \approx 10^6\mathrm{V/m}$) is not long enough. The nucleation time of the crystalline filament can be interpreted to be the physical origin behind the experimentally observed switching delay time t_d, i.e. the time span between the threshold field application and the switching event [KCJ+05, LIL10]. The holding voltage is the minimum voltage to maintain the high conductive ON-state, which is smaller than the threshold voltage [ASSO80]. According to the Karpov group the holding voltage can be related to the minimum electric field required to maintain a non positive difference between the free energies of the system with and without conductive filament [NKJI09]. Furthermore, this model can explain the dependence of the threshold voltage on layer thickness l and temperature T [KBZ+11, SJJ+10].

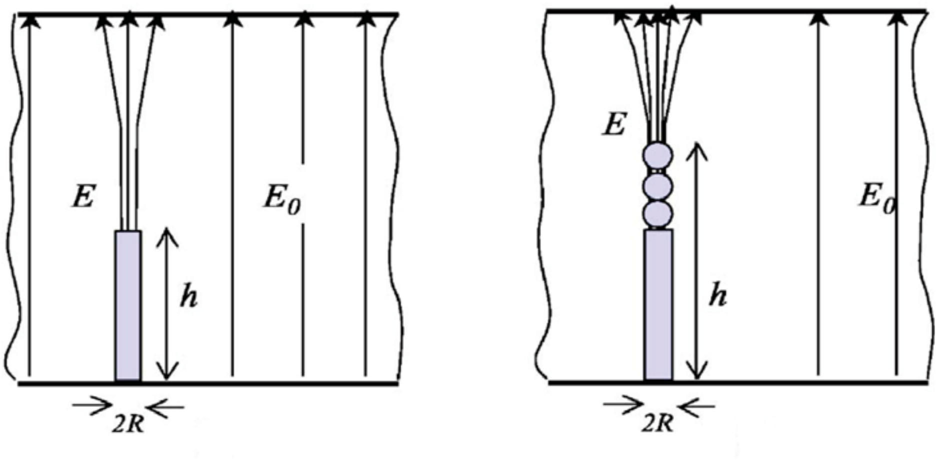

(a) Nucleation of a cylinder embryo **(b)** Nucleation of spherical particles

Figure 3.8: The Karpov group proposes a threshold switching mechanism based on a field nucleation hypothesis. The switching phenomenon starts with the nucleation of a crystalline cylinder embryo. The highly conductive cylinder in a highly resistive amorphous environment concentrates the electric field drastically at the cylinder end. The high electric field facilitates nucleation of further spherical particles. A crystalline filament starts to grow from the cylinder end forming a conductive path between both electrodes. Image source:[KKSK07]

3.2.2 Small-Polaron Model

In contrast to field induced nucleation, where the high conductive amorphous ON state is formed by a crystalline filament, the Small Polaron model links the sudden increase in conductivity to an increasing carrier mobility. A polaron is a quasi particle describing the interaction of a charged carrier moving through a environment. Around the charged carrier, polarization is induced for example by long range Coulomb forces, causing local deformation of the local lattice. Moving through the dielectric, a carrier is thus accompanied by a cloud of phonons. The induced lattice polarization acts as a potential well hindering the movement of the conducting carrier. Consequently, the formation of polarons decrease the free carrier mobility. A conducting electron in an ionic crystal is a classic example for polaron formation. Polarons are classified into large and small polarons depending on their spatial extension compared to the lattice parameter of the solid. If the spatial extension of a polaron is large, its dielectric surrounding can be treated as a polarizable continuum. In this case, the polaron is classified as *large* synonymous with a Fröhlich polaron. If the self-induced polarization caused by the carrier charge is of the order of the lattice parameter the polaron, which may arise is denoted as *small* or Holstein polaron. Whereas large polarons are governed by long-range interactions, small polarons are dominated by short-range interactions, [Dev96].

Indeed Hall mobilities measured in chalcogenide glasses such as AsTe or Sb_2Te_3 are reported in literature to be very low having room-temperature values of $\mu_{Hall} \approx 0.1 \mathrm{cm}^2/\mathrm{Vs}$

[ESQ72, BE06]. Additionally the measured Hall mobility in chalcogenide alloys is anomalously signed and shows thermal activation. Hall-effect measurements on the low conductive standard phase-change material $Ge_2Sb_2Te_5$ are difficult. However, even though Emin and co-authors report very small Hall signals they claim to observe a very low Hall-mobility near $0.07\,\mathrm{cm}^2/\mathrm{Vs}$ in a-$Ge_2Sb_2Te_5$ [BEL06]. Based on the small Hall mobilities observed in chalcogenide glasses D. Emin proposes a mechanism for threshold switching based on *small polarons* [Emi06]. He claims that the electronic transport in the low conductive amorphous OFF phase, see Fig. 2.8, is driven by small polarons as predominant charge carriers. Thereby, thermally assisted hopping between lone-pair orbitals on chalcogen atoms such as Te represent the main transport path. The small-polaron hopping mobility is orders of magnitudes smaller than the free carrier mobility in ordinary conductors. In the amorphous OFF state, the electric current in chalcogenide glasses is carried by a high density of low mobility carriers. In contrast, the carriers in the metallic electrodes have typically a very high mobility. According to Emin, the steady-state flow through the electric contacts lead to an accumulation of small polarons within the amorphous phase-change material. The higher the applied electric fields through the electrodes the higher is the small-polaron density within the amorphous phase-change alloy. In the case of very high small-polaron densities, destructive interferences between atomic displacements of different small-polarons can break up the phonon-carrier interaction. The quasi-particle composed of a charge and its accompanying phonons describing the local lattice distortion destabilizes and is converted into a conventional free carrier characterized by a high mobility forming the amorphous ON state in Fig. 2.8. In this model, the delay time, the time span between the application of the threshold voltage and the switching event, can be attributed to the time needed to reach the steady on-state condition.

However, recently the validity of the Small Polaron model has been largely questioned. In his master thesis Matthias Käs succeeded to perform high quality Hall measurements on a-$Ge_2Sb_2Te_5$. Due to their comparable high amorphous state resistivity, accurate Hall measurements in usually available set-ups are challenging and exhibit a bad signal to noise ratio [BEL06]. Therefore a sophisticated home-built set-up meeting the desired requirements has been developed at the I. Institute of Physics (IA) at the RWTH Aachen University. According to Emin the Small Polaron model predicts a certain relation between the activation energies describing the temperature dependence of the Hall mobility $E_{\mu HALL}$, Seebeck $E_{Seebeck}$ coefficient and dark conductivity E_a [BE06, ESQ72],

$$E_a = E_{\mu HALL} + E_{Seebeck} \tag{3.4}$$

In his master thesis Matthias Käs could show that this relation is not valid in a-$Ge_2Sb_2Te_5$.

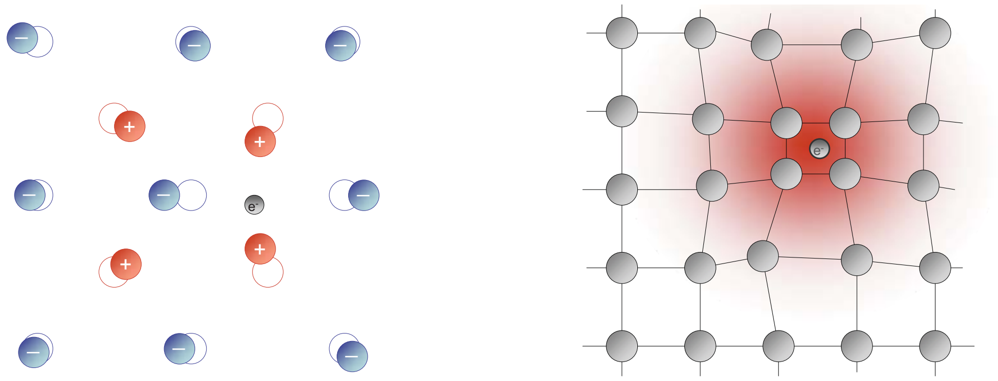

(a) Polaron in an ionic Crystal **(b)** Small Polaron

Figure 3.9: A polaron is a quasi particle describing the interaction of charged carriers drifting through a dielectric environment. A conducting electron in an ionic crystal is a classic example for polaron formation. An electron in an ionic crystal attracts the positive and repels the negative ions. The interaction between lattice and charge carriers causes a self-induced polarization, which acts back on the electron reducing its carrier mobility drastically (a). A small polaron is formed if its spatial extension is of the order of the lattice parameter (b).

According to D. Emin the electronic transport in a-PCM at low electric fields is driven by small polarons acting as charge carriers, whose density increases with increasing electric field. Above a critical value destructive interferences between atomic displacements of different small-polarons convert the quasi particle into free carriers. The *threshold switching* phenomenon is thus attributed to a drastic change in mobility of charge carriers.

3.2.3 Carrier Injection Model

The carrier injection Model is based on recombination of free carriers in localized singly charged defects states in amorphous chalcogenides [VWD75, OR73].
According to the CFO or VAP model, the Fermi level is pinned at or near the middle of the mobility band gap and a complete set of compensated positively and negatively charged defects lie below and above the Fermi level. By applying an electric field, free electrons and holes are injected from the cathode and anode, respectively see Fig. 3.10a.
Near the electrodes, these free carriers recombine with charged defect centers of the amorphous phase-change material and neutralize them. In consequence a space charge builds up, which redistributes the electric field: enhancement in the center and reduction near the electrodes Fig. 3.10b. This situation describes the amorphous OFF state of a disordered phase-change material, see Fig. 2.8.
With increasing voltage being applied to the electrodes more carriers are injected into the active material and the space charge regions grow until eventually they meet and overlap giving the switching condition, shown in Fig. 3.10c. This switching situation rapidly becomes unstable. In the region of the overlap there is no space charge, because all traps have been neutralized. Consequently, the carrier conductivity in the neutralized region is very high since the electron and hole drift is no longer hampered by trap states. Furthermore, the space charge at both electrodes decreases with increasing overlap increasing the electric field at the electrodes, Fig. 3.10d. In summary, while the conductivity in the center increases the electrical field enhancement near the electrodes results in a injection of more and more free carriers. Both effects create an unstable situation increasing the neutralized region very rapidly to its maximum limit Fig. 3.10e. Here, the bands are very flat and Schottky-type barriers are established at the electrodes. However, the high defect density expected in amorphous chalcogenides [CFO69], [BS80] yields to very thin barriers estimated to be as thin as $1\,\mathrm{nm}$ [OR73]. Consequently, free carriers can easily tunnel from the Fermi level of the metal into the conducting band of the phase-change alloy. This situation constitutes the amorphous ON state of the switching chalcogenide and is illustrated in Fig. 3.10e . The minimum voltage required to keep the ON state, known as holding voltage V_h, corresponds to the mobility band gap E_μ of the amorphous phase-change alloy, i.e. $qV_h = E_\mu$. In the carrier injection model, the delay time t_d represents the time needed to fill the traps to the switching condition of overlapping space charge regions, depicted in Fig. 3.10c.

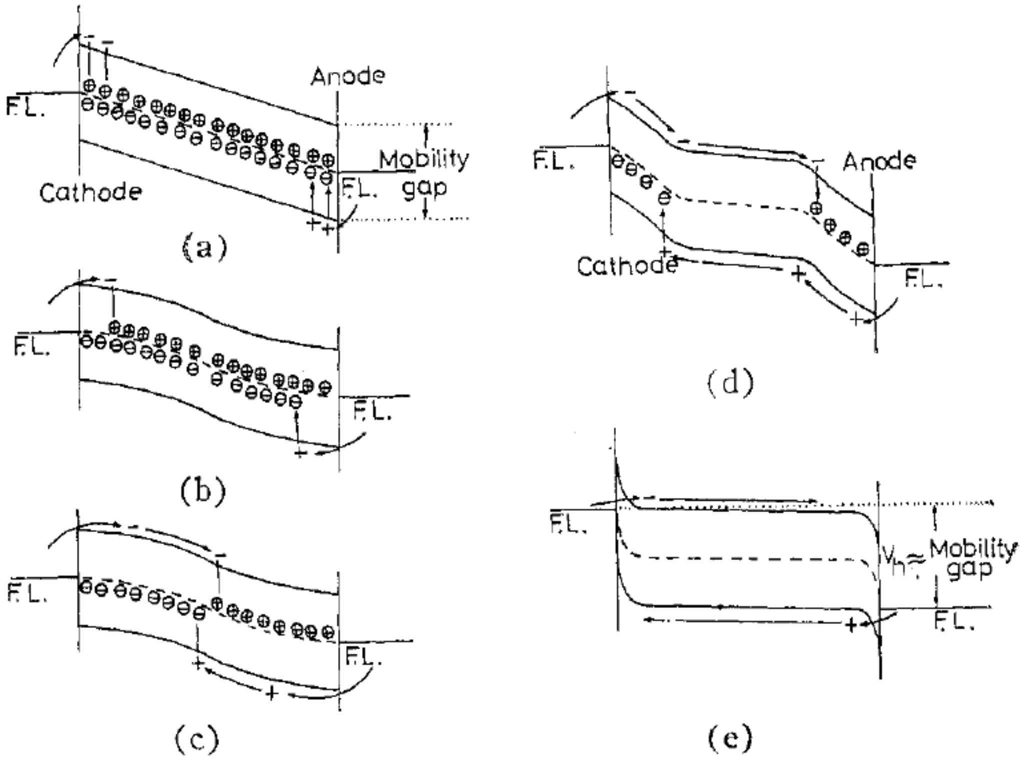

Figure 3.10: In the Carrier Injection Model, free carriers are injected via both electrodes. Due to capture of injected electrons (holes) by positively (negatively) charged defects the space charge neutrality is modified in the material (a) and uncompensated space charge builds up near the electrodes (b). The situation illustrated in (a) and (b) represents the amorphous OFF state in Fig. 2.8. With increasing applied voltage, the space charge regions increase. In the switching condition both space charge regions overlap (c). The situation in (c) is very unstable. Within the neutralized region, the conductivity is very high, because no trap states hamper the electronic transport. Additionally, the reduction of the space charge near the electrodes increases the electric field facilitating further carrier injection. Both effects increase the rate with which space charge overlap occurs (d) yielding to the amorphous ON state illustrated in (e). Image source: [OR73]

3.2.4 Poole-Frenkel Model

The Poole Frenkel model is based on thermal emission between donor like trap states, where a trap state is considered to create a Coulomb potential [IZ07, IZ06, Iel08]. The potential profiles for two neighboring donor traps under the influence of an increasing electrical field are shown in Fig. 3.11. Nowadays, the Poole-Frenkel model is the most accepted transport model for amorphous phase-change materials.

In the case where no electrical field is applied an electron trapped at energy E_T has to overcome a barrier height of $E_C - E_T$ to be excited back to the conduction band (a). The presence of an electric field changes the shape of the potential profile inducing a lowering of the barrier between traps I and II (b-c). The higher the electric field the lower is the energy barrier between both traps. Traps can be treated as isolated if they do not influence each other, i.e. the nearest neighbor trap is sufficiently far away that it does not lead to an additional change of the energy barrier. In the case of isolated traps the electrical current is given by the standard Poole-Frenkel model. Here the current depends on the square root of the applied voltage V_a:

$$\textbf{Poole-Frenkel} \qquad I = I_{PF} \cdot \exp(\beta_{PF} {V_A}^{1/2}) \tag{3.5}$$

where I_{PF} and β_{PF} are constants [IZ07]. However, in amorphous chalcogenides the trap state density is expected to be very high. Consequently nearest neighbor traps may influence each other and Eq. 3.5 does not describe the current dependency properly. In the case that traps are interacting the energy barrier is lowered in addition to the lowering induced by the electric field. This results in a current, which increases exponentially with applied voltage:

$$\textbf{Poole} \qquad I = I_{PF'} \cdot \exp(\beta_{PF'} V_A) \tag{3.6}$$

where $I_{PF'}$ and $\beta_{PF'}$ are constants [IZ07]. The exponential current dependency given in Eq. 3.5 is often denoted as Poole transport mechanism. The Poole and Poole-Frenkel transport model describe both multiple trapping processes illustrated in Fig. 3.6, with a lowered energy barrier $\Delta\phi < E_C - E_T$. The calculated barrier lowering for thermal emission back into the conduction band for different inter-trap distances Δz are shown in Fig. 3.11b. The barrier lowering shows a square root behavior on the electric field for inter-trap distances larger or equal to $\Delta z = 5\,\mathrm{nm}$. Consequently for $\Delta z \geq 5\,\mathrm{nm}$, the Coulomb potentials of different trap states do not influence each other. The traps can be treated as isolated. In contrast for small inter-trap distances $\Delta z \leq 2\,\mathrm{nm}$ neighboring traps are no longer isolated. The Coulomb potential of neighboring traps induce an additional lowering of the energy barrier. Thus the energy barrier lowering increases linearly with increasing applied voltage for small inter trap distances.

Subthreshold Conduction model

The Poole or Poole-Frenkel mechanisms describe a band limited transport model illustrated in Fig3.6. In a band limited transport model a trapped electron is thermally released out of

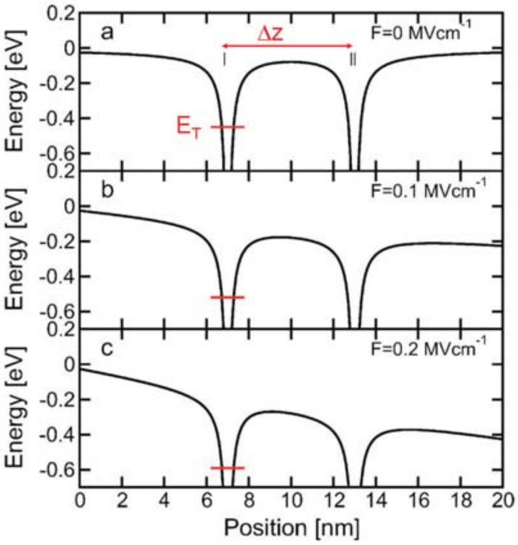

(a) An electric fields lowers the potentials barrier between two traps

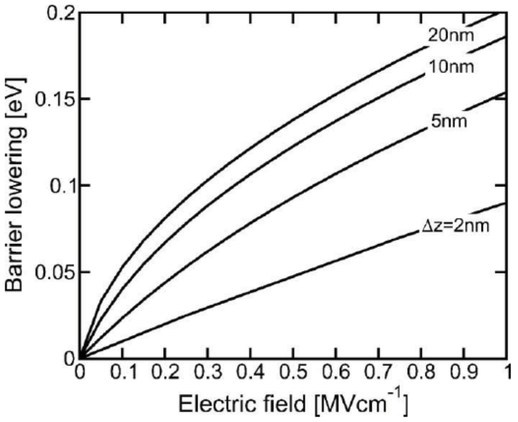

(b) Energy barrier lowering for different inter-trap distances

Figure 3.11: Potential profile between two donor-like trap states (charge 0/+) having a distance Δz from each other. The energy barrier between trap I and trap II is lowered with increasing electric field (top). The energy barrier lowering $\Delta\phi$ depends on the inter-trap distances Δz (bottom). For large inter-trap distances $\Delta z \geq 5\,\mathrm{nm}$ the Coulomb potentials of both trap states do not influence each other. For isolated traps the barrier lowering increases by a square root with increasing electric field resulting in Poole-Frenkel conduction given by Eq. 3.5. For small inter-trap distances $\Delta z \leq 2\,\mathrm{nm}$ the energy barrier is lowered by interaction between Coulomb potentials of trap states and the electric field. In this case the energy barrier increases linearly with increasing electric field yielding to Poole conduction given by Eq. 3.6. Image source:[IZ07]

the trap into the conduction band after a certain time. Here this release time out of the trap depends on the direction of the electrostatic force. Carrier transitions in the same direction as the electrostatic force take advantage of the energy barrier lowering between trap I and II shown in Fig. 3.12. Thus, a forward thermal emission is linked to the release time $\tau_{\rightarrow}$ described by:

$$\tau_{\rightarrow} = \tau_0 \cdot \exp\left(\frac{E_c - E_T\text{-}\Delta\phi}{k_b T}\right) \tag{3.7}$$

where τ_0 is the characteristic attempt-to-escape time for a carrier captured by a trap located at energy E_T. The exponent in Eq. 3.7 contains the energy barrier at zero field corrected by the barrier lowering denoted as $\Delta\phi$. Whereas carrier transitions in direction of the electrostatic force face a energy barrier lowered by $\Delta\phi$, carrier transitions in the opposite direction of the electrostatic force have to overcome the energy barrier at zero field plus $\Delta\phi$. Consequently a reverse thermal emission is attributed to higher release times $\tau_{\leftarrow}$:

$$\tau_{\leftarrow} = \tau_0 \cdot \exp(\left(\frac{E_c - E_T + \Delta\phi}{k_b T}\right) \tag{3.8}$$

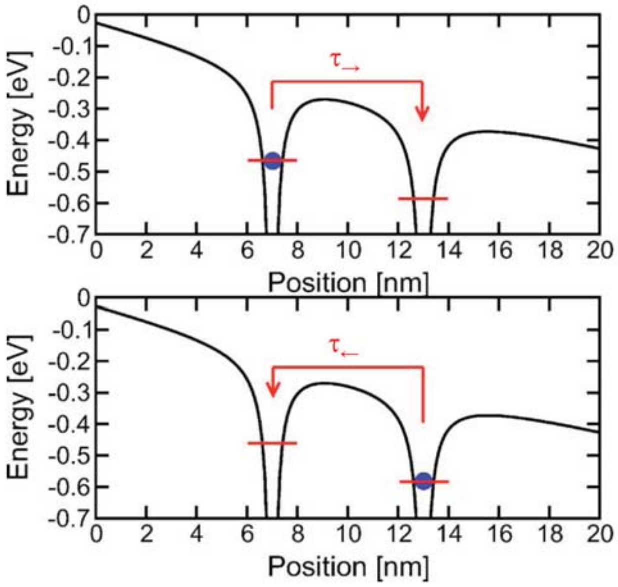

Figure 3.12: An electron captured by a donor trap can be thermally excited back to the conduction band. Thereby the release time τ depends strongly on the direction of the applied electric field. For thermal emission in the direction of the electrostatic force, the electric field lowers the energy barrier between traps by $\Delta\phi$ (top). For reverse thermal emission versus direction of the electrostatic force, the presence of an electric field increases the energy barrier by $\Delta\phi$ (bottom). This scenario shown here for electrons can be applied analogously for holes. Image source:[IZ07]

Forward and reverse thermal emissions illustrated in Fig. 3.12 lead to a forward and reverse current. At zero electric field, the reverse current equals the forward current. Consequently, no net electric current is observed if no voltage is applied. However, the reverse current is expected to influence the net current significantly for small electric fields, i.e for a soft energy barrier lowering. Considering forward and thermal emission, the net current I was shown to follow the relation [IZ07]:

$$I = 2qAN_{T,tot}\frac{\Delta z}{\tau_0} \cdot \exp(-(E_c - E_F)/k_bT) \cdot \sinh(\Delta\phi/k_bT), \quad (3.9)$$

where q denotes the elementary charge, A indicates the conduction cross section and $N_{T,tot}$ is the integral of the trap distribution in the gap above the Fermi level. The authors approximate the energy barrier lowering between two identical, positively charged traps with inter-trap distance Δz to:

$$\Delta\phi \approx qV_A\frac{\Delta z}{2u_a}, \quad (3.10)$$

where u_a is the thickness of the amorphous chalcogenide layer. For low applied voltages the $\sinh$ in Eq. 3.9 can be replaced by its linear approximation resulting in an ohmic behavior $I \propto V_A$. For high applied voltages the energy barrier lowering according to Eq. 3.10 results in a Poole conduction mechanism, i.e. the electric current I depends exponentially on the applied voltage V_A. These predictions of the Poole conduction model are experimentally verified by the authors [IZ07, IZ06, Iel08]. Indeed the subthreshold $I - V$ curves describing the amorphous OFF state defined in Fig. 2.8 show first a linear dependence. For large applied voltages the authors report an exponential increase of the current [IZ07]. The correct description of the sub-threshold regime is a great success of the Poole conduction model.

Threshold Switching model

Within the Poole and the Poole-Frenkel model the same mechanism for threshold switching can be proposed [Iel08]. This model proposed for electrons can be analogously applied to holes.

In both models, the high electric field is expected to create a non-equilibrium distribution of electrons. The distribution function $f(E)$ is changed significantly by the electric field, so that electrons occupy states well above the dark Fermi level E_F but well below E_c. In this regime $E_F < E < E_c$ the conduction is either driven by Poole or Poole-Frenkel mechanism, i.e. multiple trapping processes are dominant. Since the electric field is very high, forward thermal emission exceeds reverse thermal emission and the release time is given by $\tau_{\rightarrow}$ (see Eq. 3.7) . The release time $\tau_{\rightarrow}$ depends exponentially on the trap depth E_T. As a consequence of the electric field, electrons occupy electronic states nearer to the conduction band edge. This results in significant lower release times. Hence, the carrier mobility is strongly increased, because the electronic transport is less hampered by multiple-trapping processes.

The threshold switching mechanism in the Poole or Poole-Frenkel model is illustrated in Fig. 3.13. In the amorphous OFF state, electrons occupy trap states up to the Fermi level (a). In the high-current regime, the occupation of trap states is not uniform within the film thickness u_a. Near the injection electrode, electrons feature an equilibrium distribution, i.e. within a layer of thickness $u_{a,OFF}$ electrons fill trap states below the Fermi level like in situation (a). However, within a certain drifting distance the electrons have collected enough energy from the applied electric field. Within a layer of thickness $u_{a,ON} = u_a - u_{a,OFF}$ electrons occupy thus shallow traps well above the dark Fermi level E_F resulting in much lower release times and thus higher effective carrier mobilities.

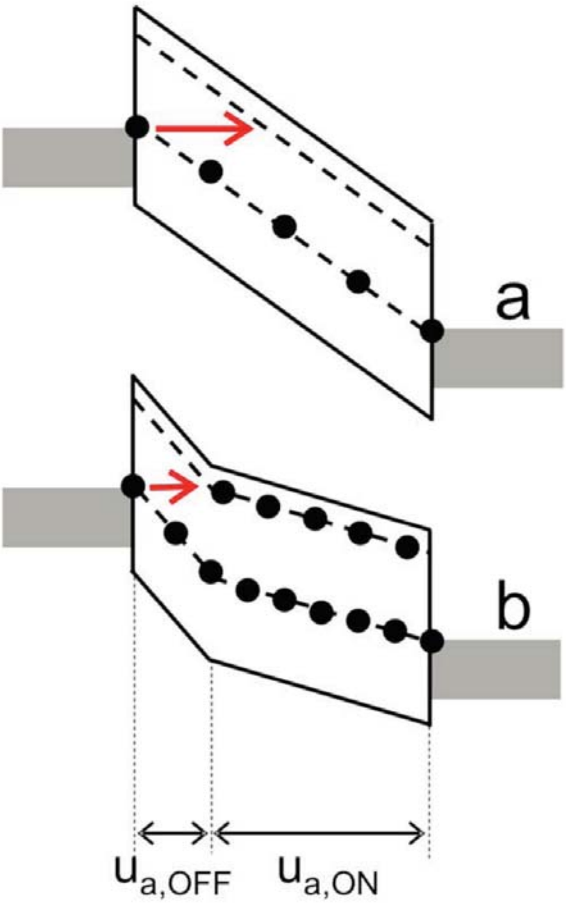

Figure 3.13: The Poole and Poole-Frenkel model attribute the sudden increase in conductivity at a critical applied voltage known as the threshold switching effect to a filling of shallow trap states near the conduction band edge. In the amorphous OFF state, electrons fulfill equilibrium statistics and fill trap states up to the dark Fermi level (a). A high electric field results in a non-equilibrium distribution function. Consequently, electrons occupy trap states well above the dark Fermi level (b). Since the release time depends exponentially on the trap depth E_T, the effective carrier mobility is largely increased in situation (b). Image source:[IZ07]

3.3 Models describing the Resistance Drift effect

In the last section we have seen that many models relate the threshold switching effect to the presence of localized trap states within the band gap. Likewise, trap states are expected to play a key role in the resistance drift effect as well. The resistance drift effect described shortly in subsection 2.3.3 denotes the steady increase of the amorphous state resistivity with time. Hereby, the increase in resistivity is reported to follow a potential law [BRP+09]:

$$\rho(t) = \rho_0 \cdot (t/t_0)^{\alpha_{\mathrm{RD}}} \tag{3.11}$$

Many models have been proposed to explain the resistance effect, which accelerates at elevated temperatures. The three most prominent models link the resistance drift effect either to trap kinetics or to structural relaxation of the glassy state and are presented in this subsection.

3.3.1 Structural relaxation described by a double-well potential

Karpov *et al.* relate the observed drift to aging phenomena, where a metastable glass structure relaxes to its more stable state [KMK+07]. This approach is reasonable, because in disordered structures some elements are expected to be excessively flexible [PT85]. Thus some atoms are able to change their atomic configuration. Even though this concept assumes different electronic properties of the meta-stable and the stable state, the proposed structural relaxation model does not necessarily invoke any trap kinetics.

The double-well potential concept offers a universal framework to describe atomic dynamics in glasses [AHV72]. Hereby, the atomic potential is assumed to form a double-well, where each well is related to a certain, not necessarily known, atomic arrangement , see Fig. 3.14. The metastable state I forms a local minimum and thus lies higher in energy than the global minimum symbolizing the stable atomic structure II of the glass. Therefore, a structural relaxation process from the metastable to the stable atomic state has to overcome a potential barrier of height ΔW_B. The structural disorder in a glass translates into fluctuations of this barrier height ΔW_B, since the energetic positions of the stable and meta-stable state fluctuate too. However, it is a commonly accepted hypothesis, that the barrier height W_B is described by a uniform probabilistic function within certain limits [KG93, AHV72]:

$$p(W_B) = 1/\Delta W_B \tag{3.12}$$

$$\Delta W_B = W_{B,max} - W_{B,min} \tag{3.13}$$

The double-well potential model introduces the exponential varying relaxation time [AHV72]. The distribution of barrier heights ΔW_B results in strongly varying relaxation times $\tau(W_B)$:

$$\tau(W_B) = \tau_0 \exp(W_B/kT) \tag{3.14}$$

An atomic configuration characterized by a low energy barrier ΔW_B relaxes rapidly into its stable state, whereas atomic configurations described by high energy barriers ΔW_B relax much slower. Consequently, the number of relaxed double-wells increases with time. The structural relaxation from the meta-stable to the stable atomic configuration is expected to induce a volume change, which is consistent with the stress release observed in amorphous phase-change materials [KSLPW03]. Hereby, the relative volume change increases with increasing number of relaxed double-wells. Karpov *et al.* claim that the observed change in resistivity can be linked to the change in volume. Typically chalcogenides show a thermally activated amorphous state resistivity.

$$\rho = \rho_0 \exp(E_a/kT). \tag{3.15}$$

In the standard approximation, a relative volume dilation results in a higher activation energy of conduction $E_a = E_F - E_v$ leading to an increase in resistivity over time. The double-well concept is able to predict the drift parameter ν defined in Eq. 3.11 to:

$$\nu = u_0 D/\Delta W_B. \tag{3.16}$$

The parameter u_0 denotes the ultimate relative volume change induced by structural relaxation at the saturation point. The deformation potential D describes the influence of the volume change on the activation energy E_a given by the standard approximation, $dE_a/du = D$ [KMK+07].

According to references given in [KMK+07] the deformation energy is typically positive and varies in the range of $D \approx 1 - 3\,\mathrm{eV}$. Furthermore the authors claim numerical values $|u_0| = 0.01$ and $\Delta W_B \approx 1\,\mathrm{eV}$. Consequently the double-well potential model predicts a drift parameter $\nu = 0.03$, which is of the order of experimentally observed drift parameters reported to be $\nu = 0.06 - 0.1$, [PLP+04, BRP+09].

The double-well potential model can explain why the resistance drift accelerates at elevated temperatures. Within the double-well concept the structural relaxation is attributed to a thermally excitation facing an energy barrier ΔW_B. Elevated temperatures facilitate overcoming the energy barrier ΔW_B. Furthermore this universal framework predicts a saturation of the resistance drift, when all atomic sites have relaxed into their stable state. This saturation is not predicted by the drift dependency given in Eq. 3.11. However, reported drift experiments are in general not performed over several months. According to the double-well potential model the saturation time is predicted to be $\approx 10^7\mathrm{s} = 116$ days at room temperature. At $T = 75°\mathrm{C}$ the saturation time is estimated to be significantly lower to be only $\approx 10^4\mathrm{s} = 2.8$ hours.
Recently, Huang and Robertson have calculated the lowest energy defect in amorphous GeTe and $Ge_2Sb_2Te_5$ [HR12]. The authors have identified that the defect of lowest energy in a-GeTe is the divalent Te. In contrast, the authors claim the the lowest cost defect in a-$Ge_2Sb_2Te_5$ is formed by the Te interstitial.

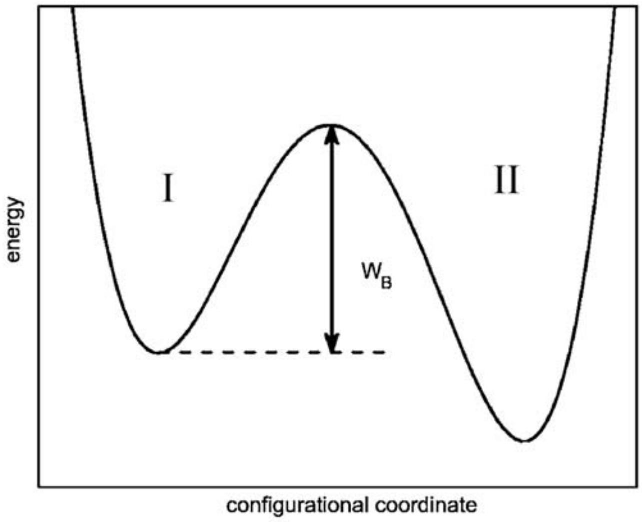

Figure 3.14: Structural relaxation of a glass can be described by the universal double-well potential concept. In disordered structures some elements are expected to be flexible. Hence, some atoms can move to an energetically more favorable atomic configuration. Thereby, this structural relaxation does not necessarily invoke any trap dynamics, i.e. breaking of bonds. The different atomic configurations are reflected by an atomic potential forming a double-well, where the meta-stable state I is separated by a potential barrier of height ΔW_B from the stable atomic state II. As a result of structural disorder the barrier height ΔW_B is randomly distributed. Strongly varying potential wells ΔW_B lead to strongly varying relaxation times. With increasing time the structural relaxation from state I into state II proceeds inducing a relative volume change. Within the double-well potential model proposed by Karpov *et al.*, the relative volume change increases the activation energy of conduction. Consequently, the amorphous state resistivity increases with increasing sample age. Image source: [KMK+07]

Experiments on phase-change nanowires, show that the drift parameter ν decreases significantly within stress free conditions [MJGA10]. Hence the resistance drift effect is significantly reduced under stress free conditions, this result strongly supports a driving mechanism based on structural relaxation going along with stress relaxation.

3.3.2 Valence Alternation Pair (VAP)-model

The VAP defect model described in subsection 3.1.2 was developed for amorphous chalcogenide glasses. The defect model concentrates on the covalent nature of bonding [KAF76a, Adl71, BS80]. Consequently, chalcogenides are expected to form chains. Broken bonds along the chalcogen chain result in overcoordinated C_3^+ and undercoordinated C_1^- defects, known as VAPs. However, recent structural studies have shown that Te-Te bonds are very seldom realized or even non-existent in GeSbTe- systems [CBK+07, AJ07, JKS+08]. Based on the VAP defect model, Pirovano *et al.* proposed a mechanism explaining the resistance drift phenomenon in

2004. Even though the validity of the VAP model is now questioned the model proposed by Pirovano *et al.* remains relevant, because this model involves defects but not necessarily VAPs.

VAP defects, see Fig. 3.15a, create a donor-like (C_3^+) and an acceptor-like (C_1^-) defect band pinning the Fermi energy E_F near mid gap, but still close to the valence band see Fig.3.15b. According to Pirovano *et al.* the resistance drift effect is attributed to an increasing number of C_3^+ and C_1^- defects, i.e. with time more and more bonds along the Te chain get broken. With increasing number of C_3^+ and C_1^- defects, the authors claim a Fermi level moving steadily towards mid gap position. This shift of the Fermi level results in an increase of the activation energy $E_a = E_F - E_v$, where the activation energy describes the thermally activated behavior of the amorphous state resistivity given by the Arrhenius law, see Eq. 3.15.
From Eq. 3.15 it is clear that an enhanced activation energy caused by an enlarging defect density over time yields to an increase in resistivity with time, too.

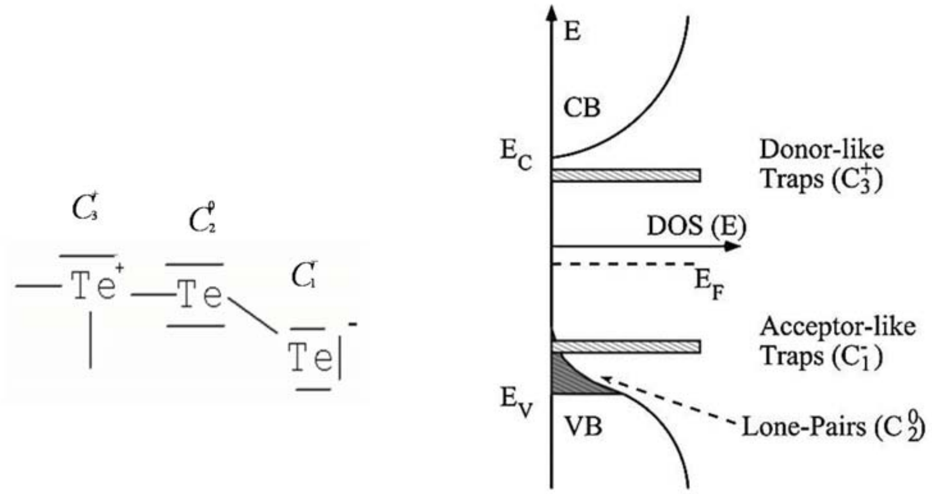

(a) Valence Alternation Pair defects in a Te chain **(b)** Density of states in the VAP model

Figure 3.15: The Valence Alternation Pair Model relies on covalent bonding of tellurium forming chains (a). Breaking bonds along the Te-chains induces structural defects. The C_3^+ defect induces a donor-like defect distribution near the conduction band edge E_c. The C_1^- defect creates an acceptor like imperfection band near the valence band edge E_v (b). Typically, phase-change materials are p-type conductors. Hence, the VAP model explains the resistance drift effect assuming a increasing number of C_3^+ and C_1^- defects with time, which shifts the Fermi level nearer to mid gap. The shift of the Fermi energy increases the activation energy of electrical conduction resulting in a higher resistivity. Image source: [PLP$^+$04]

3.3.3 The Poole/Poole-Frenkel model

The VAP model discussed in the last subsection attributes the resistance drift effect solely to trap kinetics and argues that aging of the glassy state should have no significant influence on the increase in resistivity with time. The Poole/Poole-Frenkel model tries to combine trap kinetics with structural relaxation [ILSL08, IZ07, ISLL09], even though a mechanism based on structural relaxation does not necessarily invoke any electronic process. However, studies performed on pure amorphous silicon have shown, that the structural relaxation process of the disordered state is closely linked to defect annihilation in this material [RSP+91].

Within the Poole/Poole-Frenkel model discussed in subsection 3.2.4, the defect density strongly influences the I-V curves observed in the subthreshold regime, see Fig. 3.11. For a high number of defect states, the intertrap distance is small. Hence, the energy barrier between neighbouring traps is lowered by the interaction of their Coulomb potentials and the electric field. Consequently, the cell current I depends exponentially on the applied voltage V. This behavior expressed by Eq. 3.6 is classified as Poole conduction.

For a low defect density, each trap state can be treated as isolated. In this case, the energy barrier between neighbouring trap states is lowered by the electric field alone and the current depends exponentially on the square root of the applied voltage. This conduction model described by Eq. 3.5 is known as Poole-Frenkel conduction.

If the resistance drift effect can be described within the Poole/Poole-Frenkel model, I-V curves may reveal defect annhilation. Thus I-V curves measured on a melt-quenched and post annealed amorphous phase-change memory cells could give further insight on the driving mechanism behind the resistance drift effect. Such a experiment was carried out by the group of Lacaita. They measured I-V subthreshold characteristics at room temperature of an amorphous $Ge_2Sb_2Te_5$ memory cell before and after annealing the cell at 100°C for 15 hours. Their results are shown in Fig. $3.16a$. Whereas the initial cell resistance can be well described within the Poole conduction model the same cell shows a Poole-Frenkel behavior after the annealing process. These results indicate that annealing leads to a Poole to Poole-Frenkel transition caused by defect annihilation. The Poole to Poole-Frenkel transition yields to an increase of the mobility band gap caused by the increasing energy barrier between two neighbouring traps. The increase of the mobility band gap results in an increasing amorphous state resistivity. A schematic picture of the resistance drift effect within the Poole/Poole-Frenkel model is depicted in Fig. 3.16 b, in the case that no electric field is applied.

Nowadays the Poole/Poole-Frenkel model is the most accepted transport model for amorphous phase-change materials. This model is able to give a quantitative description of the I-V curves in the subthreshold regime. Furthermore, the Poole/Poole-Frenkel model gives a conclusive explanation of the *threshold switching* and the *resistance drift* effect. Defects play an important role in this transport model.

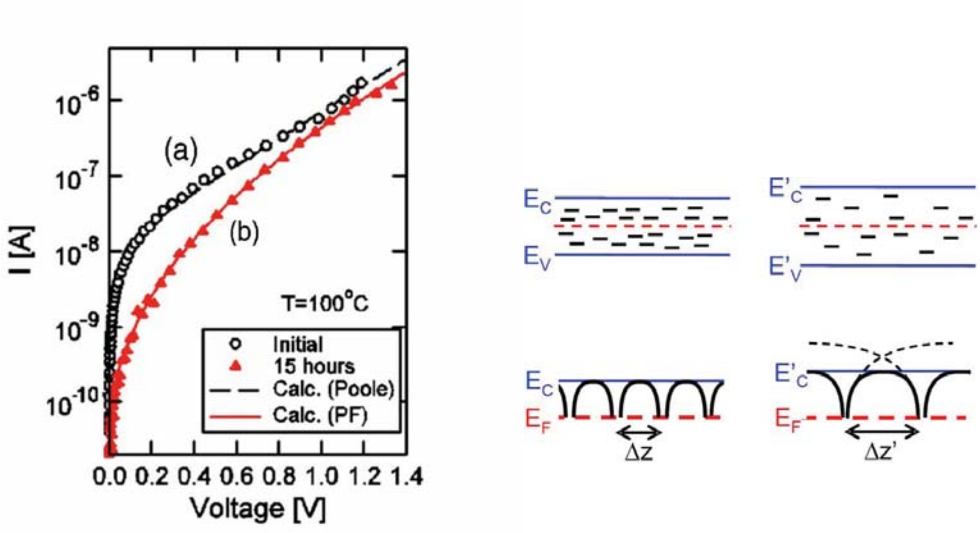

(a) Measured I-V characteristics **(b)** Schematic picture of the resistance drift

Figure 3.16: In the Poole/Poole-Frenkel model the defect density strongly affects the subthreshold I-V characteristics shown in (a). The model is based on the barrier lowering between two donor traps, where each donor trap forms a Coulomb potential (b). For a high defect density, described by a low intertrap distance Δz (left), the energy barrier between two traps is lowered by the interaction of their Coulomb potentials and the electric field. This situation results in Poole conduction. For low defect densities described by a high intertrap distance Δz the Coulomb potentials of neighboring traps do not influence each other. Consequently the energy barrier is only lowered by an electric field, known as Poole-Frenkel or PF conduction (right).
Annealing of a $Ge_2Sb_2Te_5$ memory cell yields to an transition from Poole, (current increases exponentially with applied voltage) to Poole-Frenkel conduction (current increases exponentially with the square root of the voltage). Based on these results, the Poole/Poole-Frenkel model explains the resistance drift effect by a significant defect annihilation during the structural relaxation process of the glassy state. The transition from Poole to Poole-Frenkel conduction results in an increases of the energy barrier between two neighbouring traps. Consequently, the mobility band gap and thus the amorphous state resistivity increase with decreasing number of defects. A schematic picture of the driving mechanism of the resistance drift within the Poole/Poole-Frenkel model is shown in (b), where for simplicity no applied electric field is considered. Image source: [ILSL08, ISLL09]

Chapter 4

Experimental methods

This chapter gives a short and concise overview of the methods used within this study to get more insight into the mechanisms driving threshold switching and resistance drift phenomena. The reader is referred to the literature for a more detailed discussion.
To provide a clearer overview, the purpose for which a given method is employed within this work is presented at the beginning of each section of this chapter.

4.1 Thin Film Preparation by Sputter Deposition

The sputter deposition technique is a very precise method to deposit thin films of specific compositions. The film thickness can be systematically adjusted within a wide range varying from a few nm to several $\mu\mathrm{m}$. Hence, many different compositions having optimal film thickness for each characterization method can be realized easily by the sputter deposition technique.

This work concentrates on the physical properties of dc magnetron sputter deposited phase-change materials. The principles of this sputter deposition technique are shortly explained in the following.
Fig. 4.1 shows a schematic view of a sputtering system consisting of vacuum chamber, power supply, sputter target and substrate holder. In magnetron sputter systems a permanent magnet is installed behind the sputter target. The vacuum chamber is pumped to very low background pressures before the chamber is filled with sputter gas. In general the sputter gas is inert, but sputter depositions with reactive sputter gasses are also possible. In this work all samples are produced in Ar atmosphere of $5 \cdot 10^{-3}\,\mathrm{mbar}$. A small fraction of these argon ions in the sputter chamber are ionized by atomic collisions or by interaction with cosmic radiation. An electric field applied between the sputter target and the substrate holder accelerates the ionized argon atoms towards the target surface. The argon ions bombard the target surface with an energy of several hundred electron volts and induce collision cascades at the target surface. Recoiled collision cascades reaching the target surface with an energy higher than the binding energy cause particles to be ejected from the sputtering target. The sputtered target atoms have no preferred direction. Consequently, all the surrounding walls including the substrates for thin film growth positioned in opposite of the sputtering target are covered.
An efficient sputter process needs a sufficient concentration of argon ions, which is delivered by a plasma created by a steady state electric glow discharge inside the sputter chamber. Sputter

gas ions hitting the target surface do not only eject target particles, but also electrons. These electrons are accelerated in the electric field away from the target surface and thereby ionize more argon atoms. In many sputtering systems a permanent magnetic field is used to held electrons near the target surface to increase the number of argon ions additionally. The ion bombarding events at the target surface significantly heat the target material. More than 75% of the energy entered into the glow discharge is converted into thermal energy. To prevent melting the sputtering target is generally watercooled.

The sputter deposition technique can be used to deposit conductive and insulating materials. For the deposition of conductive materials a constant current (DC) voltage is applied to build up a static electric field between target and substrate holder. In insulating materials impinging argon ions build up a positive space charge at the target surface, which reduces the electric field near the target. The use of a radio frequency (RF) voltage enables the sputter deposition of insulating materials, because a rf-voltage allows a periodic charge compensation on the target surface by collecting electrons from the plasma.

The substrates for thin film deposition can either be statically fixed or rotate with constant angular frequency above the target. Whereas the first static option results in significant higher deposition rates, the latter dynamic process is favoured to realize a homogenous film thickness over the whole sample area.

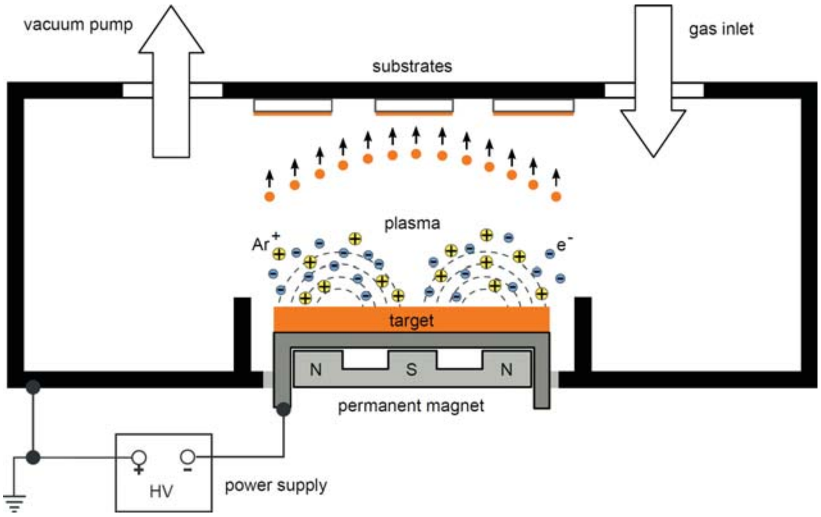

Figure 4.1: A schematic view of a magnetron sputtering system. Ionized Argon atoms bombard the target surface. Electrons are held close to the target by a magnetic field to increase the number of ion bombarding events on the target surface. Due to the momentum transfer atoms are ejected or *sputtered* from the solid target of given stoichiometry. This results in a deposition of the target material on all surfaces inside the chamber. The substrates for thin film growth are in general positioned opposite of the target. Image source modified from [Kal06]

All samples studied in this work are sputter deposited dynamically from stoichiometric targets of 99.99% purity employing an LS 320 von Ardenne sputter system. The sputter power is adjusted to 20 W. The samples are deposited in Ar atmosphere of $5 \cdot 10^{-3}\,\mathrm{mbar}$ without additional substrate cooling or heating. During the sputter process the deposition temperature was measured to be lower than 60°C at the substrate surface.

4.2 Electron Probe Micro-Analysis (EPMA)

An electron probe micro-analyzer is used to check the chemical composition after thin film deposition and thermal heating. Fundamentally it works similar to a Scanning Electron microscope (SEM). The micro-electron beam instrument enables a very precise and non-destructive in situ analysis of the elemental composition. Thin films of a few nanometres as well as layers of film with thicknesses up to several micrometres can be studied by this method.
An Electron Probe Micro-Analyzer consists of an electron gun, electromagnetic lenses, scanning coils, a movable sample stage and a detection system. A schematic picture of the set-up used is shown in Fig. 4.2.
The electron probe technique is based on the interaction of an accelerated, focused electron beam with atoms at the sample surface. The incident electron beam mainly liberates heat, but also secondary electrons and X-Rays. Whereas the Scanning Electron microscope technique uses back scattered and secondary electrons to image the sample surface, an Electron Probe Micro-Analyzer provides information about the elemental composition from the X-Ray generation. The emission of X-ray photons is caused by inelastic collision processes of the incident electron beam with the electrons of the inner shell of atoms from the sample. The X-Ray spectrum of each element consists of a small number of specific wavelengths and thus is a characteristic fingerprint of a specific element. Two different kinds of Electron Probe Micro-Analyzer can be employed to quantify the spectrum of secondary X-Rays emitted from the material under test. The emitted X-Ray spectrum can be analyzed by energy dispersive (EDS) or wavelength dispersive spectroscopy (WDS). In the EDS operation mode a solid state detector is used to distinguish between the energy of incoming photons. An EDS probe collects simultaneously the whole X-Ray spectrum and thus is a very rapid method at comparably low cost. However, higher spectral resolutions and higher precisions are possible with WDS electron probes based on Bragg's diffraction law. WDS probes use various movable and shaped monocrystals, which monochromatize the incoming X-Rays photons.

The composition of amorphous deposited and post-anneled phase-change films was measured employing a CAMECA SX-100 with an acceleration voltage of $20 - 25\,\mathrm{keV}$ and a probe current of $1\,\mathrm{nA}$. A surface of $1\,\mu\mathrm{m}^3$ was analyzed on five different positions to verify the sample homogenity. This WDS probe is one of the most precise electron probe micro-analyzers. Detection limits for this spectrometer to analyze elements from boron to uranium can be as low as 0.02 weight $\%$, i.e. 200 ppm. The EPMA measurements have been performed in collaboration with A. Piarristeguy at the Institute Charles Gerhardt University Montpellier 2.

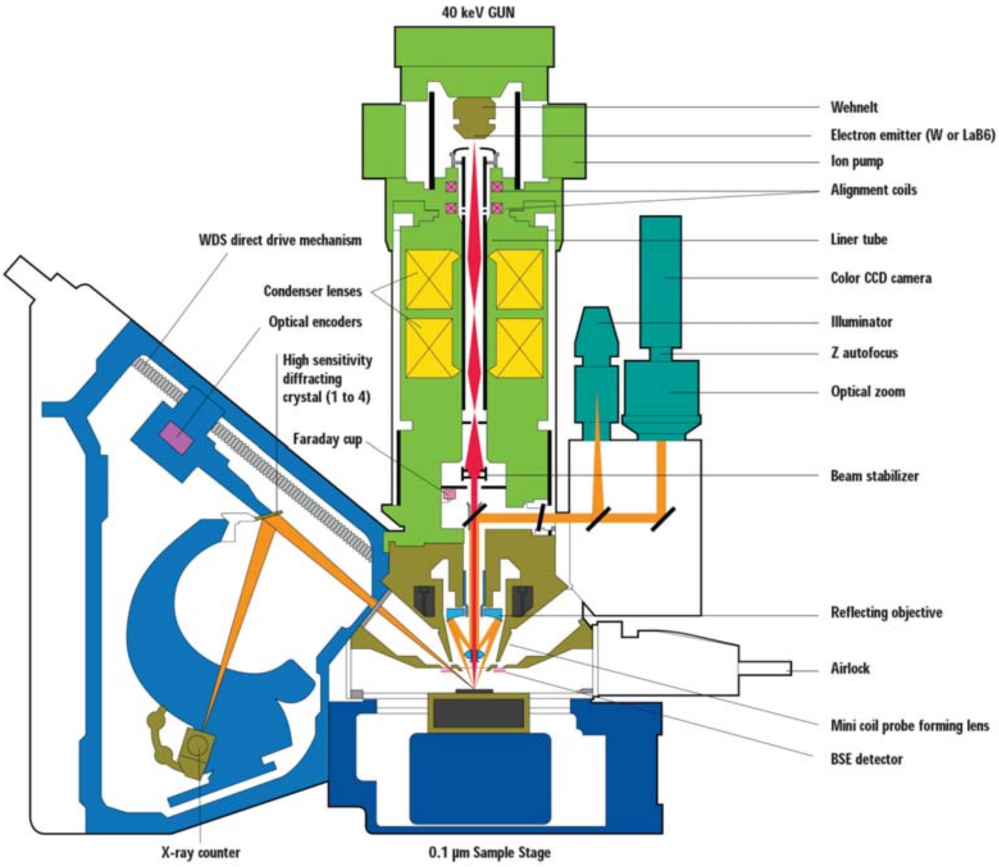

Figure 4.2: A schematic picture of an Electron Probe Micro-Analyzer. An electron gun delivers an electron beam, which is focused by electromagnetic-lenses. A movable sample stage is positioned in the focus. The incident electron beam interacts with electrons of the inner shell of atoms in the sample causing X-Ray generation. Each element emits a characteristic X-Ray spectrum, which is analyzed by wavelength dispersive spectroscopy. Based on Bragg's diffraction law various movable, shaped monocrystals can be employed to monochromatize the incoming X-Ray radiation. Image source: [EPM]

4.3 X-Ray techniques

X-Ray techniques are based on the interaction between X-Rays and the material under investigation. Reflection and diffraction of an incident X-Ray beam can be analyzed to resolve structural properties of deposited thin films.

In this work X-Ray techniques have been employed to analyze the mass density, film thickness and roughness of amorphous deposited thin films. X-Ray reflection and diffraction spectra in $\theta/2\theta$ geometry have been measured using a *Philips X'Pert Pro MRD* system at room temperature with monochromatized $\mathrm{Cu}(K_\alpha)$ irradiation ($\lambda_{Cu} = 1.54\mathring{A}$). The schematic principle of the X-Ray technique in $\theta/2\theta$ geometry is illustrated in Fig. 4.3.

4.3.1 X-Ray Reflectometry (XRR)

X-Ray Reflectometry is a non-contact and non-destructive method to determine the film thickness and roughness. The XRR-technique can be employed to study thin phase-change films having a film thickness in a range from 20 to 200 nm with a precision of $3\,\mathrm{nm}$. In addition to a very precise determination of the film thicknesses, this method can be used to measure the material density with a precision of $0.05\,\mathrm{g/cm^{-3}}$.

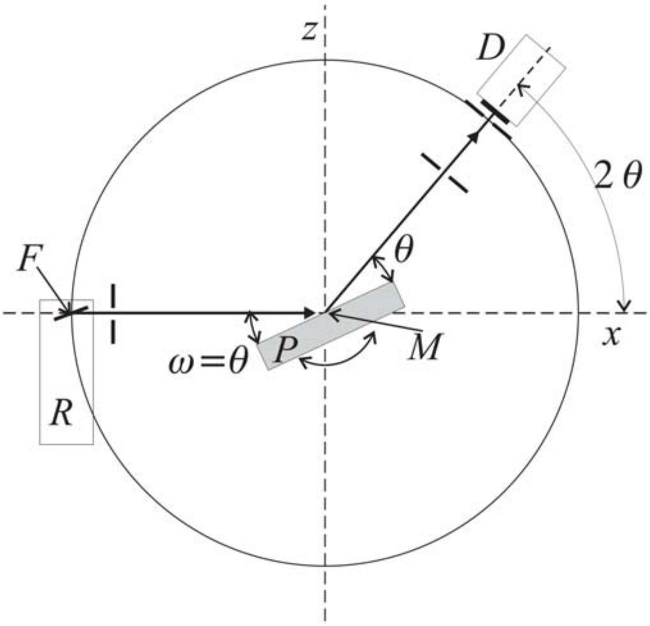

Figure 4.3: The X-Ray beam irridates the sample at an angle of incidence $\omega = \theta$. The intensity of the reflected X-Ray beam is measured by an detector (D) positioned at 2θ to the incident beam. X-Ray Reflection patterns are measured operating at grazing incidence. In contrast, X-Ray diffraction pattern are measured at steep angles of incidence. Image source [Wei02]

In XRR measurements the angle of incidence ω illustrated in Fig. 4.3 has to be kept sufficient small. Typically the angle of incidence is varied in a range from $0°$ to $3°$. At these small angles the incident X-Ray beam is not diffracted by lattice planes. Instead the incident X-Ray beam is partly reflected at the sample surface or at the interface formed by the thin film and the substrate. The incident and reflected X-Ray beam are symmetric with respect to the surface normal. Consequently, the intensity of the reflected X-Ray beam is measured by a detector (D) positioned at an angle of 2θ to the incident beam.

The measured intensity shows three characteristic regimes illustrated in Fig. 4.5: total reflexion (I), absorption edge (II) and Interference pattern (III). Total reflexion occurs for angles of incidence smaller than a critical angle θ_c shown enlarged in the inset. In the case of negligible small absorption the critical angle θ_c is sharply defined, whereas X-Ray absorption within the sample results in a broadened absorption edge [Fri00]. The regime of total reflexion is determined by Snell's law at the transition from air to the sample. According to our definition of θ illustrated in Fig. 4.3 Snell's law has the form,

$$n_1 \cos\theta = n_2 \cos\theta' \tag{4.1}$$

$$\Rightarrow \cos(\theta) = (1-\delta)\cos\theta' \tag{4.2}$$

The refractive index describing the propagation of X-Rays in condensed matter is slightly smaller than one, where the parameter δ alters typically from 10^{-7} to 10^{-5}. Consequently, the critical angle $\theta_c = \arccos 1 - \delta$ is expected to vary between 0.03° and 0.3°. In the literature it has been demonstrated that the parameter δ describing the X-Ray dispersion in compositions with molar fractions x_i is closely linked to the weighted total mass density ρ_{tot} [Wei02],

$$\delta = \lambda^2 \frac{N_A r_0}{2\pi} \sum_i x_i (Z_i + f_i') \cdot \frac{\rho_{tot}}{A_{tot}} \tag{4.3}$$

where λ denotes the wavelength of the incident X-Ray beam, r_0 is the Bohr radius, N_A is the Avogadro constant and the term $(Z + f')$ describes the charge of an atom in units of the elementary charge e with a correction factor f'. From Snell's law it follows in a first order aproximation ($\cos(\theta_c) \approx 1 - 1/2 \cdot \theta_c^2$),

$$\theta_c \approx \sqrt{2\delta} \tag{4.4}$$

$$= \lambda^2 \frac{N_A r_0}{2\pi} \sum_i x_i (Z_i + f_i') \cdot \frac{\rho_{tot}}{A_{tot}} \tag{4.5}$$

The density of a deposited thin film can thus be determined from an exact measurement of the limiting angle for total reflexion θ_c.

The film thickness d can be determined by the position of interference fringes (Region III), i.e. from the position of the m-th and m+1 th maximum or minimum of the measured intensity [Koe11],

$$d = \frac{\lambda}{2} \frac{1}{\sqrt{\theta_{m+1}^2 - \theta_c^2} - \sqrt{\theta_m^2 - \theta_c^2}} \tag{4.6}$$

Additionally, the measured reflection pattern is significantly influenced by the roughness of the film surface. The *WinGixa* software developped by *Philips* has been utilized to derive mass density, film roughness and thickness by modeling X-Ray Reflection spectra.

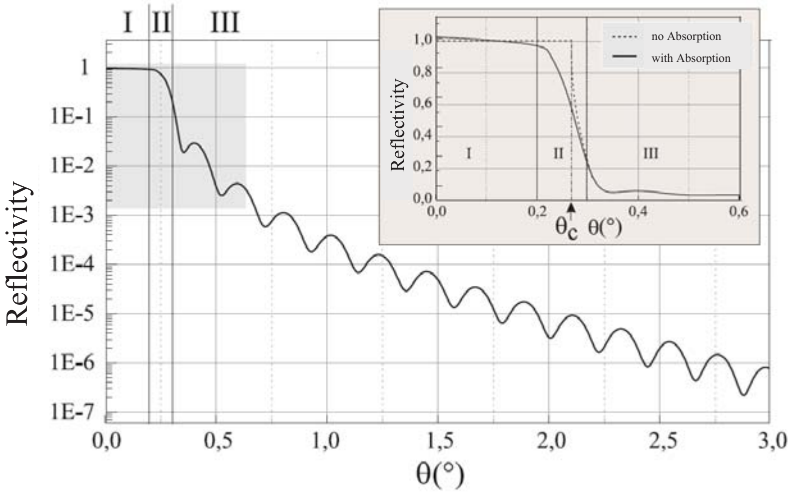

Figure 4.4: A X-Ray Reflection pattern shows three characteristic regions. At angles of incidence smaller than a critical value θ_c the incident X-Ray beam is totally reflected at the sample surface (I). For angles larger than θ_c the X-Ray irradiation can penetrate into the material under investigation (II). The total reflexion edge is shown enlarged in the inset in the case of negligible or strong X-Ray absorption within the sample. For large angles of incidence the incident beam is partly reflected at the sample surface and partly at the interface formed by film and substrate causing interference fringes in the XRR pattern (III). From the position of these interference maxima or minima the film thickness can be derived. The critical angle θ_c determines the mass density ρ_{tot}. Furthermore, the film roughness influences the form of the XRR pattern. To obtain mass density, film thickness and roughness the XRR spectra are modeled employing the *WinGixa* software developped by Philipps. Image source modified [Fri00]

4.3.2 X-Ray Diffraction (XRD)

X-Ray diffraction is a classical method to investigate the structural properties of a solid and are employed within this work to verify the amorphous structure of sputter deposited and post-annealed samples. In this type of measurement the angle of incidence θ is varied in a wide range. e.g. from 0° to 40°.
The intensity of the diffracted X-Ray beam is measured by a detector positioned at 2θ to the incident beam. The measured intensity shows sharp diffraction peaks for partly crystalline samples. Their position θ is determined by Bragg's law describing coherent scattering of X-Rays diffracted at different parallel lattice planes of distance d_{hkl},

$$m\lambda = 2d_{hkl}\sin(\theta). \tag{4.7}$$

Broad peaks in the measured XRD pattern indicate that the material under investigation has a disordered structure. This study concentrates of physical properties of amorphous deposited and amorphous post-annealed phase-change materials, whose amorphous structure has been verified by X-Ray diffraction Spectroscopy. Fig. 4.5 shows a XRD scan on a thin film $Ge_2Sb_2Te_5$ after heating the sample for one hour at 100°C. The XRD scan shows that the sample is still amorphous after the annealing process.

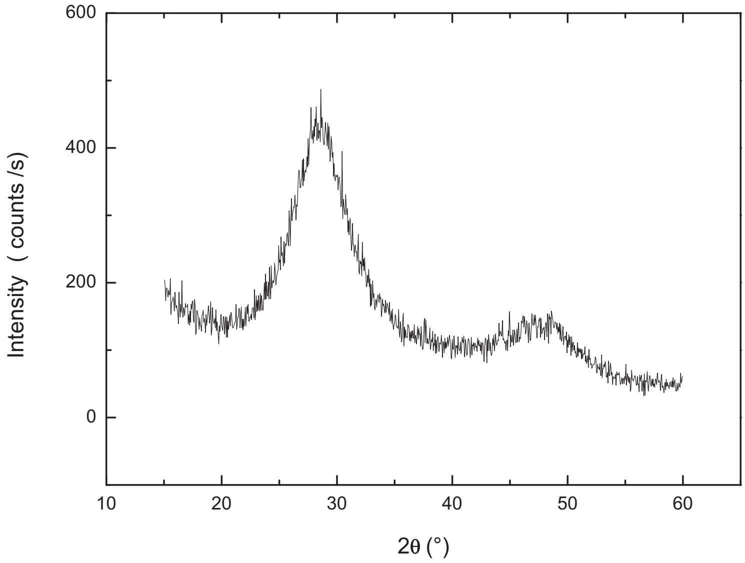

Figure 4.5: XRD-Scan in $\theta/2\theta$ or Bragg-Brentano geometry of an amorphous $Ge_2Sb_2Te_5$ thin film after heating the sample one hour at 100°C. The broad XRD peaks indicate that the sample is still amorphous after the post-annealing process.

4.4 Optical methods

The optical properties of amorphous deposited phase-change films has been analyzed. Ellipsometry measurements have been performed to characterize the optical properties at room temperature. Fourier-Transform Infrared Spectroscopy has been used to investigate optical properties such as the the optical band gap in a temperature range from 5 K to 300 K.

4.4.1 Ellipsometry

The optical properties of a solid are defined by the interaction between material and an incident electro-magnetic wave propagating with wavenumber k_0 and angular frequency ω. This interaction is completely described by two frequency dependent parameters. In a phenomenological treatment these are the refractive index n and the absorption index κ. An equivalent pair is the absorption coefficient α and the wave number in medium k_{med} [Fox02],

$$\alpha = \frac{2\kappa\omega}{c}, \tag{4.8}$$

$$k_{med} = n\,k_0. \tag{4.9}$$

In the Maxwell theory the optical properties are determined by the dielectric constant ϵ and the conductivity σ, that can be linked to the real and imaginary part of the complex dielectric function $\tilde{\epsilon}$ [IL02],

$$\tilde{\epsilon}(\omega) = \epsilon_1 + i\epsilon_2 = \epsilon + i\frac{\sigma}{\epsilon_0\omega}. \tag{4.10}$$

Both description are equivalent to describe the optical properties of a solid. Hence, both phenomenological parameter pairs are linked to those derived from Maxwell theory, [IL02]:

$$\epsilon_1 = n^2 - \kappa^2, \tag{4.11}$$

$$\epsilon_2 = 2n\kappa. \tag{4.12}$$

Another parameter pair is given in Ellipsometry experiments, known as ψ and Δ. Ellipsometry is a characterization method which enables a contactless investigation of optical properties. The principle of the method is shown in Fig. 4.6. Ellipsometers are working with natural light sources like glow-discharge lamps, emitting a continuous spectrum, which enables a frequency dependent analysis of the optical constants. Thermal radiation has no defined polarization, though a polarizer assures that the beam of incidence $\vec{E}_i$ reaches the material under investigation with a well defined polarization. In the interests of simplification the special case of linear polarization is exemplified in the following,

$$\vec{E}_i = \begin{pmatrix} \mathrm{E}_i^s \\ \mathrm{E}_i^p \end{pmatrix} = \begin{pmatrix} |\mathrm{E}_i^s|\sin(\omega t - \vec{k}_i\vec{r}) \\ |\mathrm{E}_i^p|\sin(\omega t - \vec{k}_i\vec{r}) \end{pmatrix}. \tag{4.13}$$

The oscillating electric field $\vec{E}_i$ induces vibrations of electric charges within the material, these periodic accelerated carriers emit electro magnetic waves with typical dipole characteristics. As a consequence, the s and p component of the incident light are reflected with different amplitudes and phases and the reflected light beam $\vec{E}_r$ is elliptical polarized.

$$\vec{E}_r = \begin{pmatrix} \mathrm{E}_r^s \\ \mathrm{E}_r^p \end{pmatrix} = \begin{pmatrix} |\mathrm{E}_r^s| \sin(\omega t - \vec{k}_r \vec{r} + \Delta) \\ |\mathrm{E}_r^p| \sin(\omega t - \vec{k}_r \vec{r}) \end{pmatrix}. \tag{4.14}$$

The ellipse is completely described by the ratio of amplitudes of the p and s polarized component of the reflected light beam, defined as ψ and their phase difference Δ.
Obviously the phase difference can also be described by another relation. In the case that $(\omega t - \vec{k}_r \vec{r})$ equals $(-\Delta)$ the s component of the electric field E_r^s vanishes and the p component E_r^p is equal to $|\mathrm{E}_r^p| \sin(-\Delta) = \mathrm{a}$. So the measurement quantities of the Ellipsometry method are given by,

$$\tan(\psi) = \frac{|\mathrm{E}_r^p|}{|\mathrm{E}_r^s|}; \qquad |\sin(\Delta)| = \frac{\mathrm{a}}{|\mathrm{E}_r^p|}. \tag{4.15}$$

The way how the quantities ψ and Δ are derived in experiment is not given by these relations above. However they are very helpful for a better visualization, see Fig. 4.6.
In practice a detector measures the intensity of the reflected light beam. There are at least two polarizers: one before the sample (polarizer) and one before the detector (analyzer). Different types of ellipsometer are commercially available. In Rotating Analyzer Ellipsometer instruments the polarizer is fixed, whereas the analyzer rotates. Likewise Rotating Polarizer Ellipsometer instruments are working with a fixed analyzer and a rotating polarizer. Other, so called Rotating Compensator Ellipsometer instruments, have both polarizers fixed and an additional rotating compensator in the optical path. According to its azimuthal angle a compensator adds an additional phase shift γ from -180° up to 180° to the sample induced phase difference Δ. Since the detected light intensity alternates periodically in time a Fourier analysis of this time dependent signal is possible, where $R(t)$ is the azimuth angle of the rotating component, i.e, $R(t) = \omega t$,

$$I_D = const. + \beta \sin(2R(t)) + \iota \cos(2R(t)). \tag{4.16}$$

In the Jones-Matrix-Formalism [Kre05, JWC, Die02] each electro-magnetic wave is given by a vector consisting of a p and s polarized component, as indicated in equation (4.13). Any further propagation, like passing a polarizer or reflection on a surface, is described by a matrix $\overline{M}$. Thus the detected light intensity can be derived mathematically by introducing all existing optical components by a matrix.

In the case that an air filled Rotating Compensator Ellipsometer (RCE) instrument is used and assuming a homogeneous, isotropic material under investigation of infinite thickness, the measured intensity signal I_D using the Jones-Matrix-Formalism is given by:

$$
\begin{aligned}
I_D = |\vec{E}_D|^2 &= |\overline{M}_{analyzer} \cdot \overline{M}_{compensator} \cdot \overline{M}_{sample} \cdot \vec{E}_i|^2 \\
&= \left| \begin{pmatrix} \cos^2(A) & \cos(A)\sin(A) \\ \cos(A)\sin(A) & \sin^2(A) \end{pmatrix} \begin{pmatrix} e^{[iR)} & 0 \\ 0 & 0 \end{pmatrix} \underbrace{\begin{pmatrix} \tilde{r_s} & 0 \\ 0 & \tilde{r_p} \end{pmatrix} \vec{E}_i}_{\vec{E}_r} \right|^2 \\
&= const + b(\tilde{r_p}, \tilde{r_s}, A, P) \sin(2R) + j(\tilde{r_p}, \tilde{r_s}, A, P) \cos(2R) \qquad (4.17)
\end{aligned}
$$

where A and P are the azimuthal angles of analyzer and polarizer. The coefficients b and j are functions depending on the known angles A, P and the complex Fresnel coefficients $\tilde{r_s}$ and $\tilde{r_p}$. The complex Fresnel coefficients are defined by the ratio of the p and s polarized components of the incident $\vec{E_i}$ and reflected $\vec{E_r}$ electric field.

$$
\tilde{r_s} = \frac{\mathrm{E}_r^s}{\mathrm{E}_i^s}; \qquad \tilde{r_p} = \frac{\mathrm{E}_r^p}{\mathrm{E}_i^p}; \qquad (4.18)
$$

Assuming the same amplitudes for the s and p polarized component of the incident light beam, i.e. $\mathrm{E}_i^s = \mathrm{E}_i^p$ it follows in complex notation:

$$
\frac{\tilde{r_p}}{\tilde{r_s}} = \tan(\psi) \exp(i\Delta) \qquad (4.19)
$$

Otherwise an additional constant, the ratio of of amplitudes of the s and p polarized incident light has to be considered in Eq. 4.19. This relation enables the determination of the quantities ψ and Δ, by comparing coefficients of Eqs. 4.16 and 4.17.

In classical electro-dynamics for reflection of a homogeneous, isotropic layer of infinite thickness the complex Fresnel coefficients are given by [Jac75]:

$$
\tilde{r_s} = \frac{\tilde{n_1}\cos(\Theta_i) - \frac{\mu_1}{\mu_2}\sqrt{\tilde{n_2}^2 - \tilde{n_1}^2\sin^2(\Theta_i)}}{\tilde{n_1}\cos(\Theta_i) + \frac{\mu_1}{\mu_2}\sqrt{\tilde{n_2}^2 - \tilde{n_1}^2 sin^2(\Theta_i)}} \qquad (4.20)
$$

$$
\tilde{r_p} = \frac{\frac{\mu_1}{\mu_2}\tilde{n_2}^2\cos(\Theta_i) - \tilde{n_1}\sqrt{\tilde{n_2}^2 - \tilde{n_1}^2\sin^2(\Theta_i)}}{\frac{\mu_1}{\mu_2}\tilde{n_2}^2\cos(\Theta_i) + \tilde{n_1}\sqrt{\tilde{n_2}^2 - \tilde{n_1}^2\sin^2(\Theta_i)}} \qquad (4.21)
$$

where Θ_i is the angle of incidence, $\tilde{n}_{1\backslash 2} = n_{1\backslash 2} + i\kappa_{1\backslash 2}$ and $\mu_{1\backslash 2}$ are the complex refractive indexes and magnetic permeabilities for medium 1 and 2, see Fig. 4.6. These relations link the measurement categories of Ellipsometry measurements ψ and Δ to the phenomenological optical constants n and κ.

Eq. (4.17) handles the simplified case that the incident light is only reflected at an infinite bulk system, that can not be realized in practice. In reality we have to consider a layer stack system, consisting of a substrate, material under investigation and oxide layer for instance. Thus the detected intensity I_D is given by the reflections at each interface and all possible multiple reflections. Thus the detected signal I_D, b and j are rather complicated expressions depending on the optical constants of each layer and their layer thickness. To relate the measured Fourier coefficients β and ι to the optical properties of the investigated material electrodynamic calculations, using for instance the Tauc-Lorentz [JM96] or the OJL model (O'Leary-Johnson-Lim model) [OJL97], have to be performed. The calculations can only be done indirectly: assuming the unknown optical constants and layer thicknesses the ψ and Δ spectra as a function of photon energy are calculated and compared to the measured ones. The values that show best agreement of measurement and simulation are identified with the optical constants of the solid under investigation, [Jel98b]. In this work Ellipsometry measurements have been performed using a Rotating Compensator Ellipsometer M-2000UI TM [Det03], [JWC] manufactured by J.A. Woolam Co.,Inc.

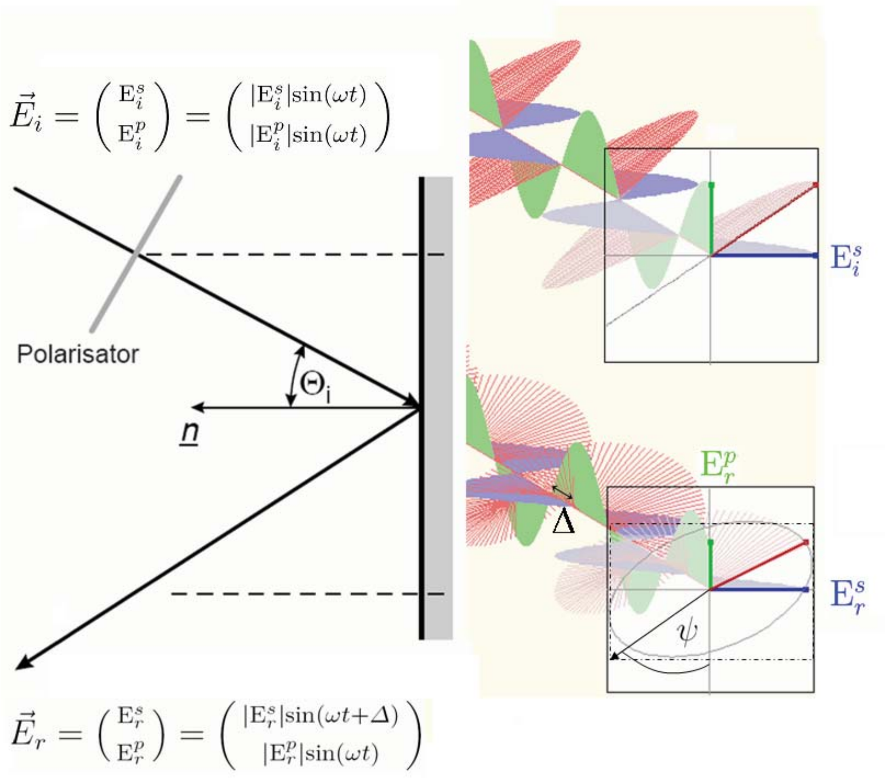

Figure 4.6: Principle of the Ellipsometry measurements. The incident beam is linearly polarized. Through dipole interactions the direction of polarization changes and the reflected light is elliptically polarized. The ellipse is completely described by Ψ, the ratio of amplitudes of the p and s polarized component of the reflected light and Δ their phase difference.

4.4.2 Fourier Transform-Infrared Spectroscopy

Within this work Fourier Transform-Infrared Spectroscopy has been used to investigate the optical properties of amorphous phase-change films at different measurement temperatures. By implementing a cryostat in the FT-IR system optical properties in a temperature range from 5 K to 800 K can be studied.

Fourier Transform-Infrared Spectroscopy measure intensities I at different photon energies corresponding to wavenumber k. The measurement principle is illustrated in Fig. 4.7. A spectral source covering the energy range of interest delivers the incident electro-magnetic wave. In the Michelson interferometer the beam splitter divides the incident beam into two components. The splitted beams are either reflected at a movable or at a fixed mirror. Both beam fractions are reunited by passing the beam splitter again. Hence, the reunited beams interfere constructively or destructively depending on the position of the movable mirror x. A detector measures the interference $I(x)$. The intensity as a function of the wavenumber $I(k)$ can be derived by Fourier Transformation of $I(x)$.

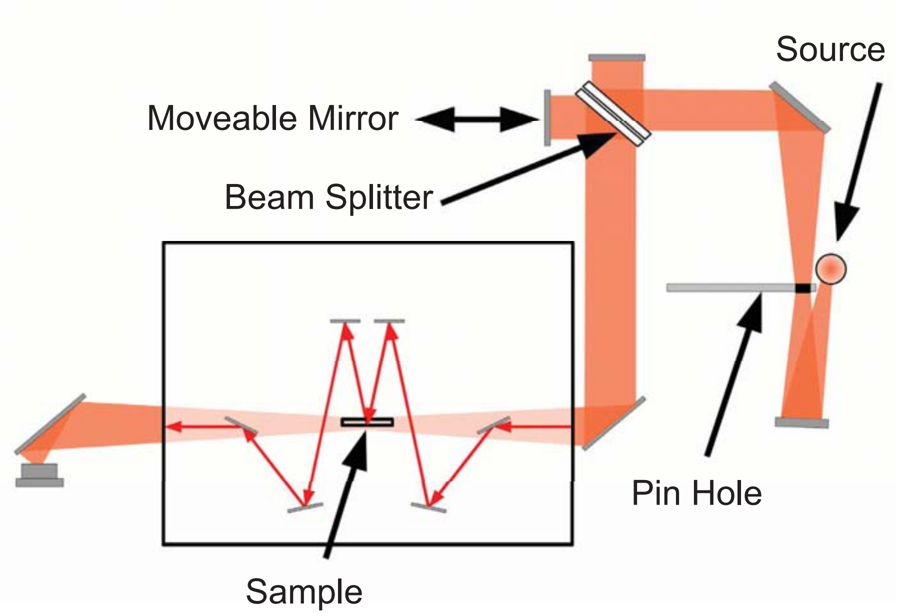

Figure 4.7: Schematic principle of the FT-IR set-up used. The detector measures the intensity as a function of the position of the moveable mirror $I(x)$. The intensity as a function of the wavenumber is derived by Fourier transformation, i.e. $I(x) \rightarrow I(k)$. FT-IR measurements in reflectance mode require a reflection unit. The beam path within the reflection unit is illustrated by arrows. The beam path in transmission mode is exemplified in lighter colors. Image source: [Jos09]

Fourier Transform-Infrared Spectroscopy can be performed in reflectance or transmission geometry. In transmission mode the intensity transmitted through the sample is compared to the intensity measured in an empty measurement. However, FT-IR measurements in reflectance mode require an additional reflection unit. Furthermore, a reference sample is needed to normalize the incident light intensity. In the mid-infrared range used gold is known to act as an almost perfect mirror ($R_{gold} \approx 0.992$). Therefore a gold film was chosen as the reference sample. To measure an optimal reflectance spectrum the material under investigation is deposited on a mirror. However, gold is observed to diffuse into phase-change materials. To avoid gold diffusion the material under investigation can be deposited on other metal reflectors such as aluminum. The intensity measured on the reference sample is compared to the intensity measured on the sample stack. Reflection spectra $R(E)$ are derived from the measured intensities. Reflection spectra measured in the amorphous and crystalline phase of the phase-change alloy $Ge_1Sb_2Te_4$ are presented in Fig. 4.8. The optical properties of the phase change layer can be obtained by analyzing the reflectance spectra $R(E)$. The incoming wave is partly reflected and transmitted at each interface of the layer stack system. The superposition of the reflected waves at different boundaries results in an interference pattern, i.e., constructive and deconstructive interference lead to minima and maxima in the measured Fabry Perot interference fringes $R(E)$. By calculating the reflectance spectrum from the dielectric functions of the layer stack these features can be fitted to obtain the dielectric function that gives the best fit. The spectra presented were analyzed using the simulation tool SCOUT from W. Theiss Hard- and Software, which enables a sophisticated analysis of reflectance, transmission, or ellipsometry spectra [The]. The dielectric functions have been simulated using a Tauc Lorentz Oscillator or Drude model [Jel98a, Fox02]. Further information on this method applied to phase-change materials can be found in [Kre09, Jos09]. The FT-IR measurements presented in this work have been performed using an IFS 66v/S from BRUKER OPTIK GmbH. The data presented have been obtained with the support of Stephan Kremers, Peter Jost and Stephanie Grothe, who performed the experiments.

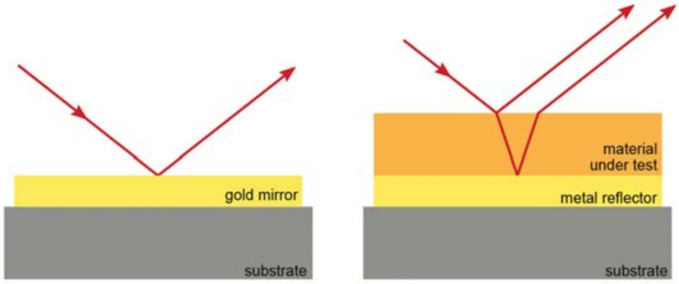

(a) Sample geometry for FT-IR measurements in Reflectance mode

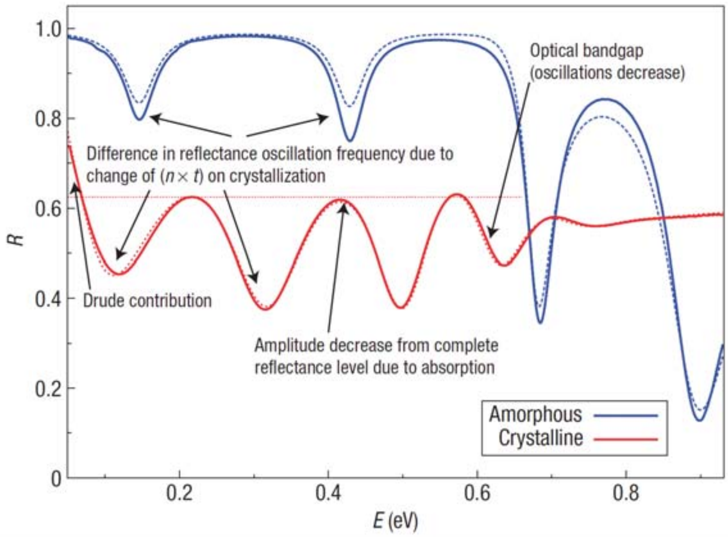

(b) Reflectance spectra measured in amorphous and crystalline $Ge_1Sb_2Te_4$

Figure 4.8: FT-IR measurements in reflectance mode compare the intensity $I_{ref}(k)$ measured on a reference sample to the intensity $I(k)$ measured on the sample stack consisting of substrate, reflecting mirror and material under test . Since gold acts as an almost perfect mirror in the mid infrared range $R_{gold} \approx 0.992$, a gold film was chosen as the reference (a).
The Reflectance spectra measured in amorphous and crystalline $Ge_1Sb_2Te_4$ (full lines). The spacing of interference minima holds information about the refraction index n, whereas the decrease in amplitude contains information about the optical absorption. Furthermore, interference fringes start to vanish if the energy of the incoming irradiation is in the vicinity of the optical band gap. To resolve the optical properties reflectance spectra are simulated by an analyzing software. The corresponding simulated fits are shown as dashed lines. Image source: [SKW$^+$08]

4.5 Electrical methods

Different thin film techniques have been combined to measure the electrical resistivity in amorphous chalcogenide and phase-change alloys. The resistivity at and above room temperature has been measured in four point Van-der-Pauw technique under argon atmosphere. Resistivities below room temperature have been measured in two point geometry in a cryostat under vacuum conditions ($\approx 10^{-5}\,\mathrm{Torr}$).

4.5.1 Heated four point Van-der-Pauw measurements

The four point Van-der-Pauw technique has been developed by Leo J. van der Pauw in 1958 [Pau58]. Nowadays, the Van-der-Pauw Method is a commonly used technique to measure the sheet resistance of homogeneous thin films. The main advantage of the van-der-Pauw technique lies in its ability to accurately measure the properties of a sample of any arbitrary shape as long as its thickness is much lower than its lateral dimensions. Furthermore, this method eliminates the influence of contact resistances. However, this method is only valid for ohmic contacts.

The Van-der-Pauw technique requires four contacts to measure the sheet resistance R_s of a two-dimensional film of any geometry. The four contacts are numbered from 1 to 4 in a counter-clockwise order, beginning at the top-left contact, see Fig. 4.9. A DC current I_{12} flowing through contacts 1 and 2 is injected and the voltage drop U_{34} along the contact 3 and 4 is measured. Ohm's law defines the resistance $R_{12,34}$,

$$R_{12,34} = \frac{U_{34}}{I_{12}}. \tag{4.22}$$

According to the Reciprocity theorem, i.e. $R_{12,34} = R_{34,12}$, the measurement accuracy can be significantly improved by averaging the results of measurements with cyclic permutation of the contacts. Consequently, one has:

$$R_{\text{vertical}} = \frac{R_{12,34} + R_{34,12}}{2} \tag{4.23}$$

$$R_{\text{horizontal}} = \frac{R_{41,23} + R_{23,41}}{2} \tag{4.24}$$

Van der Pauw showed that the sheet resistance R_s of a homogeneous thin films of arbritary shape can be determined from the resistances R_{vertical} and $R_{\text{horizontal}}$. The actual sheet resistance R_s is related to these resistances by the so-called van der Pauw formula,

$$\exp\left(-\frac{\pi R_{\text{vertical}}}{R_s}\right) + \exp\left(-\frac{\pi R_{\text{horizontal}}}{R_s}\right) = 1 \tag{4.25}$$

In general the sheet resistance R_s can not be resolved analytically from the expression above. However, in a quadratic sample geometry, where $R_{\text{vertical}} = R_{\text{horizontal}} = R'$ it follows simply,

$$R_s = \frac{\pi \cdot R'}{ln(2)} \tag{4.26}$$

In samples where $R_{\text{vertical}} \neq R_{\text{horizontal}}$ Eq. 4.26 is multiplied with a correction factor f, which depends on the chosen sample geometry. With known sheet thickness d the resistivity can be calculated from the sheet resistance according to,

$$\rho = R_s \cdot d. \tag{4.27}$$

In this work the required four contact geometry is realized by sputter depositing of four chromium contacts symmetrically on solvent cleaned glass substrates using shadow masks. A phase-change layer (1cm x 1cm) centered with respect to the contacts is deposited on top of the pre-structured substrate. The sheet thickness d of the samples studied has been determined either by X-Ray Reflection or Ellipsometry measurements.

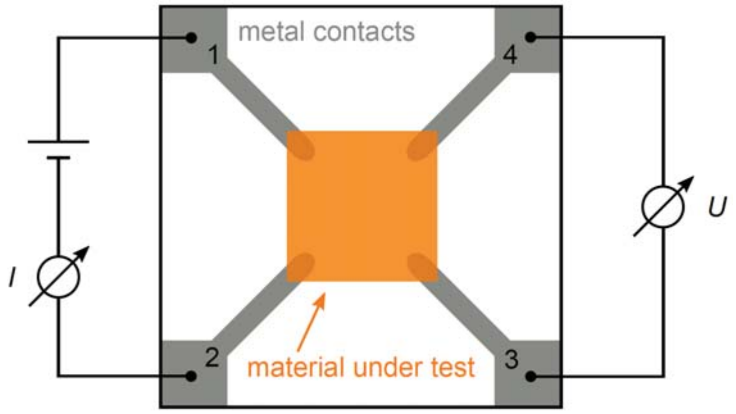

Figure 4.9: The sheet resistance of a thin film having an arbitrary sample geometry can be determined by using a four point contact method. The van der Pauw formula relates the sheet resistance R_s to resistances measured along vertical or horizontal contacts. For example the resistance $R_{12,34}$ is measured by appling an electric field to the horizontal contacts 1 and 2 while measuring the voltage drop across contacts 3 and 4. Image taken from [Kre10]

4.5.2 Dark and photoconductivity in the low temperature limit

The conductivity measurements are performed in the same cryostat as the Modulated photo current experiments. Therefore, the sample placed in the cryostat can be connected to two different measuring systems as illustrated in Fig. 4.10.

The combined system used in the Laboratoire Génie d'Électrique Paris consists of a two-stage cryogenerator of the Leybold company cat. no. 89111. The helium cooled system enables conductivity measurements down to 10 K under vacuum conditions ($\sim 10^{-5}\,\mathrm{Torr}$). To ensure thermal equilibrium, the sample is mounted on a cold finger made of copper. Furthermore, a copper lead having a glass window to pass the light to the sample surface, is put above the sample to maintain thermal contact to the cold finger. The temperature is measured on the surface of the copper cold finger. To improve the thermal contact between the cold finger and the sample, a thin foil of aluminum is used in between. A computer-controlled temperature controller of the Leybold company (Temperature controller LTC 60), ensures a stable temperature T during the measurement. A voltage supply from Keithley Instruments applies an electric field ϵ to the sample. Using light emitting diodes driven by a Lock-In-Amplifier of the Stanford Research systems (model SR830) the sample can be illuminated with homogeneous continuous or modulated light intensity. Due to band-to-band excitation, free carriers are generated within the sample. For dark and photo conductivity measurements, the current signal is detected by a Keithley 485 Autoranging pico-amperemeter. The sensitivity of the used amperemeter, Keithley 485 Autoranging, is $0.2\,\mathrm{pA}$.

To measure the dark and photoconductivity, the system is cooled down from room temperature to $50\,K$ in $10\,K$ or $5\,K$ steps. To ensure that the measurements are performed under thermal equilibrium the system stays 5 minutes at the set temperature value T, before ten measurements of the dark current are started. The results of these ten measurements are averaged to determine the dark current at temperature T. To measure the photocurrent the sample is illuminated with constant light flux of a given wavelength. To ensure steady state conditions the sample is illuminated one minute with a constant light flux F_{dc}, before the current, i.e. consisting of photo and dark current, is measured ten times in a row. These ten results are once more averaged to determine the photoconductivity of the material under investigation at a given temperature. With known sample geometry, the conductivity of the measured sample can be derived fom the maesured current I,

$$\sigma = \frac{I}{h \cdot d \cdot \epsilon}. \tag{4.28}$$

, where d is the sheet thickness, h the length of the electrodes (here 8mm) and ϵ the electric field.

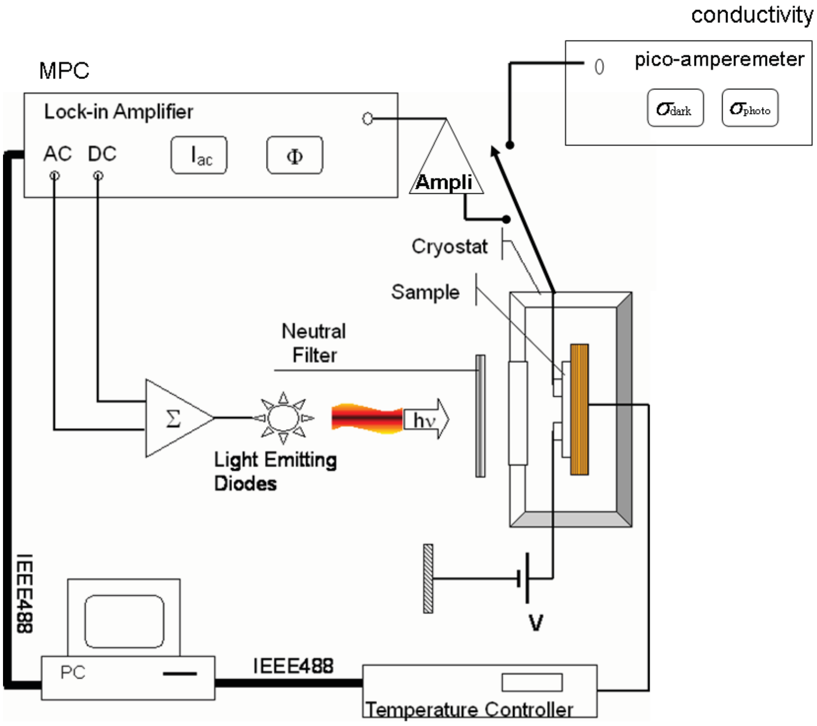

Figure 4.10: Schematic set up of the combined set-up used to perform Modulated Photo Current Experiments and measurements of the dark and photoconductivity. The dark- and photoconductivity are measured at different temperatures employing a pico amperemeter. The photoconductivity is measured using a constant light flux.

4.6 Methods to investigate DoS

The defect state density in amorphous phase change and chalcogenide alloys has been studied using Photo-thermal Spectroscopy and Modulated Photo Current Experiments. Both methods are briefly discussed in the following.

4.6.1 Modulated Photo Current Experiments (MPC)

Modulated Photo Current experiments enable us to probe defect levels within the band gap [OHE81, BMBR90, LK92]. A schematic picture of the Modulated Photo Current experiment combined with a system to measure the temperature dependence of the dark and photoconductivity is shown in Fig. 4.10.

In MPC experiments the sample under investigation is illuminated by a monochromatic light source, whose intensity or light flux F is sinusoidally modulated with an angular frequency ω,

$$F = F_{dc} + F_{ac} \cdot \sin(\omega \cdot t). \tag{4.29}$$

The wavelength of the monochromatic light source has to correspond to a photon energy $h\nu$ significantly higher than the optical band gap of the material under test. To measure the induced photocurrent as a result of band to band excitation, two parallel ohmic electrodes of length h are deposited onto the studied thin film of thickness d. Photo carriers are created within the conduction cross section $A = h \cdot d$. The photo current is measured by applying an electric field ϵ between both electrodes. The periodically changing generation rate induces a periodically change of the free carrier concentration and thus a with angular-frequency ω modulated photocurrent I which is measured by a Lock-In Amplifier after being amplified by a current voltage converter.

In general, the modulated photocurrent I is not in phase with the modulated excitation light, because the generated photo carriers interact with localized trapping levels. While propagating through the sample with free carrier mobility μ, free holes (subscript p) and electrons (subscript n) get captured by localized trap states located at energy E from the mobility band edge E_m in the forbidden energy gap of the studied material. Each trapping level is characterized by a capture coefficient c, which describes their interaction with free carriers. The higher the c-value, the more free carriers are captured from the band into the localized trap. In general, different types of trap states have different capture coefficients c. The captured carriers occupy these localized trap states within the band gap until they are released thermal back to the extended states. Due to this time delay the photocurrent I and the excitation show a phase shift ϕ,

$$I = I_{dc} + |I_{ac}| \cdot \sin(\omega \cdot t + \phi), \tag{4.30}$$

If carriers experience mostly multiple trapping and release events during their drift through the sample, the electronic transport is denoted as multiple trapping transport.

Another possible dominating process is the recombination of captured holes or electrons in the localized trap. Carrier recombination occurs if the probability for thermal emission back into the band is very small. Recombination reduces the photo current I but does not contribute to a non-zero phase shift ϕ.

Whether a trapping level located at energy E acts as multiple trapping or recombination center strongly depends on the chosen measurement conditions. Whereas temperature has a strong influence on the thermal emission rate $e(E) = \nu \cdot \exp(E/k_bT)$, the trapping rate $c_n n_{dc} + c_p p_{dc}$ is commonly assumed to be independent of temperature, but increases with increasing dc flux, see Fig. 4.11. Trapping centers having a larger trapping than emission rate act as recombination centers. Likewise trapping levels having a lower trapping than emission are multiple-trapping centers.

The distinction between multiple trapping and recombination centers is of great importance. Brüggemann et al. showed that only those trapping levels N contribute significantly to the phase shift ϕ, whose emission rate equals the excitation frequency, i.e. $e(E_\omega) = \omega > c_n n_{dc} + c_p p_{dc}$. Hence, the concentration of interacting trapping levels N at the energy E_ω can be determined analytically from the phase shift ϕ and the alternating photocurrent $|I_{ac}|$, both measurable by experiment [BMBR90, LK92],

Basic formula of the Modulated Photo Current method

$$\frac{c\,N(E_\omega)}{\mu} = \frac{2}{\pi k_b T} A\,q\,\epsilon\,G_{ac} \frac{sin(\phi)}{|I_{ac}|} \tag{4.31}$$

energy scaling given by:

$$E_c - E_\omega = k_b T\,ln\left(\frac{\nu_n}{\omega}\right) \qquad \textit{(electron controlled behavior)} \tag{4.32}$$

$$E_\omega - E_v = k_b T\,ln\left(\frac{\nu_p}{\omega}\right) \qquad \textit{(hole controlled behavior)} \tag{4.33}$$

, where q is the elementary charge and G_{ac} the ac generation rate of free carriers excited beyond the mobility band edge. A spectroscopic scan of the defect state concentration within the band gap can be realized by measuring the phase shift ϕ and the amplitude of the modulated current $|I_{ac}|$ at different temperatures T and modulation frequencies ω at a fixed dc and ac flux. From both measured quantitities and the other parameters adjusted within the MPC experiment, the relative density of states Nc/μ can be derived by the relations above. The spectroscopic scan through the MPC energy window is illustrated for two different temperatures $T_1 < T_2$ in Fig. 4.11.

The classical energy scaling given in Eqs. 4.32 - 4.33 assumes a band gap being constant at varied temperature T. The influence of a temperature dependent band gap on the MPC energy scale is a main issue of the presented thesis and is discussed in detail in section 5.1.4.

MPC measurements in this work have been performed unless stated otherwise employing a LED lightsource of wave length $\lambda = 850\,\mathrm{nm}$, i.e. $h\nu = 1.45\,\mathrm{eV}$. The constant light flux has been adjusted to $F_{dc} = 10^{16}\,\mathrm{cm}^{-2}\mathrm{s}^{-1}$ The amplitude of the alternating photon flux was chosen to be 40% of the continuous flux $F_{ac} = F_{dc}/2.5$. Indeed, amorphous phase-change materials show a rather high optical absorption at a photon energy $h\nu = 1.45\,\mathrm{eV}$ expressed by an absorption coefficient $\alpha(1.45\,\mathrm{eV}) \approx 10^5\,\mathrm{cm}^{-1}$ [Kre09]. Hence, amorphous phase change materials absorb the incoming light completely within some hundreth of nanometres. However, Eq. 4.31 has been derived under the assumption of a constant light intensity through the whole sample thickness d. The exponential decrease of the light intensity with increasing layer thickness can be easily considered in Eq. 4.31 by using of an averaged product of conduction cross section A and amplitude of the alternating part of the generation rate G_{ac} in the MPC basic formula expressed by Eq. 4.31,

$$\overline{G_{ac}A} = hF \cdot (1 - \exp(\alpha \cdot d)). \tag{4.34}$$

At a given temperature T, the data points were obtained varying the excitation frequencies $f = \omega/(2\pi)$ in a frequency range from $12\,\mathrm{Hz}$ to $40\,\mathrm{kHz}$ in a way such that $f_{i+1} = f_i \cdot 1.5$. The energy states closer to the band edge were probed with $40\,\mathrm{kHz}$ and the energy states located further from the band edge with $12\,\mathrm{Hz}$, see Fig. 4.11. Thus each data set corresponds to a certain temperature and the temperature steps have to be chosen sufficiently small, in order to create an envelope of superimposing MPC curves giving the relative density of states $cN(E_\omega)/\mu$. The temperature steps were chosen equal to 20 K for most measurements and even as low as 5 K to obtain a good resolution of the density of states.

The current is amplified with a current voltage converter with a gain of $10^7\,\mathrm{V/A}$ before its analysis with the lock-in amplifier. The converter saturates when the current is higher than $500\,\mathrm{nA}$. This may cause problems with samples presenting high dark current for it limits the field that can be applied in between the electrodes. In this case the MPC data is usually noisy and the density of states determination hampered by this noise.

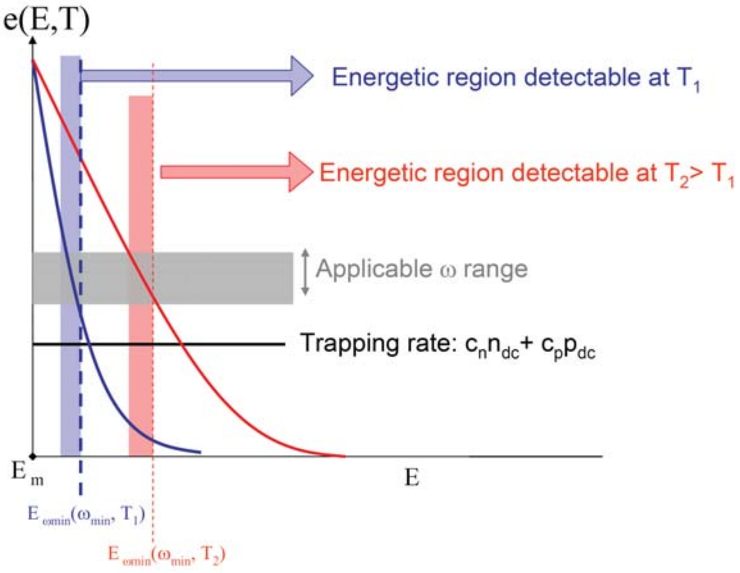

Figure 4.11: Modulated Photo Current Experiments probe the defect state concentration N of those trapping levels above the mobility band edge E_m acting as multiple trapping centers, whose emission rate $e(E)$ equals the excitation frequency ω of the excititing light source, i.e. $e(E_\omega) = \omega > c_n n_{dc} + c_p p_{dc}$. At a given temperature T states within a certain energy range can be probed using an applicable ω range (blue shaded range at T_1 and red shaded range at $T_2 > T_1$). Hence, a systematic variation of excitation frequency ω and temperature T enables a spectroscopic scan of the defect state distribution. The MPC measurement window is limited due to the non-zero trapping rate $c_n n_{dc} + c_p p_{dc}$, which defines the temperature dependent quasi-Fermi levels for trapped holes E_{tp} and trapped electrons E_{tn}.

4.6.2 Photothermal Deflection Spectroscopy (PDS)

Photothermal Deflection Spectroscopy is a highly sensitive technique to measure optical absorption. The sensitivity of Photothermal Deflection spectroscopy compared to ellipsometry and transmission/reflection techniques is shown in Fig. 4.12.
Ellipsometry as well as optical transmission and reflection techniques are very well suited to study high absorption transitions. However, the weak absorption regime near the band edges can hardly be tested by purely films limited to a thickness of several micrometers optical methods.

This challenge can be easily visualized by concentrating on the transmitted light intensity T, which can be approximated to [Str91b],

$$T = (1 - R)^2 \cdot \exp(-\alpha \cdot d). \tag{4.35}$$

Very accurate measurements of the reflected (R) and transmitted (T) intensity are required, if the absorptance - the product of absorption coefficient α and film thickness d - is small. Especially in the case of weak absorption, transmission and reflection techniques deal with small differences and large signals rising the problem of insufficient measurement accuracy. Photothermal Deflection Spectroscopy overcomes this problem by measuring the heat absorbed

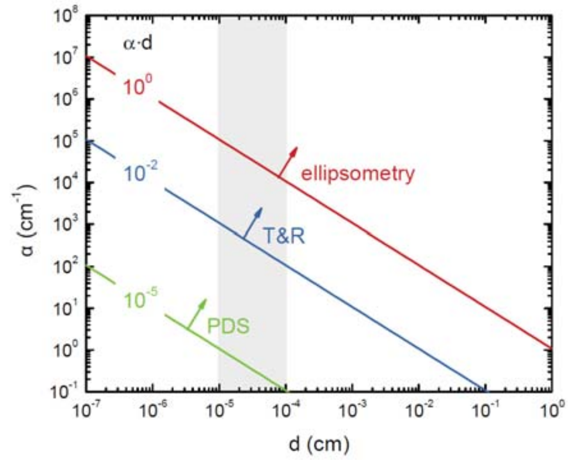

Figure 4.12: Various techniques can be used to measure the absorption coefficient α in thin films of thickness d. The figure above compares sensitivities of ellipsometry, transmission and reflection experiments to the sensitivity of Photothermal Deflection Spectroscopy. Transmission and reflection measurements are very well suited to investigate high absorption transitions having an absorptance $\alpha \cdot d \geq 10^{-2}$. The highly sensitivity of Photothermal Deflection Spectroscopy enables to probe weaker optical transitions showing absorptances as low as $\alpha \cdot d \geq 10^{-5}$. Consequently, each presented technique has a detection limit for the absorption coefficient α, which depends on the chosen film thickness d. Applicable film thicknesses for sputter deposited phase-change films lie in a range from 1 nm to 1 μm (grey). Image source [Car09]

within the investigated thin film. Hence, the PDS signal exhibits a high sensitivity, which enables the detection of low absorption transitions. Whereas transmission and reflectance techniques can be employed to detect absorptances higher than 10^{-2} the Photothermal Spectroscopy enables to detect absorbtances as low as 10^{-5}. Hence, in films of thickness $d = 1\,\mu\mathrm{m}$ PDS enables to measure absorption coefficients as low as $\alpha = 0.1\,\mathrm{cm}^{-1}$.

A schematic picture of a Photothermal Deflection Spectrometer is illustrated in Fig. 4.13. The thin film under test is immersed in a liquid, which acts as a deflection medium. A light source illuminates the surface of the immersed sample. Thereby the wavelength of the impinging light can be systematically varied by a monochromator installed in between. The light absorbed within the thin film under investigation leads to a change in refractive index of the surrounding liquid. The change in refractive index acts as a thermal lens. Consequently, a test laser beam passing just above the sample surface is deflected, where the deflection angle is proportional to the light absorbed within the sample when the absorptance is much smaller than one, i.e. $\alpha \cdot d << 1$. The absorption coefficient α is calculated from the measured deflection angle. Photothermal Spectroscopy on post-annealed and amorphous deposited phase-change films have been performed in cooperation with Reinhard Carius and Josef Klomfaß at the research center Jülich using a solid state laser with a wavelength of $\lambda = 632\,\mathrm{nm}$ and CCl_4 as the deflection medium. A detailed discussion of this method can be found in [JABF81, RW86, BFJA80]

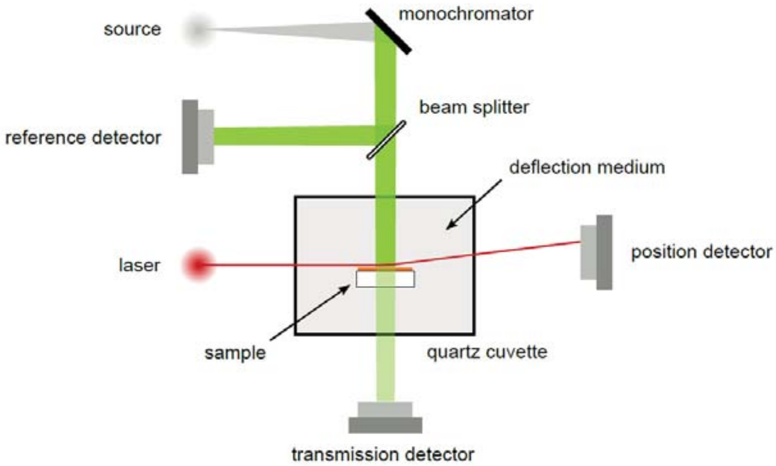

Figure 4.13: Schematic set-up of a Photothermal Spectrometer. The thin film under investigation is immersed in a liquid acting as the deflection medium. The sample surface is illuminated, where the photon energy of the impinging light can be systematically varied by a monochromator. The light absorbed within the sample leads to a thermal heating of the surrounding liquid. The corresponding change of the refractive index acts as a thermal lens for the probe laser passing just above the sample surface. For small absorptances $\alpha \cdot d$ the deflection angle is directly proportional to the light absorbed within the sample. Image taken from [Kre10]

4.7 Measurement of internal stresses employing the Wafer Curvature method

The mechanical stress during heating amorphous phase-change films has been studied for various chalcogenide alloys. The Wafer Curvature method enables us to determine mechanical stresses. Mechanical stresses in thin films attached to a substrate may arise during deposition. In addition to deposition stresses, thermal stresses can be induced at elevated temperatures due to different thermal expansion coefficients of film and substrate. Mechanical stresses induce bending moments at the interface between film and substrate. The bending moments induce a bending of the entire system including the substrate. Hence, the thin film attains a given curvature along its x- and y-axis. The relation between the mechanical stress and the radii of the thin film curvature R_f depend on the nature of the chosen substrate. For isotropic, rectangular substrates the mechanical stress σ can be calculated from the curvatures of the uncoated substrate R_s and the subsequently deposited thin film R_f,

$$\sigma = \frac{Y_s}{1-\nu_s}\frac{d_s^2}{6d_f}\left(\frac{1}{R_f} - \frac{1}{R_s}\right). \tag{4.36}$$

Eq. 4.36 is known as the Stoney equation. The Stoney equation, first proposed in 1909 [St009], holds as long as the smaller side of the rectangular substrate b is large in comparison to the substrate thickness d_s [SR06]. The Stoney equation is very practicable, because it relies only on the Young modulus Y_s and the Poisson's ratio ν_s of the substrate, which are generally known from literature or manufacturers' specifications. Hence, the Stoney equation allows to calculate the mechanical stress within the deposited thin film of known thickness d_f by measuring the radii R_s and R_f.

A scanning lasersystem which allows to measure the radii of curved samples is illustrated in Fig. 4.14. The core element of a laser scanning system is the galvanoscanner. A galvanoscanner enables a controlled tilting of a mirror by the application of a current. Hence, the incident laserbeam can be reflected by the galvanoscanner at different angles. In Fig. 4.14 the possible angular range is illustrated by the angle α visualizing the maximum and minimum reflection angles. After being reflected at the galvanoscanner, the laser beam passes a beam splitter. The use of a beamsplitter allows to position the galvanoscanner and the photo sensitive detector (PSD) at the focal distance of the plano-convex lens, however at different locations. Hence, even though the laser beam is moved through an angle α by the galvanometer the beam is parallel to the optical axis after passing the plano-convex lens. The paralleized light is directed by additional mirrors to the sample surface. Generally, the sample is placed in a vacuum chamber to minimize data noise or to avoid oxidation effects during heating at elevated temperatures. The reflection at the sample surface depends strongly on its curvature. In the case of ideally flat samples the laser beam is reflected back along the path of the incident beam and the plano-convex lens images the reflected laser beam at the focus point, i.e. at the same point on the PDS sensor for all possible angles α adjusted by the galvanoscanner. In contrast, laser beams reflected at curved sample surfaces follow a path slightly different to the path of the

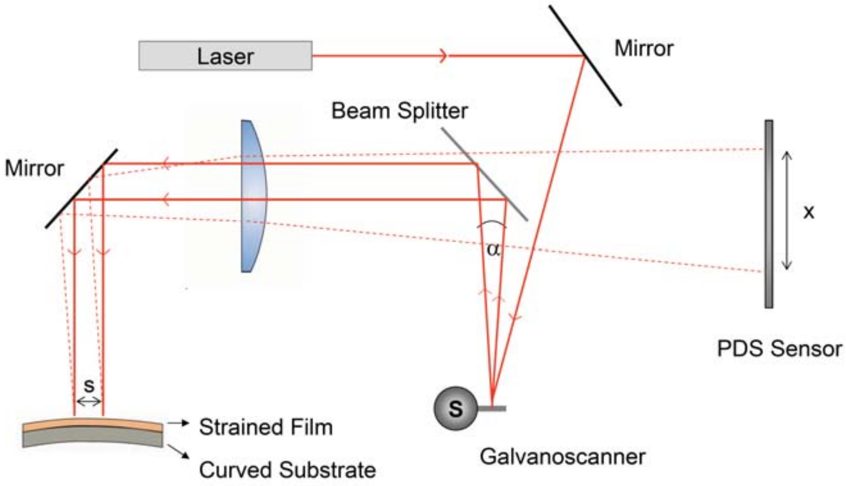

Figure 4.14: Schematic picture of a laser scanning systems to measure radii of curved samples. The position of the incident laser beam on the sample surface can be systematically altered by a galvanoscanner moving the incident laser beam through an angle α. At curved sample surfaces the reflected and the incoming laser beam follow slightly different optical paths. Hence, the plano-convex lens images the reflected laser beam at different points at the PDS sensor for different angles α. The curvature of the sample R can be determined from the distance the beam moves on the PSD x and the scanning distance on the sample surface s. Image adapted from [Koe11]

incoming beam. Consequently, the plano-convex lense images the reflected laser beam not within a single point, but over a vertical distance x over the PDS sensor. The movement of the beam on the PDS can be determined very precisely. From geometric considerations the following relation between the distance x and the radius of the reflecting sample surface R can be derived,

$$\frac{x}{s} = \frac{2f}{R}, \tag{4.37}$$

,where f is the focal length of the plano-convex lens and s denotes the scanning distance on the sample surface. Stress measurements on phase-change films have been performed on a custom built set-up at the I. Physical Institute at the RWTH University. The set-up used works with a HeNe laser of a wavelength $\lambda = 633\,\mathrm{nm}$ and a plano-convex lense having a focal distance $f = 1.0165\,\mathrm{m}$. Further information on the set-up used can be found in [Ped03].

4.8 Extended X-ray absorption fine structure (EXAFS)

The method is based on the absorption of monochromatized X-Rays of variable energy. Therefore synchrotron sources are necessary to employ this method. To resolve the X-ray absorption fine structure, the intensities of the incident and transmitted X-ray radiation are measured. After passing matter of thickness x the incident intensity I_0 is reduced. The decrease in intensity due to X-Ray absorption within matter is desribed by the Lambert-Beer law,

$$I = I_0 \exp(-\mu(E)x). \tag{4.38}$$

The absorption coefficient μ depends on the investigated material and on the energy of the incident X-Ray radiation. In case the incident X-ray energy E matches the binding energy of an electron of an atom within the sample, the absorption coefficient μ increases drastically resulting in an absorption edge. Each element is characterized by a set of unique absorption edges, which correspond to different binding energies of core electrons. Fig. 4.15 shows the absorption spectrum of the Ge K-edge measured in a-$Ge_1Sb_2Te_4$. Above the absorption edge, the X-ray absorption spectra show oscillations. These oscillations result from the absorption of X-ray quanta, knocking electrons out of the inner shell. The excited photoelectrons have a wave-like nature and interact with nearby atoms acting as scattering centers. The wavelength λ

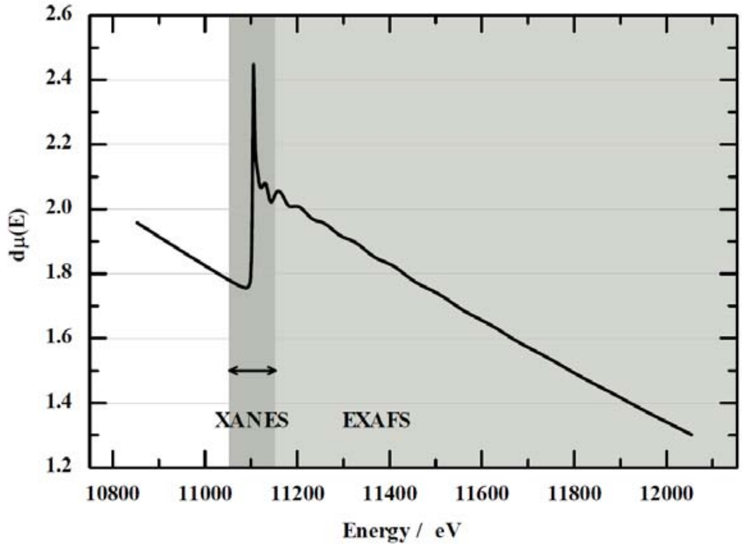

Figure 4.15: The X-ray absorption fine structure is devided into different energy regimes. The X-Ray absorption near edge structure (XANES) contains information about the oxidation state and binding energy of the absorbing atom and lies energetically ± 50 eV around the absorption edge. The extended X-ray absorption fine structure (EXAFS) lies 50 eV to 1000 eV above the absorption edge and resolves information about the next neighbour distances, their type and number. Image taken from [VE10]

of the excited photoelectron depends on the energy of the incident monochromatic X-Ray irradiation. Forward propagating and backscattered electron waves result in an intereference pattern, which leads to a modulation in the measured absorption coefficient $\mu(E)$. In the case of constructive intereference the absorption coefficient μ shows a maximum and in the case of destructive interference a minmum. Consequently, the absorption coefficient $\mu(E)$ oscillates around the absorption coefficient of an isolated atom μ_0,

$$\mu(E) = \mu_0(E)(1 + \chi(E)). \tag{4.39}$$

The oscillations $\chi(E)$, known as X-Ray absorption fine structure, contain information about the atomic environment. The X-ray absorption fine structure can be observed and analyzed in all kind of matters including gases, solids and liquids. In the analysis of X-ray absorption fine structures one distinguishes two regimes: the X-Ray absorption near edge structure (XANES) and the extended X-ray absorption fine structure (EXAFS), see Fig. 4.15. The XANES regime ranges approximately ± 50 eV around the absorption edge and provides information on the oxidation state of the atom, i.e. the binding energy of the electron. The EXAFS region lying 50 eV to 1000 eV above the absorption edge contains information about the next neighbour distances, type and number.
In the EXAFS analysis the X-Ray fine structure is analyzed as a function of the wavenumber k of the excited photoelectron, which is directly related to energy of the incident monochromatic X-ray beam E,

$$k = \sqrt{\frac{2m_e}{\hbar^2}(E - E_b)}, \tag{4.40}$$

where m_e is the electron mass and E_b the binding energy of the electron in the inner shell. The amplitude of the backscattered electron wave can be described by a spherical wave, whose amplitude depends on the backscattering atom and on the amplitude of the incident wave. Each backscattering atom j is characterized by an element specific backscattering function $F_j(k)$. Atoms acting as scattering centers at the same distance R_j to the absorbing atom of the same element contribute equally to the EXAFS signal. This group of atoms is denoted as a coordination shell and is characterized by the number of backscattering atoms N_j. Disorder and thermal vibration influence the distance distribution between the absorbing and backscattering atom. Hence, the contribution of atoms in the first coordination shell show an additional phase difference. This phase difference caused by thermal vibration and disorder reduces the EXAFS signal $\chi(K)$ by the factor $\exp(-2k^2\sigma^2_{\text{EXAFS}})$, where the factor σ^2_{EXAFS} is the EXAFS Deby Waller factor. The EXAFS Deby-Wallerfactor indicates the displacement $\vec{u} - \vec{u_0}$ of the absorbing and backscattering atom along the equilbrium bond direction $\vec{r}$,

$$\sigma_{\text{EXAFS}} = \sqrt{< [\vec{r} \cdot (\vec{u} - \vec{u_0})]^2 >}. \tag{4.41}$$

At this point one should note that the EXAFS-Debye Waller factor is not equivalent to the Debye-Waller factor known from X-Ray diffraction. The Debye-Waller factor known from X-Ray diffraction σ_{XRD} describes the mean square displacement.

$$\sigma_{\mathrm{XRD}} = \sqrt{< [\vec{r} \cdot \vec{u}]^2 >}. \tag{4.42}$$

Hence, the value of the EXAFS Debye-Waller factor is in general smaller than the Deby-Waller factor σ_{XRD} determined from X-ray diffraction. Furthermore, the X-Ray absorption fine structure in the EXAFS energy range is also influenced by the lifetime of the excited photoelectron, which is of the order of $10^{-15}s^{-1}$. The limited lifetime induces a damping of the observed oscillations. In general, coordination shells in a distance of more than 10 Å from the absorbing atom show no longer a significant contribution to the measured EXAFS spectrum. The damping can be described by the term $\exp(-2r/\lambda(k))$, where λ is the so called mean free path length. Additionally, a factor S_0^2 describes the amplitude reduction resulting from the creation of a core hole. Even though S_0^2 is known to be weakly temperature dependent, its value is usually approximated by a constant. In summary, the X-Ray absorption fine structure $\chi(k)$ within the EXAFS energy range can be analysed employing the following formula,

$$\chi(k) = \sum_j N_j S_0^2 F_j(K) \exp(-2R_j/\lambda(k)) \exp(-2k^2\sigma^2_{\mathrm{EXAFS}}) \frac{\sin(2kR_j + \delta_j)}{kR_j^2}. \tag{4.43}$$

However, in literature often the Fourier transform of $\chi(k)$ is reported, weighted by a window function $w(k)$ and a factor k^n,

$$\chi(R)_n = \frac{1}{\sqrt{2\pi}} \int_{k_{min}}^{k_{max}} \chi(k) e^{i2kR} w(k) k^n dk. \tag{4.44}$$

Different types of window functions can be used. The EXAFS spectra presented in this work are analysed using the Hanning function. The weighting factor k^n is added in Eq. 4.44 to compensate effects which diminish the amplitude with increasing k, such as the decrease of the backscattering amplitude $F(k)$ following a $1/k$ dependence. The weighting factor k^n should be chosen in a way that $k^n \cdot \chi(k)$ has a constant amplitude over the k-range $[k_{min}, k_{max}]$ used in the Fourier transformation given in Eq. 4.43. An example of EXAFS spectra taken on amorphous and crystalline GeTe powder samples are presented in Fig. 4.16. Disorder strongly affects the measured EXAFS signal. The Fourier transfomed EXAFS signal $\chi(R)$ is much higher in the crystalline than in the amorphous phase. Such a behavior is usually expected, because the EXAFS Debye-Waller factor σ_{EXAFS} is in general higher in the disordered amorphous than in the ordered crystalline phases. The observed change in peak position reflecting the nearest neighbour distance indicates a different local order in the amorphous and crystalline phase of GeTe. Further information about the EXAFS technique applied to phase-change materials can be found in [VE10]. The EXAFS results on a-GeTe thin films presented in this work have been achieved together with Peter Zalden, who performed the experiment at the beamline CEMO at HASYLAB, Hamburg.

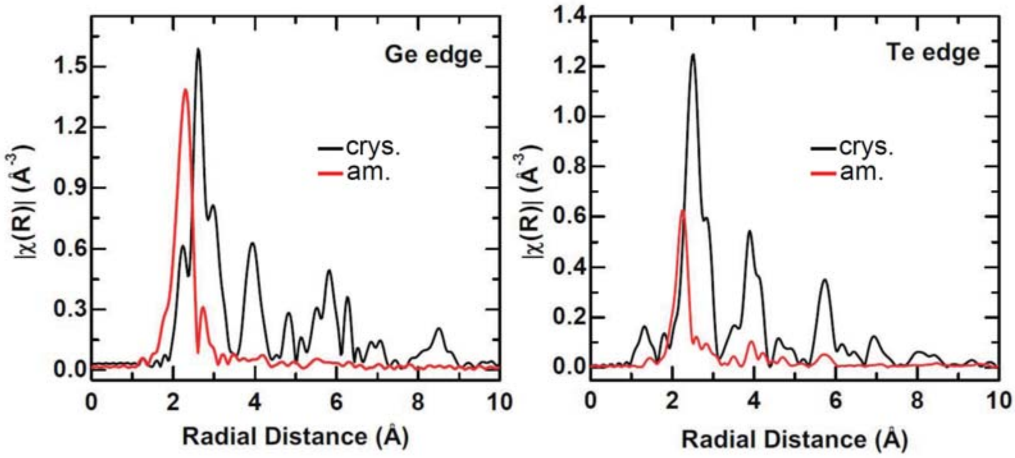

Figure 4.16: EXAFS spectra of amorphous and crystalline GeTe measured at 10 K. Disorder has a strong influence on the shown Fourier transformed EXAFS signal $\chi(R)_{n=2}$. The EXAFS signal is much higher in the ordered crystalline than in the disordered amorphous phase. The EXAFS Debye-Waller factor σ_D indicates the displacement of the absorbing and backscattering atom along the equilbrium bond direction. Hence, in general the amorphous phase has a higher value σ_{EXAFS} than the crystalline phase resulting in a lower EXAFS signal, see Eq. 4.43. Furthermore, the peak positions reflecting the nearest neighbour distances are diffrent in the amorphous and crystalline phases in GeTe. Image taken from [VE10]

.

Chapter 5

Investigation of defect states in amorphous phase-change materials

Many transport models proposed for amorphous phase-change materials involve localized defect states. Therefore, it is important to develop a sophisticated defect state model for amorphous phase-change materials. This issue gains importance especially since the validity of the VAP defect model based on chalcogen chains was shown to be questionable for a-GeTe and a-$Ge_2Sb_2Te_5$, [CBK$^+$07, AJ07, JKS$^+$08].
This chapter concentrates on the defect state density measured in amorphous phase-change and chalcogenide alloys. In the first section; a defect state model based on experimental findings is proposed for a-GeTe. In the second section; the defect state density in switchable chalcogenides in their amorphous phase is studied to investigate the relation between defect states within the band gap and the electrical threshold field.

5.1 Defect states in a-GeTe

Different characterization methods are combined to provide knowledge about the defect state density in amorphous GeTe. Indirect conclusions can be drawn from dark and photoconductivity measurements. A direct measurement of localized traps within the band gap is enabled by Photothermal Deflection Spectroscopy (PDS) and Modulated Photo Current experiments (MPC).

5.1.1 Dark- and Photoconductivity in a-GeTe

Many studies published in the literature analyze the temperature dependent dark and photoconductivity to resolve information about the transport path and defect state distribution in disordered structures, [ME71, OT89, SA84, Bar06]. In the following, the most commonly employed concepts are presented. Finally, these concepts are applied to amorphous GeTe.

Dark conductivity dominated by carriers in extended states

Within the standard transport model introduced by Thomas and Overhof [OT89], the electronic transport is controlled by carriers in extended states beyond the mobility band edges. Henceforth, carriers occupying energetic states beyond the mobility band edges are referred to as free carriers. The standard transport model is known as multiple trapping transport and is illustrated for free electrons in Fig. 3.6. However, it is reported in literature, that hole conduction predominates in amorphous GeTe, [Adl71]. The density of free holes excited below the valence band edge E_v, is given by the integral over the density of states $N(E)$ weighted with the probability that a hole occupies the energy level E,

$$p = 2\int_{-\infty}^{E_v} N(E)\,(1 - f(E))\,dE. \tag{5.1}$$

The factor of 2 considers the two possible spin orientations. In dark equilibrium, the occupation function $f(E)$ is given by the Fermi-Dirac distribution function,

$$f_{Dirac}(E) = \frac{1}{1 + \exp\frac{E-E_F}{k_bT}}\ . \tag{5.2}$$

For energies E high compared to k_bT, the Fermi-Dirac distribution function converges to Maxwell-Boltzmann statistics. In non-degenerated amorphous semiconductors, the Fermi level E_F lies per definition several k_bT away from both mobility band edges. Therefore, the term $1 - f(E)$ can be replaced by the corresponding Boltzmann approximation within the integral boundaries given in Eq. 5.1,

$$1 - f_{Dirac} \approx \exp\left(\frac{E - E_F}{k_bT}\right). \tag{5.3}$$

Under the assumption that the density of states does not change significantly above the mobility edge on a k_bT scale, the density of free holes can be analytically derived from Eq. 5.3 and Eq. 5.1. Hence, the free hole density in nondegenerated semiconductors is described by,

$$p = 2N(E_v)k_bT\exp\left(-\frac{E_F - E_v}{k_bT}\right). \tag{5.4}$$

The dc conductivity is determined by the product of carrier charge q, free carrier density n and free carrier mobility for holes μ_p and electrons μ_n, respectively. Thus, the temperature dependence of the dark conductivity $\sigma(T)$ in nondegenerated p-type semiconductors is given by,

$$\sigma(T) = q\mu_p p = q\mu_p 2N(E_v)k_bT\exp\left(-\frac{E_F - E_v}{k_bT}\right). \tag{5.5}$$

In summary, we expect a temperature activated dark conductivity, if the transport is entirely due to one type of carriers in extended states. In p-type conductors the activation energy E_a equals the energetic distance between the Fermi level and the valence band edge. The thermally activated temperature dependence of the dark conductivity is also referred to as Arrhenius behavior.

$$\textbf{Arrhenius} \qquad \sigma(T) = \sigma_0 \exp\left(-\frac{E_a}{k_b T}\right) \tag{5.6}$$

As a final remark it should be mentioned here, that in materials having a Fermi level close to mid gap and comparable mobilities of holes and electrons, the electronic conduction will take part in both bands as a sum of independent contributions from both carriers, where the electron contribution is calculated in an equivalent manner as for holes.

Dark conductivity dominated by carrier hopping between localized states

The presence of localized defect states within the band gap opens an additional possible transport path. Especially at low temperatures, carrier transitions between localized trap states may contribute significantly to the electronic conductivity. This carrier hopping transport is depicted in Fig. 3.7. The probability of a carrier transition from one trap state at energy E to a neighbouring trap energetically located at E' in distance $R_{EE'}$ depends strongly on the hopping direction. A downward hop denotes a carrier transition to a localized state at lower energy. The probability of a downward hop is determined by the overlap of both trap wave functions. In general a trap state is assumed to have an exponential decaying wave function, where the localization length α defines its spatial width,

$$\psi_{trap}(r) \propto \exp\left(-\frac{r}{\alpha}\right). \tag{5.7}$$

Hence, the transition probability of an downward hop is defined by the ratio of the distance between both traps $R_{EE'}$ and the localization length α,

$$W_{\downarrow} = \nu_0 \exp\left(\frac{-2R_{EE'}}{\alpha}\right). \tag{5.8}$$

Likewise, an upward hop denotes a carrier transition to an energetic state at higher energy. Hopping transitions to higher energy levels require the absorption of a phonon to bridge the energy difference. Consequently, the hopping upward probability includes the probability of phonon absorption and the tunneling probability,

$$W_{\uparrow} = \nu_0 \exp\left(\frac{-2R_{EE'}}{\alpha}\right) \exp\left(-\frac{E'-E}{k_b T}\right) \quad \text{where} \quad E' > E. \tag{5.9}$$

Hopping to lower energy levels occurs even at zero K. In contrast carrier transitions to higher energies are only possible at non-zero temperatures. However, carrier transitions at zero K temperature do not contribute to a steady state conductivity. In the hopping down case excited carriers tunnel to lower energy states until they return either to the Fermi level or the distance to neighbour trap states is so large that the hopping probability becomes negligibly small. The described process is known as thermalization. Thermalization gives rise to a transient current after carrier excitation, but is a non-equilibrium process. As a consequence, a steady hopping conductivity occurs only at non-zero temperature.
Several detailed calculations based on Eq. 5.8 and Eq. 5.9 have been carried out to determine the temperature dependent hopping conductivity. However, the physical mechanism are best illustrated using the variable range hopping model proposed by Mott [Mot68]. According to Mott, the hopping conductivity is dominated by carrier transitions between states at an average distance $< R_{EE'} >$. This includes thermal assisted carrier transitions to higher energy levels within a range ΔE from the Fermi level E_F. Assuming a density of states, that changes insignificantly around the Fermi level over several $k_b T$, the average distance between trap states in the range $E_F \pm \Delta E$ is given by,

$$R_{EE'} = [N(E_F)\Delta E]^{-1/3} \tag{5.10}$$

The total hopping conductivity is limited by carriers, which have to overcome the highest possible energy barrier, i.e. $E - E' = \Delta E$. Consequently, the total conductivity maximizes when the hopping rate exponent in Eq. 5.9 is minimized, i.e. $\frac{d}{dR_{EE'}}\left(\frac{2R_{EE'}}{\alpha} + \frac{\Delta E(R_{EE'})}{k_b T}\right) = 0$. It can be easily shown that this occurs when the average hopping distance is,

$$< R_{EE'} > = \left[\frac{3\alpha}{2k_b T N(E_F)}\right]^{1/4}. \tag{5.11}$$

Since the average hopping distance is not constant, but decreases with increasing temperature, this transport is denoted as variable range hopping. The variable range hopping conductivity shows typically a $T^{-1/4}$ dependence known as Mott's law,

$$\textbf{Mott's law} \qquad \sigma(T) = \sigma_M \exp\left(-\left(\frac{T_0}{T}\right)^{1/4}\right). \tag{5.12}$$

where the characteristic temperature T_0 is described by,

$$T_0 = \beta/(k_b T N(E_F)\alpha^3). \tag{5.13}$$

Various studies in three-dimensional systems suggest β values in the range from 10 to 38.8 [SP74]. Based on the assumption of a constant density of states in the vicinity of the Fermi level, Mott's law can be generalized for other density of states distributions. For example Efros and Shlovskii have shown that the exponent in Eq. 5.12 is equal to $1/2$ in the presence of a Coulomb gap [SA84]. Typically, disordered systems show a dark conductivity of the form:

$$\sigma(T) = \sigma_* \exp\left(-\left(\frac{M}{T}\right)^{l*}\right). \tag{5.14}$$

The preexponential factor σ_* depends on the underlying system and the power exponent $l*$ is strongly linked to the density of states of the material under investigation. Sometimes the power exponent $l*$ is reported to depend also on the temperature range in which the dc conductivity is studied [Bar06].

Even though the assumption of an constant density of states around the dark Fermi level is not guaranteed in general, it should also be mentioned that even in systems meeting this requirement an data analysis according to Eqs. 5.12 – 5.13 leads to erroneous values for $N(E_F)$. In the Mott model a discrepancy arises from identifying the dominant hopping distance as the radius of a sphere in which hopping takes place. Indeed, Marshall and Main have shown that the dominant hopping distance may fall to less than 1% of the sphere radius. Due to these inconsistencies underlying Mott's $T^{-1/4}$ model an analysation of the dark conductivity according to Eq. 5.12 often yields to unreasonable values for the density of states at the Fermi level $N(E_F)$ [MM08].

Photoconductivity described by Shockley-Read Statistics

Light excitation generates additional photo carriers due to band to band excitation. Additionally, the interaction of photo carriers with existing trapping centers influences the value of the occupation function $f(E)$. Consequently, Fermi-Dirac statistics can not be applied to describe the probability distribution in illuminated disordered materials. The challenge to derive statistics under constant illumination in the presence of traps was first addressed by Shockley and Read considering one trapping center within the band gap [SR52]. Simmons and Taylor generalized this theory for an arbitrary distribution of defect levels, [ST71].

The authors show, that the interaction of photo carriers with localized trap states leads to a splitting of the dark Fermi level E_F into two quasi Fermi levels for trapped holes E_{tp} and trapped electrons E_{tn}, respectively. Hence, the occupation function $f(E)$ associated to illuminated materials possessing an arbitrary distribution of traps is given by a two step function, see Fig. 5.1. Trap states lying in the energetic region W in-between both quasi Fermi levels have a larger capture than emission probability. Consequently, these states are occupied by carriers with a certain probability in-between one and zero. In comparison with the dark equilibrium Fermi distribution describing a one step function, the occupancy described by Shockley-Read statistics is increased above the dark Fermi level E_F due to electrons trapped at these sites. Likewise, the occupancy is reduced within the energy range $[E_{tp}; E_F]$ as a result of trapped holes. Since carriers captured by traps in the energetic region W are rather recombined than re-emitted to the corresponding band edge, this region is denoted as recombination zone. The width W of the recombination zone, given by the energy interval $[E_{tp}; E_{tn}]$, depends on the density of states around the dark equilibrium Fermi level, on temperature and on the intensity of the exciting light.

The width of the recombination zone for different generation conditions is qualitatively illustrated in Fig. 5.1 for a fixed density of states. At constant temperature, the width W increases with increasing light intensity. On the other hand, at constant excitation rate the width W increases with decreasing temperature. This can be easily explained phenomenologically. Illumination, i.e. generation of additional free carriers, represents a perturbance of the thermal equilibrium. To return to thermal equilibrium a physical mechanism is needed, which eliminates these additionally generated free carriers. Within the recombination zone trapped carriers are unlikely to be re-emitted but rather recombine. Consequently, the more free carriers are generated by increasing intensity of the excitation light the more carriers have to be eliminated and the larger must be the number of recombination centers, i.e. the width of the recombination zone W. On the other hand the perturbance of the thermal equilibrium due to photo-generated carriers is less significant at high temperatures, where a high concentration of thermally excited carriers dominates. Hence, the width W decreases with increasing temperature.

Obviously, the splitting of the Fermi level depends also on the density of states around the equilibrium Fermi level E_F, since the total number of recombination centers is of importance. Under identical generation conditions a low defect density leads to a larger recombination zone than a high trap density does.

The quasi Fermi levels for trapped holes E_{tp} and electrons E_{tn} describe the occupation of localized trap states in the energy gap. Likewise, the free carrier concentrations under constant illumination are described by quasi Fermi levels for free holes E_{fp} and free electrons E_{fn}. Thereby the quasi Fermi level for free holes is always positioned above the quasi Fermi level for trapped holes, i.e. $E_{fp} \geq E_{tp}$. In the case that holes contribute the majority carriers under constant illumination, both quasi Fermi levels coincide, i.e. $E_{fp} = E_{tp}$, when thermal equilibrium is attained. In non-equilibrium, The quasi Fermi level for free electrons E_{fn} lies always below the quasi Fermi level for trapped electrons, i.e. $E_{fn} \leq E_{tn}$. This relation is also valid in thermal equilibrium if the photoconductivity is dominated by holes. In the case that the photo current is dominated by electrons, E_{fn} and E_{ft} coincide at thermal equilibrium, where $E_{fp} \geq E_{tp}$. Hence, the observed photoconductivity is controlled by the width of the recombination zone. The stronger the splitting of the dark Fermi level into two quasi Fermi levels due to light exposure the higher is the observed photoconductivity at a given temperature.

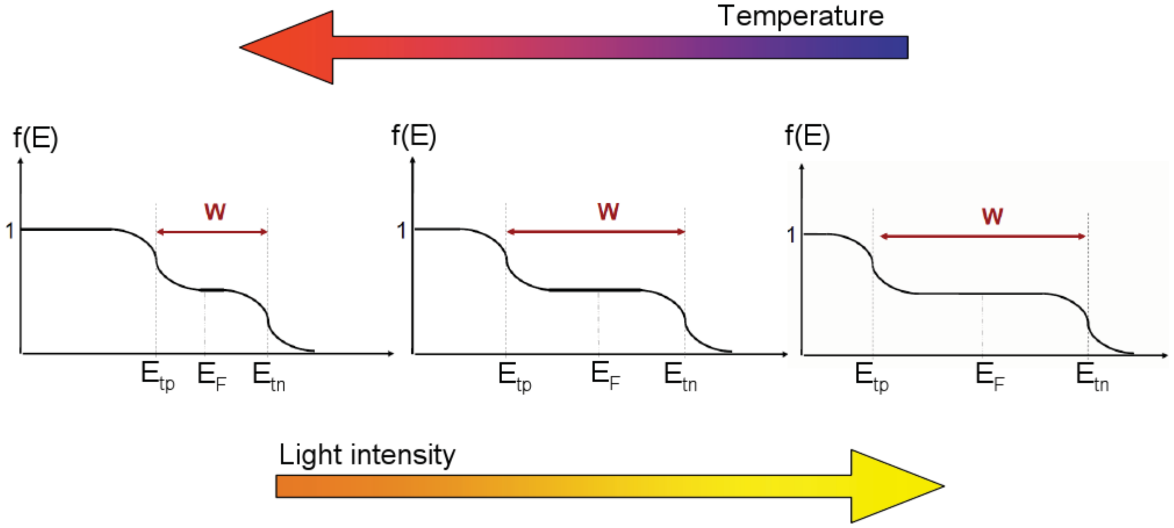

Figure 5.1: Shockley-Read statistics describe illuminated materials possessing an arbitrary distribution of traps within the band gap. Interaction of generated photo carriers with localized trap states leads to a splitting of the dark Fermi level E_F into two quasi Fermi levels for trapped holes E_{tp} and trapped electrons E_{tn}. Consequently, the occupation function $f(E)$ describes a two step function. Carriers captured at traps lying energetically within the energetic region W in-between both quasi Fermi levels, rather recombine than being re-emitted to the bands. The width W of the recombination zone depends on light intensity, temperature and defect state density in the vicinity of the dark Fermi level E_F. For a given DoS the recombination zone increases with increasing light intensity and decreases with increasing temperature at constant light flux. This dependence on the generation conditions is qualitatively illustrated in the figure above, where the smoothing of the Fermi edge with temperature is not considered. Under identical generation conditions a high density of states around the Fermi level results in a smaller recombination zone than a small defect density does. The stronger the splitting of the Fermi on light exposure at given temperature the higher is the observed photoconductivity.

Concepts applied to a-GeTe

To gain a better insight into the electronic transport mechanisms in amorphous phase change materials, the before mentioned concepts are applied to amorphous GeTe. The conductivity of a 100 nm thick amorphous GeTe thin film was measured at different temperatures in the dark and under constant illumination of the sample surface. For this purpose a LED light source of wavelength $\lambda = 850\,\mathrm{nm}$ delivering a continuous flux $F_{dc} = 10^{16}\,\mathrm{cm^{-2}s^{-1}}$ was used. The corresponding photon energy of $1.45\,\mathrm{eV}$ lies well above the optical band gap of $0.78\,\mathrm{eV}$ listed in Tab. 2.1. Fig. 5.2 presents the same data using different scales.

Fig. 5.2a shows the dark conductivity compared to the conductivity measured under constant illumination. The conductivity does not change significantly on light exposure for $T > 175\,\mathrm{K}$. This implies a large defect state density within the band gap, because the splitting of the dark Fermi level illustrated in Fig. 5.1 is very low. At constant flux the width of the recombination region increases with decreasing temperature. Consequently, the conductivity under illumination is expected to be significantly larger than the dark conductivity at low temperatures. In a-GeTe the conductivity under constant illumination differs significantly from the dark conductivity for temperatures below $175\,\mathrm{K}$. The difference increases steadily with decreasing temperature. At $90\,\mathrm{K}$ the conductivity change on light exposure is slightly more than two orders of magnitude.
The photoconductivity is determined by subtracting the dark conductivity from the conductivity under constant illumination. The photoconductivity derived in this manner is shown in Fig. 5.2b. The photoconductivity is observed to increase exponentially with increasing temperature. At $175\,\mathrm{K}$ the photoconductivity passes a maximum, hence at that temperatures the conductivity under light exposure does no longer differ significantly from the dark conductivity. The same qualitative behavior of the photoconductivity has been reported by Howard and Tsu, [HT70]. The fact that in a-GeTe no significant photoconductivity can be observed at room temperature suggests a high density of gap states at the vicinity of the Fermi level leading to a low splitting of the dark Fermi level under constant illumination.

Focusing in the following on the dark conductivity, its temperature dependence is analyzed according to Eq. 5.6 and Eq. 5.12. To obtain the activation energy E_a, the dark conductivity is plotted versus the reciprocal temperature $1000/T$, see Fig. 5.2 c. The presented Arrhenius plot clearly shows, that no single activation energy exists in a-GeTe over the whole investigated temperature range varied from 90 K to 300 K. Consequently, the transport in a-GeTe can not be described within the standard transport model proposed by Thomas and Overhof. The curvature observed in the Arrhenius plot implies a complex transport mechanism in amorphous phase-change materials. The observed curvature may be caused by a temperature dependent Fermi level or temperature dependent mobility band edges. Furthermore, superposition of two transport channels leads to a non singly activated dark conductivity. However, the dark conductivity measured on a-GeTe shows a good thermally activated behavior in the high temperature range (T> 230 K). The corresponding activation energy is determined to be $E_a = 0.36\,\mathrm{eV}$. Thomas and Overhof showed that within the standard linear approximation the

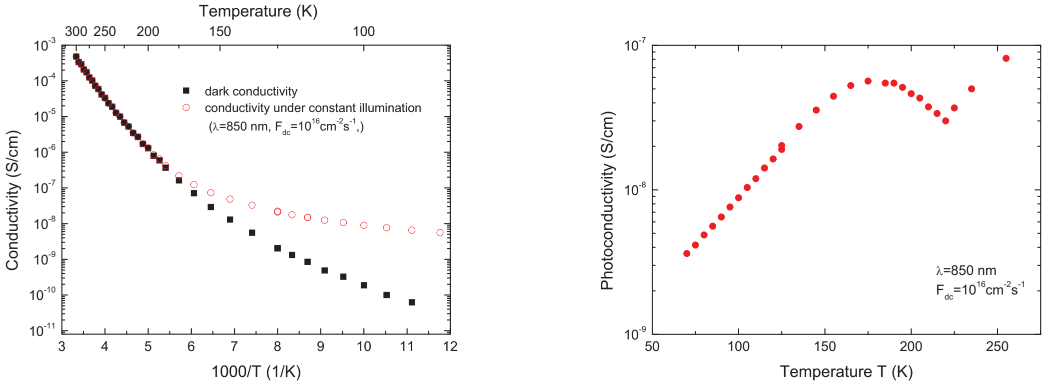

(a) Conductivity change on the exposure of light

(b) Photoconductivity

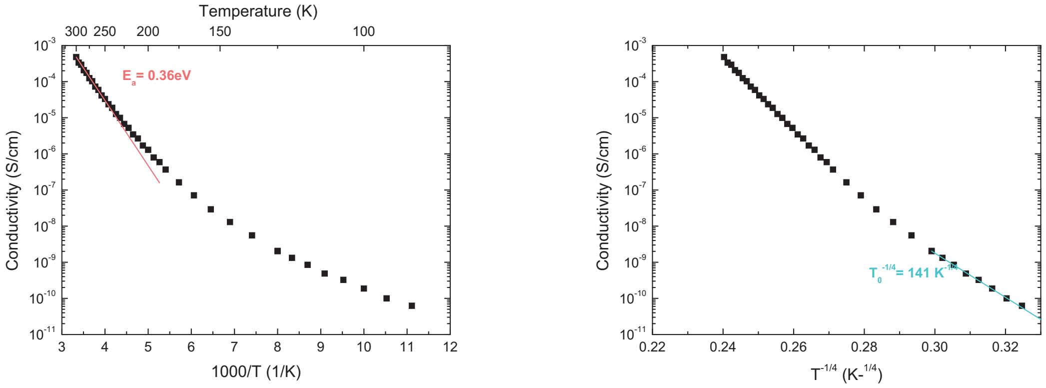

(c) Dark conductivity in Arrhenius Plot

(d) Dark conductivity in Mott's Plot

Figure 5.2: Conductivities measured in the dark and under constant illumination of the sample surface. A LED light source of wavelength $\lambda = 850\,\mathrm{nm}$ delivering a constant light flux of $F_{dc} = 10^{16}\,\mathrm{cm}^{-2}\mathrm{s}^{-1}$ was employed. Light exposure with given source shows to have a significant effect on the measured conductivity for temperatures below 175 K (a). This implies a large density of states at the Fermi level, i.e. a low splitting of the dark Fermi level as illustrated in Fig. 5.1. The photoconductivity is determined by the difference of the conductivity under illumination and dark conductivity (b). The photoconductivity first increases exponentially with increasing temperature and passes a maximum at $T_{max}175\,\mathrm{K}$. For temperatures higher than temperature T_{max} the the conductivity under constant illumination is no longer significantly larger than the dark conductivity. The same data of the measured dark conductivity are plotted in (a),(c) and (d). The Arrhenius plot shows clearly that no single activation energy exists in a-GeTe (c). This indicates a complex transport mechanism in amorphous phase-change materials. However, a-GeTe shows a good thermally activated behavior in the high temperature limit revealing an activation energy of $E_a = 0.36\,\mathrm{eV}$, which is approximately half of the optical band gap. Furthermore, Mott's variable range hopping models does not properly describe the dark conductivity data within the whole studied temperature range (d). Applying Mott's law to the data points obtained at lowest temperatures ranging from 90 K to 120 K, the characteristic temperature is determined to be $T_0^{1/4} = 141\,\mathrm{K}^{1/4}$. This characteristic temperature corresponds according to Eq. 5.13 to a defect density at the Fermi level of approximately $N(E_F) \approx 1 \cdot 10^{16}\,\mathrm{cm}^{-3}\mathrm{eV}^{-1}$ assuming a typical localization length of $\alpha = 2 \cdot 10^{-7}\,\mathrm{cm}$.

activation energy obtained in the high temperature range can be identified with the energetic distance of the valence band edge to the Fermi level at zero K temperature.
To analyze the dark conductivity under the view point of Mott's variable range hopping model, the same data are plotted versus $T^{-1/4}$, see Fig. 5.2 d. No good accordance to Mott's law can be observed within the whole probed temperature range. However, assuming that the data obtained at lowest temperatures ranging from 90 K to 120 K can be properly described by Mott's law, the density of states at the Fermi level $N(E_F)$ can be estimated from Eq. 5.13. Assuming a typical localization length of $\alpha = 2 \cdot 10^{-7}\,\mathrm{cm}$ the characteristic temperature $T_0^{1/4} = 141\,\mathrm{K}^{1/4}$ corresponds to a density of states at the Fermi level of the order $N(E_F) \approx 10^{16}\,\mathrm{cm}^{-3}\mathrm{eV}^{-1}$.

5.1.2 Photothermal Deflection Spectroscopy on a-GeTe

In general defect transitions induce only very weak optical absorptions. Consequently, optical transmission experiments can not be applied to investigate defect state densities within the band gap. Photothermal Deflection Spectroscopy proved to be a very sensitive method to investigate defect states. The PDS method exploits information from a thermally induced change in refractive index of a deflection medium surrounding the illuminated sample surface. Hence, Photothermal Deflection Spectroscopy is sensitive to all the possible optical transitions, which cause a heating of the sample surface.
In the vicinity of the band gap, disordered solids typically show an exponential dependent optical absorption with varying photon energy E. This behavior was first observed in alkali halide crystals and is known as the Urbach edge, [Urb53].

$$\alpha(E) = \alpha_0 \cdot \exp\left(\frac{E}{E_u}\right) \tag{5.15}$$

The Urbach energy E_u describes the exponential increasing absorption coefficient α and is typically $50 - 100\,\mathrm{meV}$. Since the Urbach edge seems to be a universal property in disorder materials, the underlying physics are expected to be both simple and general. However, in past decades the origin of the Urbach edge was heavily discussed in science. Some authors favor an explanation in terms of energy dependent matrix elements [DR72], whereas other scientist link the Urbach absorption edge to the exponentially decaying band tails in the density of states, [JSCE86]. Nowadays, a model favoring an explanation by changing matrix elements has been largely discarded. Currently, it is commonly accepted that the Urbach edge reflects the joint density of states and thus is closely linked to the shape of the valence and conduction band tail.

The absorption edge studied in a-GeTe via Photothermal Deflection spectroscopy at room temperature are shown in Fig. 5.3 for energies varied from $0.5\,\mathrm{eV}$ to $1.8\,\mathrm{eV}$. PDS spectra show typically saturation once all incoming light is absorbed within the thin film. This saturation depends on the film thickness and occurs for energies higher than $E = 1.2\,\mathrm{eV}$ in the $1\,\mu\mathrm{m}$ thick sample studied. For energies lower than $E = 1.2\,\mathrm{eV}$ the absorption coefficient describes a square root behavior reflecting the parabolic bands. Between $60\,\mathrm{cm}^{-1}$ and $1000\,\mathrm{cm}^{-1}$ the absorption coefficient shows an exponential dependence revealing an Urbach edge of $E_u =$

$68\,\mathrm{meV}$. However, even though expected from photoconductiviy measurements Photothermal Deflection Spectroscopy could not prove the existence of any deep gap states within the probed energy range. However, Photothermal Deflection spectroscopy performed in a lower energy range from 0.1 eV to 0.5 eV should be successful to detect defect levels.

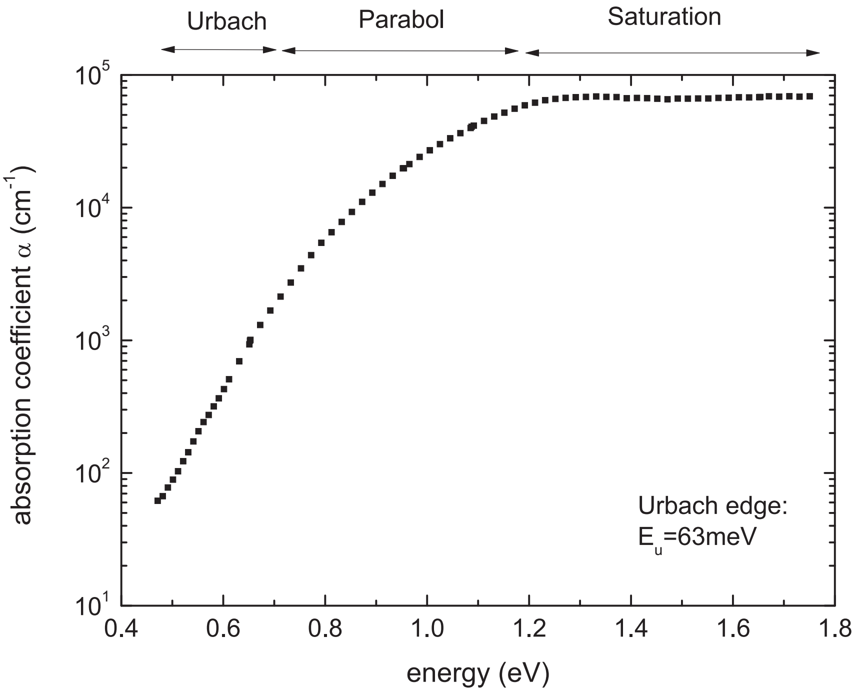

Figure 5.3: Absorption coefficient measured at room temperature on a $1\,\mu\mathrm{m}$ thick a-GeTe thin film employing Photothermal Deflection Spectroscopy. The measured absorption coefficient shows three characteristic regimes. For energies higher than $E = 1.2\,\mathrm{eV}$ the absorption coefficient saturates, since all the light illuminating the sample surface is absorbed within the sample. For lower energies the absorption coefficient shows a square root behavior reflecting the parabolic bands. Typically exponential dependence is observed for absorption coefficients ranging from $60\,\mathrm{cm}^{-1}$ and $1000\,\mathrm{cm}^{-1}$. The corresponding Urbach edge is $E_u = 68\,\mathrm{meV}$. Within the studied limits Photothermal Spectroscopy does not prove the existence of any deep gap states within the gap, which could be detectable at lower energies.

5.1.3 Modulated Photo Current Experiments performed on a-GeTe

Modulated Photo Current Experiments enable a spectroscopy of the defect state distribution within the band gap. These experiments link the trap state density to the photocurrent induced by a periodically modulated monochromatic light source illuminating the sample surface [OHE81]. Due to the interaction of generated charge carriers with localized trap states, the modulated photo current is not in phase with the excitation light. The defect density $N(E)$ can be experimentally derived from this phase shift ϕ and the photo current amplitude $|I_{ac}|$, [BMBR90, LK92]:

Basic formula of the Modulated Photo Current method

$$\frac{c_p\,N(E_\omega)}{\mu_p} = \frac{2}{\pi k_b T} A\,q\,\epsilon\,G_{ac} \frac{sin(\phi)}{|I_{ac}|} \tag{5.16}$$

Classic energy scaling given by:

$$E_\omega - E_v = k_b T\,ln\left(\frac{\nu_p}{\omega}\right) \qquad \textit{(hole controlled behavior)} \tag{5.17}$$

The constants on the left hand side in Eq. 5.16 are well known from optical measurements and the MPC experiment itself. The parameter ϵ denotes the electric field applied to the parallel electrodes and q describes the elementary charge. The conduction cross section A, the product of the film thickness d and the electrode length l, can be adjusted by the chosen sample geometry. The amplitude of the light intensity modulated with an angular frequency ω and the optical absorption of the material under investigation determine the ac generation rate of free carriers G_{ac}.

Eq. 5.16 is only valid as long as multiple trapping and release processes dominate the electronic transport. Consequently, the MPC method gives only reliable results for trap states acting as multiple trapping centers. Trap states, in which captured carriers recombine instead of being re-emitted to the bands can not be analyzed via Eq. 5.16. Thus, the energy range probed by MPC experiments is limited. For a very low splitting of the dark Fermi level illustrated in Fig. 5.1, the probed energy ranges from one band edge to the dark Fermi level at the most.

In p-type materials, such as a-GeTe, the energetic position E_ω given in Eq. 5.17 is defined by the classic energy scaling, i.e. $e_p(E_\omega) = \nu_p \cdot [E_\omega - E_v/k_b T] = \omega$, [OHE81, BMBR90].

Whereas the capture coefficient c_p describes the ability of a trap state to capture a free hole from the valence band, the attempt-to-escape frequency ν_p describes the release process of a hole trapped in a state beyond the valence band edge. The attempt-to-escape frequency ν_p can not be determined by experiment, but an order of magnitude can be derived within the analysis of MPC data, [LKK+99].

The combination of Eq. 5.16 and Eq. 5.17 enables a spectroscopy of the relative density Nc/μ by measuring couples of $(\phi, |I_{ac}|)$ at different excitation frequencies ω and temperatures T. Additionally, the absolute density of states $N(E)$ can be derived from the measured MPC spectra as long as the free hole mobility μ_p and the capture coefficient c_p are known.

Modulated Photo Current experiments have been widely employed to study the evolution of mid gap states in photovoltaic materials, such as hydrogenated amorphous silicon (a-Si:H), [ZC93, SB89, Kou01, HWS94, HAA+94, KSA02, BKL+00, PCYG00, LKC00].
Even though the photoconductivity is much lower in amorphous phase-change materials, Modulated Photo Current experiments proved to be a very successful method to investigate the defect state distribution within the band gap in a-GeTe [Luc08, LKS+10].
Modulated Photo Current measurements were performed on a-GeTe thin films deposited by dynamic sputtering. The results are shown in Fig. 5.4. To check reproducibility, samples were deposited on different substrates in different sputter processes under the same deposition conditions. The X-ray patterns of all thin films, measured in grazing incidence geometry, showed broad peaks indicating that the obtained materials were amorphous after deposition. Modulated Photo Current experiments were performed on each sample employing the same generation conditions. A monochromatic light source of wavelength $\lambda = 850\,\mathrm{nm}$ was employed. The chosen wavelength corresponds to a photon energy of 1.45 eV being significant larger than the optical band gap of a-GeTe, which is approximately 0.8 eV at 300 K. To ensure a good signal to noise ratio the dc part of the modulated light flux was adjusted to $F_{dc} = 10^{16}\,\mathrm{cm}^{-2}\mathrm{s}^{-1}$. The amplitude of the alternating photon flux is chosen to be 40% of the continous flux F_{dc}. At fixed temperatures, couples of $(\phi, |I_{ac}|)$ were measured by varying the excitation frequency $f = \omega/2\pi$ from $12\,\mathrm{Hz}$ to $40\,\mathrm{kHz}$. With Eq. 5.16 and Eq. 5.17 the corresponding density of states Nc/μ and their energetic position E_ω within the band gap are determined. In Fig. 5.4 each MPC curve taken at a fixed temperature with varying excitation frequency is indicated by a certain symbol. At a fixed temperature energy states closer to the valence band edge were probed with $40\,\mathrm{kHz}$ while states the furthest away from the band edge are probed with $12\,\mathrm{Hz}$. The temperature steps have to be chosen sufficiently small, since only the envelope of superimposing MPC curves reveals the density of states. The temperature steps were chosen to be at the most 20 K and if necessary to obtain a good data resolution even as low as 2 K. According to Eq. 5.17 MPC curves taken at different temperatures do not superimpose if a wrong attempt-to-escape frequency ν_p is assumed to calculate the energy scale. In the case that the attempt-to-escape frequency ν_p is chosen too large MPC curves show no overlap and if the ν-value is taken too low, they cross each other. Consequently, an order of magnitude of the attempt-to-escape frequency ν_p can be determined by maximizing the overlap of MPC curves taken at different temperatures. Thereby, it is possible that the MPC curves describing different kind of defects within the band gap scale with different attempt-to-escape frequencies ν_p, which is the product of the equivalent density at the valence band edge N_v and the capture coefficient c_p, i.e. :

$$\nu_p = N_v \cdot c_p \tag{5.18}$$

Consequently, the larger the capture coefficient c_p the higher is the attempt-to-escape frequency ν_p. Hence, a large value of the attempt-to-escape frequency ν_p reflects a strong interaction between defect states and free holes.

In Fig. 5.4 MPC spectra taken on three a-GeTe samples, each deposited on a different substrate demonstrate all the same characteristic features. In all three samples the observed defect state density shows a valence band tail, a shallow defect and deep defect levels near mid gap.

The valence band tail

The valence band tail is probed at low temperatures between 60 K and 220 K. The overlap of MPC curves describing the valence band tail is maximized for an attempt-to-escape frequency $\nu_p = 10^{12}\,\mathrm{s}^{-1}$. Different MPC curves overlap only in the high frequency range. The lower the frequency ω of the modulated light source the larger is the deviation from the envelope. In the next section of this chapter it is shown, that this deviation at low excitation frequency mostly vanishes if the temperature dependence of the band gap is taken into account.

The shallow defect

In the temperature ranging from 230 K to 250 K a shallow defect is probed. The MPC curves describing this shallow defect do not superimpose with an attempt-to-escape frequency $\nu_p = 10^{12}\,\mathrm{s}^{-1}$. A much lower value of $\nu_p = 2.5 \cdot 10^{8}\,\mathrm{s}^{-1}$ has to be assumed in the classical energy scaling procedure to maximize the overlap. In general we expect attempt-to-escape frequencies in the range of phonon frequencies. Consequently, such low values of the attempt-to-escape frequency seem to be unphysical, but are commonly reported in literature for other materials, too [OTY+82]. In the next section of this chapter it will be shown, that such low values of the attempt-to-escape frequency derived by the classical energy scaling procedure using Eq. 5.17 can be a consequence of neglecting the temperature dependence of the band gap. Considering the influence of a temperature dependent band gap on the MPC energy scale, the shallow defect scales with a much higher attempt-to-escape frequency of $\nu_p = 10^{10}\,\mathrm{s}^{-1}$. However, a temperature dependent band gap has no influence on the value of the observed relative density Nc/μ. In the three investigated samples, the maximal observed defect density of the shallow defect varies by one order of magnitude from $Nc/\mu = 10^{10}\,\mathrm{cm}^{-2}\mathrm{VeV}^{-1}$ to $10^{11}\,\mathrm{cm}^{-2}\mathrm{VeV}^{-1}$.

Deep defect levels

MPC curves taken at temperatures from 260 K to 300 K describe a deep defect level, which shows a rather high concentration of approximately $Nc/\mu \approx 10^{11}\,\mathrm{cm}^{-2}\mathrm{VeV}^{-1}$ in all three samples. The spectra derived in the high temperature limit are rather noisy. The shown mid gap states are scaled with an attempt-to-escape frequency of $\nu_p = 10^{12}\,\mathrm{s}^{-1}$. Later on we will see that this attempt-to-escape frequency describes the deep defect levels still properly, if the influence of a temperature dependent band gap is taken into account.

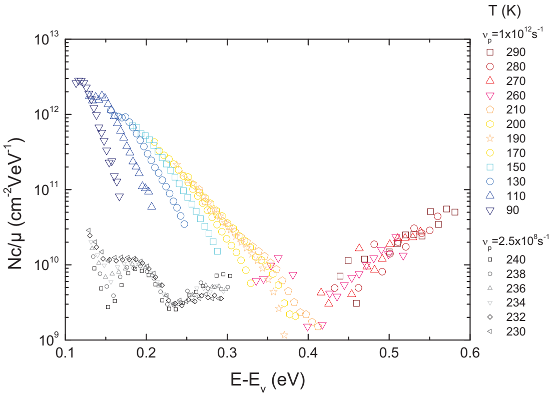

(a) Sapphire substrate

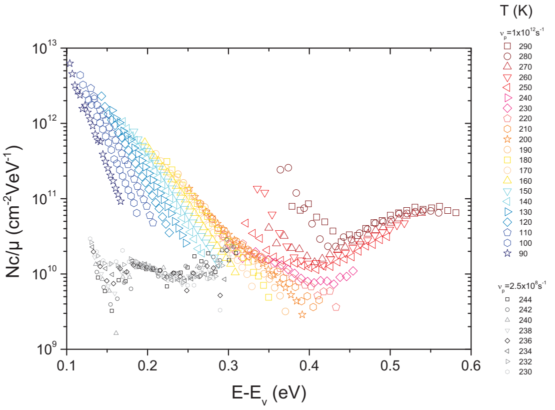

(b) Corning glass substrate

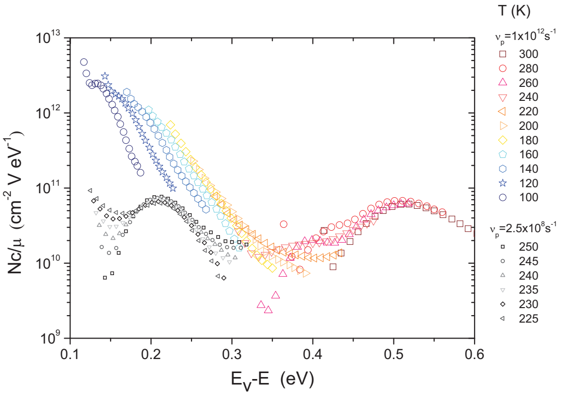

(c) Menzel glass substrate

Figure 5.4: MPC spectra measured on amorphous deposited GeTe samples. Each sample was deposited on a different substrate in different processes under same sputtering conditions. All the samples show the same characteristic features: the valence band tail probed from 90 K to 220 K, a shallow defect probed from 230 K to 250 K and deep defect levels probed from 260 K to 300 K. The valence band tail states and the deep defect levels are described by an attempt-to-escape frequency $\nu_p = 10^{12}\,\mathrm{s}^{-1}$, whereas in the presented classical energy scale defined by Eq. 5.17, the shallow defect scales with a much lower value $\nu_p = 2.5 \cdot 10^8\,\mathrm{s}^{-1}$.

Conclusion

The shallow defect and the deep defect have very different attempt-to-escape frequencies. The low ν_p value describing the shallow defect reflects the very low interaction of free carriers with these defect levels. In contrast, the interaction between free carriers and valence band tail states or deep defect levels is rather strong. At the first glance it seems surprisingly that the shallow defect can be probed at all, since its defect density Nc/μ is much lower than the defect density of the valence band tail. The detection of the shallow defect by the MPC technique is only possible, because the corresponding attempt-to-escape frequency is significantly lower than those describing the valence band tail states. Consequently, valence band tail and shallow defect states respond in a different temperature range. This enables to reveal the existence of the shallow defect via MPC. However, PDS detects all possible optical transitions. The contribution to the PDS signal arising from the shallow defect, whose interaction with photo carriers is very low, is negligible in comparison to the strong absorption of photo carriers by the tail states. However, the deep defect levels showing a strong interaction with photo carriers are expected to contribute to the PDS signal. Since these states lie close to mid gap these states should be probably detected around 0.4 eV. This energy lies beyond the studied energy range of PDS data presented in Fig. 5.3.

5.1.4 Influence of a temperature dependent band gap on the energy scale of Modulated Photo Current experiments

In the classical MPC energy scaling expressed by Eq. 5.17 the band edge energies are assumed to be independent of temperature. Nevertheless, it is quite a common feature in crystalline and amorphous materials as well, that the band gap displays a clear temperature dependence [VAR67, SK07b].

In MPC experiments the density of states is constructed out of MPC curves taken at different temperatures. Hence, the classical MPC energy scaling procedure according to Eq. 5.17 will be prone to inaccuracy in materials showing a strongly temperature dependent band gap. The goal of this section is to discuss the influence of a temperature dependent band gap on the MPC energy scale in amorphous phase-change materials and amorphous hydrogenated silicon.

Temperature dependent band gaps

Variation of band gaps as a function of temperature are commonly observed in crystalline and disordered materials. The optical band gap of most semiconductors decreases with increasing temperature. Empirically the temperature dependence of the optical band gap E_g was found to follow the relation,

$$E_g(T) = E_g(0) - \frac{\eta T^2}{T + \beta}. \tag{5.19}$$

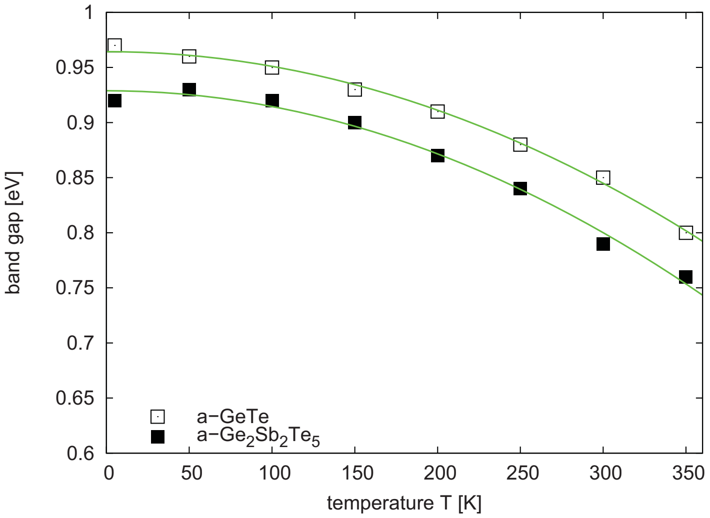

Figure 5.5: Optical band gap of a-GeTe and a-$Ge_2Sb_2Te_5$ measured by FT-IR at different temperatures T varied from 5K to 350K. To define a band gap in an amorphous system the E_{04} method is applied. In this method the optical band gap is identified as the energy at which the absorption coefficient $\alpha(E)$ equals $10^4\,\mathrm{cm}^{-1}$. Both phase-change alloys show a strong decrease of the optical band gap with increasing temperature. The measured temperature dependence is reversible and is properly described by the simplified Varshni formula describing the low temperature limit ($T << \beta$). Image taken from [LKK+11]

where η and β are material dependent constants. Eq. 5.19 is known as the empiric Varshni law and describes an optical band gap decreasing parabolically at low and linearly at high temperatures. Values for η and β reported in literature for different amorphous and crystalline materials are listed in Tab. 5.1.

The temperature dependence of the optical band gap in amorphous phase-change materials are measured by FT-IR technique in reflectance mode. The wavenumber of the incident beam illuminating the sample surface has been varied from $350\,\mathrm{cm}^{-1}$ to $8000\,\mathrm{cm}^{-1}$. These wave numbers in the mid-infrared range correspond to photon energies E from $0.04\,\mathrm{eV}$ to $1\,\mathrm{eV}$. The optical band gap has been derived from the modulated absorption spectra $\alpha(E)$ according to the E_{04} method, i.e. the energy at which the absorption coefficient α equals $10^4\,\mathrm{cm}^{-1}$ is identified with the optical band gap, i.e. $E_g = E_{04}$. The optical band gaps measured for a-GeTe and a-$Ge_2Sb_2Te_5$ varying the temperature from 5K to 300K are shown in Fig. 5.5.
In both alloys the optical band gap decreases by more than 150 meV upon increasing the temperature from 5 K to 350 K. The temperature dependence in both alloys can be properly described by the simplified form of the Varshni formula,

$$E_g(T) = E_g(0) - \xi T^2, \tag{5.20}$$

This simplified Varshni formula is valid in the low temperature limit, i.e. $T << \beta$ where ξ is equal to η/β.

The values $E_g(0)$ and ξ derived for amorphous and crystalline phase-change materials in comparison to other materials known from literature are listed in Tab. 5.1. According to Tab. 5.1 the band gap in amorphous chalcogenides shows a strong decrease with increasing temperature. In contrast, amorphous and crystalline silicon belong to the materials showing low temperature dependencies of the optical band gap. For example the band gap in a-GeTe shrinks by more than 10%, whereras the band gap of amorphous silicon decreases only by 3%. In the following the influence of temperature dependent band gaps on the MPC energy scale is discussed and exemplified in a-GeTe and a-Si:H.

Table 5.1: List of the coefficients involved in the empirical Varshni law describing the temperature dependent band gap in diamond and common semiconductors (top), amorphous chalcogenides (middle) and phase-change materials (bottom). The approximate ξ coefficient describing the low temperature limiting case are also given.

Material	$E_g(0)$ (eV)	η (meV/K)	β (K)	$\xi = \eta/\beta$ 10^{-6} eV/K^2	Reference
Diamond	5.4125	-0.1979	-1437	0.14	[VAR67]
c-Si	1.169	0.49	655	0.75	[SK07b]
a-Si	1.1495	0.494	646.6	0.76	[DNKL+92]
a-Si:H	1.81	16.8	16500	1.02	[FP79]
a-As_2S_3	2.56	0.94	202.8	4.64	[TTN+00]
a-As_2Se_3	1.99	0.77	142	5.42	[TTN+00]
a-$GeSe_2$	2.24	0.92	180	5.11	[TTN+00]
a-Se	2.13	0.95	135	7.04	[TTN+00]
c-$Ge_{50}Te_{50}$	0.78	-	-	0.445	[Kre09]
a-$Ge_{50}Te_{50}$	0.96	-	-	1.325	[LKK+11]
c-$Ge_2Sb_2Te_5$	0.59	-	-	0.605	[Kre09]
a-$Ge_2Sb_2Te_5$	0.93	-	-	1.43	[LKK+11]

Introducing correction terms to the classic MPC energy scaling procedure to take the temperature dependent band gaps into account

Brüggemann *et al.* showed that the modulated photocurrent is dominated by traps at the energy E_ω whose emission rate $e(E_\omega)$ is equal to the angular frequency ω of the modulated light flux [BMBR90, LK92].
The trapping and emission rates of carriers captured from the bands into trap states at energy E determine the alternating photocurrent I. The amplitude $|I_{ac}|$ is fixed by the trapping rate, while the phase shift ϕ between photocurrent and excitation light is fixed by the temperature dependent emission rate $e(E,T)$. It was shown by Brüggemann *et al.* that only those traps releasing carriers at the same frequency as the excitation ω can induce a phase shift ϕ. Consequently, the influence of energy levels $E \neq E_\omega$ on the alternating photocurrent is small. Resulting from the relation $e(E_\omega) = \omega$ the classic MPC energy scaling is derived from the emission rate for trapped holes: $e_p(E) = \nu_p \exp[-(E_\omega - E_v)/k_bT]$. Likewise, the emission rate $e_n(E) = \nu_n \exp[-(E_c - E_\omega)/k_bT]$ describes the release of trapped electrons. Obviously, the classical MPC energy scale neglects temperature dependent band edges. In the following it is demonstrated that the temperature dependence of the band gap can be considered by adding correction terms to the classic energy scale. Correction terms for p-type amorphous phase-change materials and n-type hydrogenated amorphous silicon and their influence on the MPC energy scale are discussed.

Correction terms to the classic MPC energy scale for a-GeTe

Typically hole conduction dominates in amorphous phase-change materials, such as a-GeTe and a-$Ge_2Sb_2Te_5$. Hence, the classical energy scaling in these p-type materials is defined as,

classical energy scale

$$E_\omega = E_v + k_bT\ln(\nu_p/\omega). \tag{5.21}$$

Both phase-change alloys show a strong decrease in the optical band gap E_{04} with increasing temperature. To measure the temperature dependence of the energetic distance from the Fermi level E_F to the edge of majority carriers E_v thermoelectric Seebeck measurements have been performed [Jos]. These measurements can be interpreted in a way that the observed decrease in band gap results from a shift of states related to the valence band edge towards a fixed conduction band. Consequently, the energy position of states related to the valence band changes with temperature according to,

$$E_v(T) = E_v(T = 0K) + \xi T^2, \tag{5.22}$$

In consequence of Eq. 5.22 MPC curves taken at a different temperatures T do not refer to the same zero point in energy. In order to consider the shift of the zero point with temperature MPC curves need to be rescaled in the MPC energy scaling procedure. Two different methods are proposed to define the same origin $E_v(T = 0K) = 0$. The proposed rescaling methods differ in the assumptions made on the energetic position of trap states within the decreasing energy band gap. Indeed, no references on this issue are reported in literature.

However, on one hand one may consider that the decrease in band gap resulting from extended states moving closer to the fixed conduction band leaves the energy positions of the defects within the gap unchanged. In this situation MPC curves can be simply rescaled to the same energy zero point by subtracting the term ξT^2 from the classical energy scaling formula 5.21 . This ξ-corrected energy scale results in Eq. 5.23.

On the other hand, one may consider that the shrinking of the gap results in a modification of the trap position proportional to their initial positions at 0 K, i.e., states near the valence band edge shift by the full correction term $-\xi T^2$ and mid gap states only by $0.5 \cdot \xi T^2$. In this second case, the correction is made prorata to the energy position of the traps resulting in Eq. 5.24.

ξ corrected energy scale

$$E - E_v|_{\mathit{rescaled}} = k_b T \ln(\nu_p/\omega) - \xi T^2, \tag{5.23}$$

prorata corrected energy scale

$$E = E_v + \frac{k_b T \ln(\nu_p/\omega) - \xi T^2}{1 - \xi T^2/E_{04}(0)}. \tag{5.24}$$

Both formulas 5.23 and 5.24 are valid for trapping states located at E_ω exchanging carriers with the valence band extended states.

Correction terms to the classic MPC energy scale for a-Si:H

Amorphous hydrogenated silicon belongs to the class of n-type conductors. The classical MPC energy scale in n-type materials is given by,

classical energy scale

$$E_\omega = E_c - k_b T \ln(\nu_n/\omega). \tag{5.25}$$

In a-Si:H the temperature dependence of the band gap is properly described by the empirical Varshni law. Consequently, we derive similar correction terms like already discussed above for amorphous phase-change materials. Under the assumption that the decrease of the observed optical band gap in a-Si:H results from a conduction band shifting towards a fixed valence band leaving the trap state position within the band gap unchanged to their original position, one has:

Varshni corrected energy scale

$$E_c - E = k_b T \ln(\nu_n/\omega) - \frac{\eta T^2}{(T+\beta)}. \tag{5.26}$$

In the case that trap states change their energetic position within the band gap prorata one obtains,

prorata corrected energy scale

$$E_c - E = \frac{k_b T \ln(\nu_n/\omega) - \eta T^2/(T+\beta)}{1 - \eta T^2/(E_{04}) \cdot (T+\beta)}. \tag{5.27}$$

The efficacy of the proposed correction terms within the analysis of Modulated Photo Current Experiments is illustrated on the example of a-GeTe and a-Si:H.

Efficacy of the proposed correction terms on a-GeTe

The effect of the temperature dependent band gap in a-GeTe is illustrated in Fig. 5.6 on the MPC spectrum already shown in Fig. 5.4a. In Fig. 5.6 the same density of states Nc/μ is displayed in the classical (a), the prorata corrected (b) and the fully ξ corrected energy scale (c). The proposed correction terms have been calculated using the parameters listed in Tab. 5.1. The defect state density observed in a-GeTe shows three kind of defects: valence band tail states, shallow defect states and mid gap states. The influence of a temperature dependent band gap by adding correction terms to the classical energy scale is discussed for valence band tail states and deep defect levels.

First the effect of the proposed correction terms on the MPC spectra is discussed for valence band tail states. MPC curves describing the valence band tail are derived from temperatures varied between 100 K and 200 K in 20 K steps. In the classical energy scaling procedure, MPC curves taken at different temperature superimpose only in a few data points obtained at high modulation frequencies. Data points obtained with low excitation frequencies depart significantly from the envelope. It is shown that this deviation at low frequencies is probably caused by neglecting the temperature dependence of the energy band gap.
Because of the small overlap in the classical energy scale, it is difficult to extract the exact value of the attempt-to-escape frequency v_p. Within the MPC analysis the ν_p value is adjusted by maximizing the overlap of MPC curves taken at different temperatures. The parts of MPC curves obtained at high frequencies superimpose rather well for attempt-to-escape frequencies v_p ranging within one order of magnitude, namely from $\nu_p = 5 \cdot 10^{11}\,\mathrm{s}^{-1}$ to $5 \cdot 10^{12}\,\mathrm{s}^{-1}$. MPC curves would cross each other for lower ν_p values, whereas a scaling with higher ν_p values would not lead to any common points. For this reason the valence band tail in the classical energy scale is plotted using a mean value of $1 \cdot 10^{12}\,\mathrm{s}^{-1}$.

In both corrected energy scales the overlap of MPC curves taken at different temperatures significantly improves, especially at low frequencies. Due to the maximized overlap the attempt-to-escape frequency ν_p is adjustable and is found to be $1 \cdot 10^{12}\,\mathrm{s}^{-1}$. Furthermore, in both corrected energy scales the valence band tail approximates a straight line in the chosen semi logarithmic plot. This suggests that the valence band decays exponentially in a-GeTe according to,

$$N_{\mathrm{VBT}} = N(E = E_v) \cdot \exp(-E/E_w) \tag{5.28}$$

Exponentially decaying band tails are commonly reported in literature for disordered materials [IL02]. The band width E_{wv} describing the exponential decay of the valence band is determined from the ξ corrected MPC spectrum to be E_{wv}=33 meV and E_{wv}=41 meV in the classical energy scale. Hence, the Urbach energy derived to E_u=63 meV is mainly governed by the conduction band tail giving a width of $E_{wd} \approx$ 60 meV.
The shallow defect is probed in a temperature range varied from 220K to 250 K. In this temperature range the MPC spectrum exhibits a bell-shaped peak with a clear maximum. In each energy scale defined by Eqs. 5.21, 5.23, 5.24 these MPC curves taken at different measurement temperatures superimpose, if a correct value for the attempt-to-escape frequency ν_p is chosen. The ν_p-value reflects the interaction between free carriers and defect states, i.e, the higher its value the stronger is the interaction through trapping and release processes. In the classical treatment, the superposition of different MPC spectra describing the shallow defect is obtained for an attempt-to-escape frequency of $\nu_p = 2.5 \cdot 10^{-8}\,\mathrm{s}^{-1}$, a rather low value since, values for ν_p are expected to be in the range of phonon frequencies, i.e. $10^{12}\,\mathrm{s}^{-1} - 10^{13}\,\mathrm{s}^{-1}$. However, such low values for the attempt-to-escape frequency of the order $10^{-8}\,\mathrm{s}^{-1}$ have been reported in literature for amorphous silicon, too. The origin of such unphysical low ν values have been heavily discussed. However, the observation of such low values for the attempt-to-escape frequency could be a consequence of a temperature dependent energy band gap. If the temperature dependence of the band gap is neglected, i.e. no correction term is subtracted to define the same energy zero point, MPC curves are shifted towards mid gap with increasing temperature. Within the MPC analysis, this shift resulting from a temperature dependent band gap, can be counteracted by assuming a lower value for the attempt-to-escape frequency, see 5.21. Consequently, in materials showing a strongly temperature dependent energy band gap the observation of very low attempt-to-escape frequencies is very likely, if the classical energy scale is employed. In fact, the shallow defect is described by a much higher value of the attempt-to-escape frequency $\nu_p = 1{\cdot}10^{-10}\,\mathrm{s}^{-1}$ in both corrected energy scales.

Mid gap states are observed from 260 K to 290 K. In all three proposed energy scales these MPC curves superimpose adjusting ν_p to $1 \cdot 10^{12}\,\mathrm{s}^{-1}$. However, mid gap states reach 0.55 eV from the valence band edge into the gap in the classical energy scale. As mentioned before, the measurement window of MPC measurements is limited. In p-type semiconductors mostly trap states lying within the energy range between the valence band edge E_v and the dark Fermi level E_F can be probed. In p-type materials, the energy region from the Fermi level to the conduction band edge can not be probed with the MPC technique. Consequently, the classical energy scale suggests a dark Fermi level $E_F(300K)$ positioned at least 0.55 eV away from the valence band edge. The optical band gap measured at room temperature is ≈ 0.8 eV. As long as mobility band gap and optical band do not differ drastically, MPC measurements analyzed in the classical energy scaling procedure suggest a dark Fermi level $E_F(300K)$ positioned nearer to the conduction than to the valence band edge. However, thermoelectric Seebeck measurements performed at the I. Physical Institute RWTH Aachen clearly prove that hole conduction dominates in a-GeTe at 300 K [Jos]. The p-type character in a-GeTe is also commonly reported by various groups in literature. Initially this possible contradiction observed in amorphous phase-change materials pushed forward a revision of the classical energy scaling of MPC data. Indeed, both proposed correction terms taking the temperature dependence of the band gap into account contract the energy scale. Consequently, mid gap states shift closer to the valence band edge. In the fully ξ-corrected energy scale mid gap states reach only 0.45 eV into the energy gap. This seems to be a more realistic energy position of mid gap states. Hence, the influence of a temperature dependent energy gap on the MPC energy scale solves the possible contradiction regarding MPC data and p-type conductivity in amorphous phase-change materials.

Efficacy of the proposed correction terms on a-Si:H

Hydrogenated amorphous silicon has been widely studied by the MPC technique. Its band gap varies only slightly with temperature. According to Tab. 5.1 the band gap decreases by 5$\%$, while increasing the temperature from 0 to 300 K.

In the last section the efficacy of corrected energy scales has been discussed for a-GeTe, where the band gap changes by more than 10$\%$. This section discusses the influence of a temperature dependent gap in intrinsic a-Si:H. Details on the deposition conditions can be found in Ref. [LSK06] (sample 310031). Taking the data from Ref. [LSK06] the MPC-DoS Nc/μ has been calculated. The classical energy scale has been derived from Eq. 5.25. The corrected energy scales have been calculated according to Eq. 5.26 and Eq. 5.27.

The purpose of this section is not to study a-Si:H very closely, but to investigate the influence of the proposed correction methods on MPC spectra reported in literature. The results are presented in Fig. 5.7. The two correction methods lead to very close MPC DoS because the correction is very small.

In the present example, two different dc fluxes (with F_{ac}/F_{dc} = 2/5) in two different temperature ranges were used. Indeed, even though a high flux ensures a good signal to noise ratio, it also generates a large recombination zone in the middle of the gap. The width of this recombination zone is also influenced by the defect density: the lower the trap state density the wider the recombination zone. The MPC technique in a-Si:H is only sensitive to empty trapping states. Especially for high fluxes, states answering the modulation at high temperatures or low excitation frequencies may be located in the recombination zone, where the analysis of MPC data by formula 5.16 is no longer valid. Consequently, trap states lying in the recombination zone can not be properly detected by the MPC technique. With increasing frequency, the MPC technique probes states closer to the extended states, i.e. farther away

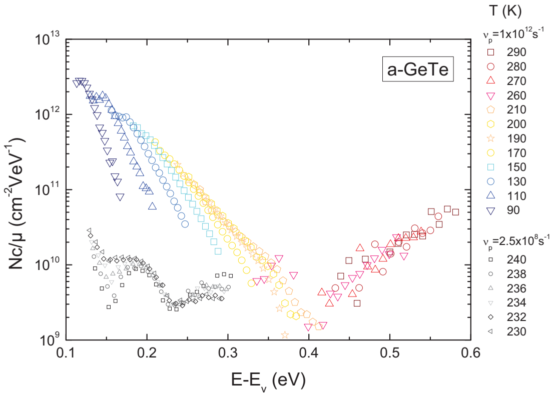

(a) Classical energy scale

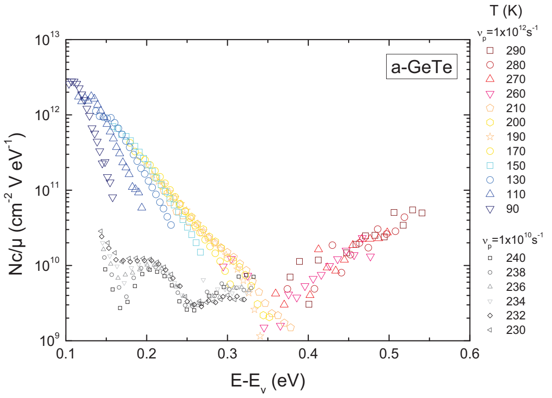

(b) Prorata corrected energy scale

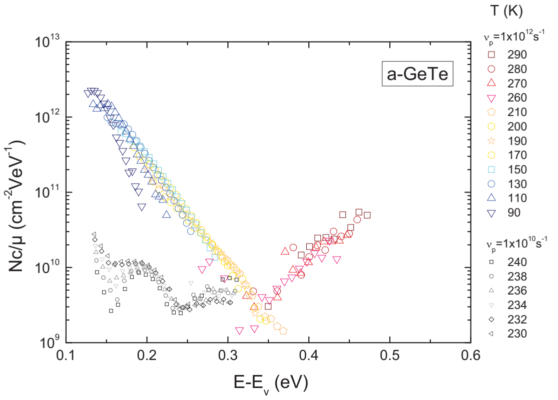

(c) ξ-corrected energy scale

Figure 5.6: DoS spectroscopy achieved by the MPC technique applied to a-GeTe. The energy scaling was calculated following the classical (a), the the pro rata corrected (b) and the fully ξ-corrected method (c). Both correction terms contract the MPC energy scale. Consequently, mid gap states shift closer to the valence band edge. Shallow defect states scale with a much higher attempt-to-escape frequency $\nu_p = 1 \cdot 10^{-10}\,\mathrm{s}^{-1}$ in both corrected energy scales. Furthermore, band tail states approximate a straight line in the semi logarithmic plot. This suggests that the valence band decays exponentially in a-GeTe.

from the recombination zone. Hence, the response of the system corresponds to the real defect state density. That is why the flux has to be kept as low as possible, while keeping a good signal to noise ratio. A criterion for the measurement quality is the presence of a maximized overlap of MPC curves obtained at different temperatures, especially at high frequencies. These parts of the spectra are expected to correspond to the probed true defect density and, therefore, are supposed to fit together for slightly different temperatures. In a-Si:H temperature steps of 30 K have proven to be sufficiently small.

The MPC data presented in Fig. 5.7 are recorded over a large temperature range varied from 120 K to 450 K. The MPC spectrum measured in a-Si:H shows conduction band tail and deep defect states scaling with $\nu_n = 1 \cdot 10^{12}\,\mathrm{s}^{-1}$. The low density of deep states could be resolved using a low flux $F_{dc} = 2 \cdot 10^{12}\,\mathrm{cm}^{-2}\mathrm{s}^{-1}$. This low flux is needed to minimize the influence of the recombination zone. To detect conduction band tail states it was necessary to improve the signal to noise ratio of MPC measurements by increasing the flux to $F_{dc} = 1 \cdot 10^{14}\,\mathrm{cm}^{-2}\mathrm{s}^{-1}$. The influence of the flux on the MPC spectrum is clearly demonstrated by those MPC curves obtained at the same temperature using these two different fluxes. The deviation of data points from the envelope is clearly enhanced with increasing flux. However, for the conduction band tail it seems completely unrealistic that the deviation from the envelope results from the widening of the recombination zone, since its broadening is limited by the exponential increase of tail states. Another explanation of the observed deviation at low excitation frequency would be the influence of hopping conduction. Indeed, literature reports that hopping conduction induces a deviation from the MPC envelope at low excitation frequency. However, in the case of a-Si:H, hopping transport starts to be important for temperatures below 100 K and the MPC curves displayed in Fig. 5.7 has been recorded for temperatures above 120 K [LT].
For these reasons an explanation attributing the observed mismatch to the neglected temperature dependence of the band gap is favourable. The optical band gap in a-Si:H decreases with temperature according to the empiric Varshni law, see Eq. 5.19. The MPC spectra shown in Fig. 5.7 have been plotted in the classical , the pro rata corrected and the fully ξ corrected energy scale. In both corrected energy scales the overlap of MPC curves taken at different temperatures is significantly increased in the whole investigated temperature range. The best superimposition of MPC curves is obtained employing a prorata corrected energy scale.

The results presented in Figs. 5.10 and 5.7 clearly demonstrate that disregarding the temperature dependence of the band gap may lead to wrong interpretations of MPC data. In summary, corrected MPC energy scaling procedures significantly improve the data interpretation and enables a more sophisticated study of defect state densities measured by Modulated Photo Current experiments.

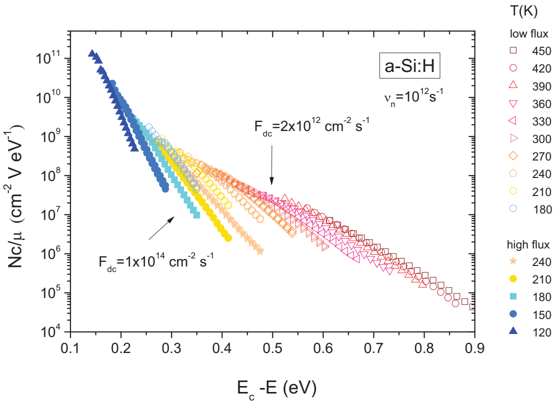

(a) Classical energy scale

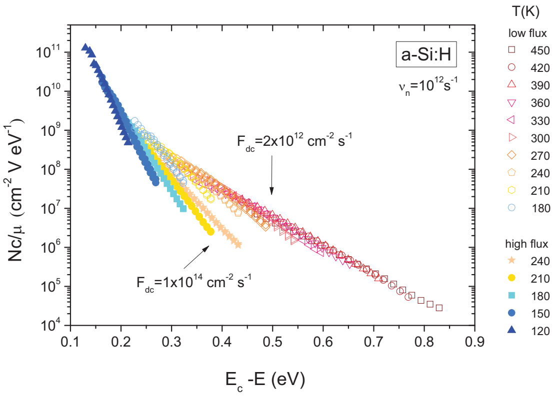

(b) Pro rata corrected energy scale

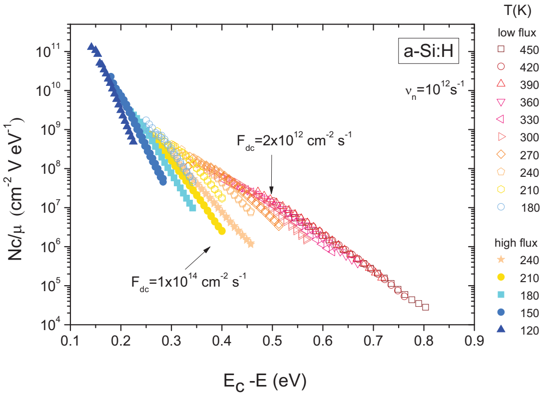

(c) ξ-corrected energy scale

Figure 5.7: Influence of a temperature dependent band gap in a-Si:H. MPC measurements have been performed using different fluxes; $F_{dc} = 1 \cdot 10^{14}\,\text{cm}^{-2}\text{s}^{-1}$ to resolve conduction band tail states (full symbols) and $F_{dc} = 2 \cdot 10^{12}\,\text{cm}^{-2}\text{s}^{-1}$ to study deep defect levels (open symbols).
The MPC DoS derived for a-Si:H is shown in the classical (a), the pro rata corrected (b) and the fully Varshni-corrected (c) energy scale . In all three energy scaling procedures an attempt-to-escape of $\nu_n = 1 \cdot 10^{12}\,\text{s}^{-1}$ has been taken. In the classical energy scale data points obtained with low excitation frequency largely deviate from the envelope of superimposing MPC curves. This deviation significantly reduces in both corrected energy scales, in which the temperature dependence of the band gap has been taken into account. Image taken from [LKK⁺11]

5.2 Study of photoconductivities and defect state densities in switchable chalcogenide glasses

Electrically switchable materials show a strongly enhanced amorphous state conductivity for electric fields above a critical value. In fact, electrical threshold switching behavior is observed in many chalcogenide glasses.

Previous studies have shown that the critical threshold field is influenced by the optical band gap. In Fig. 5.8 the electrical threshold fields of amorphous deposited materials are compared to their optical band gap measured at 300 K. Materials having a very low band gap value such as $Ge_{15}Sb_{85}$ and AgInSbTe show also low electric threshold fields. However, a correlation solely on the band gap value is not possible for $Ge_2Sb_2Te_5$ and $Ge_{15}Te_{85}$. Furthermore, a threshold field of 143 V/μm has been reported recently for amorphous deposited GeTe [RCD⁺11]. The optical band gap of amorphous deposited GeTe is ≈ 0.8 eV at room temperature. Hence, even

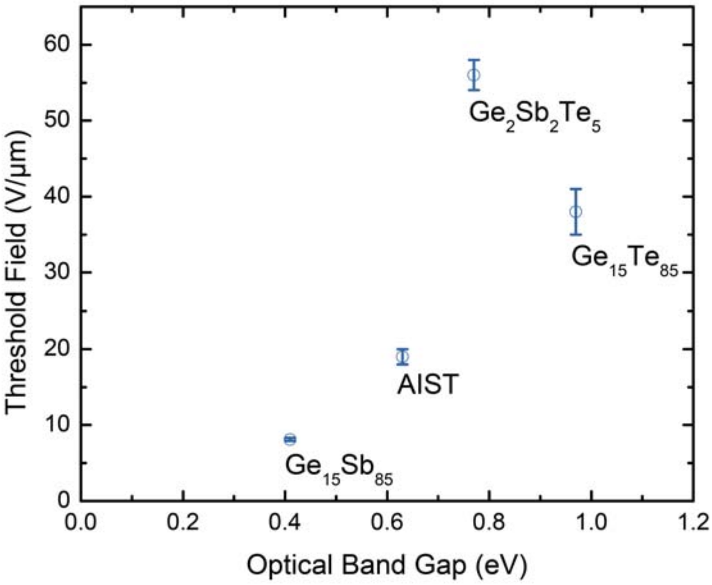

Figure 5.8: Threshold fields compared to optical band gaps measured at 300 K for various amorphous deposited chalcogenide glasses. The threshold field seems to be strongly influenced by the optical band gap value. However, the statement the higher the band gap the higher the electrical threshold field does not hold for $Ge_2Sb_2Te_5$ and $Ge_{15}Te_{85}$. Recently, a threshold field of 143 V/μm has been reported in a-GeTe, having an optical band gap of 0.8 eV. Even though amorphous deposited $Ge_2Sb_2Te_5$, $Ge_{15}Te_{85}$ and GeTe have similar band gap values these materials show a large variation in the observed threshold fields. If the threshold switching effect is driven by a generation/recombination process, the strong variation threshold fields could arise from a significant change in defect state density. In the generation/recombination model proposed originally by Adler *et al.* the electric field generates additional carriers, which can recombine in localized trapping levels within the band gap. The threshold switching event occurs if generation exceeds recombination. Image source: [Kre10]

though band gap values in amorphous deposited GeTe, $Ge_{15}Te_{85}$ and $Ge_2Sb_2Te_5$ are rather similar their corresponding threshold fields vary largely.
A correlation between band gap and electrical threshold field suggests that the threshold switching effect is driven by a generation and recombination mechanism. This model was first proposed by Adler *et al.* in 1980 [ASSO80]. A modified version is the Poole-Poole Frenkel model explained in section 3.2.4. In a generation/recombination model the electric field generates free carriers, which recombine in localized trap states within the band gap. Threshold switching to a highly conductive state occurs if the generation exceeds recombination. Consequently, if the generation/recombination model does apply, the large variation in threshold fields observed in a-GeTe, a-$Ge_{15}Te_{85}$ and a-$Ge_2Sb_2Te_5$ could arise from a significant difference in defect state density.

5.2.1 Photoconductivity

Photoconductivity measurements have been performed in a-GeTe, a-$Ge_{15}Te_{85}$ and a-$Ge_2Sb_2Te_5$ to gain indirect information about the defect state distribution. Therefore, the dark current and the current measured under constant illumination have been measured at different temperatures T. The photoconductivity is calculated with known film thickness by the subtraction of both measured currents. Conductivity measurements under constant illumination have been performed using a LED light source having a wavelength $\lambda = 850\,\mathrm{nm}$ equal to $E_{ph} = 1.45\,\mathrm{eV}$. The presented measurements have been performed adjusting the continuous light flux to $F_{dc} = 10^{16}\,\mathrm{cm}^{-2}\mathrm{s}^{-1}$. The results are shown in Fig. 5.9.

In all three investigated chalcogen alloys the photoconductivity increases first exponentially with increasing temperature, where the exponential growth factor g is largest for a-$Ge_{15}Te_{85}$, see Tab. 5.2,

$$\sigma_{ph} = \sigma_{ph}(0K) \cdot \exp(g \cdot T) \tag{5.29}$$

Table 5.2: In the low temperature limit the photoconductovity is observed to increase exponentially with increasing temperature. The corresponding exponential growth factor g is material dependent. The g-values describing the exponential increase in various amorphous deposited chalcogenides are listed below.

Material	exponential growth factor g (1/K)	T_{max} (K)
a-$Ge_{50}Te_{50}$	0.038	170
a-$Ge_2Sb_2Te_5$	0.035	190
a-$Ge_{15}Te_{85}$	0.052	250

The measured photoconductivity passes a maximum at that temperature T_{max} at which the conductivity under constant illumination is no longer significantly larger than the dark conductivity. Consequently, for temperatures larger than T_{max} the concentration of free carriers induced by temperature is larger than those induced by additional light excitation. The dark conductivity is defined by the position of the dark Fermi level. Under constant illumination the dark Fermi level E_F in disordered materials splits into two quasi Fermi levels E_F^n and E_F^p. The splitting of the dark Fermi level is described by Shockley-Read statistics and depends on light flux, temperature and the defect state density near the dark Fermi level, see Fig. 5.1. The splitting of the dark Fermi level increases with increasing flux and decreases with increasing temperature. At given generation conditions, i.e. same temperature and flux, the splitting of the dark Fermi level is large in materials having a low defect state density around the dark Fermi level. Likewise the splitting of the dark Fermi level is low in materials having a high defect state density in the vicinity of the dark Fermi level. A significant photoconductivity is observed if a sufficient splitting of the dark Fermi level is induced. Since the continuous flux has been kept constant in the measurement of photoconductivity the splitting of the Fermi level at given flux is governed by the temperature. The splitting of the dark Fermi level into two quasi Fermi levels increases with decreasing temperature. Hence, a higher density of mid gap states is expected in materials showing a lower temperature T_{max}, at which the dark conductivity equals the conductivity derived under constant illumination. The lowest value for T_{max}=170 K is observed in a-GeTe. A slightly higher value of T_{max}=190 K is observed in a-$Ge_2Sb_2Te_5$, whereas a-$Ge_{15}Te_{85}$ is characterized by a rather high value of T_{max}= 250 K. This finding suggests that a-GeTe possesses the highest and a-$Ge_{15}Te_{85}$ the lowest density of mid gap states. This indirect result is verified in the following by MPC experiments.

5.2.2 Defect state densities

Modulated Photo Current proved to be very successful to resolve defect state densities in amorphous chalcogenides. Fig. 5.10 shows the relative defect density Nc/μ derived for amorphous deposited a-GeTe, a-$Ge_2Sb_2Te_5$ and a-$Ge_{15}Te_{85}$. The MPC spectra are presented in the classical energy scale, since we are interested in the observed defect density Nc/μ in the vicinity of the Fermi level and the defect state density value Nc/μ is not influenced by a temperature dependent band gap. Furthermore, it should be mentioned at this point that as long as the electrical transport is governed by multiple trapping processes, the relative density Nc/μ and not the absolute density N describe transport phenomena properly. The electrical conduction is dominated by the relative density Nc/μ, since the number of trapping events is determined by both the free carrier mobility μ and the total trap state density N weighted with their corresponding capture coefficient c.

The MPC spectra derived for the amorphous phase change alloys a-GeTe and a-$Ge_2Sb_2Te_5$ are rather similar. Both materials show shallow defect states scaling with ν_p = $2.5{\cdot}10^8\ \mathrm{s}^{-1}$ as well as mid gap and valence band tail states described by ν_p = $1 \cdot 10^{12}\ \mathrm{s}^{-1}$. Amorphous phase change alloys are bad glass formers, because their amorphous phase can only by melt-quenching, i.e. very rapid cooling of the melt. In contrast good glass formers such as a-$Ge_{15}Te_{85}$ showing low

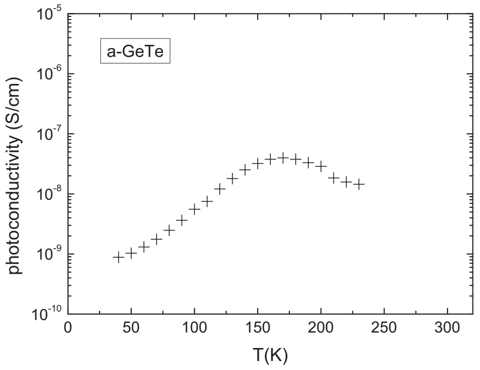

(a) Photoconductivity in a-GeTe

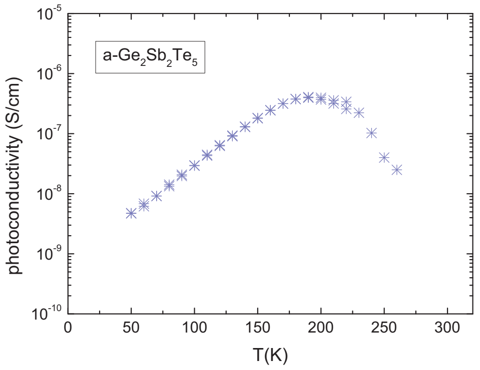

(b) Photoconductivity in a-$Ge_2Sb_2Te_5$

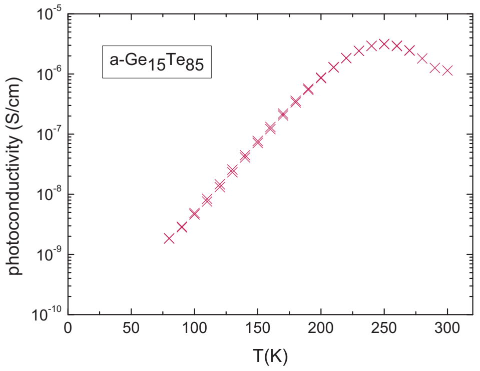

(c) Photoconductivity in a-$Ge_{15}Te_{85}$

Figure 5.9: Photoconductivity measured in amorphous deposited chalcogenides ($\lambda = 850\,\mathrm{nm}$, $F_{dc} = 10^{16}\,\mathrm{cm}^{-2}\mathrm{s}^{-1}$). The photoconductivity increases first exponentially before passing a maximum at T_{max}. The temperature T_{max} is the temperature at which the conductivity under constant illumination does no longer differ significantly from the dark conductivity. According to Shockley-Read statistics a low value of T_{max} is expected for materials having a large number of defect states in the vicinity of the dark Fermi level E_F.

crystallization kinetics can be easily obtained from the melt using comparable low cooling rates. The MPC spectrum measured on a-$\mathrm{Ge_{15}Te_{85}}$ shows no peaked defect state distributions. In a-$\mathrm{Ge_{15}Te_{85}}$ valence band tail states scaling with $\nu_p = 1 \cdot 10^{12}\,\mathrm{s^{-1}}$ are probed within the whole investigated temperature range. Like expected from photoconductivity measurements, the highest density of mid gap states $Nc/\mu = 1 \cdot 10^{11}\,\mathrm{cm^{-2}VeV^{-1}}$ is observed in amorphous deposited a-GeTe. The density of mid gap states decreases by one order of magnitude in amorphous deposited $\mathrm{Ge_2Sb_2Te_5}$. A very low defect state density of only $Nc/\mu = 1 \cdot 10^{8}\,\mathrm{cm^{-2}VeV^{-1}}$ is observed in a-$\mathrm{Ge_{15}Te_{85}}$.

5.2.3 Conclusion

In a generation/recombination model the application of a strong electric field is expected to fill states above the dark Fermi level. The change in occupation function changes the free carrier density. The excited carriers recombine in localized trapping levels within the band gap. The threshold switching event takes place if generation exceeds recombination. Consequently, in the generation/recombination model high threshold fields should arise from either large optical band gaps or high trap state densities. This study on switchable chalcogenide alloys having similar band gap values shows that the defect density of mid gap states is observed to increase with increasing threshold field. This results suggests that a generation/recombination model could explain threshold switching phenomena in amorphous chalcogenides. Furthermore, this study has shown that temperature dependent photoconductivity measurements could be useful to predict qualitatively threshold fields in different materials. As long as the change in state occupancy induced by constant light intensity or by application of an electric field are comparable, those materials showing a low T_{max} should also be characterized by a high threshold field.

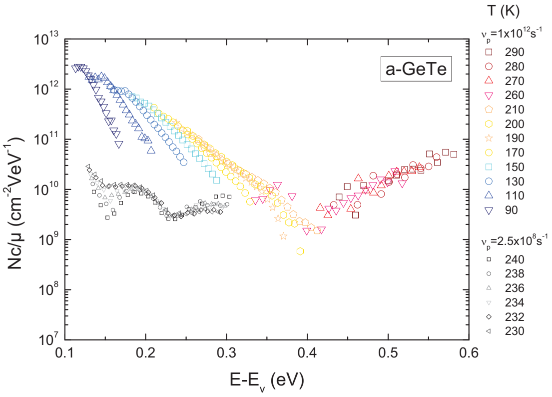

(a) a-GeTe

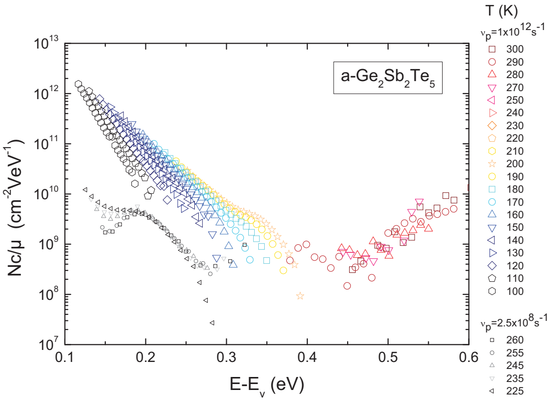

(b) a-Ge$_2$Sb$_2$Te$_5$

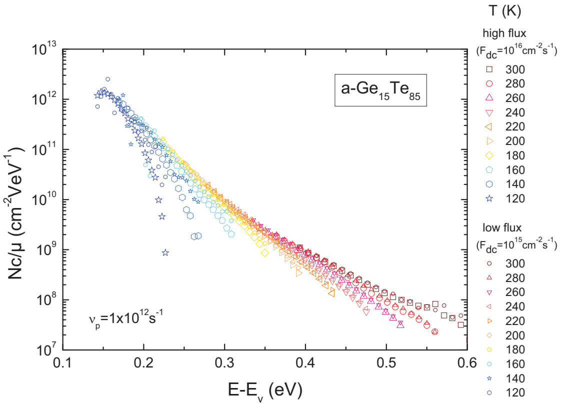

(c) a-Ge$_{15}$Te$_{85}$

Figure 5.10: MPC DoS measured in different switchable chalcogenides having similar optical band gaps. Those chalcogenides exhibiting a high electrical threshold field show also a high density of gap states in their amorphous deposited phase. This suggests that the threshold switching effect is driven by a recombination/generation mechanism originally proposed by Adler *et al.* [ASSO80].

Chapter 6

Resistance drift phenomena

This chapter concentrates on resistance drift phenomena in amorphous phase-change materials and covalent glasses. The first section presents an experimental study of drift phenomena measured in amorphous GeTe thin films. In the second section, these experimental results on a-GeTe are compared to drift phenomena reported in literature for covalent glasses such as a-Si and a-Si:H.

The development of non-volatile electronic phase-change memory devices requires an active material showing a high crystallization temperature and fast crystallization speed. Indeed, the phase-change alloy GeTe meets both of these requirements. However, this alloy shows a strong resistance drift effect. A phase-change alloy having a stable amorphous state resistivity is favoured regarding multilevel storage systems based on phase-change technology. With the aim to identify phase-change materials showing a stable amorphous state resistivity, the stoichiometric dependence of drift phenomena in a-GeSnTe systems and other phase-change alloys is studied in section 6.3. Finally, the link between stress relaxation and resistance drift phenomena is adressed in section 6.4.

6.1 Drift phenomena in a-GeTe

To get a better insight into resistance drift phenomena, the dark and photoconductivity have been measured in aged and post-annealed samples. Furthermore, a study of the evolution of trap state density may provide a direct experimental proof for the proposed mechanisms explaining the resistance drift effect by a change in defect density, see chapter 3. Therefore, the defect state density has been measured in aged and post-annealed a-GeTe thin films employing Photothermal Deflection Spectroscopy and Modulated Photo Current Experiments. Furthermore, the relaxation of mechanical stress within the phase-change film has been measured during heating using the Curvature method. The relaxation of mechanical stress is often referred to an irreversible structural relaxation. To get a better understanding of the structural relaxation process taking place in a-GeTe thin film, X-ray Absorption Fine Structure (EXAFS) has been performed on amorphous deposited and post-annealed amorphous GeTe thin films.

6.1.1 Dark and photoconductivity in aged and post-annealed a-GeTe thin films

The dark and photoconductivity has been studied in aged and post-annealed a-GeTe thin films. Resistivity in the temperature range above room temperature has been measured with a four point Van-Der-Pauw technique, whereas the resistivity at lower temperatures has been studied by a cryostat working in two point geometry.

Fig. 6.1 compares the resistivity measured in a-GeTe films while heating each sample to a different holding temperature T_{HOLD}. To enable a measurement of the activation energy of electric conduction at the beginning of the drift, a small heating rate of 5 K/min has been chosen. Shortly after deposition, the four samples produced in the same sputter process have exhibited very similar resistivities varying from 1103 Ωcm to 1145 Ωcm at room temperature. In the high temperature limit, the resistivity decreases with increasing temperature following an Arrhenius law. The corresponding activation energy of electrical conduction E_a^{start} measured at the beginning of the drift, varies only slightly from sample to sample lying in a range from 0.364 eV to 0.366 eV.
During the heating process, the resistivity increases and the strongest change in resistivity

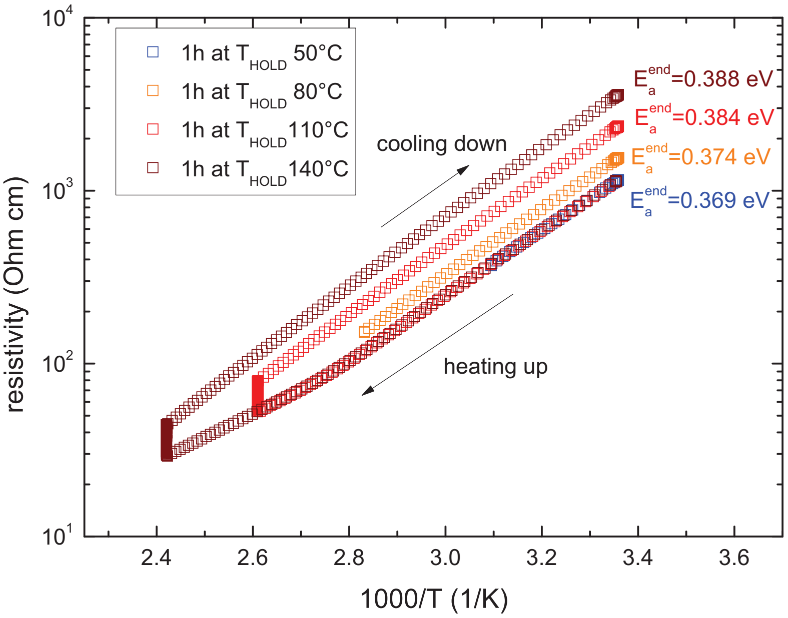

Figure 6.1: Resistivity measured upon heating 190 nm thick a-GeTe films with a heating rate of 5 K/min to different holding temperatures T_{HOLD}. The higher the holding temperature the stronger is the increase in resistivity. The change in resistivity is linked to an increase in activation energy, that increases by 25 meV after heating the sample for one hour at 140°C and 5 meV at 50°C.

is observed for the highest holding temperature T_{HOLD} = 140 °C. The observed increase in resistivity is closely linked to an increasing activation energy of electrical conduction. After heating the samples for one hour at the indicated holding temperature, the activation energy of electric conduction is remarkably increased in all four a-GeTe thin films. Indeed, the largest change in activation energy is observed in the a-GeTe thin film heated to the highest holding temperature T_{HOLD} = 140 °C, where the activation energy of electric conduction changes by 25 meV. In comparison the sample heated for one hour to T_{HOLD} = 50 °C shows only a low, but still measurable increase in the activation energy of 5 meV. This finding clearly demonstrates, that the resistance drift effect accelerates at higher holding temperatures and is strongly related to an increase of the activation energy of electrical conduction.

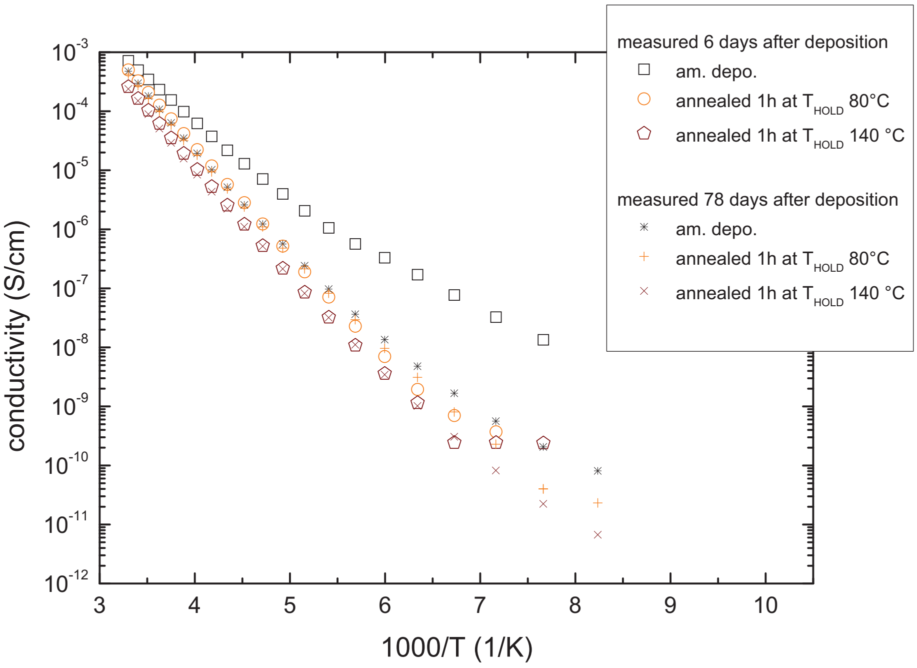

Figure 6.2: Dark conductivity measured in post-annealed and longer aged a-GeTe thin films. Two out of three a-GeTe thin films deposited in the same sputter run have been heated for one hour at different holding temperatures T_{HOLD}. The dark conductivity of the amorphous deposited and post annealed samples has been measured shortly after the deposition and once more three months later. The presented results show, that ageing and post annealing have the same influence on the measured dark conductivity: the conductivity decreases within the whole temperature range and approximates a straight line in the chosen semi logarithmic scale. Furthermore, these results illustrate that storing the samples three months at room temperature has almost the same effect on the measured conductivity as annealing an a-GeTe thin film for one hour at 80°C.

Furthermore, dark conductivity has been studied in aged and post-annealed samples in the low temperature limit. The temperature has been varied from 120 K to 300 K. To compare the influence of post-annealing and altering at room temperature, the dark conductivity has been measured in 200 nm thin a-GeTe films. The studied samples have been deposited in the same sputtering process on sapphire substrates. Directly after deposition, two out of these three a-GeTe samples have been heated for one hour at a holding temperature of either T_{HOLD} = $80\,°\mathrm{C}$ or T_{HOLD} = $140\,°\mathrm{C}$. The dark conductivity has been measured in the amorphous deposited and in both post-annealed a-GeTe thin films 6 and 78 days after deposition. Fig. 6.2 presents the dark conductivity measured in the post-annealed and altered samples. In the Arrhenius plot presented, the amorphous sample measured 6 days after deposition shows a strong curvature. With annealing the measured conductivity decreases over the whole investigated temperature range. Additionally, the bending of the curve reduces and the measured dark conductivity approximates a straight line in the chosen semi-logarithmic scale.

The same samples have been measured almost three months later. Ageing shows the largest effect on the amorphous sample, where the dark conductivity drastically decreases with increasing sample age. Furthermore, the bending of the measured $\sigma(T)$ curve reduces significantly. These results demonstrate clearly that annealing and ageing induce the same effects on the dark conductivity in the low temperature limit. Thus, storing an a-GeTe thin film three months at room temperature seems to be equivalent to heating the sample for one hour at 80°C. The influence of ageing on the measured dark conductivity is stronger on the amorphous than on the post-annealed samples. However, for all the samples the dark conductivity is observed to decrease with increasing sample age. In agreement with resistivity measurements in the high temperature range, the observed decrease in conductivity is linked to an increase in activation energy of electrical conduction E_a, see Tab 6.1.

For the samples studied 78 days after deposition, the photoconductivity has been measured at different temperatures additionally to the dark conductivity. The results are presented in Fig. 6.3. The photoconductivity first increases exponentially with increasing measurement temperature before passing a maximum at T_{max}. The temperature T_{max} indicates the temperature at which the photoconductivity is no longer significantly larger than the dark conductivity. The position of the maximum T_{max} is different in the amorphous deposited and post-annealed a-GeTe thin films. With increasing holding temperature T_{HOLD} the temperature T_{max} shifts to a higher temperature. Furthermore, the photoconductivity is observed to decrease with increasing holding temperature. In the temperature range from 120 to 180 K the photoconductivity decreases by a factor of three.

The following discussion relies on the concepts presented in section 5.1. The decrease in photoconductivity with increasing annealing temperature T_{HOLD} indicates that the distance between the quasi Fermi level for free holes E_{fn} and the valence band edge E_v increases. Furthermore, the shift in T_{max} to higher temperatures with increasing holding temperature T_{HOLD} demonstrates that a significant splitting of the dark Fermi E_f level into quasi Fermi levels E_{tp} and E_{tn} occurs at a higher temperature in post-annealed samples. Under the same generation conditions, i.e. temperature and light intensity, the splitting of the dark Fermi level into quasi Fermi levels increases the lower the density of states in the vicinity of the dark Fermi level. Additionally, the splitting of the Fermi level increases with decreasing temperature at constant light intensity and defect density. Consequently, samples showing a low density of states near the dark Fermi level reveal a photoconductivity, which is significantly larger than the dark conductivity at a higher measurement temperature T_{max}. However, the absolute value of the photoconductivity is governed by the energetic distance of the quasi Fermi level for free holes $E_{tf} \geq E_{tp}$ and the valence band edge E_v, which is expected to increase upon annealing due to the observed increase of the activation energy of electric conduction presented in Fig. 6.1.

Table 6.1: Activation energies E_a describing the dark conductivity near room temperature and growth factors g as well as maximal temperatutre T_{max} describing the photoconductivity in post-annealed and aged a-GeTe thin films. For the definition of g and T_{max} see text above and Eq. 5.29.

days measured after deposition	Sample	E_a (eV)	exponential growth factor g (1/K)	T_{max} (K)
	as depo.	0.294	-	-
6	80 °C	0.365	-	-
	140°C	0.381	-	-
	amo. depo.	0.385	0.046	180
78	80 °C	0.386	0.053	185
	140°C	0.402	0.052	190

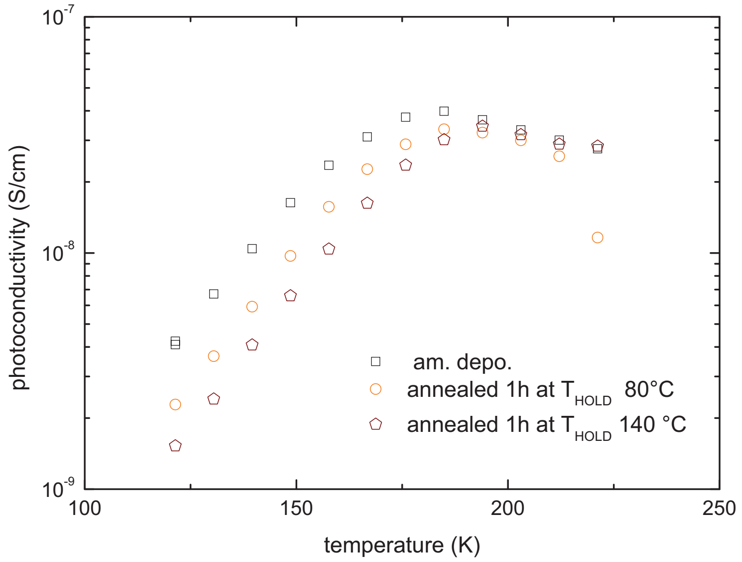

Figure 6.3: Photoconductivity measured in post-annealed a-GeTe thin films. The photoconductivity increases first exponentially with increasing temperature before passing a maximum at the temperature T_{max}, see chapter 5. The photoconductivity in the low temperature range decreases with increasing holding temperature T_{HOLD}. Furthermore, the maximum temperature T_{max} increases with increasing annealing temperature T_{HOLD}. The later finding indicates a decreasing number of defect states at the vicinity of the dark Fermi level, whereas the decrease in the photoconductivity indicates an increasing energetic distance between the quasi Fermi level for trapped holes E_{tp} and the valence band edge E_v.

6.1.2 Defect state density in post-annealed and aged a-GeTe thin films

Photoconductivity measurements on altered a-GeTe thin films indicate that annealing induces an annihilation of defect states in the vicinity of the Fermi level and an increasing energetic distance between the quasi Fermi level for free holes E_{fp} and the valence band edge E_v. To give a direct experimental proof for defect annihilation, the defect state concentration has been studied in post-annealed and aged amorphous GeTe thin films employing Photo Thermal Deflection Spectroscopy and Modulated Photo Current experiments.

Photothermal Deflection Spectroscopy

PDS spectra have been measured in two amorphous 500 nm thick GeTe films. Both studied samples have been produced in the same deposition process and one sample has been heated one hour at a holding temperature of 140 °C. Fig. 6.4 compares the absorption spectra measured

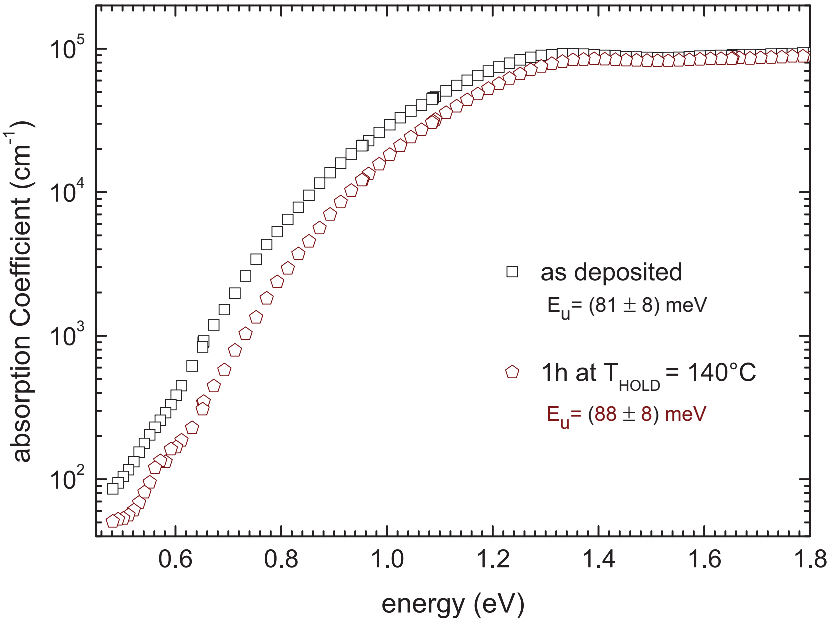

Figure 6.4: PDS spectra measured in post-annealed a-GeTe thin films. Both presented samples have been produced in the same deposition process and one sample has been heated for one hour at a holding temperature of 140 °C. Annealing shows, within error, no effect on the Urbach slope E_u. However, the absorption curve measured in the pre-annealed sample is shifted to higher energies after annealing. The observed shift of the absorption curve probably results from an increased optical band gap.

on both samples. The amorphous deposited sample shows an Urbach energy of $81 \pm 8\,\mathrm{meV}$. The Urbach edge describing the post-annealed sample is determined to $88 \pm 8\,\mathrm{meV}$. Hence, within error no change in the Urbach energy can be observed. Even though no significant change in the Urbach energy can be stated, the results presented show a clear shift of the measured absorption curve to higher energies. This shift of the absorption curve indicates that the observed increase in activation energy of electrical conduction during heating results from an opening of the optical band gap.

Modulated Photo Current Experiments

The evolution of the defect state density within the band gap has been studied upon ageing employing Modulated Photo Current Experiments. For this purpose, the same sample has been measured at different sample ages. Fig. 6.5 presents the evolution in the measured dark conductivity. The activation energy of electrical conduction is observed to increase by 19 meV with increasing sample age. Furthermore, the a-GeTe thin film shows a better thermally activated behavior of the dark conductivity at a sample age of 108 days than 29 days after deposition.

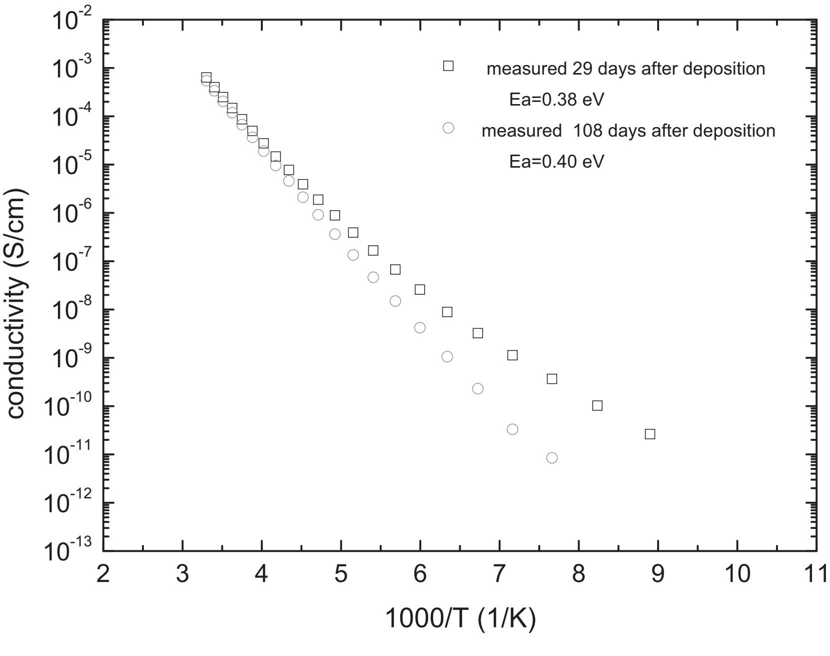

Figure 6.5: Dark conductivity measured in the same a-GeTe thin film at different sample ages. With increasing sample age the activation energy of electrical conduction E_a is significantly increased. Furthermore, the longer aged sample shows a better thermally activated behavior.

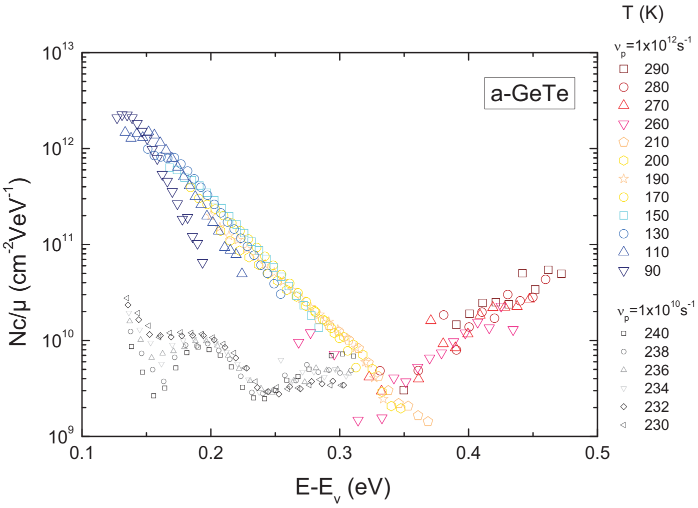

(a) 29 days after deposition

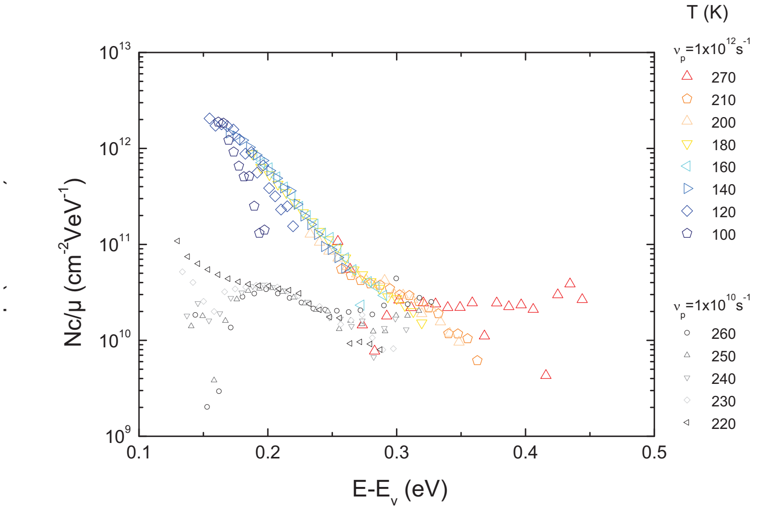

(b) 108 days after deposition

Figure 6.6: MPC spectra measured in a-GeTe thin film at different sample ages. At a sample age of 29 days the measured MPC spectrum reveals valence band tail states probed from 90 K to 210 K, shallow defect levels measured in a rather small temperature window from 230 K to 240 K and midgap states measured from 260 K to 290 K.
Ageing shows to have a significant influence on the measured MPC spectra, in particular on the defect levels. With increasing sample age the MPC DoS describing the shallow defect increases from $Nc/\mu = 1\cdot10^{10}\,\mathrm{cm}^{-2}\mathrm{VeV}^{-1}$ to $Nc/\mu = 4\cdot10^{10}\,\mathrm{cm}^{-2}\mathrm{VeV}^{-1}$. Furthermore, shallow defect levels can be detected in a larger temperature window, i.e. from 220 K to 260 K. In contrast, deep defect levels can be detected in a smaller temperature window. Nevertheless, the MPC curve taken at 270 K differs drastically with increasing sample age. In the MPC spectrum measured 29 days after deposition the MPC curve taken at 270 K describes a proper flank of mid gap states having a maximum density $Nc/\mu = 5\cdot10^{10}\,\mathrm{cm}^{-2}\mathrm{VeV}^{-1}$ (a). On the other hand the MPC curve taken at 270 K describes a broad flat plateau of defect states with $Nc/\mu = 2\cdot10^{10}\,\mathrm{cm}^{-2}\mathrm{VeV}^{-1}$ (b).

The corresponding MPC spectra measured 29 and 108 days after deposition are shown in Fig. 6.6. Both spectra are presented in a fully ξ-corrected energy scale taking the value from Tab. 5.1.

Sample age 29 days

At a sample age of 29 days the a-GeTe thin film studied shows those three characteristic features (which have been already discussed in section 5.1.3): valence band tail states, shallow defect states and deep mid gap states.
Valence band tail states are probed in a temperature range from 90 K to 210 K. Shallow trap states are revealed within a rather narrow temperature window ranging from 230 K to 240 K. Mid gap states of a maximum density $Nc/\mu = 5 \cdot 10^{10}\,\mathrm{cm}^{-2}\mathrm{VeV}^{-1}$ are observed at higher temperatures from 260 K to 290 K.

Sample age 108 days

Ageing shows to have a significant influence on the measured MPC spectrum, especially on the shallow and deep defect level. However, the evolution in trap state density shows no simple picture. The MPC DoS describing shallow defect states increases with increasing sample age from $Nc/\mu = 1 \cdot 10^{10}\,\mathrm{cm}^{-2}\mathrm{VeV}^{-1}$ to $Nc/\mu = 4 \cdot 10^{10}\,\mathrm{cm}^{-2}\mathrm{VeV}^{-1}$. Furthermore, the measurement window enlarges. At a sample age of 108 days shallow defects can be observed in a rather large temperature range from 220 K to 260 K. In contrast, the measurement window in which mid gap states could be detected narrows. The signal to noise ratio hampered recording proper data above 270 K. However, the MPC curve measured at 270 K differs drastically with increasing sample age. At a sample age of 29 days the MPC curve taken at 270 K describes a proper flank of a distribution of states with a maximum value $5 \cdot 10^{10}\,\mathrm{cm}^{-2}\mathrm{VeV}^{-1}$. In contrast at a sample age of 108 days the MPC curve taken at 270 K describes a broad flat plateau of defect states of a height $Nc/\mu = 2 \cdot 10^{10}\,\mathrm{cm}^{-2}\mathrm{VeV}^{-1}$. Hence, the presented MPC data denote a decrease in mid gap states with increasing sample age, which is consistent with the presented photoconductivity data. Furthermore, the observed defect annihilation in the vicinity of the Fermi level support the nowadays commonly accepted Ielmini model explaining resistance drift phenomena. The width of the mobility band gap is determined by the tail state densities. Thereby the mobility band gap increases with decreasing tail concentration. In this framework, the Ielmini model has proposed an opening of the mobility band gap due to defect annihilation. However, in accordance with the presented Photothermal Deflection data, no significant change in the defect densities describing the band tails could be observed. Hence, annealing has no influence on the tail states the origin of the observed band gap opening stays an open question.

6.1.3 Band gap in post-annealed a-GeTe thin films

PDS measurements suggest that the band gap in a-GeTe opens upon heating. To clarify this issue the optical band gap in post-annealed a-GeTe thin films has been studied by Fourier-Transform Infrared Spectroscopy. Optical band gaps derived from FT-IR measurements performed on amorphous and post annealed a-GeTe thin films at ambient temperature are presented in Fig. 6.7a. To come to a better conclusion the optical band gap has been measured additionally before heating each sample. Indeed, the optical band gap describing the amorphous phase is very similar in all three samples presented , which have been produced in the same sputter deposition. After heating the sample for one hour at a given holding temperature the optical band gap has been measured again. The band gap increases by 28 meV after heating the sample for one hour at 80°C. Heating one hour at a holding temperature of 140°C induces a stronger band gap opening of 72 meV.

Tab. 6.2 compares the measured increase of the optical band gap to the increase in activation energy of electric conduction shown in Fig. 6.1. The comparison in Tab. 6.2 demonstrates that the band gap opening has a strong impact on the observed increase in activation energy of electrical conduction yielding to an increase of the amorphous state resistivity.

The temperature dependence of the optical band gap in a-PCM is described by the simplified Varshni formula given by Eq. 5.20. With the aim to investigate the influence of the Varshni parameters E_0 and ξ on the band gap opening observed at room temperature, the optical band gap has been measured in both post-annealed a-GeTe thin films at different measurement temperatures. Fig. 6.7b presents the optical band gap derived from FT-IR reflectance spectra taken from 5 K to 300 K in 50 K steps on both post-annealed a-GeTe samples. Both spectra are well described by the simplified Varshni formula describing a parabolic decrease of the optical band gap with increasing measurement temperature. The corresponding Varshni parameters $E_g(0K)$ and ξ are given in Tab. 6.2. According to Tab. 6.2 the increase of the room temperature optical band gap upon heating is strongly linked to an increasing 0 K band gap $E_g(0K)$. However, since MPC and PDS measurements have shown that this band gap opening does not originate from decreasing tail state densities. Consequently, the physical mechanism behind the optical band gap opening stays unclear.

Table 6.2: Activation energies E_a compared to band gap opening induced by heating the a-GeTe thin film for one hour at a given holding temperature. The change in activation energy ΔE_a derived from Fig. 6.1 and the band gap opening illustrated in Fig. 6.7 are listed for comparison.

T_{HOLD} (°C)	E_a (eV)	$E_g(300K)$ (eV)	$E_g(300K)/E_a$ (eV)	$E_g(0K)$	ξ (10^{-6} eV/K^2)
amo. depo.	0.364	0.806	2.21	-	-
80°C	0.374	0.834	2.23	0.962	1.49
140°C	0.388	0.878	2.26	0.994	1.31

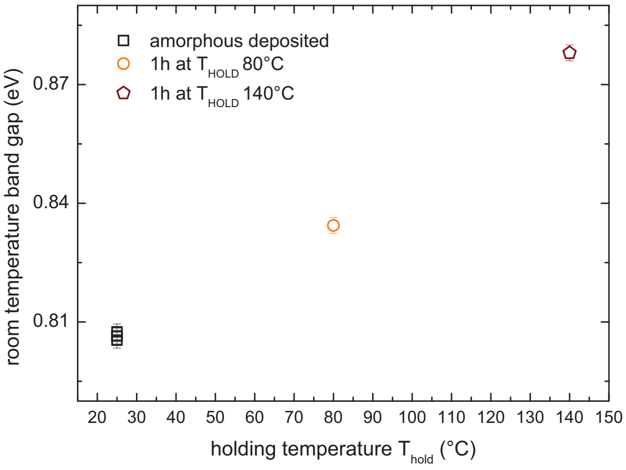

(a) Optical band gaps measured at ambient temperature

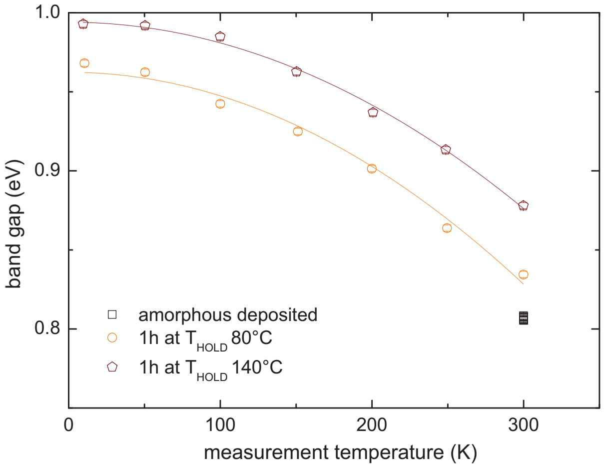

(b) Temperature dependence of the optical band gap

Figure 6.7: Optical band gaps studied in post-annealed a-GeTe thin films at varied measurement and holding temperatures. The post-annealed samples have been annealed for one hour at the indicated holding temperature T_{HOLD}. FT-IR measurements have been performed at the indicated measurement temperature before and after annealing the sample. The optical band gaps measured at room temperature are displayed in (a). All the investigated samples have very similar optical band gaps after deposition. In a-GeTe, annealing induces a significant increase of the optical band gap value. Annealing one hour at a holding temperature of 80°C induces a band gap opening of 28 meV. Annealing one hour at 140°C results in a band gap change of 72 meV. In both post-annealed samples the optical band-gap has been studied at different measurement temperatures (b). The band gap is observed to decrease parabolically with increasing measurement temperature, like predicted by the empirical Varshni law given in Eq. 5.20. The corresponding Varshni parameters derived by a Fit routine (line) are listed in Tab. 6.2. Obviously, the increasing band gap at 0 K has a strong influence on the band gap opening observed at ambient temperature, too.

6.1.4 Stress relaxation in a-GeTe thin films

Former works carried out on GeSbTe and AgSbInTe systems have shown that stress relaxation takes place in amorphous deposited thin films during heating [Kal06, KSLPW03].
The change in stress during heating can be measured by the curvature method. The evolution in film stress has been recorded by a curvature set-up during heating a 500 nm thick GeTe film 48 hours at 50 °C. The result is illustrated in Fig. 6.8.
Shortly after deposition the a-GeTe thin film shows a small compressive stress of -49 MPa. Heating the sample to 50°C induces a thermal stress, because the dilatation of the glass substrate is lower than that of the amorphous phase-change film. Having reached a sample temperature of 50 °C a maximal compressive stress of -55 MPa is recorded by the curvature method. During heating the sample at 50 °C the measured compressive stress within the thin film decreases very fast within the first 25 hours. After 25 hours the observed stress relaxation occurs more slowly, but is still measurable. Whereas in the first 25 hours the stress decreases by 15 MPa further heating at 50 °C induces a stress relaxation of only 0.5 MPa. After 48 hours the sample is cooled back again to room temperature. During cooling the measured stress decreases additionally due to the difference in dilatation coefficients of substrate and phase-change alloy under test. After heating the a-GeTe thin film for 48 hours at 50 °C the phase-change film shows a compressive stress of -32 MPa at room temperature.

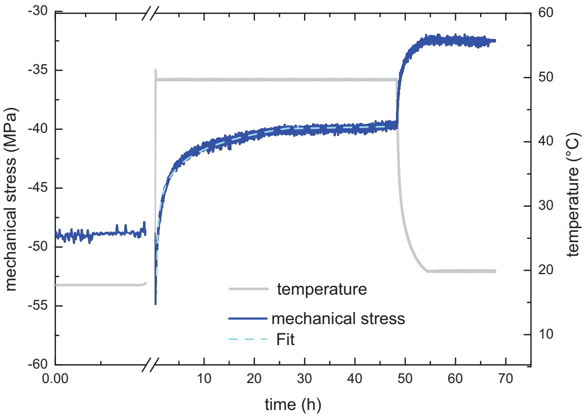

Figure 6.8: Mechanical stress measured in a 500 nm thick a-GeTe film by a curvature set-up. Shortly after deposition a compressive stress of -49 MPa is measured. Heating the sample up to 50 °C induces an additional thermal stress, because the phase-change alloy expands more than the substrate underneath. During heating the measured stress decreases. The mechanical stress decreases by 15 MPa within the first 25 hours, whereas further heating induces a comparable small stress relaxation of only 0.5 MPa. After heating the a-GeTe thin film for 48 hours at 50 °C, the sample is cooled down to room temperature. Cooling induces a stress relaxation resulting from the difference in dilatation coefficients of substrate and material under test. Finally, the curvature set-up records at room temperature a compressive stress of -32 MPa.

6.1.5 Extended X-Ray Absorption Fine Structure measured in post-annealed a-GeTe thin films

The observed decrease in stress measured by the curvature method is commonly referred to a structural relaxation process deforming the material under test. Extended X-ray absorption fine structure (EXAFS) is an excellent method to investigate structural rearrangements. To investigate a possible structural origin of drift phenomena, EXAFS spectra have been taken on a-GeTe thin films. Fig. 6.9 compares the Fourier Transformed EXAFS spectra measured at room temperature on amorphous deposited and post-annealed a-GeTe thin films. The post-annealed samples have been heated for 24 hours at 50°C or 80°C, respectively. Obviously, heat treatment affects the measured EXAFS spectra significantly. With increasing annealing temperature the EXAFS signal increases, too. This finding indicates that annealing improves the structural ordering of the amorphous deposited phase.
A careful analysis of EXAFS data enables to determine the total coordination number of Ge bonds and partial bond length of Ge-Ge and Ge-Te bonds. Furthermore, the Debye Waller factor of homopolar Ge-Ge and heteropolar Ge-Te bonds can be calculated from the EXAFS spectra. However, unambiguous results can be only obtained from EXAFS spectra of good data quality. The presented data measured at room temperature lack the required data quality to draw clear conclusions. Hence, it can not be verified if the significant increase in the measured EXAFS signal results from a decrease in bond lengths or from a decrease in the EXAFS Debye Waller factor. The EXAFS data quality can be significantly improved by performing these measurements at lower measurement temperature. Future works on post-annealed a-GeTe thin films could clarify this issue. Nevertheless, the presented results show clearly that the resistance drift effect is closely linked to a structural rearrangement in the a-GeTe thin films. Consequently, this finding points toward a structural origin behind the resistance drift effect. Furthermore one should note at this point that the EXAFS spectra taken on amorphous GeTe thin films attached to a glass substrate is different to the EXAFS spectra measured in amorphous GeTe powder, where a single peak without significant shoulder has been observed see Fig. 4.16.

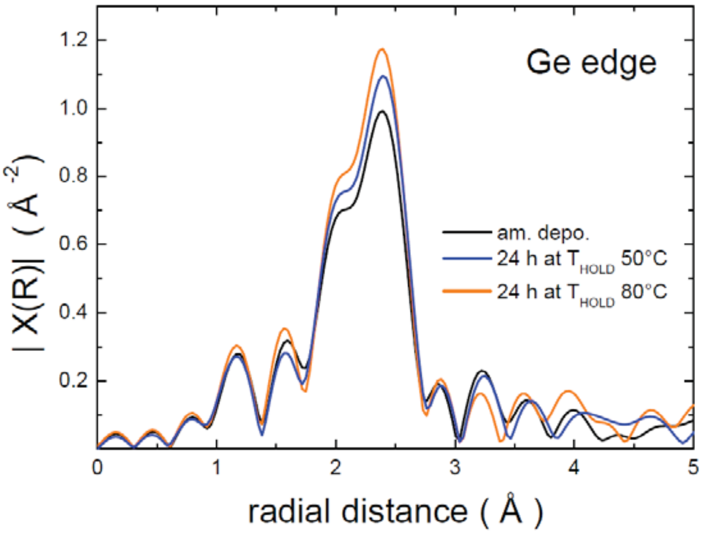

Figure 6.9: Extended X-ray Absorption Fine Structure measured at the Ge edge in post-annealed and amorphous deposited a-GeTe thin films at room temperature. Both post-annealed amorphous samples have been heated for 24 hours at the indicated holding temperature T_{HOLD}. The EXAFS signals measured in the amorphous deposited and post-annealed samples differ and show a systematic trend. The EXAFS signal increases with increasing holding temperature T_{HOLD}. This finding indicates that the structural ordering of the amorphous deposited phase is improving by annealing an a-GeTe thin film. Hence, this result suggests a structural origin behind the resistance drift effect.

6.2 Drift phenomena in covalent glasses

Drift phenomena in optical and electrical properties have been studied extensively in covalent glasses. This section discusses drift phenomena reported in literature for amorphous silicon a-Si and hydrogenated amorphous silicon a-Si:H. The aim of this section is to identify differences and similarities to drift phenomena observed in amorphous phase-change materials.

6.2.1 Defect state density in a-Si/a-Si:H

Many studies report a change in defect state density in a-Si or a-Si:H, respectively. The defect state density in both materials can be studied by various methods including Photo Thermal Spectroscopy, Modulated Photo Current experiments and Electron Spin Resonance. In these covalent systems the concentration of hydrogen plays an important role on the optical and electrical properties.

Effect of substrate temperature on the defect state density studied by Electron Spin resonance

The effect of the substrate temperature on the defect state density of glow-discharged a-Si:H has been studied by Shirafuji *et al.* employing Electron Spin resonance [JSI84]. A strong link between substrate temperature and ESR spin density measured at room temperature has been found, see Fig. 6.10a. The ESR signal is commonly attributed to the concentration of unsatisfied valence electrons on a Si atom. This defect is commonly attributed to a silicon dangling bond. The concentration of dangling bonds depends strongly on the hydrogen content, which can be controlled by the substrate temperature in a deposition via glow discharge. The lowest concentration of dangling bond defects is obtained for substrate temperatures near 200°C. For substrate temperatures lower than 200°C no good forming of Si-H bonds is possible, see Fig. 6.10b. However, heating the substrate well above 200°C removes hydrogen out of the Si thin film and thus the concentration of dangling bonds increases. Additionally the substrate temperature has a significant influence on the optical band gap. Their exists no clear link between the defect state density observed by ESR and the optical band gap value, but the optical band gap is observed to decreases with decreasing total hydrogen content, see Fig. 6.10b and Fig. 6.10c. In contrast to hydrogenated amorphous silicon no ESR signal can be detected in amorphous phase-change materials. Electron Spin Resonance is only sensitive to detect trap states occupied by a single electrons. Without a strong electron-phonon interaction the single occupied state lies lower in energy than the doubly occupied state, like in a-Si. However, in the case of a strong electron-phonon coupling the addition of an electron to a localized state changes the local bonding. In consequence, the total electron correlation energy U being the sum of Coulomb and relaxation energies can be negative, i.e. $U = \frac{e^2}{4\pi\varepsilon_0\varepsilon r} - W < 0$.
Hence, no ESR signal can be detected in amorphous phase-change alloys these materials are characterized by a negative electron correlation energy. Negative U-centers have been also observed in other amorphous chalcogenides such as As_2Se_3 [And75, SM75, KAF76b, KKO+98] and are responsible for a strong pinning of the dark Fermi level.

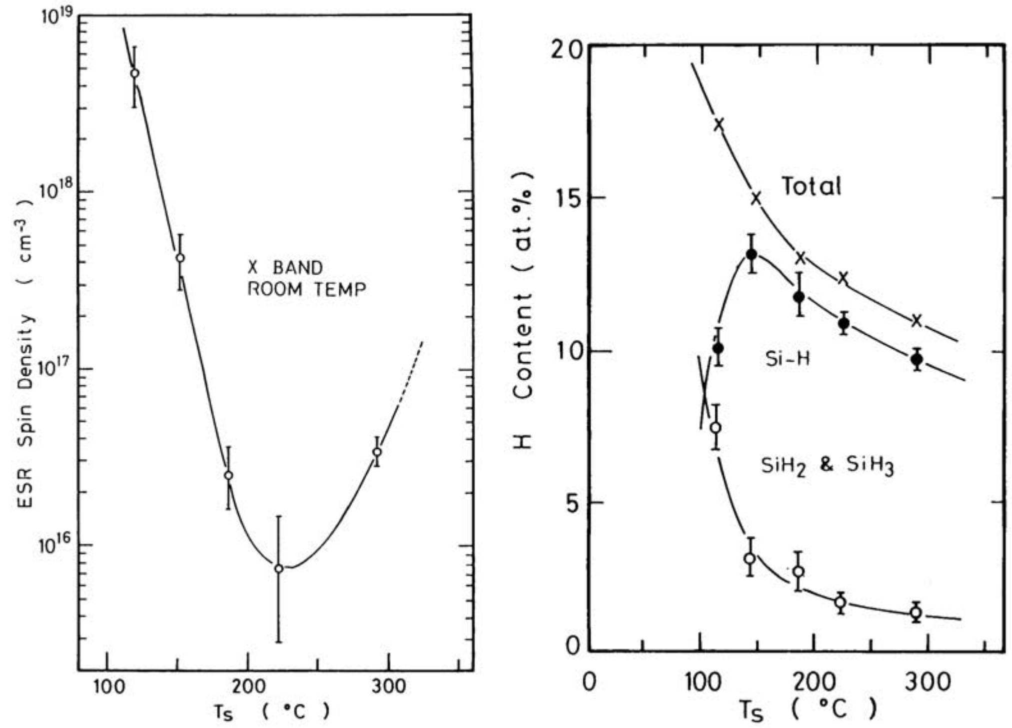

(a) ESR spin density **(b)** Concentration of Si-H bonds

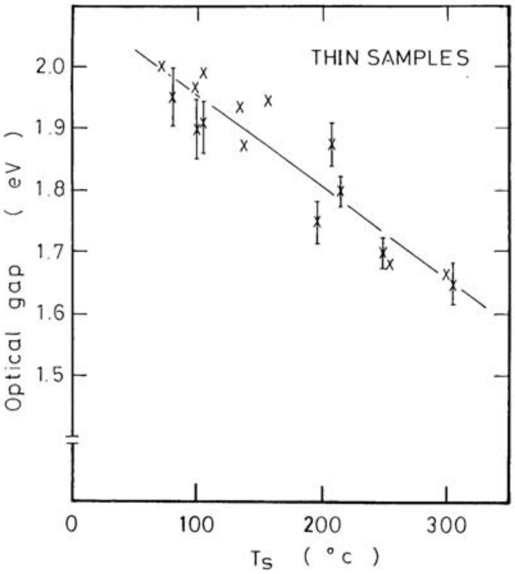

(c) Optical band gap

Figure 6.10: ESR spin density and optical band gaps measured at room tempeature on a-Si:H deposited via glow discharge at different substrate temperatures T_S. Image source: [JSI84]

Photothermal Deflection Spectroscopy on post-annealed a-Si:H thin films

The optical absorption edge of hydrogenated silicon has been studied by Cody *et al.*, see Fig. 6.11. Photo Thermal Deflection Spectra have been measured in amorphous deposited and post-annealed samples at different temperatures T_M. The post-annealed samples have been heated for 30 minutes at the indicated holding temperature T_H. Photo Thermal Deflection Spectroscopy reveals a significant broadening of the absorption edge with increasing holding temperature. The broadening of the absorption edge results from the thermal evolution of hydrogen. At temperatures higher than 200°C hydrogen is removed and the increased concentration of dangling bonds induces a higher structural disorder, which is reflected by an increasing Urbach edge energy. Furthermore, the Urbach energy increases with increasing measurement temperature T_M, which reflects the increasing thermal disorder.
In contrast to a-Si:H, no broadening of the absorption edge upon heating could be stated in amorphous GeTe thin films shown in Fig. 6.4.

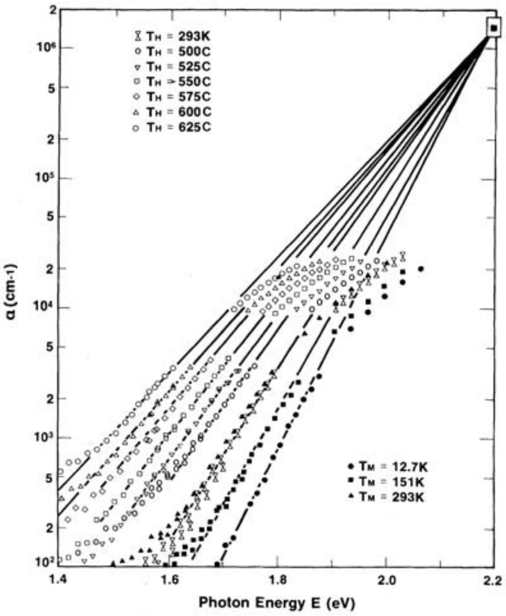

Figure 6.11: Optical absorption edge of a-Si:H measured by Photo Thermal Deflection Spectroscopy. PDS spectra have been recorded in amorphous deposited and post-annealed samples. The post-annealed samples have been heated in vacuum conditions for 30 minutes at the indicated holding temperature T_H. The absorption edge broadens with increasing holding temperature T_H. Furthermore, the absorption edge increases with increasing measurement temperature T_M. In contrast, PDS measurements performed on a-GeTe have shown no change in the Urbach slope. Image source: [CTA⁺81]

6.2.2 Stress relaxation and viscous flow in a-Si

The relaxation of thermal stress in ion-beam-sputtered amorphous silicon thin films has been studied by A. Witvrouw and F. Spaepen [WS93]. Fig. 6.12 shows the change in mechanical stress measured by the curvature method during heating an amorphous silicon thin film at 201°C. The presented curvature $1/R$ is directly proportional to the stress σ. The proportionality factor depends on the film thickness and the chosen substrate and is 2977 MPa for the presented example.

The measured stress relaxation reported for a-Si is very similar to the stress relaxation measured in a-GeTe. In both materials the mechanical stress decreases irreversibly, which is commonly attributed to a structural relaxation.

In amorphous silicon the structural relaxation is proposed to be governed by dangling bonds. A model of viscous flow based on dangling bonds acting as *flow defects* is illustrated in Fig. 6.12a. The initial state demonstrates a single dangling bond defect (left). Nearby a Si-bond is broken thermally with an activation enthalpy Q' (middle). The initial dangling bond forms a covalent Si bond with a neighboring atom (right). Thereby the *jumping flow defect* creates a new dangling bond and a local shear. The illustrated *jumping of flow defects* repeats until two dangling bond recombine. The defect annihilation of dangling bond defects during heating a-Si thin films has been verified by Electro Spin Resonance [RSP+91].

Annihilation by the interaction of two *flow defects* are commonly described by bimolecular stress relaxation kinetics. Former works have reported bimolecular stress relaxation kinetics in GeSbTe and AgInSbTe systems, too [Kal06, KSLPW03]. However, the nature of flow defects in amorphous phase-change materials is still unclear.

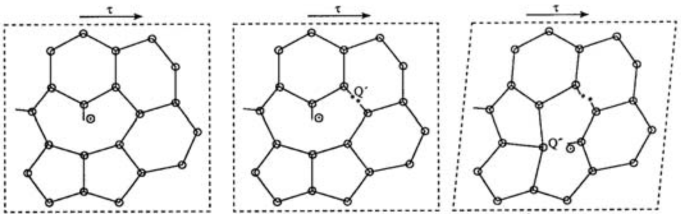

(a) Model of viscous flow in a-Si

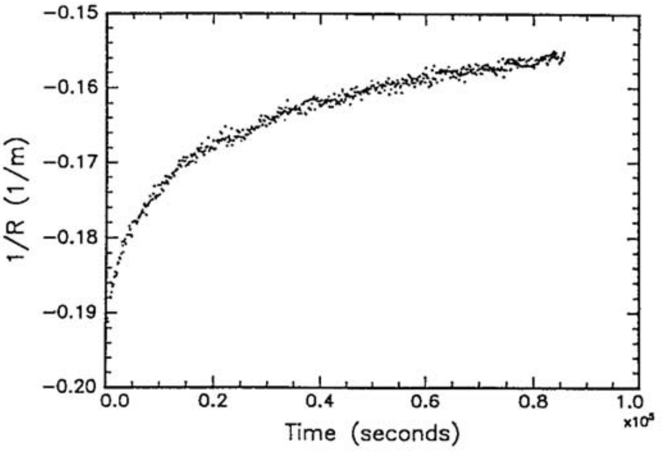

(b) Stress relaxation in a-Si

Figure 6.12: The mechanical stress, which is directly proportional to the presented curvature $1/R$, decreases irreversibly during heating ion-sputtered-amorphous silicon at 201°C (b). The irreversible change in mechanical stress is commonly referred to an irreversible structural relaxation. In amorphous silicon a structural relaxation based on recombination of two dangling bonds flowing through the specimen is proposed (a). Annihilation by the interaction of two defects are commonly described by bimolecular stress relaxation kinetics. Former works have reported bimolecular relaxation kinetics in GeSbTe and AgInSbTe systems,too. However, the nature of flow defects in amorphous phase-change materials is still unclear. Image source:[WS93]

6.2.3 X-Ray Absorption Fine Structure in a-Si

X-Ray Absorption Fine Structure in the EXAFS and XANES energy range has been studied in ion-beam-sputtered a-Si films by Di Cicco *et al.* [DCBCR90].

Fig. 6.13 compares the measured X-Ray absorption fine structure of a-Si thin films deposited on beryllium substrates at three different substrate temperatures. Even though a-Si thin films deposited at ambient temperature, 200°C or 400°C should demonstrate a significant different concentration of dangling bond defects (see Fig. 6.10a), no change of the X-Ray Absorption Fine Structure within the EXAFS energy range could be stated. However, the authors claimed that the analysis of the XANES absorption edge shown in the inset of Fig. 6.13 reveals a structural change with increasing substrate temperature.

No significant change in the EXAFS energy range can be observed in a-Si films deposited at varied substrate temperatures, which have been shown to possess different concentrations of dangling bond defects as measured by ESR, see Fig. 6.10a. In contrast EXAFS data taken on post-annealed amorphous GeTe thin films show a systematic increase of the measured EXAFS signal with increasing holding temperature. This remarkable difference suggests a very different nature or at least concentration of flow defects driving the structural relaxation process in a-Si and a-GeTe.

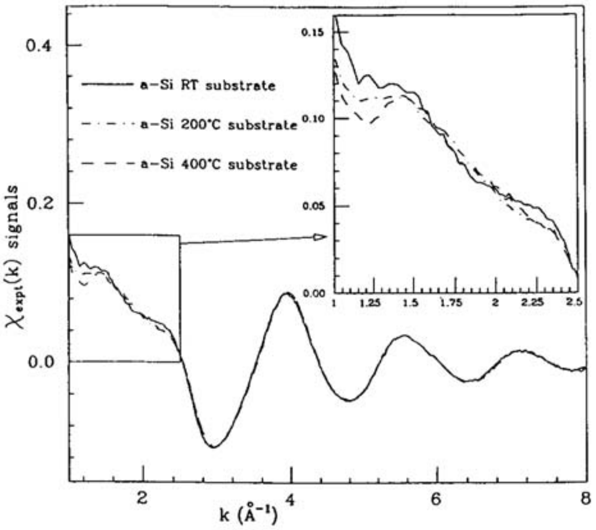

Figure 6.13: EXAFS and XANES spectra measured in a-Si:H samples deposited by ion-beam sputtering at three different substrate temperatures. The substrate temperature has no influence on the X-Ray Absorption Fine Structure in the EXAFS regime. However, the authors claim a significant structural change in the XANES energy range shown in the inset.

In contrast, X-Ray Absorption Fine Structure performed on post-annealed amorphous GeTe films show a systematic change within the EXAFS energy range with increasing annealing temperature. This finding suggests different natures of flow defects driving the structural relaxation process observed in both amorphous materials by the curvature method. Image source:[DCBCR90]

6.2.4 Dark and photoconductivity in a-Si/a-Si:H - The Staebler Wronski Effect

The covalent glasses a-Si and a-Si:H find broad application in the photovoltaic industry. Hence, these materials show, in contrast to amorphous phase-change materials, a significant photoconductivity at room temperature. Fig. 6.14a shows the change in conductivity measured in discharge produced amorphous Si during and after light exposure ($200\,\mathrm{mW/cm^2}$, $600-900\,\mathrm{nm}$).

Under light exposure the conductivity measured at room temperature increases by more than one order of magnitude. However, during light exposure the conductivity decreases significantly. Within four hours the conductivity measured under constant illumination decreases by nearly a factor eight. Light exposure is observed to have even a stronger impact on the dark conductivity. The dark conductivity is lowered by nearly four orders of magnitude from its initial state A. The decrease in the dark and photoconductivity is commonly attributed to the creation of dangling bond defects caused by illumination that breaks some SiH bonds.. However, the sample can be returned to its initial high conductive state A by heating it to about 150°C. The heat treatment at approximately 150°C is known to improve the forming of Si-H bonds and thus decreases the concentration of dangling bonds. This reversible photoelectronic effect has been first observed in 1977 by Staebler and Wronski [SW77], but even more than 30 years after its discovery the physical origins behind the Staebler-Wronski effect offer a broad field of research and many different models have been proposed for its explanation.

In contrast to a-Si no reversible photo-electronic effect is known in a-PCM. Furthermore, heating treatment shows to have opposite effects in covalent glasses and amorphous phase change materials. The amorphous state resistivity in a-PCM increases upon heating, whereas in a-Si and a-Si:H the resistivity is observed to decrease at elevated temperature around 150°C. Furthermore, the increase of the amorphous state resistivity is strongly linked to an increase of the activation energy of electric conduction in amorphous phase-change materials . Fig. 6.14b shows the dark conductivity measured in glow discharged amorphous Si. The sample can be reversibly switched between the high conductive state A and low conductive state B both illustrated Fig. 6.14 a. Heating the sample at 150°C for four hours induces a change in the activation energy of electric conduction, which decreases from 0.87 eV (state B) to 0.57 eV (state A) [SW77].

Conclusion

This section shows that, as for most semiconductors, the defect density has a large influence on the optical and electrical properties of a-Si and a-Si:H. However, these properties are also intimately linked to the concentration of hydrogen present in the material and to the way it links to silicon atoms. Such a situation for which the quality of the film is linked to an additional compound and its incorporation is not observed in a-GeTe. Besides, even though the stress relaxation in a-GeTe and a-Si is very similar the nature of the defect controlling the structural relaxation is expected to be very different in both materials.

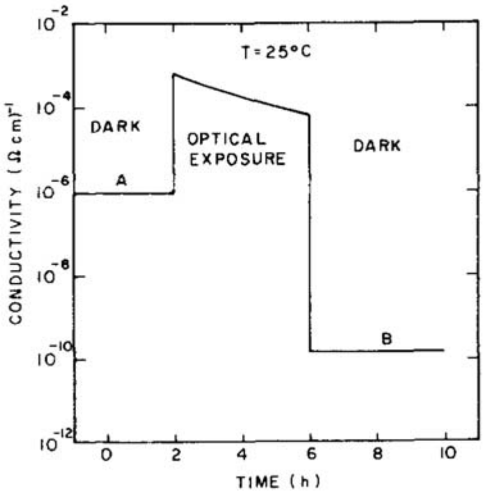

(a) Conductivity change in a-Si upon light exposure

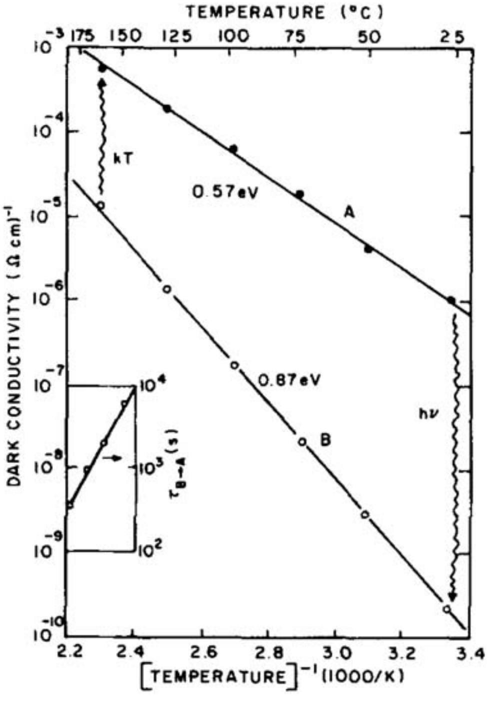

(b) Reversible photoelectronic effect in a-Si

Figure 6.14: Glow-discharge amorphous silicon shows a reversible photoelectronic effect between a high conductive state A and a low conductive state B (a). Light exposure decreases the dark and photoconductivity ($A \to B$), whereas heating above 150°C increases the dark and photoconductivity again ($B \to A$). This reversible phenomenon is known as the Staebler-Wronski Effect. In contrast, the resistance drift effect in amorphous phase-change materials is not known to be reversible. Furthermore, during heating the amorphous state resistivity and activation energy of electrical conduction increase in a-PCM and decrease in both covalent glasses a-Si and a-Si:H. Image source: [SW77]

.

6.3 Stoichiometry dependence of resistance drift phenomena in a-PCM

In the previous sections the origin of resistance drift phenomena in amorphous phase-change materials and covalent glasses has been discussed. It was shown that the increase in resistivity with time and temperature has most probably a structural origin in a-GeTe. In covalent glasses, such as a-Si and a-Si:H, the dangling bonds and hydrogen concentration strongly influence the optical and electrical properties. In contrast the nature of the defects driving the structural relaxation leading to an increasing amorphous state resistivity in a-GeTe is still unclear, but seems to differ from those observed in a-Si and a-Si:H.

With the objective to identify a phase-change material showing a low resistance drift effect the stoichiometry dependence of resistance drift phenomena in amorphous GeSnTe phase-change alloys has been studied. This section presents a systematic analysis of the electrical and optical properties including the defect state density studied in GeTe, $Ge_3Sn_1Te_4$ and $Ge_2Sn_2Te_4$. Furthermore, the drift behavior in a-GeSnTe systems is compared to the drift behavior observed in GeSbTe and AgSbInTe systems. Finally, the link between resistance drift phenomena and stress relaxation is discussed.

6.3.1 Resistivity change upon crystallization in GeSnTe phase-change alloys

The resistivity measured upon crystallization has been measured in amorphous GeSnTe thin films. The results are shown in Fig. 6.15. At the crystallization temperature T_c the resistivity of the phase-change layer drops significantly. The crystallization temperature is observed to decrease with increasing Sn content from 180°C for GeTe to 120°C for $Ge_2Sn_2Te_4$, see Tab. 6.3. GeSnTe films show a drastic difference in resistivity between the amorphous and the crystalline phase of more than three orders of magnitude. Whereas the crystalline state resistivity varies only slightly with increasing Sn content the amorphous state resistivity decreases very strongly. For instance at room temperature, a-$Ge_3Sn_1Te_4$ is ten times more conductive and a-$Ge_2Sn_2Te_4$ is even hundred times more conductive than a-GeTe. In comparison the conductivity in amorphous GeSbTe systems is rather stable with varying Sb content (GeTe = $4.5 \cdot 10^{-4}\,\mathrm{S/cm}$, $Ge_2Sb_2Te_5$ = $6.8 \cdot 10^{-4}\,\mathrm{S/cm}$ [LKS+10]). Hence, the conductivity of the crystalline state stays rather unaffected in a-GeSnTe systems the remarkable property contrast upon substitution of Ge by Sn observed in the amorphous state resistivity reveals an additional degree of freedom for the design of multi-level storage systems. Furthermore, the measured amorphous state resistivity is thermally activated in a large temperature range from 200 K to 350 K. The activation energy E_a is determined by the Arrhenius law given in Eq. 5.6. The substitution of Ge by Sn yields to a significant decrease of the activation energy of electrical conduction from $E_a = 0.38\,\mathrm{eV}$ in a-GeTe down to $E_a = 0.27\,\mathrm{eV}$ for a-$Ge_2Sn_2Te_4$, see Fig. 6.15 and Tab. 6.3.

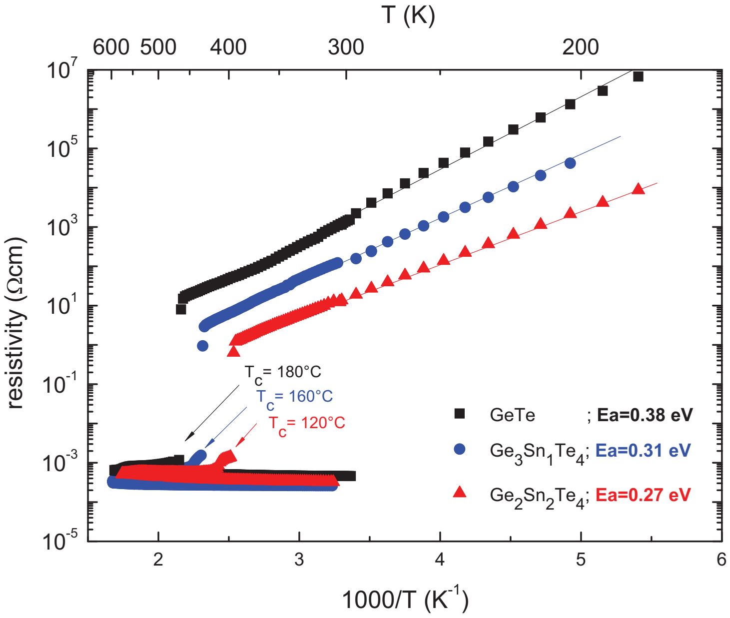

Figure 6.15: Resistivity measured in thin GeSnTe films (symbols). The highly resistive amorphous state shows a thermally activated behavior (line fits). The corresponding activation energy E_a decreases strongly with increasing Sn content. The measured resistivity drops at the crystallization temperature T_c . The crystallization temperature decreases with increasing tin concentration from T_c=180°C for GeTe to T_c=120°C for $Ge_2Sn_2Te_4$.

6.3.2 Optical band gaps in a-GeSnTe phase-change alloys

In many phase change materials it is observed that the optical band gap measured at room temperature is twice as large the activation energy of electric conduction, see Tab. 6.2. A common interpretation of this experimental observation is that the Fermi level is pinned at mid gap. To relate the optical band gap of a-GeSnTe films to the measured activation energies shown in Fig. 6.15 FT-IR experiments have been performed. Reflectance spectra versus photon energy were measured from room temperature down to 5 K in 50 K steps. The Reflectance spectra are analyzed using the simulation tool SCOUT from W. Theiss Hard- and Software [The].

The optical band gap E_g is defined according to the E_{04} method, where E_{04} is the energy at which the absorption coefficient α equals $1 \cdot 10^4\,\mathrm{cm}^{-1}$ [Stu70]. The optical band gaps $E_g(T) = E_{04}(T)$ of a-GeTe, a- $Ge_3Sn_1Te_4$ and a-$Ge_2Sn_2Te_4$ films measured at different temperatures T are shown in Fig. 6.16. Obviously, the band gap significantly decreases with increasing Sn content. In amorphous phase-change materials the temperature dependence of the optical band gap can be described by the simplified Varshni formula described by Eq. 5.20, where the coefficients $E_g(0)$ and ξ are material specific constants. The parameter $E_g(0)$ denotes the band gap at zero K temperature. The ξ parameter describes the parabolic decrease of the optical band gap with increasing measurement temperature. The change of the optical band gap with measurement temperature originates partly from the thermal expansion and partly from the renormalization of band energies by phonon electron interactions [AC83]. The optical band gaps measured by FT-IR experiments are fitted according to the simplified Varshni formula given by Eq. 5.20. The derived fit parameters $E_g(0)$ and ξ are listed in Tab. 6.3. The ξ-value does not change drastically with changing composition. In contrast, the optical band gap at zero K $E_g(0)$ changes by 120 meV with increasing Sn content. Consequently, the decrease in optical band gap observed at room temperature with increasing Sn concentration results mostly from a change in $E_g(0)$.

Tab. 6.3 compares the optical band gap to the activation energy of electrical conduction for each studied GeSnTe compound. This comparison strongly suggests that the decrease of the activation energy with increasing Sn concentration is attributed to the decrease in band gap. However, there is a systematic deviation from the relation $E_g(300K) = 2 \cdot E_a$ indicating that the Fermi level may shift away from mid gap with increasing Sn content.

Table 6.3: Activation energies E_a, optical band gaps at T = 300 K $E_g(300)$, and T = 0 K $E_g(0)$ compared to ξ values measured for different a GeSnTe phase-change alloys.

Material	E_a (eV)	$E_g(300K)$ (eV)	$E_g(0K)$ (eV)	ξ (10^{-6} eV/K^2)	$E_g(300K)/E_a$
a-GeTe	0.38	0.847	0.96	1.33	2.2
a-$Ge_3Sn_1Te_4$	0.31	0.741	0.87	1.56	2.4
a-$Ge_2Sn_2Te_4$	0.27	0.711	0.84	1.57	2.6

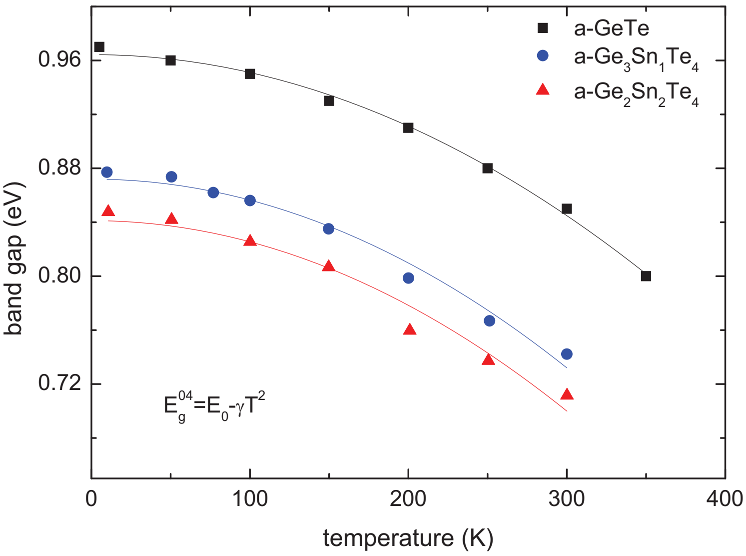

Figure 6.16: Optical band gap in a-GeSnTe systems measured by FT-IR at different temperatures (symbols). Over the whole investigated temperature range the optical band gap decreases with increasing Sn content. In all investigated GeSnTe alloys the optical band gap decreases parabolically with increasing temperature (line = fitting parabola). The systematic deviation of the relation $E_g(300K) = 2 \cdot E_a$, which is commonly observed in amorphous chalcogenides, indicates that the Fermi level may shift away from mid gap with increasing tin concentration.

6.3.3 Defect state densities in a-GeSnTe phase-change alloys

In amorphous materials localized defect states within the band gap have a strong influence on the position of the Fermi level. Their presence is a direct consequence of variable bond lengths and bond angles in disordered structures. The lack of long range order results in exponentially decaying band tails from the band edges. Additional structural defects, like dopants, form distributed defect peaks. To gain a better insight on the origin of the position of the Fermi level shifting systematically away from mid gap with increasing Sn content, the trap state density within the band gap is investigated for different GeSnTe alloys. These defect densities were probed employing the Modulated Photo Current technique.

MPC spectra measured on a-GeTe, a-$Ge_3Sn_1Te_4$ and a-$Ge_2Sn_2Te_4$ films are presented in Fig. 6.17. These measurements were performed with a LED (light emitting diode) light source of wavelength $\lambda = 850\,\mathrm{nm}$ using a continuous photon flux of $F_{dc} = 10^{16}\,\mathrm{cm^{-2}s^{-1}}$. The amplitude of the alternating photon flux was chosen to be 40% of the continuous flux. At a given temperature a MPC curve has been taken varying the excitation frequency $f = \omega/2\pi$ from 12 Hz to 40 kHz in a way such that $f_{i+1} = f_i \cdot 1.5$. According to the equations describing the energy scale , see Eqs. 5.21, 5.23 and 5.24 at a given temperature, states closer to the valence band edge were probed at 40 kHz, whereas energy states located further away from the band edges were sampled at 12 Hz. Since the envelope of the MPC curves taken at different temperatures reveals the relative density of states Nc/μ the temperature steps have to be chosen sufficient small. In this study MPC curves were taken at least each 20 K. To obtain a good resolution of the density of states the temperature step was reduced to a value as low as 5 K if necessary.

MPC measurements performed on a-GeTe reveal the existence of a valence band tail probed from 100K to 220K. A distributed shallow defect is sampled from 220K to 240K. Mid gap states are observed from 260 K to 290K. The MPC spectra presented in Fig. 6.17 are shown in the fully ξ-corrected energy scale assuming an attempt-to-escape frequency of either $\nu_p = 1 \cdot 10^{12}\,\mathrm{s^{-1}}$ (band tails and mid gap states) or $\nu_p = 1 \cdot 10^{10}\,\mathrm{s^{-1}}$ (shallow defect), because this choice of the attempt to escape frequency maximized the overlap of MPC curves taken at different temperatures. In contrast to a-GeTe, both Sn-rich compositions show only the existence of the valence band tail over the whole investigated temperature range varied from 60K to 230K. Furthermore, a systematic trend in the defect state density Nc/μ is found in GeSnTe systems: with increasing Sn content the defect density Nc/μ describing the valence band tail decreases. Thus, a-GeTe shows the highest and a-$Ge_2Sn_2Te_4$ the lowest trap state density Nc/μ. The shift of the Fermi level away from mid gap may be attributed to the lowering in defect density, which makes probably a pinning of the Fermi level in mid gap more difficult.

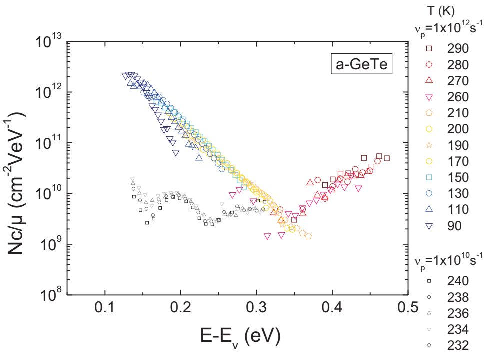

(a) a-GeTe

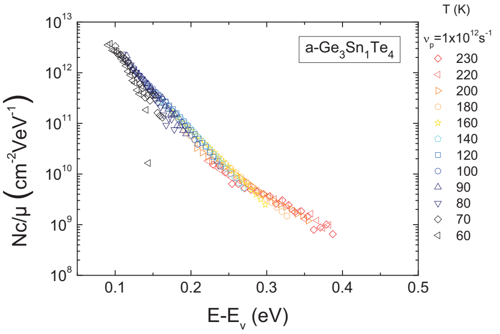

(b) a-$Ge_3Sn_1Te_4$

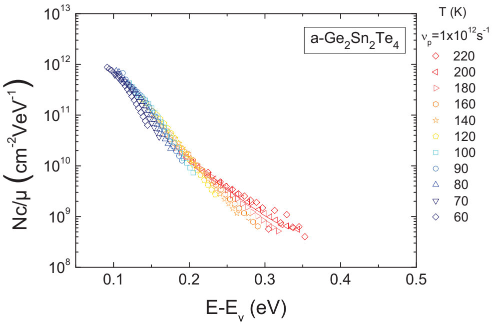

(c) a-$Ge_2Sn_2Te_4$

Figure 6.17: Defect state density measured by MPC on different GeSnTe systems. The electronic transport is governed by the absolute defect state N weighted by the ratio of capture coefficient c and free carrier mobility μ. This relative defect state density Nc/μ can be measured by Modulated Photo Current Experiments (MPC). The higher the capture coefficient c, which is directly proportional to the attempt-to-escape frequency , the stronger is the interaction between trap states and free carriers. Thus the attempt-to-escape frequency ν_p can be different for different kinds of traps. This is the case for a-GeTe: Mid gap and band tail states are described by $\nu_p = 10^{12}s^{-1}$ (large symbols) and shallow defects by $\nu_p = 10^{10}s^{-1}$ (small grey symbols). In a-$Ge_3Sn_1Te_4$ and a-$Ge_2Sn_2Te_4$ only band tail states described by $\nu_p = 10^{12}s^{-1}$ are measured within the whole investigated temperature range. Amorphous GeSnTe alloys show a systematic trend in the relative defect state density Nc/μ: the defect density describing band tail states decreases with increasing Sn concentration. Consequently, a-GeTe shows the highest and a-$Ge_2Sn_2Te_4$ the lowest trap state density Nc/μ. The lowering in defect density makes probably a pinning of the Fermi level at mid gap more difficult.

6.3.4 Resistance drift measured in amorphous phase-change and chalcogenide alloys

In a-GeSnTe phase-change alloys, systematic trends in the amorphous state resistivity ρ, activation energy of electric conduction E_a, optical band gap E_g and trap state density Nc/μ have been found with increasing Sn content. Since many models link the resistance drift effect to trap kinetics or band gap opening due to structural relaxation of the glassy state a significant change in the drift behavior in a-GeSnTe systems would be expected, too.

The evolution of the amorphous state resistivity over time t was studied in thin a-GeSnTe films while heating the samples for 48 h at 50°C in Ar atmosphere. Additionally the resistivity has been measured during the heating up and cooling down process to determine the activation energy of electric conduction at the start and the end of the annealing procedure. The observed increase in resistivity measured in thin phase change films is properly described by the relation,

$$\rho(t) = \rho_0 \cdot (1 + t/ts)^{\alpha_{\mathrm{RD}}} = \rho_0^* \cdot (t + ts)^{\alpha_{\mathrm{RD}}}. \tag{6.1}$$

The resistivity measured at the starting of the drift process is given by ρ_0. The temporal drift is described by the drift coefficient α_{RD}, i.e. the stronger the drift the higher the value of α_{RD} at a given temperature. The parameter t_s illustrates that the start point of the measurement defined to $t = 0\,\mathrm{s}$ does not match with the start of the drift mechanism, which should be expected to

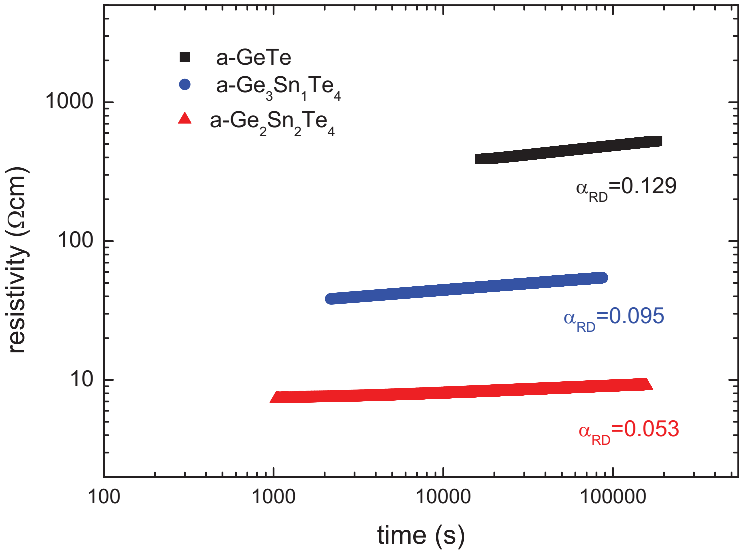

Figure 6.18: Resistivity measured in a-GeSnTe thin films while heating the films at 50°C for 48h. The evolution in resistivity with time follows a power law, see Eq. 6.1. The higher the drift parameter α_{RD} the stronger is the drift at a given temperature with time. The drift coefficient α_{RD} decreases significantly with increasing Sn content from α_{RD}=0.129 for a-GeTe to α_{RD}=0.053 for a-Ge$_2$Sn$_2$Te$_4$.

occur already in the deposition process. Fig. 6.18 presents the measured $\rho(t)$ data, where the time scale for each GeSnTe alloy was shifted by t_s to have a better visualization of the drift parameter α_{RD} in a double logarithmic plot (t_s(GeTe)=16455 s, t_s ($Ge_3Sn_1Te_4$)=745s, t_s ($Ge_2Sn_2Te_4$)=1781 s). Even though many theoretical models have been proposed, see chapter 3, the underlying physics explaining the resistance drift effect in amorphous chalcogenides is until now not completely understood. Nevertheless, this study on a-GeSnTe system shows, that the drift coefficient is strongly influenced by the Sn content: the drift coefficient α_{RD} measured at 50°C decreases significantly from α_{RD}=0.129 (a-GeTe) to α_{RD}=0.053 (a-$Ge_2Sn_2Te_4$) by adding Sn, see Fig. 6.18.

In comparison the drift parameters derived for a-GeTe and a-$Ge_2Sb_2Te_5$ differ only slightly, see Tab. 6.4. Like already observed in a-$Ge_2$$Sb_2Te_5$, an increase in activation energy is found upon annealing a-GeSnTe thin films, see Tab. 6.4. The change in activation energy is most pronounced in a-GeTe. In a-$Ge_2Sn_2Te_4$ the increase in activation energy is so small that it can not be resolved within error. This suggests that the drift parameter is closely linked to the activation energy. Fig. 6.19 compares the drift coefficient α_{RD} measured while heating different amorphous chalcogenides and phase-change alloys at 50°C versus their activation energy of electric conduction measured at the beginning of the annealing process E_a^{start}. Most measured compounds show a quite linear dependence between both quantities, where only $Ge_{15}Sb_{85}$ and $Ge_{15}Te_{85}$ form exceptions. Consequently, low drifting materials are characterized by a low activation energy of electric conduction.

Table 6.4: Drift coefficient at 50°C and activation energy E_a at the beginning and at the end of the annealing time for different GeSnTe alloys.

Material	$\alpha_{\mathrm{RD}}(50°C)$	E_a^{start} (eV)	E_a^{end} (eV)
a-GeTe	0.129± 0.002	0.37	0.39
a-$Ge_3Sn_1Te_4$	0.095± 0.002	0.30	0.31
a-$Ge_2Sn_2Te_4$	0.053± 0.002	0.27	0.27
a-$Ge_2Sb_2Te_5$	0.138±0.002	0.39	0.40
a-$Ge_8Sb_2Te_11$	0.139±0.002	0.38	0.40
a-$Ge_1Sb_2Te_4$	0.084±0.002	0.34	-
a-$Ag_4In_3Sb_{67}Te_{26}$	0.059±0.002	0.29	0.29
a-$Ag_{5.5}In_{6.5}Sb_{59}Te_{29}$	0.056±0.002	0.30	0.32
a-Sb_2Te	0.054±0.002	0.28	0.28
a-$Ge_{15}Sb_{85}$	0.133±0.002	0.22	0.22
a-$Ge_{15}Te_{85}$	0.052±0.002	0.44	0.46

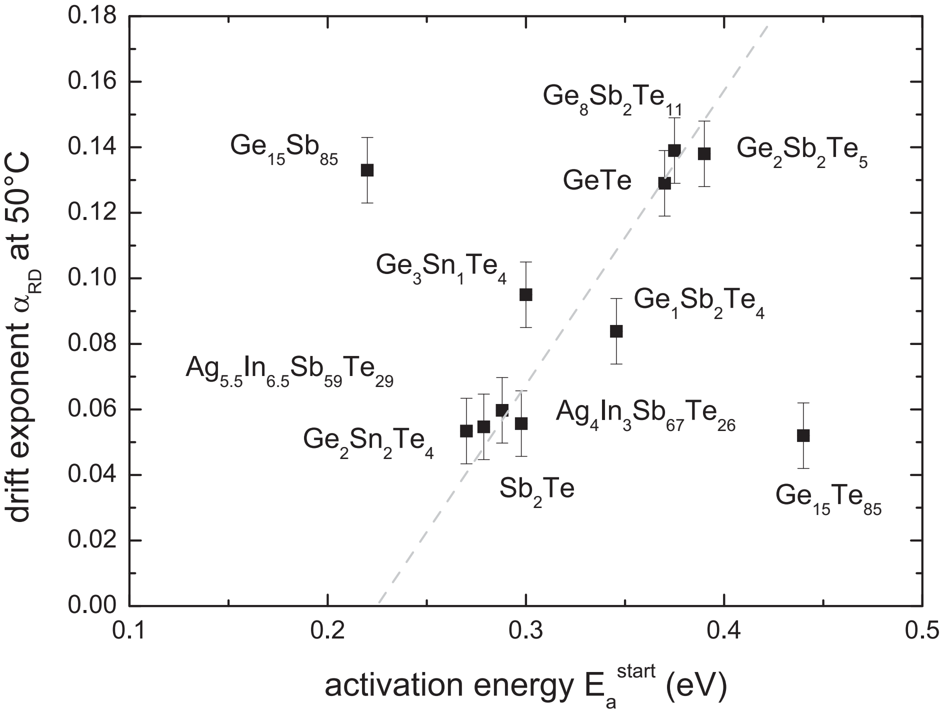

Figure 6.19: Comparison of drift exponents describing the increase in resistivity measured during heating amorphous phase-change materials and chalcogenides at 50°C. In most of the studied materials the resistance drift is linked to the activation energy of electrical conduction E_a^{start} measured at the start of the drift, where a-$Ge_{15}Te_{85}$ and a-$Ge_{15}Sb_{85}$ form exceptions.

6.4 Link between Stress relaxation and Resistance drift phenomena in a-PCM

To investigate a possible link between resistance drift and stress relaxation phenomena, the mechanical stress during heating has been studied in a-GeTe, a material showing a strong resistance drift and a-$Ge_2Sn_2Te_4$, which is one of the materials showing the lowest increase in resistivity with time. In accordance with the irreversible stress relaxation presented in section 6.1.4, the resistance drift is obviously linked to a structural relaxation of the glassy state.

Many works address the structural relaxation in glasses. One of the most prominent models to describe stress relaxation is the flow defect model [WS93, Spa81]. According to this model the irreversible structural relaxation can be described by a decreasing concentration of flow defects n causing irreversible shear rearrangements. Thereby the nature of flow defects can be very different: in amorphous silicon the flow defect could be identified as a dangling bond, whereas flow defects in metallic glasses are free volume fluctuations.
Former studies have demonstrated that the stress relaxation in GeSbTe and AgInSbTe systems is driven by bimolecular relaxation kinetics [Kal06, KSLPW03]. Bimolecular relaxation kinetics describes the flow defect annihilation by the interaction of two flow defects. For bimolecular annihilation reaction the change in flow defect concentration n is defined by $\dot{n} = -k_{r,b}n^2$, where $k_{r,b}$ is a thermally activated rate equation constant. At a constant temperature, bimolecular annihilation reaction of flow defects results in a linear increase in viscosity η,

$$\eta = \eta_0 + \dot{\eta} \cdot t. \tag{6.2}$$

The parameters n_0 and η_0 denote the initial flow defect concentration and initial viscosity at the specific temperature. Furthermore, $\dot{\eta} := n_0\eta_0 k_{r,b}$ describing the linear increase in viscosity is a constant at constant temperature. Far away from the equilibrium bimolecular stress relaxation results in a power law for the stress, where the corresponding drift exponent α_s is given by the mechanical properties of the amorphous phase-change material, such as the Young's modulus Y_f,

$$\ln\left(\frac{\sigma(t)}{\sigma_0}\right) = -\frac{Y_f}{6\dot{\eta}} \cdot \ln\left(1 + \frac{\dot{\eta}}{\eta_0} \cdot t\right) \tag{6.3}$$

$$\Leftrightarrow \sigma(t) = \sigma_0 \cdot \left(1 + \frac{\dot{\eta}}{\eta_0} \cdot t\right)^{-\frac{Y_f}{6\dot{\eta}}} \tag{6.4}$$

$$\Leftrightarrow \alpha_s = \frac{Y_f}{6 \cdot \dot{\eta}} \tag{6.5}$$

Hence, stress relaxation and resistance drift phenomena can be both described by rather similar power laws, compare Eq. 6.5 and Eq. 6.1. This finding suggests a strong link between resistance drift and stress relaxation phenomena.

Comparison of Resistance drift and stress relaxation phenomena

During heating an a-$Ge_2Sn_2Te_4$ thin film for 48 hours at 50°C the increase in resistivity has been measured in four point geometry, see Fig. 6.20a. For a better visualization of the very similar evolution of stress $\sigma(t)$ and resistivity $\rho(t)$ expressed by Eqs. 6.5 and 6.1 the data already presented in Fig. 6.18 is plotted in a linear scale without t_s correction in Fig. 6.20a. The evolution of the mechanical stress during heating an a-$Ge_2Sn_2Te_4$ thin film for 48 hours at 50 °C has been measured by the curvature method, see Fig. 6.20b. Both data, are properly described by a power law like predicted by Eq. 6.5 or Eq. 6.1, respectively. The drift exponent $\alpha_{RD} = 0.053$ describing the increase in resistivity over time is three times the drift exponent $\alpha_s = -0.017$ describing stress relaxation.

In a-GeTe the drift in resistivity at 50°C is described by $\alpha_{RD} = 0.129$. The stress relaxation in a-GeTe is observed to follow a power law having an exponent $\alpha_s = -0.044$. Consequently, a ratio $r = \alpha_{RD}/\alpha_s(50°C) \approx -3$ is found in a-GeTe and a-$Ge_2Sn_2Te_4$. This finding suggests the following relation between film stress σ and amorphous state resistivity ρ:

$$\rho(t) \propto \sigma(t)^r \tag{6.6}$$

$$\Rightarrow \alpha_{RD} = -r\frac{Y_f}{6\dot{\eta}} \tag{6.7}$$

It is remarkable that both phase-change alloys a-GeTe and a-$Ge_2Sn_2Te_4$ demonstrate the relation $\alpha_{RD}/\alpha_s(50°C) \approx -3$. This finding suggests that this ratio is valid for all those amorphous phase-change alloys in which the activation energy of electrical conduction predicts the resistance drift. Consequently, the resistance drift would be governed by parameters attributed to the glassy state, i.e. the bulk Young modulus Y_f and the parameter $\dot{\eta}$ describing the increase in viscosity.

According to the proposed relation, phase-change materials showing a high Young modulus Y_f and low parameter $\dot{\eta}$ are expected to show a strong drift. The Y_f values have been measured for a-$Ge_2Sb_2Te_5$ and a-$Ag_{5.5}In_{6.5}Sb_{59}Te_{29}$ by Kalb et al. employing the curvature method discussed in chapter 4. The authors find a Young modulus $Y_f = 27.6\,\mathrm{GPa}$ for a-$Ge_2Sb_2Te_5$ ($\alpha_{RD} = 0.138$) in comparision to $Y_f = 10.5\,\mathrm{GPa}$ for a-$Ag_{5.5}In_{6.5}Sb_{59}Te_{29}$ ($\alpha_{RD} = 0.056$).

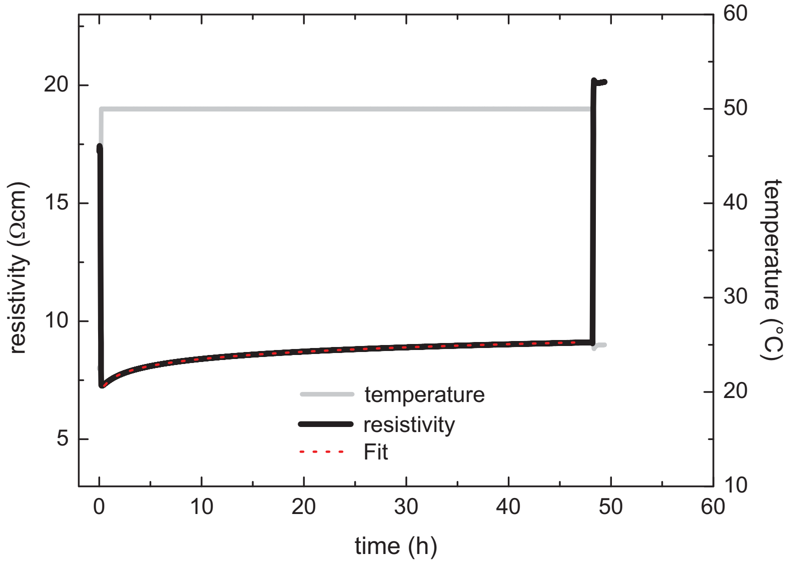

(a) Evolution of the amorphous state resistivity in a-$Ge_2Sn_2Te_4$

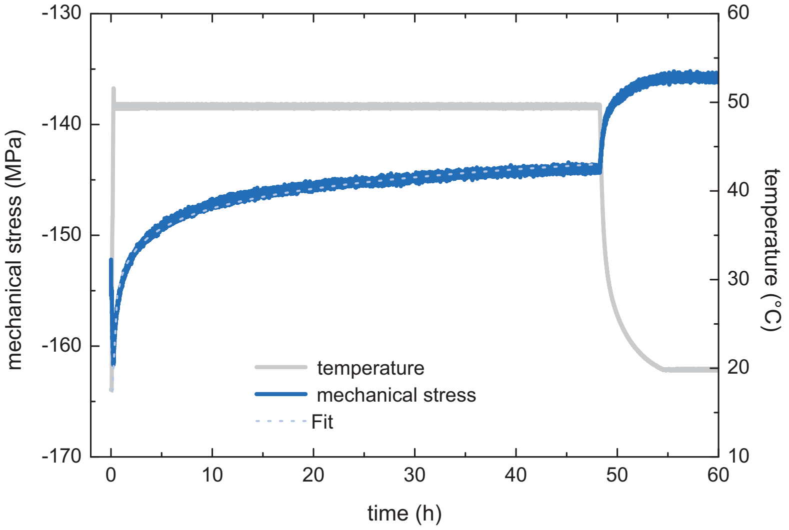

(b) Evolution of the mechanical stress in a-$Ge_2Sn_2Te_4$

Figure 6.20: Evolution of the amorphous state resistivity (a) and mechanical stress in a-$Ge_2Sn_2Te_4$ (b) during heating a-$Ge_2Sn_2Te_4$ for 48 hours at 50°C. Both phenomena can be described by a power law. The drift exponent describing the stress relaxation process is $\nu_s = -0.017$. The absolute value of the exponent describing the drift in resistivity is three times as large $\alpha_{RD} = 0.053$. A similar ratio between α_{RD} and ν_s has been found in a-GeTe. During heating a-GeTe at 50°C $\alpha_{RD}/\alpha_s(50°C) = 0.129/-0.044 = -2.9$ is found.

Conclusion and Perspectives

This thesis presents a detailed study of defect states in amorphous phase-change materials. Based on Modulated Photo Current experiments (MPC) and Photothermal Deflection Spectroscopy (PDS) a sophisticated band model has been developed for the binary phase-change alloy a-GeTe. This band model has been shown to consist of a deep defect level at mid gap, a shallow defect located ≈ 0.2 eV above the valence band edge and band tail states.

The interpretation of MPC data could be significantly improved by taking the temperature dependence of the band gap into account. On the example of a-GeTe and a-Si:H it has been demonstrated that the decrease of the optical band gap value with increasing measurement temperature can be considered by adding correction terms to the classic MPC energy scale defined by Brüggemann. Both proposed correction methods contract the MPC energy scale. Furthermore, in the case of a-GeTe it has been shown that both corrected energy scales resolve the problem of unphysical low values for the atttempt-to-escape frequencies. As exemplified on a-GeTe, unphysical low values for the atttempt-to-escape frequency derived by related detection methods may arise by neglecting temperature dependent band gaps of the material under study. In the fully ξ-corrected energy scale the width of the valence band has been determined to ≈ 30 meV, whereas PDS measurements reveal a much broader conduction band tail of a width of ≈ 60 meV.

The focus of this study has been to investigate the influence of defect states on electronic transport phenomena. For the studied chlacogenide glasses GeTe, $\mathrm{Ge_{15}Te_{85}}$ and $\mathrm{Ge_2Sb_2Te_5}$, it was demonstrated that those alloys exhibiting a high electrical threshold switching field also show a high density of mid gap states Nc/μ. This finding suggests a generation and recombination mechanism behind the threshold switching phenomenon.

The origin of resistance drift phenomena has been studied extensively in a-GeTe. The results of this study clearly demonstrate that the observed increase in the amorphous state resistivity is induced by an irreversible structural relaxation. This structural relaxation in the glassy state results in a defect annihilation of mid gap states, whereas the density of shallow defects positioned ≈ 0.2 eV above the valence band edge is observed to increase with time. In contrast to both defect levels, the valence and conduction band tail remain unchanged upon ageing or annealing. Despite unchanged band tai densities, the resistance drift effect has been shown to

be closely linked to band gap opening.
The resistance drift in a-GeTe characterized by a drift exponent $\alpha_{\mathrm{RS}} = 0.129$ is found to be rather strong. Phase-change alloys showing a low resistance drift such as a-$Ge_2Sn_2Te_4$ ($\alpha_{\mathrm{RS}} = 0.053$) could be identified. Thereby low drifting phase.change materials exhibit a low activation energy of electronic conduction as shown on the example of GeSnTe, GeSbTe and AgInSbTe systems.

Furthermore, a possible correlation between relaxation of internal film stresses and resistance drift phenomena has been studied in this thesis. Both phenomena, stress relaxation and resistance drift observed during heating are shown to follow a power law in a-GeTe and a-$Ge_2Sn_2Te_4$ thin films. Hence, resistance drift phenomena could be related to the materials properties of the glassy state, such as the YOUNG modulus Y_f or viscosity η. However, the relation between stress relaxation and resistance drift phenomena should be extended in future works for further materials and annealing temperatures.

Additionally, future research should be concentrated on the identification of the initial and final state behind the structural relaxation of the amorphous phase, which are expected to be very different from those observed in covalent glasses such as a-Si or a-Si : H. Therefore Photothermal Deflection Spectroscopy employing photon energies lower than 0.5eV provides an excellent characterizing tool. The structural relaxation on the atomic scale can be further analyzed by Extended X-Ray Absorption Fine Structure performed in their low temperature limit and Neutron Scattering experiments. Furthermore, Modulated Photo Current Experiments in combination with Raman Spectroscopy could help to identify the nature of the defect levels in a-GeTe.

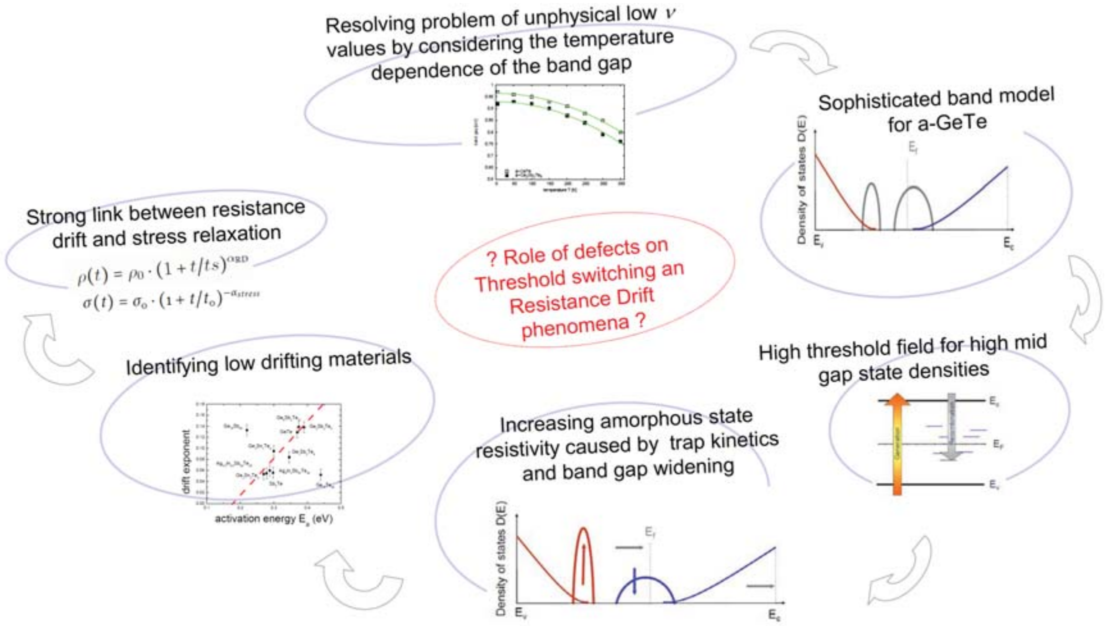
Resolving problem of unphysical low ν values by considering the temperature dependence of the band gap
temperature T (K)
Sophisticated band model for a-GeTe
Density of states D(E)
E_f
E_v
E_c
? Role of defects on Threshold switching an Resistance Drift phenomena ?
Strong link between resistance drift and stress relaxation
$\rho(t) = \rho_0 \cdot (1 + t/ts)^{\alpha_{RD}}$
$\sigma(t) = \sigma_0 \cdot (1 + t/t_0)^{-\alpha_{stress}}$
High threshold field for high mid gap state densities
E_c
E_F
E_v
Generation
Identifying low drifting materials
drift exponent
activation energy E_a (eV)
GeTe
Increasing amorphous state resistivity caused by trap kinetics and band gap widening
Density of states D(E)
E_f
E_v
E_c

Acknowledgements

First of all I would like to thank both my thesis advisors Christophe Longeaud and Matthias Wuttig, who made it possible that I could work on this interdisciplinary research project in two institutes within the framework of a joined PhD. In the last years I profited a lot of their support, knowledge and expertise. I really enjoyed to work and study at the University Paris-11 and the RWTH Aachen University and I am very happy to have this experience. Thank you for this time!

A special word of thanks is owed to my thesis reporters Christophe Bichara and Charles Main.

It is my sincere pleasure to thank my thesis committee members Chistophe Longeaud, Matthias Wuttig, Jean-Paul Kleider, Christophe Bichara, Charles Main and Volker Meden.

I am very thankful to Reinhard Carius and Josef Klomfaß for their interest on defects states in amorphous phase-change materials. My thesis work has been largely enriched by high qualitative PDS measurements and related scientific discussions.

A warm thanks goes to my former office mate Andrea Piarristeguy for nice discussions on GeSnTe systems and the WDX measurements performed at the University of Montpellier 2.

My thanks to all my colleagues in Aachen which have supported me in electronic transport measurements in amorphous phase-change materials, namely: Daniel Krebs, Janika Boltz, Stephan Kremers, Peter Jost, Stephanie Grothe, Hanno Volker, Gunnar Bruns, Carl Schlockermann and Rüdiger Schmidt. I am especially thankful for the good cooperation and discussions with Daniel and Peter about defect states and their impact on electronic and optical properties.

I would like to thank Peter Zalden and Pascal Rausch for fruitful discussions related to the structure of the amorphous phase. I always enjoyed the work with you and will keep this time in good memory. A special thanks owes to Peter for his effort regarding EXAFS measurements on annealed a-GeTe thin films.

Furthermore, I would like to thank Andreas Kaldenbach for valuable discussions on crystallization kinetics.

Josefine Elbert and Sarah Schlenter I am thankful for their help and advise regarding all kind of administrative tasks.

Then I would like to say a big thank to Ayana Bhaduri, Peiqing Yu, Vanessa Gorge, Olga Maslova, Boris Morel, Wilfried Favre, Irène Ngo, Djicknoum Diouf, Renaud Varache and José Alvarez for the nice time we had together at the LGEP and at all the other places we travelled together.

Besides the people from the I. Institute of Physics (IA) at the RWTH Aachen University and the Laboratoire de Génie Electrique de Paris, I am indebted to several people from other research facilities. Especially Sergei Baranovski from the Philipps-University Marburg, Theo Siegrist from the Florida State University and Jean-Yves Raty from the University of Liège. I am very thankful for the fruitful cooperation and valuable discussions concerning the transport and structure of amorphous phase-change materials.

A warm thanks to Denise-Schmandt Besserat who provided me with nice pictures to highlight the introduction part of my thesis.

Above all, my thanks goes to my family Patricia, Herbert and Nadine Luckas and my husband Guido Hontheim for their love and support during my life.

Bibliography

[AC83] Allen, P. B. ; Cardona, M.: Temperature dependence of the direct gap of Si and Ge. In: *Phys. Rev. B* 27 (1983), S. 4760–4769

[Adl71] Adler, D.: *Amorphous semiconductors*. THE BUTTERWORTH GROUP, 1971

[AHV72] Anderson, P.W. ; Halperin, B.I. ; Varma, C.M: Anomalous low-temperature thermal properties of glasses and spin glasses. In: *Philosophical Magazine* 25 (1972), S. 1–9

[AJ07] Akola, J. ; Jones, R. O.: Structural phase transitions on the nanoscale: The crucial pattern in the phase-change materials $Ge2Sb2Te5$ and GeTe. In: *Phys. Rev. B* 76 (2007), Nr. 23, S. 235201

[And75] Anderson, P. W.: Model for the Electronic Structure of Amorphous Semiconductors. In: *Phys. Rev. Lett.* 34 (1975), S. 953–955

[ASSO80] Adler, D. ; Shur, M. S. ; Silver, M. ; Ovshinsky, S. R.: Threshold Switching In Chalcogenide-Glass Thin-Films. In: *Journal Of Applied Physics* 51 (1980), S. 3289–3309

[Bar06] Baranovski, S.: *Charge Transport in Disordered Solids with Applications in Electronics*. John Wiley and Son, 2006

[BDM$^+$11] Bordovsky, G.A. ; Dashina, A.Y. ; Marchenko, A.V. ; Seregin, P.P. ; Terukov, E.I.: Impurity Centers of Tin in Glassy Arsenic Chalcogenides. In: *SEMICONDUCTORS* 45 (2011), S. 783–787

[BE06] Baily, S. A. ; Emin, D.: Transport properties of amorphous antimony telluride. In: *Phys. Rev. B* 73 (2006), S. 165211

[BEL06] Baily, S. A. ; Emin, D. ; Li, H.: Hall mobility of amorphous Ge2Sb2Te5. In: *Solid State Communications* 139 (2006), S. 161–164

[BFJA80] Boccara, A.C. ; Fournier, D. ; Jackson, W.b. ; Amer, N.M.: Sensitive photothermal deflection technique for measuring absorption in optically thin media. In: *Optics Letters* 5 (1980), S. 377–379

[BK87] Baranovski, S. ; Karpov, V. G.: Localized Electron-States In Glassy Semiconductors. In: *Soviet Physics Semiconductors-Ussr, Amer Inst Physics* 21 (1987), S. 1–10

[BKL+00] Brüggemann, R. ; Kleider, J.P. ; Longeaud, C. ; Mencaraglia, D. ; Guillet, J. ; Bourée, J.E. ; Niikura, C.: Electronic properties of silicon thin films prepared by hot-wire chemical vapour deposition. In: *Journal of Non-Crystalline Solids* 266-269 (2000), S. 258–262

[BMBR90] Brüggemann, R. ; Main, C. ; Berkin, J. ; Reynolds, S.: An Evaluation Of Phase-Shift Analysis Of Modulated Photocurrents. In: *Philosophical Magazine B-Physics Of Condensed Matter Statistical Mechanics Electronic Optical And Magnetic Properties* 62 (1990), Juli, Nr. 1, S. 29–45

[BMS+09] Bruns, G. ; Merkelbach, P. ; Schlockermann, C. ; Salinga, M. ; Wuttig, M. ; Happ, T.D. ; Philipp, J.B ; Kund, M.: Nanosecond switching in GeTe phase change memory cells. In: *Appl. Phys. Lett.* 95 (2009), S. 043108

[BRP+09] Boniardi, M. ; Redaelli, A. ; Pirovano, A. ; Tortorelli, I. ; Ielmini, D. ; Pellizzer, F.: A physics-based model of electrical conduction decrease with time in amorphous Ge2Sb2Te5. In: *Journal of Applied Physics* 105 (2009), S. 084506

[Bru07] Bruns, G.: *Der elektrisch induzierte Phasenwechsel in Tellur- und Antimonhaltigen Legierungen auf der Nanosekundenskala*, RWTH Aachen, Diplomarbeit, 2007

[BS80] Biegelsen, D. K. ; Street, R. A.: Photoinduced Defects in Chalcogenide Glasses. In: *Phys. Rev. Lett.* 44 (1980), Mar, Nr. 12, S. 803–806

[Car09] Carius, R.: *Tutorial 3: Characterization techniques.* 23rd International Conference on Amorphous and Nanocrystalline Semiconductors (ICANS 23), 2009

[CBK+07] Caravati, S. ; Bernasconi, M. ; Kühne, T.D. ; Krack, M. ; Parrinello, M.: Coexistence of tetrahedral- and octahedral-like sites in amorphous phase change materials. In: *Appl. Phys. Lett.* 91 (2007), S. 171906

[CFO69] Cohen, M. H. ; Fritzsche, H. ; Ovshinsky, S. R.: Simple Band Model For Amorphous Semiconducting Alloys. In: *Physical Review Letters* 22 (1969), Nr. 20, S. 1065

[Che89] Chevalier, P.Y.: A thermodynamic evaluation of the Ge-In, Ge-Pb, Ge-Sb, Ge-Tl and Ge-Zn systems. In: *Thermochimica Acta* 155 (1989), S. 227–240

[Che06] Chen, Y. C. et a.: Ultra thin Phase-Change Bridge Memory Device Using GeSb. In: *Proceedings of the IEEE International Electron Devices Meeting, San Francisco* (2006), S. 30.3.1.–30.3.4

[CP78] Chelikowsky, J. R. ; Phillips, J. C.: Quantum-defect Theory of Heats of Formation and Structural Transition Energies of Liquid and Solid Simple Metal-alloys and Compounds. In: *Physical Review B* 17 (1978), S. 2453

[CRB86] Chen, M. ; Rubin, K. A. ; Barton, R. W.: Compound Materials For Reversible, Phase-Change Optical-Data Storage. In: *Applied Physics Letters* 49 (1986), September, Nr. 9, S. 502–504

[CTA+81] Cody, G. D. ; Tiedje, T. ; Abeles, B. ; Brooks, B. ; Goldstein, Y.: Disorder and the Optical-Absorption Edge of Hydrogenated Amorphous Silicon. In: *Phys. Rev. Lett.* 47 (1981), S. 1480–1483

[DCBCR90] Di Cicco, A. ; Bianconi, A. ; Coluzza, C. ; Rudolf, P.: Xanes study of structural disorder in amorphous silicon. In: *Journal of Non-Crystalline Solids* 116 (1990), S. 27–32

[Det03] Detemple, R.: *Strukturelle und kinetische Aspekte der kombinatorischen Materialsynthese am Beispiel Phasenwechselmaterialien*, RWTH Aachen, Diss., 2003

[Dev96] Devreese, J.T.: Polarons. In: *Encyclopedia of Applied Physics* 14 (1996), S. 383 – 409

[Die02] Dieker, H.: *Chalkogenidlegierungsschichten mittels Röntgenreflektrometrie und spektroskopische Ellipsometrie*. 2002

[DNKL+92] Do ; N. Klees, L. ; Leung, P. T. ; Tong, F. ; Leung, W.P. ; Tam, A.C.: Temperature dependence of optical constants for amorphous silicon. In: *Appl. Phys. Lett.* 60 (1992), S. 2186

[DR72] Dow, J. D. ; Redfield, D.: Toward a Unified Theory of Urbach's Rule and Exponential Absorption Edges. In: *Phys. Rev. B* 5 (1972), S. 594–610

[Emi06] Emin, D.: Current-driven threshold switching of a small polaron semiconductor to a metastable conductor. In: *Phys. Rev. B* 74 (2006), Jul, Nr. 3, S. 035206

[EPM] Operating the Cameca SX 100 Electron Microprobe. In: *CAMECA SX 100 Instrument*

[ESQ72] Emin, David ; Seager, C. H. ; Quinn, Rod K.: Small-Polaron Hopping Motion in Some Chalcogenide Glasses. In: *Phys. Rev. Lett.* 28 (1972), S. 813–816

[FdMO71] Feinleib, J. ; deNeufville, J. ; Moss, S.C. ; Ovshinsky, S.R.: Rapid reversible light-induced crystallization of amorphous semiconductors. In: *Applied Physics Letters* 18 (1971), S. 254

[Fox02] Fox, M.: *Optical Properties of Solids*. Oxford University Press, 2002

[FP79] Freeman, Eva C. ; Paul, William: Optical constants of rf sputtered hydrogenated amorphous Si. In: *Journal of Physics and Chemistry of Solids* 20 (1979), S. 716–728

[Fri00] Friedrich, I.: *Optische Datenspeicherung mit Phasenwechselmedien - Präparation und Charakterisierung von GeSbTe Schichten*, RWTH Aachen, Diss., 2000

[GLP02] Gill, M. ; Lowrey, T. ; Park, J.: Ovonic unified memory - a high-performance nonvolatile memory technology for stand-alone memory and embedded applications. In: *Solid-State Circuits Conference, 2002. Digest of Technical Papers. ISSCC. 2002 IEEE International* 1 (2002), S. 202 – 459

[HAA+94] Hattori, K. ; Adachi, Y. ; Anzai, M. ; Okamoto, H. ; Hamakawa, Y.: Modulated photoconductivity study of charged and neutral defects in undoped amorphous silicon. In: *J. Appl. Phys.* 76 (1994), S. 2841

[HE08] Hegedüs, J. ; Elliot, S.R.: Microscopic origin of the fast crystallization ability of Ge–Sb–Te phase-change memory materials. In: *Nature Materials* 7 (2008), S. 399

[HR10] Huang, B. ; Robertson, J.: Bonding origin of optical contrast in phase-change memory materials. In: *Physical Review B* 81 (2010), S. 081204

[HR12] Huang, B. ; Robertson, J.: Nature of defects and gap states in GeTe model phase change materials. In: *Phys. Rev. B* 85 (2012), S. 125305

[Hro97] Hrouda, B.: *Mesopotamien*. C.H. Beck in der Beck'schen Reihe, Munich, 1997

[HT70] Howard, W. ; Tsu, R.: Photoconductivity and Density of States in Amorphous GeTe. In: *Physical review* 1 (1970), Nr. 12, S. 4709–4719

[HWS94] Herberholz, R. ; Walter, T. ; Schock, H.W.: Density of states in CuIn(SSe)2 thin films from modulated photocurrent measurements. In: *J. Appl. Phys.* 76 (1994), S. 2904

[Iel08] Ielmini, Daniele: Threshold switching mechanism by high-field energy gain in the hopping transport of chalcogenide glasses. In: *Phys. Rev. B* 78 (2008), S. 035308

[IL02] Ibach, H. ; Lüth, H.: *Festkörperphysik-Einführung in die Grundlagen*. Springer-Verlag Berlin Heidelberg New York, 2002

[ILSL08] Ielmini, D. ; Lavizzari, S. ; Sharma, D. ; Lacaita, A.L.: Temperature acceleration of structural relaxation in amorphous Ge2Sb2Te5. In: *Appl. Phys. Lett* 92 (2008), S. 193511

[ISLL09] Ielmini, D. ; Sharma, D. ; Lavizzari, S. ; Lacaita, A.L.: Reliability Impact of Chalcogenide-Structure Relaxation in Phase-Change Memory (PCM) Cells—Part I: Experimental Study. In: *IEEE Transaction on Electron Devices* 56 (2009), S. 1070

[IZ06] Ielmini, D. ; Zhang, Y.: Physics-based analytical model of chalcogenide-based memories for array simulation. In: *In Electron Devices Meeting, 2006. IEDM '06. International* (2006), S. 1–4

[IZ07] Ielmini, D. ; Zhang, Y.: Analytical model for subthreshold conduction and threshold switching in chalcogenide-based memory devices. In: *J. Appl. Phys.* 102 (2007), S. 054517

[JABF81] Jackson, W.B. ; Amer, N.M. ; Boccara, A.C. ; Fournier, D.: Photothermal Deflection Spectroscopy and Detection. In: *Applied Optics* 20 (1981), S. 1333–1344

[Jac75] Jackson, J.D.: *Classical Electrodynamics*. John Wiley and Sons, New York, 1975

[Jel98a] Jellison, G.E.: Spectroscopic ellipsometry data analysis: measured versus calculated quantities. In: *Thin Solid Films* 33 (1998), S. 313–314

[Jel98b] Jellison, G.E. J.: Spectroscopic ellipsometry data analysis: measured versus calculated quantities. In: *Thin Solid Films* 313-314 (1998), S. 33–39

[JKS⁺08] Jóvári, P. ; Kaban, I. ; Steiner, J. ; Beuneu, B. ; Schöps, A. ; Webb, M. A.: Local order in amorphous $Ge2Sb2Te5$ and $GeSb2Te4$. In: *Phys. Rev. B* 77 (2008), Nr. 3, S. 035202

[JM96] Jellison, G.E. J. ; Modine, F.A.: Parameterization of the optical functions of amorphous materials in the interband region. In: *Applied Physics Letters* 69 (1996), S. 371–373

[Jos] Jost, Peter:

[Jos09] Jost, P.: *Elektrischer Transport in Phasenwechselmaterialien - Untersuchungen mittels Infrarotspektroskopie und Seebeck-Messungen*. 2009

[JSCE86] John, S. ; Soukoulis, C. ; Cohen, M. H. ; Economou, E. N.: Theory of Electron Band Tails and the Urbach Optical-Absorption Edge. In: *Phys. Rev. Lett.* 57 (1986), S. 1777–1780

[JSI84] Junji Shirafuji, Taka'aki S. Mamoru Kuwagaki K. Mamoru Kuwagaki ; Inuishi, Yoshio: Effect of Substrate Temperature on Properties of Glow-Discharged Hydrogenated Amorphous Silicon. In: *Jpn. J. Appl. Phys.* 23 (1984), S. 1278–1286

[JWC] J.A. Woollam Co., Inc.: *Guide to Using WVASE32*

[KAF76a] Kastner, Marc ; Adler, David ; Fritzsche, H.: Valence-Alternation Model for Localized Gap States in Lone-Pair Semiconductors. In: *Phys. Rev. Lett.* 37 (1976), Nov, Nr. 22, S. 1504–1507

[KAF76b] Kastner, Marc ; Adler, David ; Fritzsche, H.: Valence-Alternation Model for Localized Gap States in Lone-Pair Semiconductors. In: *Phys. Rev. Lett.* 37 (1976), S. 1504–1507

[Kal06] Kalb, J.: *Crystallization kinetics in antimony and tellurium alloys used for phase change recording*, RWTH Aachen, Diss., 2006

[KBZ⁺11] Kim, S. ; Bae, BJ. ; Zhang, Y. ; Jeyasingh, R.G.D. ; Kim, Y. ; Baek, I.G. ; Park, S. ; Nam, SW ; Wong, H.S.P.: One-Dimensional Thickness Scaling Study of Phase Change Material Ge2Sb2Te5 Using a Pseudo 3-Terminal Device. In: *Electron Devices, IEEE Transactions on Issue Date: May 2011* 58 (2011), S. 1483 – 1489

[KC06] Kim, K. ; Choi, J.: Future Outlook on NAND Flash Technology for 40 nm Node and Beyond. In: *Proceedings of the IEEE Non-Volatile Semiconductor Memory Workshop* (2006), S. 9–11

[KCJ⁺05] Kang, D. H. ; Cheong, B. ; Jeong, J. ; Lee, T. S. ; Kim, I. H. ; Kim, W. M. ; Huh, J. Y.: Time-resolved analysis of the set process in an electrical phase-change memory device. In: *Appl. Phys. Lett.* 87 (2005), S. 253504

[KG93] Karpov, V. G. ; Grimsditch, M.: Pressure-induced transformations in glasses. In: *Phys. Rev. B* 48 (1993), S. 6941–6948

[KKI⁺07] Kim, J.J ; Kobayashi, K. ; Ikenaga, E. ; Kobata, M. ; Ueda, S. ; Matsunaga, T. ; Kifune, K. ; Kojima, R. ; Yamada, N.: Electronic structure of amorphous and crystalline (GeTe)1-x(Sb2Te3)x investigated using hard x-ray photoemission spectroscopy. In: *Physical Review B* 76 (2007), S. 115124

[KKO⁺98] Kolobov, A. V. ; Kondo, M. ; Oyanagi, H. ; Matsuda, A. ; Tanaka, K.: Negative correlation energy and valence alternation in amorphous selenium: An *in situ* optically induced ESR study. In: *Phys. Rev. B* 58 (1998), S. 12004–12010

[KKSK07] Karpov, V. G. ; Kryukov, Y. A. ; Savransky, S.D. ; Karpov, I. V.: Field-induced nucleation in phase change memory. In: *Appl. Phys. Lett.* 90 (2007), S. 123504

[KMK⁺07] Karpov, I.V. ; Mitra, M. ; Kau, D. ; Spadini, G. ; Kryukov, Y.A. ; Karpov, V.G.: Fundamental drift of parameters in chalcogenide phase change memory. In: *J. Appl. Phys.* 102 (2007), S. 124503

[Koe11] KOEHL, D.: *The influence of energetic bombardment on the structure formation of sputtered zinc oxide films - Development of an atomistic growth model and its application to tailor thin film properties*, RWTH Aachen, Diss., 2011

[Kou01] KOUNAVIS, P.: Analysis of the modulated photocurrent experiment. In: *Phys. Rev. B* 64 (2001), S. 045204

[Kre05] KREMERS, S.: *Wachstum, Struktur und optische Eigenschaften organischer MolekÄulschichten*. 2005

[Kre09] KREMERS, S.: *Optische Eigenschaften von Phasenwechselmaterialien für zukünftige optische und elektronische Speicheranwendungen*, RWTH Aachen, Diss., 2009

[Kre10] KREBS, D.: *Electrical Transport and Switching in Phase Change Materials*, RWTH Aachen, Diss., 2010

[KRR+09] KREBS, D. ; RAOUX, S. ; RETTNER, C.T. ; BURR, G.W. ; SALINGA, M. ; WUTTIG, M.: Threshold field of phase change memory materials measured using phase change bridge device. In: *Appl. Phys. Lett.* 95 (2009), S. 082101

[KSA02] KOROPECKI, R.R. ; SCHMIDT, J.A. ; ARCE, R.: Density of states in the gap of amorphous semiconductors determined from modulated photocurrent measurements in the recombination regime. In: *J. Appl. Phys.* 91 (2002), S. 8965

[KSLPW03] KALB, J. ; SPAEPEN, F. ; LEERVAD PEDERSEN, T. P. ; WUTTIG, M.: Viscosity and elastic constants of thin films of amorphous Te alloys used for optical data storage. In: *J. Appl. Phys.* 94 (2003), S. 4908

[Kur01] KURZWEIL, R.: The Law of Accelerating Returns. In: *KurzweilAI.net* (2001)

[Kur05] KURZWEIL, R.: *The Singularity is Near*. Viking Adult, 2005

[Lai08] LAI, S.K.: Flash memories: Successes and Chalenges. In: *IBM J. Res. and Dev.* 52 (2008), Nr. 4/5, S. 529–535

[Len10] LENCER, D.: *Design Rules, Local Structure and Lattice-Dynamics of Phase-Change Materials for Data Storage Applications*, RWTH Aachen, Diss., 2010

[LIL10] LAVIZZARI, S. ; IELMINI, D. ; LACAITA, A.L.: Transient Simulation of Delay and Switching Effects in Phase-Change Memories. In: *IEEE Transactions on Electron Devices* 57 (2010), S. 3257 – 3264

[Lit80a] LITTLEWOOD, P.B.: The crystal-structure of IV-VI compounds 1: Classification and Description. In: *Journal Physical C: Solid State Physics* 13 (1980), S. 4855

[Lit80b] Littlewood, P.B.: The crystal-structure of IV-VI compounds 2: A microscopic model for cubic-rhombohedral materials. In: *Journal Physical C: Solid State Physics* 13 (1980), S. 4875

[LK92] Longeaud, C. ; Kleider, J. P.: General-Analysis Of The Modulated-Photocurrent Experiment Including The Contributions Of Holes And Electrons. In: *Physical Review B* 45 (1992), Mai, Nr. 20, S. 11672–11684

[LKC00] Longeaud, C. ; Kleider, J.P. ; Cuniot, M.: Density of states in the gap of CdTe:V deduced from the modulated photocurrent technique. In: *Optical Materials* 4 (2000), S. 271–275

[LKK+99] Longeaud, C. ; Kleider, J.P. ; Kaminski, P. ; Koslowski, R. ; Pawlowski, M. ; Cwirko, J.: Investigation of defect levels in semi-insulating materials by modulated and transient photocurrent: comparison of methods. In: *Semiconductors Science Technology* 14 (1999), S. 747 – 756

[LKK+11] Luckas, J. ; Kremers, S. ; Krebs, D. ; Salinga, M. ; Wuttig, M. ; Longeaud, C.: The influence of a temperature dependent bandgap on the energy scale of modulated photocurrent experiments. In: *Journal of Applied Physics* 110 (2011), S. 013719–1

[LKS+10] Luckas, J. ; Krebs, D. ; Salinga, M. ; Wuttig, M. ; Longeaud, C.: Investigation of defect states in the amorphous phase of phase change alloys GeTe and Ge2Sb2Te5. In: *Physica Status Solidi C* 7 (2010), S. 852–856

[LKW05] Lankhorst, M.H.R. ; Ketelaars, B.W.S.M. ; Wolters, R.A.M: Low-cost and nanoscale non-volatile memory concept for future silicon chips. In: *Nature Materials* 4 (2005), S. 347 – 352

[LPS+03] Lankhorst, M.H.R. ; Pieterson, L. van ; Schijndel, M. van ; Jacobs, B.A.J. ; Rijpers, J.C.N.: Prospects of Doped Sb–Te Phase-Change Materials for High-Speed Recording. In: *Jpn. J. Appl. Phys.* 42 (2003), S. 863

[LSG+08] Lencer, D. ; Salinga, M. ; Grabowski, B. ; Hickel, T. ; Neugebauer, J. ; Wuttig, M.: A map for phase-change materials. In: *Nature Materials* 7 (2008), S. 972

[LSK06] Longeaud, C. ; Schmidt, J. A. ; Koropecki, R. R.: Determination of semiconductor band gap state parameters from photoconductivity measurements. II. Experimental results. In: *Phys. Rev. B* 73 (2006), S. 235317

[LSW11] Lencer, D. ; Salinga, M. ; Wuttig, M.: Design Rules for Phase-Change Materials in Data Storage Applications. In: *Advanced Materials* 23 (2011), S. 2030

[LT] Longeaud, C. ; Tobbeche, S.: Influence of hopping on the modulated photoconductivity. In: *unpublished yet*

[Luc08] Luckas, J.: *Investigating defect states in phase-change materials using modulated photo current experiments.* 2008

[MAK+11] Matsunaga, T. ; Akola, J. ; Kohara, S. ; Honma, T. ; Kobayashi, K. ; Ikenaga, E. ; Jones, R.O. ; Yamada, N. ; Takata, M. ; Kojima, R.: From local structure to nanosecond recrystallization dynamics in AgInSbTe phase-change materials. In: *Nature Materials* 10 (2011), S. 129

[ME71] Mott, N.F. ; E.A., Davis: *Electronic processes in non-crystalline materials.* CLARENDON PRESS, Oxford, 1971

[Mer11] Merkelbach, P.: *Crystalline Phase Change Materials: Disorder, Medium-Range Order and Electrical Switching*, RWTH Aachen, Diss., 2011

[MJGA10] Mitra, M. ; Jung, Y. ; Gianola, D.S. ; Agarwal, R.: Extremely low drift of resistance and threshold voltage in amorphous phase change nanowire devices. In: *Appl. Phys. Lett* 96 (2010), S. 222111

[MM08] Marshall, J.M. ; Main, C.: A new procedure for calculating the density and energy distribution of localized hopping sites in disordered semiconductors, using low-temperature electrical conductivity data. In: *J. Phys.: Condens. Matter* 20 (2008), S. 285210

[Moo65] Mooore, G.E.: Cramming More Components onto Integrated Circuits. In: *Electronics* 38 (1965), Nr. 8, S. 114–117

[Moo05] Mooore, G.E.: Excerpts from a Conversation with Gordon Moore: Moores's Law. In: *Intel Corporation* (2005), S. 1

[Mot68] Mott, N.F.: Conduction in glasses containing transition metal ions. In: *Journal of Non-Crystalline Solids* 1 (1968), S. 1–17

[MY02] Matsunaga, T. ; Yamada, N.: A Study of Highly Symmetrical Crystal Structures, Commonly Seen in High-Speed Phase-Change Materials, Using Synchrotron Radiation. In: *Jpn. J. Appl. Phys.* 41 (2002), S. 1674–1678

[Nem94] Nemilov, Sergei V.: *Thermodynamic and Kinetic Aspects of the Vitreous State.* CRC-Press, 1994

[NKJI09] Nardone, M. ; Karpov, V.G. ; Jackson, D.C.S. ; I.V, Karpov: A unified model of nucleation switching. In: *Appl. Phys. Lett.* 94 (2009), S. 103509

[NOT+00] Nonaka, T. ; Ohbayashi, G. ; Toriumi, Y. ; Mori, Y. ; Hashimoto, H.: Crystal structure of GeTe and Ge2Sb2Te5 meta-stable phase. In: *Thin Solid Films* 370 (2000), S. 258–261

[OHE81] OHEDA, H.: Phase-Shift Analysis Of Modulated Photocurrent - Its Application To The Determination Of The Energetic Distribution Of Gap States. In: *Journal Of Applied Physics* 52 (1981), Nr. 11, S. 6693–6700

[OJL97] OLeary, S. K. ; Johnson, S. R. ; Lim, P. K.: The relationship between the distribution of electronic states and the optical absorption spectrum of an amorphous semiconductor: An empirical analysis. In: *Journal Of Applied Physics* 82 (1997), Oktober, Nr. 7, S. 3334–3340

[OR73] Owen, A.E. ; Robertson, J. M.: Electronic Conduction and Switching in Chalcogenide Glasses. In: *IEEE Transaction on Electron Devices* 20 (1973), S. 105

[OT89] Overhof, H. ; Thomas, P.: *Electronic Transport in Hydrogenated Amorphous Semiconductors*. Springer-Verlag, 1989

[OTY+82] Okushi, H. ; Tokumaru, Y. ; Yamasaki, S. ; Oheda, H. ; Tanaka, K.: Energy dependence of electron-capture cross section of gap states in n-type a-Si:H. In: *Phys. Rev. B* 25 (1982), S. 4313–4316

[Ovs68] Ovshinsky, S.R.: Reversible electrical switching phenomena in disordered structures . In: *Physical Review Letters* 21 (1968), S. 1450

[Pau58] Pauw, L. J. d.: A Method of Measuring Specific Resistivity and Hall Effect of Discs of Arbitrary Shape. In: *Philips Research Reports* 13 (1958), S. 1

[PCYG00] Palinginis, K.C. ; Cohen, J.D. ; Yang, J.C. ; Guha, S.: Defect bands in a-Si–Ge:H alloys with low Ge content. In: *Journal of Non-Crystalline Solids* 266-269 (2000), S. 665–669

[Ped03] Pedersen, T.: *Mechanical Stresses upon Phase Transitions*, RWTH Aachen, Diss., 2003

[PH71] Pryor, R. W. ; Henisch, H. K.: MECHANISM OF THRESHOLD SWITCHING. In: *Appl. Phys. Lett.* 18 (1971), S. 324

[PLP+04] Pirovano, A. ; Lacaita, A.L. ; Pellizzer, F. ; Kostylev, S.A. ; Benvenuti, A. ; Bez, R.: Low-field amorphous state resistance and threshold voltage drift in chalcogenide materials. In: *IEEE Transaction on Electron Devices* 51 (2004), S. 714

[PPL+07] Park, J.B. ; Park, H.S. G.S.and B. G.S.and Baik ; Lee, J.H. ; Jeong, H. ; Kim, K.: Phase-Change Behavior of Stoichiometric Ge2Sb2Te5 in Phase-Change Random Access Memory. In: *Journal Of The Electrochemical Society* 154 (2007), S. H139–H141

[PPM+11a] Papandreou, N. ; Pozidis, H. ; Mittelholzer, T. ; Close, G. ; Breitwisch, M. ; Lam, C. ; Eleftheriou, E.: Drift-Tolerant Multilevel Phase-Change Memory. In: *3rd IEEE International Memory Workshop (IMW), IEEE* (2011)

[PPM+11b] Papandreou, N. ; Pozidis, H. ; Mittelholzer, T. ; Close, G.F. ; Breitwischy, M. ; Lamy, C. ; Eleftheriou, E.: Drift-Tolerant Multilevel Phase-Change Memory. In: *IEEE Transaction on Electron Devices* 11 (2011), S. 978–1–4577–0226–6

[PPS+10] Papandreou, N. ; Pantazi, A. ; Sebastian, A. ; Breitwisch, M. ; Lam, C. ; Pozidis, H. ; Eleftheriou, E.: Multilevel phase-change memory. In: *Electronics, Circuits, and Systems (ICECS), 2010 17th IEEE International Conference* (2010), S. 1017 – 1020

[PSRK03] Pieterson, L. van ; Schijndel, M. van ; Rijpers, J.C.N. ; Kaiser, M.: Prospects of Doped Sb–Te Phase-Change Materials for High-Speed Recording. In: *Appl. Phys. Lett.* 83 (2003), S. 1373

[PT85] Phillips, J. C. ; Thorpe, M. F.: Constraint Theory, Vector Percolation And Glass-Formation. In: *Solid State Communications* 53 (1985), Nr. 8, S. 699–702

[RBB+08] Raoux, S. ; Burr, G.W. ; Breitwisch, M.J. ; Rettner, C.T. ; Chen, Y.C. ; Shelby, R.M. ; Salinga, M. ; Krebs, D. ; Chen, S.H. ; Lung, H.L. ; Lam, C.H.: Phase-change random access memory: A scalable technology. In: *IBM Journal Of Research And Development* 52 (2008), S. 465–479

[RCD+11] Raoux, S. ; Cabrera, D. ; Devasia, A. ; Kurinec, S. ; Cheng, H. ; Zhu, Y. ; Breslin, C. ; Jordan-Sweet, J.: Influence of dopants o the Crystallization Temperature, Crystal Structure, Resistance, and Threshold Field for $Ge_2Sb_2Te_5$ and GeTe Phase change Materials. In: *E/PCOS Symposium* (2011)

[RJ87] Rabe, K. M. ; Joannopoulos, J. D.: Structural properties of GeTe at T=0. In: *Phys. Rev. B* 36 (1987), S. 3319–3324

[Rob07] Robinson, A.: *The Story of writing*. Thames & Hudson, London, 2007

[RSP+91] Roorda, S. ; Sinke, W. C. ; Poate, J. M. ; Jacobson, D. C. ; Dierker, S. ; Dennis, B. S. ; Eaglesham, D. J. ; Spaepen, F. ; Fuoss, P.: Structural relaxation and defect annihilation in pure amorphous silicon. In: *Phys. Rev. B* 44 (1991), Nr. 8, S. 3702–3725

[RW86] Ritter, D. ; Weiser, K.: Supression of Interference-fringes in Absorption measurements on thin films. In: *Optics Communications* 57 (1986), S. 336–338

[RXP07] Robertson, J. ; Xiong, K. ; Peacock, P.W.: Electronic and atomic structure of Ge2Sb2Te5 phase change memory material. In: *Thin Solid Films* 515 (2007), S. 7538–7541

[RYC⁺06] Ryu, S. O. ; Yoon, S. M. ; Choi, K. J. ; Lee, N. Y. ; Park, Y. S. ; Lee, S. Y. ; Yu, B. G. ; Park, J. B. ; Shin, W. C.: Crystallization behavior and physical properties of Sb-excess Ge2Sb2+xTe5 thin films for phase change memory (PCM) devices. In: *Journal Of The Electrochemical Society* 153 (2006), S. G234–G237

[SA84] Shklovskii, B.I. ; A.L., Efros: *Electronic Properties of Doped Semiconductors*. Springer-Verlag, 1984

[Sal08] Salinga, M.: *Phase Change Materials for Non-volatile Electronic Memories*, RWTH Aachen, Diss., 2008

[SATM94] Solis, J. ; Afonso, C.N. ; Trull, J.F. ; Morilla, M.C.: Fast crystallizing GeSb alloys for optical data storage. In: *J. Appl. Phys.* 75 (1994), S. 7788

[SBa] `http://www.utexas.edu/courses/classicalarch/images1/sealbullaetokens.jpg`

[SBb] Schmandt-Besserat, D.: *The earliest precursor of writing*. `http://en.finaly.org/index.php/The_earliest_precursor_of_writing`

[SB73] Simons, G. ; Bloch, A.N.: Pauli-force model potential for solids. In: *Physical Review B* 7 (1973), S. 2754

[SB89] Schumm, G. ; Bauer, G. H.: Spatially resolved and energy-resolved defect kinetics in *a* -Si:H: A comprehensive study by phase-shift analysis of modulated photocurrents. In: *Phys. Rev. B* 39 (1989), S. 5311–5326

[SB02] Schmandt-Besserat, D.: Signs of life. In: *Odyssey* Jan./Feb. (2002), S. 6

[SB09] Schmandt-Besserat, D.: Tokens and writing: the cognitive development. In: *Scripta* 1 (2009), S. 145–154

[Sel05] Selz, G.J.: *Sumerer und Akkader*. C.H. Beck in der Beck'schen Reihe, Munich, 2005

[SJB74] St John, J. ; Bloch, A.N.: Quantum-defect theory electronegativity scale for nontransitions elements. In: *Physical Review Letters* 33 (1974), S. 1095

[SJJ⁺10] Suyoun, L. ; Jeong, D.S. ; Jeong, J. ; Zhe, W. ; Park, Y. ; Ahn, H. ; Cheong, B.: A study on the temperature dependence of the threshold switching characteristics of Ge2Sb2Te5. In: *Appl. Phys. Lett.* 96 (2010), S. 023501

[SK07a] Sze, S.M. ; Kwok, K.Ng: *Physics of Semiconductor Devices*. Wiley Interscience, 2007

[SK07b] Sze, S.M. ; Kwok, K.NG.: *Physics of Semiconductor Devices*. John Wiley and Son, 2007

[SKW+08] Shportko, K. ; Kremers, S. ; Woda, M. ; Lencer, D. ; Robertson, J. ; Wuttig, M.: Resonant bonding in crystalline phase-change materials. In: *Nature Materials* 7 (2008), S. 653

[SM75] Street, R. A. ; Mott, N. F.: States in the Gap in Glassy Semiconductors. In: *Phys. Rev. Lett.* 35 (1975), S. 1293–1296

[SP74] Seager, C. H. ; Pike, G. E.: Percolation and conductivity: A computer study. II. In: *Phys. Rev. B* 10 (1974), S. 1435–1446

[Spa81] Spaepen, F.: *Physics of Defects*. Les Houches Lectures XXXV, North-Holland Amsterdam, 1981

[SR52] Shockley, W. ; Read, W. T.: Statistics Of The Recombinations Of Holes And Electrons. In: *Physical Review* 87 (1952), Nr. 5, S. 835–842

[SR06] Schwarzer, N. ; Richter, F.: On the determination of film stresses from substrate bending: Stoney's formula and its limits. (2006). `http://nbn-resolving.de/urn:nbn:de:swb:ch1-200600111`

[ST71] Simmons, J. G. ; Taylor, G. W.: Nonequilibrium Steady-State Statistics And Associated Effects For Insulators And Semiconductors Containing An Arbitraty Distribution Of Traps. In: *Physical Review B* 4 (1971), Nr. 2, S. 502–&

[Sto09] Stoney, G.G.: The tension in metallic films deposited by electrolysis. In: *Proc. R. Soc. London* 82 (1909), S. 172–175

[Str91a] Street, R. A.: *Hydrogenated Amorphous Silicon*. Cambridge University Press, 1991

[Str91b] Street, R.A.: *Hydrogenated amorphous silicon*. Cambridge University Press, 1991

[Stu70] Stuke, J.: Review of optical and electrical properties of amorphous semiconductors. In: *Journal of non-crystalline solids* (1970)

[SW77] Staebler, D. L. ; Wronski, C. R.: Reversible conductivity changes in discharge-produced amorphous Si. In: *Appl. Phys. Rev. Lett.* 31 (1977), S. 292

[The] Theiss, W.: *W.Theiss Hard- and Software*. `http://wtheiss.com/`

[TTN+00] Tichá, H. ; Tichý, L. ; Nagels, P. ; Sleeckx, E. ; Callaerts, R.: Temperature dependence of the optical gap in thin amorphous films of As2S3, As2Se3 and other basic non-crystalline chalcogenides. In: *Journal of Physics and Chemistry of Solids* 61 (2000), S. 545–550

[Urb53] Urbach, F.: The Long-Wavelength Edge of Photographic Sensitivity and of the Electronic Absorption of Solids. In: *Phys. Rev.* 92 (1953), S. 1324

[VAR67] VARSHNI, Y. P.: Temperature Dependence Of Energy Gap In Semiconductors. In: *Physica* 34 (1967), Nr. 1, S. 149–&

[VE10] Van Eijk, J.: *Structural Analysis of Phase-Change Materials using X-Ray Absorption Measurements*, RWTH Aachen, Diss., 2010

[VWD75] Vezzoli, G.C. ; Walsh, P. J. ; Doremus, L. W.: Threshold switching and the on-state in non-crystalline chalcogenide semiconductors: An interpretation of threshold-switching research. In: *Journal of Non-Crystalline Solids* 18 (1975), S. 333–373

[Wal89] Walukiewicz, W.: Amphoteric native defects in semiconductors. In: *Appl. Phys. Lett.* 54 (1989), S. 2094

[Wei02] Weis, H.: *Untersuchung gasochrom schaltender Wolframoxide*, RWTH Aachen, Diss., 2002

[WLW+07] Wuttig, M. ; Lüsebrink, D. ; Wamwangi, D. ; Welnic, W. ; M., Gillessen ; Dronskowski, R.: The role of vacancies and local distortions in the design of new phase-change materials. In: *Nature Materials* 6 (2007), S. 122–128

[WPD+06] Welnic, W. ; Pamungkas, A. ; Detemple, R. ; Steimer, C. ; Blügel, S. ; Wuttig, M.: Unravelling the interplay of local structure and physical properties in phase-change materials. In: *Nature Materials* 5 (2006), S. 56

[WS93] Witvrouw, A. ; Spaepen, F.: Viscosity and elastic constants of amorphous Si and Ge. In: *J. Appl. Phys.* 74 (1993), S. 7154

[WY07] Wuttig, M. ; Yamada, N.: Phase-change materials for rewriteable data storage. In: *Nature Materials* 6 (2007), S. 824–832

[YA75] Yoffa, Ellen J. ; Adler, David: Fermi energy and electronic specific heat in Mott insulators. In: *Phys. Rev. B* 12 (1975), S. 2260–2264

[YM00] Yamada, N. ; Matsunaga, T.: Structure of laser-crystallized Ge2Sb2+xTe5 sputtered thin films for use in optical memory. In: *J. Appl. Phys.* 88 (2000), S. 7020–7028

[YOA+87] Yamada, N. ; Ohno, E. ; Akahira, N. ; Nishiuchi, K. ; Nagata, K. ; Takao, M.: High Speed Overwritable Phase Change Optical Disk Material. In: *Jpn. J. Appl. Phys.* 26 (1987), S. 61

[YONA91] Yamada, N. ; Ohno, E. ; Nishiuchi, K. ; Akahira, N.: Rapid-phase transition of GeTe-Sb2Te3 pseudobinary amorphous thin films for an optical disk memory. In: *Journal of Applied Physics* 69 (1991), S. 2849

[Zal83] Zallen, R.: *The Physics of Amorphous Solids*. John Wiley and Sons, New York, 1983

[ZBE+10] Zalden, P. ; Bichara, C. ; Eijk, J. van ; Braun, C. ; Bensch, W. ; Wuttig, M.: Atomic structure of amorphous and crystallized Ge15Sb85. In: *J. Appl. Phys.* 107 (2010), S. 104312

[ZC93] Zhong, Fan ; Cohen, J. D.: Measured and calculated distributions of deep defect states in hydrogenated amorphous silicon: Verification of deep defect relaxation dynamics. In: *Phys. Rev. Lett.* 71 (1993), S. 597–600